# Modeling of the mechanical behavior of polytetrafluoroethylene (PTFE) compounds during their compaction at room temperature

Carole Frédy

## To cite this version:

Carole Frédy. Modeling of the mechanical behavior of polytetrafluoroethylene (PTFE) compounds during their compaction at room temperature. Mechanics of materials [physics.class-ph]. Université Pierre et Marie Curie - Paris VI, 2015. English. NNT : 2015PA066601 . tel-01336422

## HAL Id: tel-01336422

## https://theses.hal.science/tel-01336422

Submitted on 23 Jun 2016

*UPMC-2015/2016*

**THESE DE DOCTORAT**
**DE L'UNIVERSITÉ PIERRE ET MARIE CURIE**

Présentée par

## Carole FREDY

pour obtenir le grade de

**DOCTEUR DE L' UNIVERSITÉ PIERRE ET MARIE CURIE**

Domaine

**MÉCANIQUE - GÉNIE MÉCANIQUE - GÉNIE CIVIL**

Sujet de la thèse

# Modeling of the mechanical behavior of PolyTetraFluoroEthylene (PTFE) compounds during their compaction at room temperature

Soutenue à Cachan le 6 novembre 2015 devant le jury composé de :

| | | |
|---|---|---|
| Laurent Orgéas | Directeur de Recherche CNRS, UGA | Rapporteur |
| Gilles Régnier | Professeur, ENSAM | Rapporteur |
| Djimédo Kondo | Professeur, UPMC | Examinateur |
| Roland Séguéla | Directeur de Recherche CNRS, INSA de Lyon | Examinateur |
| Rodrigo B. Canto | Associate Professor, UFSCar | Invité |
| René Billardon | Professeur, ENS de Cachan | Directeur de thèse |
| Nicolas Schmitt | Professeur, UPEC/ENS de Cachan | Co-encadrant |
| René Gy | Directeur de département TMM, SGR | Encadrant industriel |

**LMT-Cachan**
ENS Cachan / CNRS / Université Paris Saclay
61 avenue du Président Wilson, F-94235 Cachan cedex, France

# Acknowledgements

≪ Nul ami influent ne m'aurait mieux servi. Il m'avait donné une chance de me risquer un peu – de m'assurer de ce je savais faire. [...] Je n'aime pas le travail – personne ne l'aime – mais j'aime ce que le travail recèle – la chance de se trouver. Sa réalité propre – pour soi-même, pas pour les autres –, ce que personne d'autre ne pourra jamais savoir. ≫

Joseph Conrad

Ce n'est pas du navire du capitaine Marlow dont il s'agit ici, mais de cette ultime étape de mon parcours universitaire qu'est le doctorat. De ce travail, je sors finalement grandie. Et ce long voyage n'aurait jamais pu être aussi enrichissant sans vous.

Ainsi, merci.

Merci à Laurent Orgéas et Gilles Régnier d'avoir accepté de lire ce manuscrit avec tant d'attention. Merci à Djimédo Kondo d'avoir présidé ce jury et à Roland Séguéla d'y avoir participé malgré son nouveau statut.

Merci à Rodrigo Canto, qui malgré la distance, l'heure matinale et quelques aléas de connexion transatlantique, a également pris part à ce jury. J'ai été fière de pouvoir te présenter ma suite de l'histoire. Merci pour cette collaboration franco-brésilienne très enrichissante construite au fil de tes séjours parisiens et de nos nombreuses conversations Skype.

Merci à Nicolas Schmitt d'avoir co-encadré mon travail avec une infinie patience. Merci pour tes idées, ton enthousiasme et ton soutien. Merci d'avoir toujours cru à l'aboutissement de ce projet.

Merci à René Billardon pour ce coup de téléphone reçu il y a bientôt cinq ans me proposant une thèse qui remplissait étonnamment tous les critères que je m'étais fixés. Un sujet dense, sur une poudre exotique, en pure collaboration avec des populations aux dimensions internationales, sur fond de challenge lancé par un industriel reconnu et innovant. Merci d'avoir été aussi confiant en mes capacités et mon autonomie. Certaines périodes ont été délicates à gérer mais je n'ai pas de regret, je n'aurais pas pu avoir meilleure formation.

Thank you to Monika Brodeßer, Julia Ziegler, Nafih Mekhilef, Alexis Ponnouradjou, Joerg Heldmann, Mathilde Leboeuf, Georges Moineau and the teams of Willich, Kontich and Northboro. Thank you for welcoming me to your plants and for helping me to make the link between a tiny 5 cm side cube to a hollow cylinder of several meters high. Merci à Flavien pour ce bout de LMT retrouvé en Webex et tes décriptages. Merci aux équipes du CREE et particulièrement Jérôme Brulin, Adrien Roman et Nassira Benameur pour nos échanges et pour m'avoir permis de réaliser certains de mes essais sur votre site.

Merci à René Gy et Xavier Brajer d'avoir porté vos regards d'industriels proactifs et bienveillants sur mes travaux de thèse. Merci pour la confiance que vous m'avez témoignée en me permettant de continuer l'aventure à SGR et en m'initiant à tous ces nouveaux domaines, notamment la mécanique du verre. Merci à l'équipe TMM pour votre accueil, votre soutien aux pauses café et votre bonne humeur.

Merci à Stéphane Roux. Tu n'apparais pas dans la liste des encadrants et tu considères que tu ne dois pas y figurer. Mais tu fais bel et bien parti des personnes qui m'ont le plus appris. Merci de m'avoir ouvert les yeux, de m'avoir poussée à prendre du recul et de m'avoir aidée à choisir les bonnes directions. Merci aussi de t'être investi dans ce travail avec tant de générosité. Sans ton aide, beaucoup de choses seraient restées conjectures.

Merci à Anna Trauth pour son rigoureux combat contre la DRX et à Caiuã C. Melo pour qui les mouchetis à la poudre n'ont plus de secrets. Un grand merci à vous deux pour votre contribution à ce travail. Je n'aurais pu rêver meilleurs stagiaires.

Merci à toutes les personnes du LMT de faire de ce laboratoire ce qu'il est, un endroit où il fait bon vivre, où discussions scientifiques passionnées, débats politiques enflammés et blagues potaches assumées coexistent en toute simplicité. Tout particulièrement, pour m'avoir appris à dompter certaines machines : merci à Boubou, Martin et Florent pour ASTREE, merci à Olivier et Patrick pour la DRX. Merci à tous les participants des réunions UTR avec qui j'ai pu partager connaissances et idées.

Merci à vous pour toutes nos discussions au bar et ailleurs, pour tous vos coups de pouce, pour tous ces bons moments : Aurélien, Benoit, Florent, Erwan, Enrico, Ionut, John-Eric, Martin, Matteo, Maxime F., Maxime W., Pierre B., Pierre G., Pierre M., Renaud. Et outre tous ces messieurs, merci aux précieuses copines de labo, Lise et Andreea.

Merci aux FDL, merci pour tous ces moments de détente, de confidences et de rigolades, merci pour votre amitié. Une histoire de plus à ajouter à notre long palmarès. J'ai tellement hâte de vivre les suivantes !

Merci à ma famille pour m'avoir fourni tous les outils et l'amour qui m'ont permis d'arriver jusqu'ici. Et je n'oublie pas les Luu ! Merci pour votre hospitalité et votre soutien.

Merci à toi Guillaume sans qui rien n'aurait la même saveur, sans qui les victoires n'en seraient pas vraiment, sans qui je ne me serais jamais trouvée. Merci d'avoir veillé sur notre cap et d'avoir toujours gardé la jauge du bonheur dans le vert, même dans les moments les plus durs.

Et finalement quelques mots clés : Rungis, micro, hexagone, boudin, paix, Yohann-gallery, caresse des îles, ti amo, Shkodër.

# Contents

# Introduction

In western countries, friction and wear phenomena cause losses up to 4% of the Gross Domestic Product GDP ([Frêne et Zaïdi, 2014]). In modern automobile, more than 25% of the power supplied by engine is lost by friction. In a time where energy saving should be a concern at the heart of the development of new technologies, tribological solutions are to be mobilized. PolyTetraFluoroEthylene or PTFE is one of the flagship materials for these applications.

PTFE is a semi crystalline polymer widely used for its very low friction coefficient but also for its numerous other advantages such as electrical insulation, high resistivity to corrosion and high thermal stability. It is used in many fields from engine to domestic cooking pan, from the chemical industry to electric insulation system, from architectural structure to surgical implant.

Because of its high viscosity at melting temperature, raw PTFE cannot be manufactured thanks to usual processes developed for thermoplastics like injection or melt extrusion. One of the production pathways (the one favored for bulk material) is inspired from the process used for ceramic or metallic powders, viz. powder compaction at room temperature followed by a thermal treatment, commonly named sintering. It is this production route that will be the focus of the present work. Other production processes are lubricated paste extrusion, impregnation of glass fabrics or coating on metallic substrates. However they are limited to specific applications and represent a small fraction of the total production. This PhD study is a project involving a partnership between the Laboratoire de Mécanique et Technologie de Cachan (LMT-Cachan), one of the research departments of ENS-Cachan, and two entities of the industrial partner Saint-Gobain: Saint-Gobain Recherche and Saint-Gobain Performance Plastics. Large billets of pure and filled PTFE are produced in their plants. Developing numerical tools to model the manufacturing process of these parts to improve the production is their long term objective.

The goal of this study is to propose a modeling of the mechanical behavior of filled PTFE compounds during their pressing at room temperature.

## 1 Two examples of application

Mechanical and physical properties of PTFE are unique in the field of polymeric materials ([Ebnesajjad, 2002], [Sperati et Starkweather Jr, 1961]). The table 1 provides a quantitative comparison of PTFE and PolyEthylene (PE) for mechanical and physical properties.

**Table 1:** Comparison of PTFE and PE physical properties from [Ebnesajjad, 2002]

| PROPERTY | PTFE | PE |
|---|---|---|
| Density | 2.2 - 3.3 | 0.92 - 1 |
| Melting Temperature (°C) | 342 (first)<br>327 (second) | 105 - 140 |
| Dielectric Constant, 1 kHz | 2.0 | 2.3 |
| Surface Energy (dynes/g) | 18 | 33 |
| Resistance to Solvents and Chemicals | Excellent<br>No solvent known | Susceptible to hot hydrocarbons |
| Thermal Stability | | |
| $T_{1/2}$ (°C) | 505 | 404 |
| $k_{350}$ (%/min) | 0.000002 | 0.008 |
| $E_{act}$ (kJ/mol) | 339 | 264 |
| Melt Viscosity (Poise) | $10^{10}$ - $10^{12}$ | - |
| Refractive Index | 1.35 | 1.51 |
| Chain Branching Propensity | No | Yes |

The noteworthiest advantages and particularities of PTFE are:

- low friction coefficient,
- high electrical resistivity, low dielectric constant, low dissipation factor,
- insolubility in most solvents and resistance to acid and basic solution,
- wide thermal stability range, enabling a continuous use across a large temperature range,
- high fire resistance,
- hydrophobicity,
- cryogenic properties, even at a temperature of 4K, ductility is still present.

Citing [Rae et Dattelbaum, 2004] "*During deformation, PTFE stores much more of the work done as structural change (30%) than typical metals (<10%)*". Even in the brittle state, the dissipation of energy associated with the propagation of crack in PTFE is more than one order of magnitude greater than common structural engineering polymer ([Brown et Dattelbaum, 2005]).

Consequently, PTFE finds its place in various fields and applications. For instance, thanks to the low surface energy stability, good mechanical properties and high chemical resistance, it is used in medical applications such as ligament replacements or cardiovascular grafts. For the construction industry, fiberglass fabric may be coated with PTFE for stadium and airport roof for its excellent weatherability, flame resistance, low surface energy, resistance to UV and white color.

Hereunder two applications developed by Saint-Gobain Performance Plastics are described in more detail.

OmniSeal® seals are used in rotary mechanisms (figure 1). The use of PTFE allows for an easy rotation due to its low friction coefficient as well as the possibility of using it in aggressive chemical and thermal conditions, encountered for instance in oil and gas industry or engine applications. Specific fillers may be added to the raw PTFE to improve its wear properties of the part without depreciating its friction characteristics.

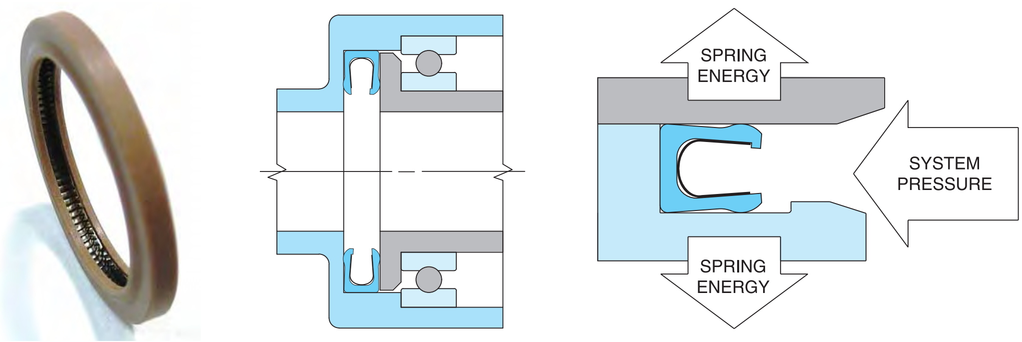

(a) OmniSeal®  (b) Scheme of a typical installation  (c) zoom

**Figure 1:** Example - OmniSeal® seals are used in rotary mechanisms (from OmniSeal® brochure). They are composed of a filled PTFE part in which an energized spring is inserted. When the pressure applied on the seal is increased, the spring opens and squeezes the polymer lips against the rotating part in order to avoid any leakage while allowing the rotation of the parts.

An other remarkable application is Norglide® bearings, which are maintenance-free bearings composed of a PTFE film coating the inner surface of a metallic part (figure 2). This way, bearings are able to withstand high loads without the need for adding lubricant. As additional benefits, noise level is reduced and vibration damping is good. Here again, adding fillers offers a better wear resistance of the PTFE film. Figure 2.(e) gives an overview of different applications of Norglide® bearings in a single car.

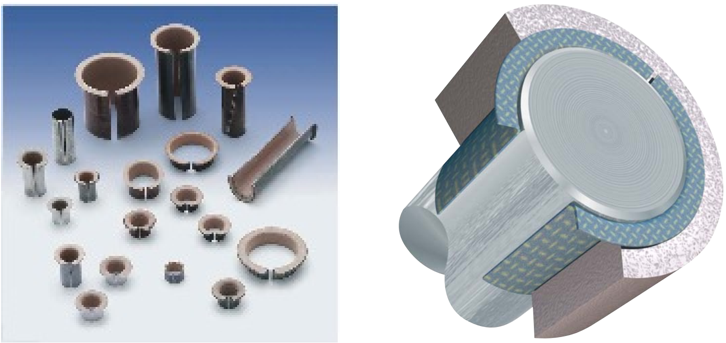

(a) Norglide® (b) Scheme

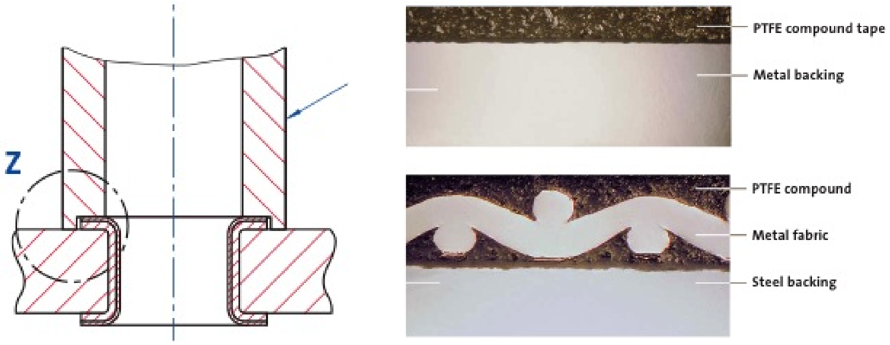

(c) Assembly (d) zoom

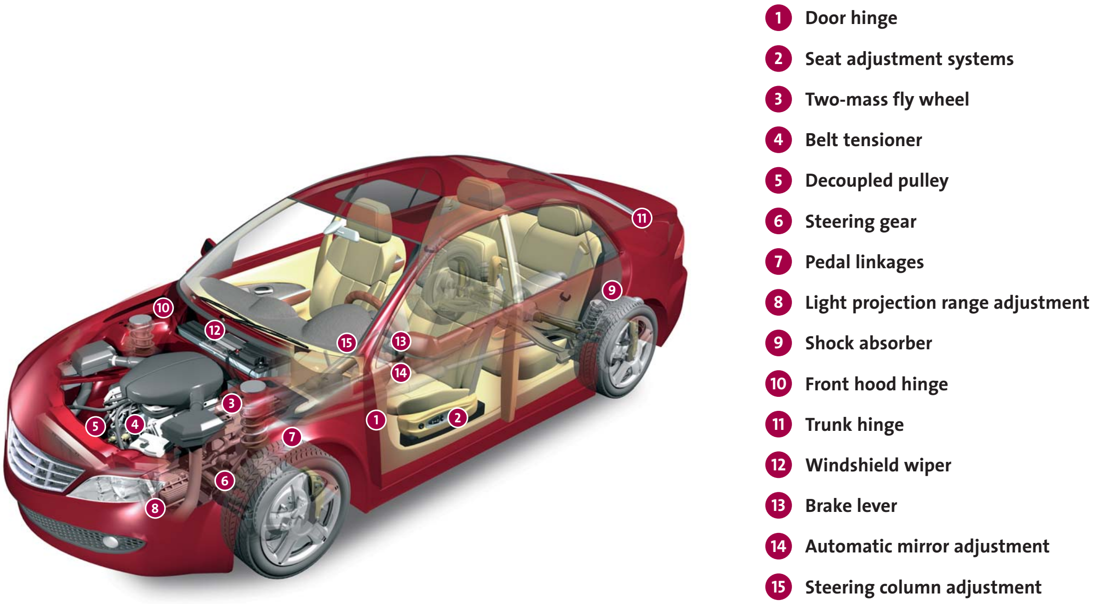

(e) Applications in a car

**Figure 2:** Example - Norglide® are maintenance-free bearings composed of a PTFE film coating the inner surface of a metallic part. Structural stability and strength of the part can be reinforced with metal fabrics, whose cross-sectional view of the assembly is presented figure (d). In figure (e), the different applications of Norglide® bearings in a car are listed.

# 2 PolyTetraFluoroEthylene - from atomic to macroscopic scale

**Discovery** The discovery of PTFE is one of the most famous examples of serendipity. Indeed, PTFE was accidentally discovered in 1938 by Dr. Roy Plunkett of DuPont de Nemours Company. Dr. Plunckett was pursuing studies on a safer and non inflammable refrigerant liquid, based on TetraFluoroEthylene (TFE). During one of his tests, by cooling down a compressed TFE sample, he produced a white powder which appeared not to be dissolved in any solvent, acid or base and which formed a clear gel without flow up to melting. This turned out to be the first PTFE powder production. His discovery was quickly developed in collaboration with the US Army in the frame of the Manhattan project during Word War II. The first application of PTFE was for gaskets, packings and liners in the chain of production of the Uranium 235 as no other polymers were able to undergo such critical environment. The first commercialization of PTFE by DuPont de Nemours took placed in 1945 under the brand name Teflon®.

**Chemical structure** PTFE is a semi crystalline polymer whose chemical structure $(CF_2\text{-}CF_2)_n$ consists of long carbon chains which are surrounded by fluorine atoms. Its molecular weight is high, in the order of $10^7$g/mol. The atomic structure is similar to the one of polyethylene PE where hydrogen is replaced by fluorine. They are highly reactive with the highest electronegativity of all elements. The carbon-carbon and carbon-fluorine bonds are extremely strong (607kJ/mole for C-C and 552kJ/mole for C-F). Due to the size of the fluorine atom, the carbon chain looks like surrounded by a continuous capsule of fluorine and thus protected and insulated. This particular structure provides PTFE with a wide range of advantages, such as the highest chemical resistance among organic polymers, one of the highest thermal stability, the lowest energy surface and low friction coefficient.

PTFE molecules have:

- low polarizability or ionization coefficient which minimizes the nonpolar force between PTFE molecules or PTFE molecules and other molecules,
- no permanent dipoles which minimizes the dipole-dipole force,
- neutral electronic state and geometric symmetry which prevents PTFE molecules from hydrogen bonding,
- no side groups nor branching during the polymerization which prevents chains from cross-linking.

As a consequence, PTFE chains may easily slide on each other or on other material. It gives rise to properties like low friction coefficient, low surface energy, high elongation and low tensile strength.

To accommodate the large size of the fluorine atoms, the chains adopt a helical conformation (figure 3). The planar zigzag conformation, observed in PE chains for instance, is, in the case of the PTFE, a metastable conformation which is strain-induced and reached only at high level of pressure (more than 500 MPa). This is common to polymers with helical structure as described by [Seguela, 2005].

Besides this phase transformation occurring at high stress levels, PTFE exhibits two crystalline phase transitions, at atmospheric pressure ([Clark, 1999], [Rigby et Bunn, 1949]). Figure 3, from [Brown *et al.*, 2007], shows the different phases, their associated conformation and their domain of existence in the hydrostatic stress vs. temperature diagram. At atmospheric pressure, below 19°C, the chains form an helix such that 13 $CF_2$ groups are required to complete a 180° twist to the helix (phase II). The crystalline system is triclinic. Around 19°C, a first order transition occurs. Between 19°C and 30°C (phase IV) the twist angle of the helix decreases, and 15 instead of 13 $CF_2$ groups are required for a 180° twist. The crystalline system changes to hexagonal. Above 30°C, the structure becomes disordered (phase I). A last crystalline change occurs around 340-350˚C during heating of the as-received PTFE (virgin of any previous thermal treatment). The crystalline phase progressively disappears during melting and the material becomes amorphous. The amorphous part of the material presents also two transitions which occur at atmospheric pressure at -97°C and 127°C ([McCrum, 1959]).

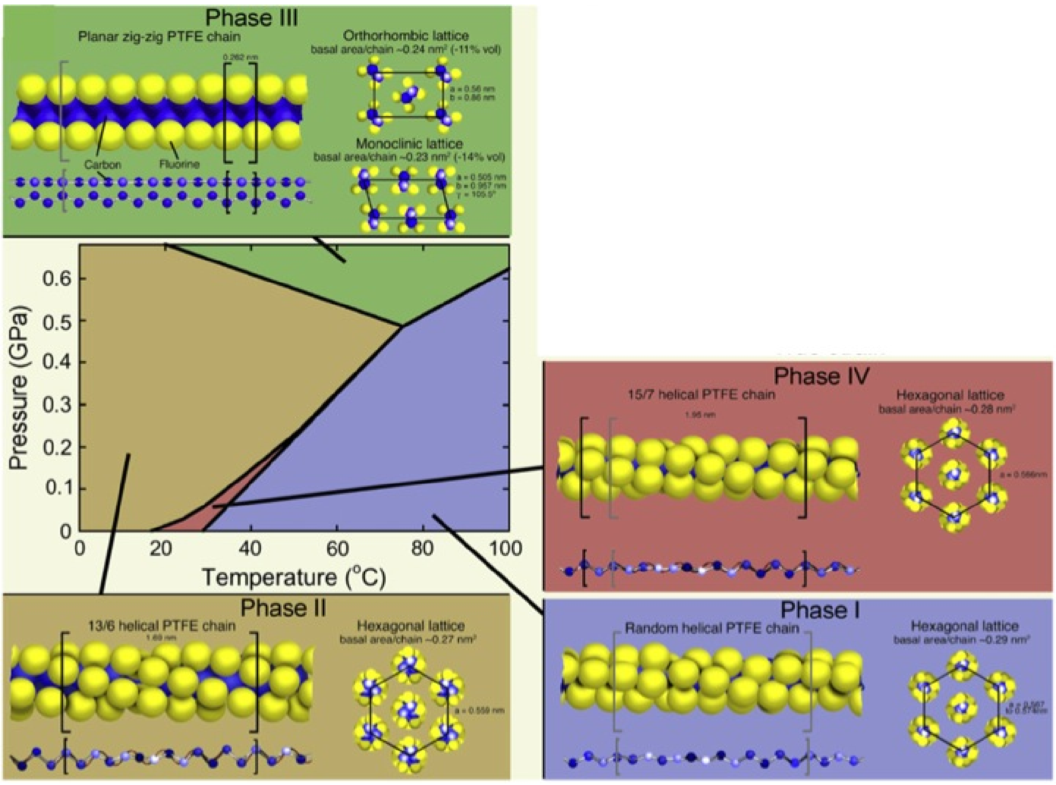

**Figure 3:** Conformation and phase diagram of PTFE from [Brown *et al.*, 2007]. The phase transformations (II-IV) and (IV-III) are important as they occur in a small range of temperature close to room temperature and can be triggered by relatively low loadings.

A distinction has to be made between the nascent material, obtained after polymerization, and a material which has been subjected to a thermal treatment above the melting temperature. The nascent PTFE is highly crystalline. The crystallinity is in the range of 92-98%, but will never be reached again after any thermal treatment ([Ebnesajjad, 2002]).

In contrast with most polymers like polyethylene which form spherolitic structures, PTFE molecules organize themselves as banded structures, or lamellae, with approximately 10-100 $\mu$m length and 0.2-1 $\mu$m width depending on the cooling rate of the molten polymer. These lamellae consist of 20-30 nm thick crystalline ‘slices’, which are formed by the folding over and the stacking of crystalline segments and separated by amorphous phases as shown figure 2. The amorphous orientation or the transition zone between crystalline and amorphous regions are not well defined. It is therefore probable that pure PTFE is a three component material composed of crystalline, amorphous and quasi-ordered materials.

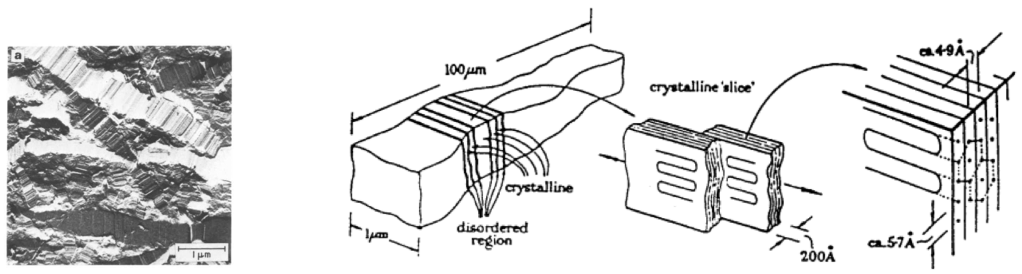

(a) Electron micrographic observation of sintered PTFE from [Bowden et Young, 1974]

(b) Scheme of the PTFE structure from [Ebnesajjad, 2002]

**Figure 4:** Microstructure of PTFE

# 3 Manufacturing process

The molecular weight of the nascent material is high, $10^7$ g/mol. So, even at melt temperature around 340°C, the viscosity remains too high, around $10^{10} - 10^{12}$ P ([Sperati et Starkweather Jr, 1961], [Ebnesajjad, 2002]), to allow the PTFE to be melt-processible. Only rare examples like the medium crystallin weight HD-PTFE®, enable standard melting processes to be used ([Tervoort *et al.*, 2002]). The main techniques to manufacture PTFE parts are lubricated granular extrusion, aqueous dispersion of PTFE or molding and sintering of granular PTFE. All of these techniques start with the same raw material under powder form, with more or less fine particles.

**Production of the PTFE powder** The production of PTFE is based on the free-radical polymerization of TFE in the presence of a small amount of oxygen or initiators like persulfates, at a temperature between 60°C and 140°C and at a pressure up to 7 MPa. The polymerization is strongly exothermic (105kJ/mol) so that it is generally made in an aqueous medium to evacuate the heat and to better control the reaction rate. PTFE can be manufactured under different techniques: emulsion, suspension or solution ([Sperati et Starkweather Jr, 1961],[Feldman, 1996], [Ebnesajjad, 2002]). To produce granular PTFE, a vigorous agitation with little or no emulsifier is employed so that particles whose size is in the range of 50 to 100 $\mu$m are finally obtained.

Then, fine cut or low flow resin is produced by size reduction by grinding of the particles obtained by suspension. Pelletized or free flow resin is obtained by agglomeration of the particles. These two types of powder may both be shaped by compaction and sintering process. Fine cut resins allow to reach excellent physical and electrical final properties while pelletized resins are easiest to machine and shape, and isostatic pressing can be used ( [Ebnesajjad, 2002], [Subhash V. Gangal, 2002]). Dispersion polymerization, where surfactant agent are added to avoid the agglomeration of particles, allows the production of finer particles of about 0.2 to 0.3 $\mu$m size. This powder is basically used in the lubricated ram extrusion paste process ([Hatzikiriakos *et al.*, 2002]).

**Die pressing and sintering** The solution studied here, used for fine cut resin and pelletized free flow resin, is similar to the one used for ceramic or metallic powders. PTFE is compacted at room temperature and then sintered ([Bigg, 1977], [Jog, 1993], [Ebnesajjad, 2002], [Subhash V. Gangal, 2002]) (figure 5).

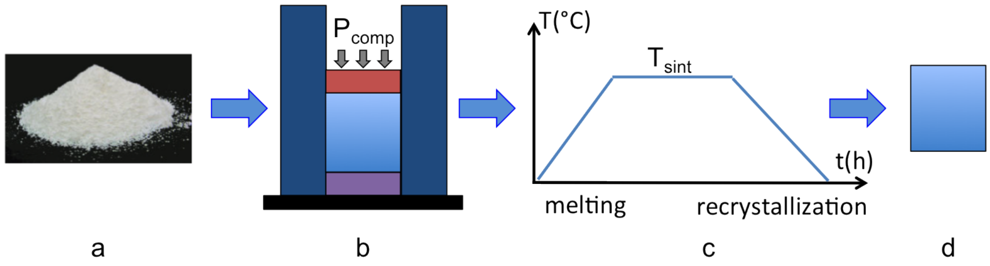

**Figure 5:** Schematic representation of the main steps of the manufacturing process of PTFE - (a) preparation of the powder - (b) compaction step - (c) sintering step - (d) final part.

**Preparation of the compounds** If filled PTFE parts are produced, the first step consists of the incorporation of filler particles in the PTFE powder in a mixer. The bulk density of the material is very low, generally between 200 and 500g/L for fine cut resin for instance. The initial density of the powder is highly variable depending on the preparation conditions, the handling during the filling or the shape of the mold. The bulk density is higher, around 900g/L, and less dispersed for free flow pelletized powders whose flowability, and thus filling ability, are higher.

**Pressing** One of the technics used to compact PTFE parts is die pressing, which is studied here. PTFE powder is poured into a die (cylindrical, parallelepipedic, or with a more complex shape) and compacted thanks to a piston in the axial direction. During the first stage of the compaction, at low level of pressure, the particles rearrange themselves. The air between particles is pressed out of the powder, contacts between particles are created. While the load is rising to higher levels of pressure, the contact area between particles increases, particles deform and porosity tends to form closed air pockets. The compaction has to be slow enough to ensure the outflow of air and uniform distribution of the load. The density and the cohesion of the material increase and, finally, the solid part may be handled. Once unloaded, the obtained part, named *green part*, is ejected from the tool. The green part is left still to allow for the relaxation of the polymer and remaining entrapped air to diffuse out of the part (figure 6).

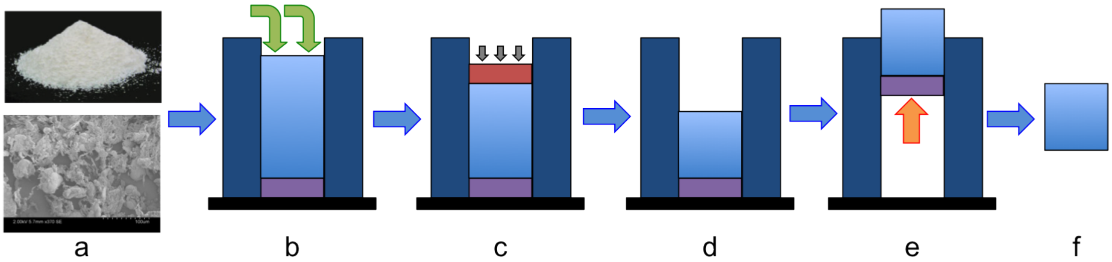

**Figure 6:** Schematic representation of the main steps of the compaction process - (a) preparation of the powder - (b) filling of the die - (c) compaction step - (d) unloading - (e) ejection - (f) rest time

A final pressure of 15 MPa to 70 MPa is generally applied, which is low compared to the stresses involved into the pressing of ceramic or metallic powder, which usually overpass hundreds of MPa. However, the variation of volume from the powder state to the compacted one is important. A ratio of 2.5/1 to 6/1 between initial to final volume is generally measured depending on the type of used granular powder. This high ratio requires industrial press to be several meters tall.

Another technique, which is generally used with pelletized resin, is isostatic pressing. Smaller parts or hollow parts like bottles may be preformed. The powder is poured into an elastomeric bag, which is placed in porous mold to obtain the desired shape. The whole device is surrounded by fluid under pressure. In this case, the air is not continuously removed, it can only completely escape when the pressure is released and the bag opened ([Gamboni *et al.*, ]).

**Sintering** A thermal treatment is then applied while the green part is free of any mechanical loading, apart from gravity. Temperature is increased above the *melting* point at around 370 - 380°C. This temperature has to be carefully controlled so that the material reaches the melting state without degradation. The Thermo-Gravimetry

Analysis (TGA) shows a mass loss of about 1%/hour at 400°C ([Jr et Kasprzak, 1993], [Canto *et al.*, 2011]).

During heating, particles coalesce and voids close. As the temperature reaches the melting point of the material, the crystalline phase turns into an amorphous state. The high temperature allows for the *reptation* of the chains from one grains to its neighbor. During the cooling step, the material re-crystallizes while the temperature is lowered to the ambient level. Due to the chain diffusion, co-crystallisation between neighboring particles occur, which create strong bonding between particles ([Hambir *et al.*, 1994], also described for Ultra High Molecular Weight PolyEthylene (UHMWPE) in [Gao *et al.*, 1996] and [Jauffrès *et al.*, 2009]). The crystallinity of the final part depends on the maximal applied temperature, hold time and cooling rate ([Canto *et al.*, 2011], [Sperati et Starkweather Jr, 1961]). It directly determines the final properties of the part ([Rae et Dattelbaum, 2004], [Rae et Brown, 2005], [Sperati et Starkweather Jr, 1961]). Note that the crystallinity is lower than the one of the nascent phase. A common crystalline ratio would be 40-50%. The cohesion has been highly increased so that the part can then be machined as other polymeric materials ([Hambir *et al.*, 1994]). Example of bearing manufacture after compaction and sintering of a hollow cylinder is shown in figure 7.

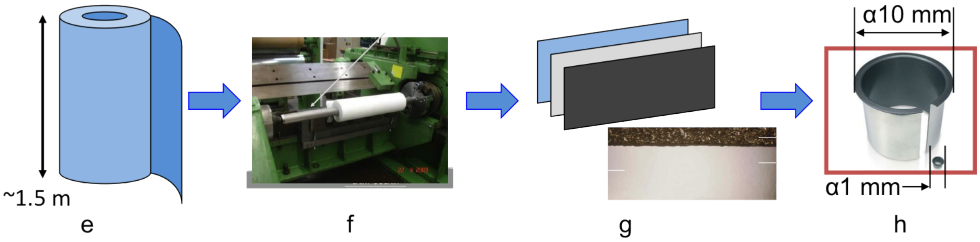

**Figure 7:** In the case of the production of bearings, after the sintering step, the cylindrical billets (e) are hafted on an axis and skived into a film (f). After being etched, the film is laminated with a metal sheet (g). The composite material is then cut in slices which are shaped in bearings (h)

High Velocity Compaction is a technique which combines these two steps and is used for high density polymers. The polymeric powder is filled in a heated mold and compacted thanks to several impacts with a high displacement rate. The dissipated energy induces the self-heating of the material above the melting temperature. Nascent polymeric powder is partially sintered ([Jauffrès *et al.*, 2007], [Jauffrès *et al.*, 2009] for UHWPE) and several successive compaction may be applied.

# 4 Fillers

The main weaknesses of PTFE are its low wear resistance and its susceptibility to creep flow. To enhance these properties while keeping the genuine properties of this material, fillers may be added, that reduce by several orders of magnitude the wear rate of pure PTFE. In some applications, the electrical conductivity may also be tailored by adding fillers.

Some examples of common fillers, whose characteristics are presented in table 2 and their main specific advantages. The advantage of glass fibers is the chemical inertness that makes it a good candidate for application in oxidizing environment. Thanks to its crystalline structure, in presence of a sufficient amount of moisture, graphite has an extremely friction coefficient ([Lancaster, 1990]). Amorphous carbon particles may be added to graphite fillers. Carbon graphite reduces creep, increases hardness and thermal conductivity of PTFE. Carbon graphite compounds have good wear resistance and perform well in non-lubricated applications. They are less abrasive on the matting surface than glass fiber compounds. Aromatic polyester fillers, another polymer with a high thermal resistance, also enhance the wear properties. They are often used in dynamic applications and demonstrate particularly good properties in contact with soft metals because of the absence of abrasion of the counterpart compared to harder fillers. They are less conductive than carbon/graphite compounds ([Ebnesajjad, 2002], [Friedrich *et al.*, 2005]).

Besides the tribological aspects, fillers have an impact on the mechanical and other physical properties of the material. Studies have been led on the characterization of filled sintered PTFE for PTFE filled with glass fibers [Bergström et Hilbert, 2005] or for PTFE filled with aluminium powder in [Joyce et Joyce, 2004] for instance. In table 3 from [Subhash V. Gangal, 2002], a summary of the influence of fillers on some physical and mechanical properties of the sintered PTFE base part is presented.

**Table 2:** Main types of fillers added in PTFE and their properties [Ebnesajjad, 2002]

| Filler | Material Description | Particle Size ($\mu$m) | Particle Shape | Density (g/cm$^3$) |
|---|---|---|---|---|
| Glass | E glass | Diameter 13 mm<br>Length 0.8 mm<br>Aspect ratio $> 10$ | Milled fibers | 2.5 |
| Carbon | Amorphous petroleum coke | Diameter $< 75$ $\mu$m | Roundish | 1.8 |
| Carbon Fiber | Pitch or PAN* based | | Short fibers | |
| Graphite | $> 99\%$ C,<br>Synthetic or natural | $< 75\mu$m | Irregular shape | 2.26 |
| Bronze | 9/1 Copper to tin ratio | $<60$ $\mu$m | Spherical or irregular shape | |
| Molybdenum Disulfide | Mineral (98% pure) | $< 65$ $\mu$m | | 4.9 |

* PAN is an abbreviation for polyacrylonitrile. PAN fibers are thermally carbonized to obtain carbon fiber.

**Table 3:** Influence of fillers on the final properties of sintered PTFE from [Subhash V. Gangal, 2002]

| Property | Unfilled | Glass fiber, wt% |  | Graphite, 15 wt% | Bronze, 60 wt% |
|---|---|---|---|---|---|
|  |  | 15 | 25 |  |  |
| Specific gravity | 2.18 | 2.21 | 2.24 | 2.16 | 3.74 |
| Tensile strength, MPa[b] | 28 | 25 | 17.5 | 21 | 14 |
| Elongation, % | 350 | 300 | 250 | 250 | 150 |
| Stress at 10% elongation, MPa[b] | 11 | 8.5 | 8.5 | 11 | 14 |
| Thermal conductivity, mW/(m·K) | 0.244 | 0.37 | 0.45 | 0.45 | 0.46 |
| Creep modulus, kN/m[c] | 2 | 2.21 | 2.1 | 3.4 | 6.2 |
| Hardness durometer, Shore D | 51 | 54 | 57 | 61 | 70 |
| Izod impact, J/m[d] | 152 | 146 | 119 |  |  |
| PV[e] for 0.13-mm radial wear in 1000 h, unlubricated, (kPa·m)/s[f] | 0.70 | 106 | 177 | 52 | 281 |
| Wear factor, 1/Pa[g] | $5 \times 10^{-14}$ | $28 \times 10^{-17}$ | $26 \times 10^{-17}$ | $100 \times 10^{-17}$ | $12 \times 10^{-17}$ |
| Coefficient of friction |  |  |  |  |  |
| static, 3.4 MPa[b] load | 0.08 | 0.13 | 0.13 | 0.10 | 0.10 |
| dynamic at PV[e] = 172 (kPa.m)/s[f] |  | 0.15–0.24 | 0.17 | 0.15 | 0.15 |
| V = 900 m/s | 0.01 |  | −0.24 | −0.18 | −0.22 |

# 5 Issues

Until the 80's, PTFE has been widely studied through many different aspects in the literature. After 20-25 years of lack of interest for this original material from a mechanical and process point of view, research teams started again the investigations around this polymer. Compared to other materials, few studies exist about the mechanical behavior of the finished PTFE (PTFE after sintering) and its manufacturing process. The links between the different steps of the process and the final properties of PTFE parts are complex as explained in the following section.

## 5.1 Compaction step

The first difficulty is the description of the initial state. Before the compaction step, the compound is first poured inside the mold. Due to different parameters like the environment (temperature, humidity), the handling of the powder, the flowability of the powder and the interaction between the mold and the particles, the initial density and the repartition of the fillers inside the mold at the end of the filling may be non homogeneous ([Roudsari et Puri, 2009], [Wu *et al.*, 2003]). PTFE is difficult to blend with other particles because of its chemical inertness. Thanks to the geometry of the particles, low flow fine cut resins are easier to mix than free flow pelletized resins.

For instance, the initial density of the powder measured in the as-received material is between $3 \times 10^5$ and $4 \times 10^5$ g/m$^3$. But, in the case of the industrial process, the average density at the end of the tool filling, which corresponds to the ratio between the total mass of powder poured inside the tool and the volume of the column of powder is between $5.5\times10^5$ and $7\times10^5$g/m$^3$. This difference may be explained by the interaction between the mold and the powder, the self compaction of the powder because of gravity, the preparation of the compounds before filling and the filling technique (more or less shaking, plugging...). The higher the powder column is, the higher the density gradient. The prediction of the initial packing of irregular shaped material would require a very precise knowledge of the powder preparation and its reproductibility ([Latham et Munjiza, 2004]).

Then, during the compaction step, viz. application of the load, unloading and ejection of the part, because of the interaction between the particles and the surface of the mold, additional heterogeneities are created. During uniaxial simple effect die pressing, part of the pressure exerted by the piston is opposed by wall friction, and hence it decreases progressively along the loading axis. This induces a gradient of density and mechanical properties. Thereby heterogeneous stresses induced by density profile may persist. Moreover, if the applied compaction is too high, severe plastic deformation can cause ‘plane slippage’ and apparition of microcracks ([Ebnesajjad, 2002]). If the cohesion of the material is too low, cracks may appear during the ejection step.

The microstructure, the physical and mechanical properties of the green part as well as their heterogeneities and the defaults, that are set up during the compaction step, influence the following steps of the manufacturing process.

## 5.2 Influence of the compaction on the sintering stage

As it may be observed in other compacted powder materials, like in metallic or ceramic powders, anisotropic shrinkage of the parts occur during the thermal treatment and is found to be linked, through different mechanisms, to the pre-compaction step. Large anisotropic deformations are observed ([Andena *et al.*, 2004], [Canto *et al.*, 2011], [Huang et Yu, 2012]) both at laboratory and industrial scales for PTFE parts. They are caused by different mechanisms, viz. reversible thermal expansion, void closure, phase changes during the melting and the re-crystallisation, which are directly linked to the compaction process. As shown in [Canto *et al.*, 2011], in the case of isostatically compacted green parts, the deformations during the thermal loading remain isotropic. On the other hand, in the case of a sample compacted through an anisotropic loading, deformations are different in direction of compaction and an additional recovery mechanism (not present for isostatic sample) appears (figure 8).

Although the nascent crystalline phase melts into the amorphous state and recrystallizes in a new crystalline phase during cooling, the anisotropic texture created during the pressing step persists above the melting temperature and is still visible during a second heating phase of the sintered material ([Andena *et al.*, 2004]).

So, in addition to an heterogeneous local thermal expansion caused by a non uniform thermal history through the thickness of a part (example of the gap between the applied thermal loading and the effective temperature in a billet is given [Andena *et al.*, 2004]), an additional dimensional change, which may be highly anisotropic, is added, and directly linked to the heterogeneities initially present in the green part. It may contribute to the

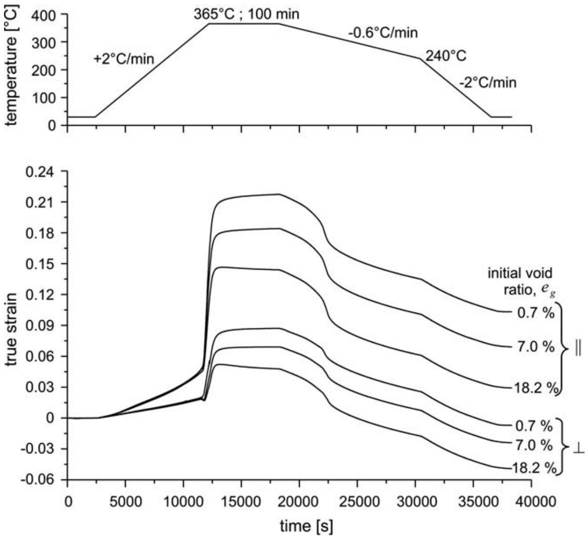

**Figure 8:** Dilatometry measurements along the transverse and parallel directions on œdometric PTFE samples compacted with different level of applied stress during their sintering ([Canto *et al.*, 2011])

appearance of residual stresses, which may lead to dramatic cracks if they are too high ([Huang et Yu, 2012]). Knowledge of the mechanical and thermal properties of the green part are required to precisely describe the behavior of the material during sintering.

The influence of the compaction step is also visible on the properties of the final product. The influence of the level of the applied pressure during the compaction on the tensile strength is shown in [Hambir *et al.*, 1994] and in [Bigg, 1977] on polyethylene. The higher the applied pressure, the higher the strength. In [Brown et Dattelbaum, 2005], the fracture toughness of sintered PTFE samples and its evolution as a function of the temperature is shown to depend on the direction of compaction and the anisotropy of the material created during the pressing is highlighted.

The nature of the powder also influences the final properties of the part as highlighted in [Hambir *et al.*, 1994]. Two PTFE powders with particle average size of 35 $\mu$m and 550 $\mu$m are compacted and sintered with the same procedure. The smaller the particles, the shorter the time at maximal temperature required to reach the same level of tensile strength. The differences may be attributed to a higher surface of contact in the case of the smaller particles.

Because of the polymer specificities and its wide spectrum of usage, standard models developed for commonly used polymers must be adapted. Few constitutive models have been dedicated to the mechanical behavior of sintered fluoropolymers. Worth mentioning are those by [Jordan *et al.*, 2007] or the one by [Bergström et Hilbert, 2005] that model the large deformation thermo-mechanical behavior and takes into account the influence of temperature and of strain rate, the asymmetry in tension and compression (also thoroughly experimentally investigated by [Rae et Dattelbaum, 2004] and [Rae et Brown, 2005] where the Poisson's ratio, the Young's modulus and the failure stress are compared) and the shape memory effect.

In the scientific stakes, the thermo-mechanical behavior of finished fluoropolymer is still poorly defined and calls for a more systematic investigation. The same observation may be done concerning the process of fabrication. To the best of the author's knowledge, only few studies were led on the compaction of polymeric powders, and more particularly on PTFE compounds aiming to link the compaction parameters and the properties of the powder to the sintering step and the final properties. No modeling have been proposed to describe the whole process. Moreover, by adding fillers, the mechanical, tribological and other physical properties of the final part are modified. In the same way, the mechanical behavior of the compounds during their pressing and sintering is changed, depending on the type of fillers and has to be characterized.

# 6 Aim of the study

To sum up, a reliable and accurate prediction of the final properties of the green part obtained at the end of the compaction step is necessary to understand and predict the deformations and the residual stresses involved during the thermal treatment and the properties of the final product.

In the case of the industrial process studied here, large billets of approximately 1 to 1.5 m height and 500 mm diameter are produced. Because of the compactability ratio of the materials, an initial column of powder of 3 to 4 m height has to be compacted. Considering the above mentioned problems, added to the large deformations and large scales involved in the process, specific parameters of compaction and sintering have to be carefully tailored to obtain the desired level of property homogeneity in the final product and to prevent the occurrence of defects.

Up to now, the industrial process has been set up by trials and errors. However, considering the cost of the installation (press, mold, ejection system, oven) and of the raw material, empirical approaches are costly, both in time and money.

## 6.1 Presentation of the studied materials

The aim of the PhD study is to develop and identify a modeling of the mechanical behavior of pure and filled PTFE compounds during the pressing step a room temperature in order to predict the final state of the green part depending on the parameters of compaction and the type of material.

The industrial plant deals with tens of formulations which have all their own specificities and optimal mechanical and thermal loading path. In the present study, four different materials are considereds :

- virgin PTFE,

- PTFE + filler 1,
- PTFE + filler 2,
- virgin PTFE B.

To reveal the influence of the type of PTFE powders on their mechanical behaviour, two pure PTFE resins — with the same chemical properties — were tested, the virgin PTFE and the virgin PTFE B, which are respectively a fine cut resin and a pelletized powder.

The geometry of the virgin PTFE particles, and their size are highly dispersed with an average of around 50 $\mu$m. The material appears as stringy shaped flakes of various sizes and shapes, from roundish agglomerations of flakes particles to fibrils structure, mainly because of the size reduction process. Scanning Electron Microscopic, SEM, observations are presented figure 9.

Virgin PTFE B is a free flowing pelletized resin, obtained by agglomeration of initial particles into so-called pellets, see Figure 10. The large size of the pellets (D50 at 550$\mu$m) — compared to the size of the original flakes — and their almost spherical shape induce excellent flowing properties and higher apparent density. Conversely, the fine cut resin allows for a finer mix with various fillers and or pigments, and leads to better final physical properties.

Then, comparisons between virgin PTFE and the two compounds of PTFE + filler 1 and PTFE + filler 2 sheds some lights on the influence of the fillers during the compaction step. SEM observations of the fillers in the compounds are presented figure 10.

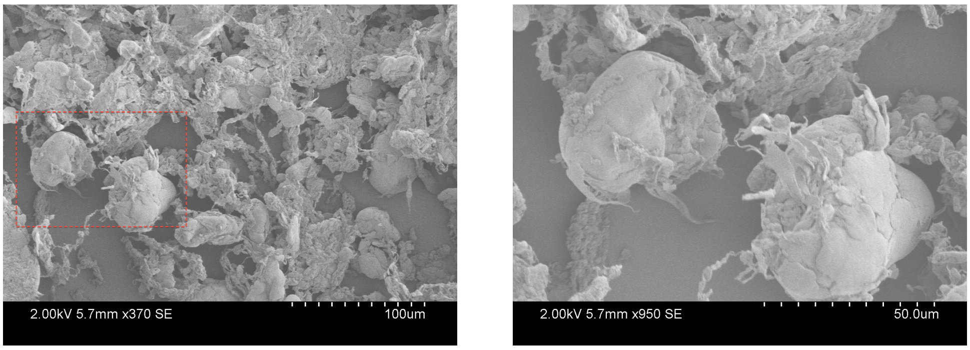

(a) virgin PTFE (b) zoom on big particles

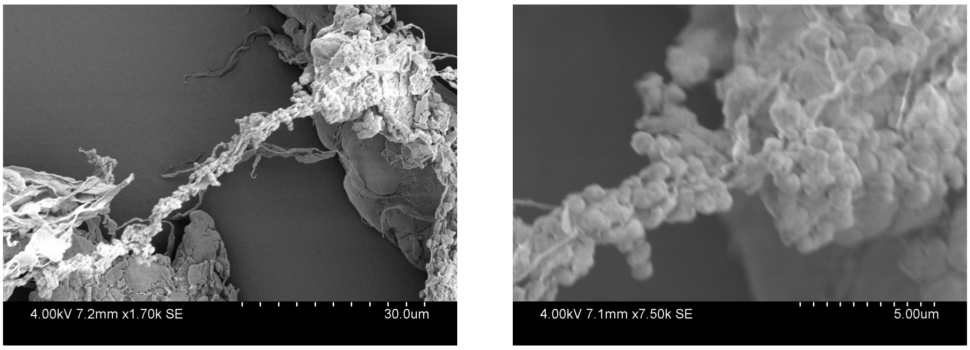

(c) smaller particles (d) zoom on smaller particles

**Figure 9:** Detailed SEM observations of the virgin PTFE

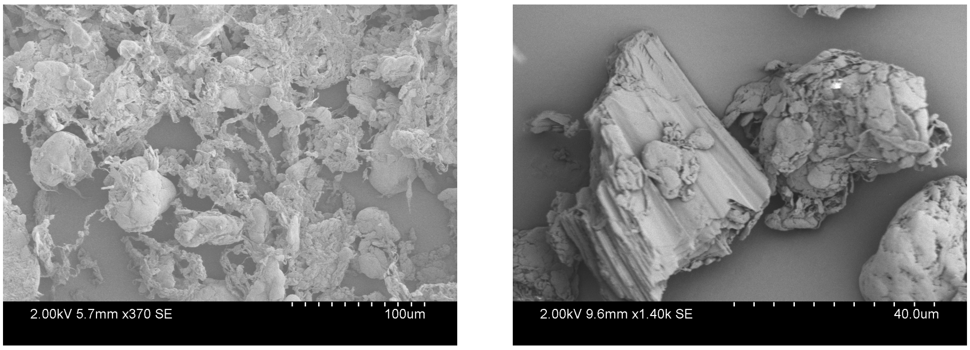

(a) SEM observation of virgin PTFE (b) SEM observation of PTFE + filler 1

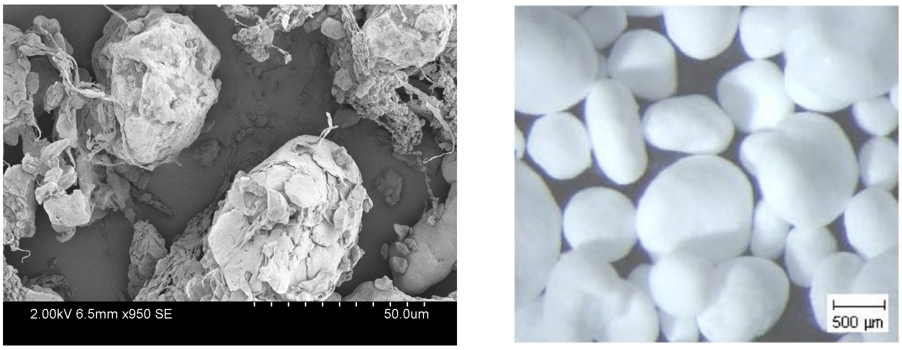

(c) SEM observation of PTFE + filler 2 (d) Photograph of virgin PTFE B

**Figure 10:** Observations of the four studied materials

## 6.2 Structure of the manuscript

**Chapter 1** Phenomena involved during the compaction step and a review of the different modeling approaches used to model it are presented. A focus is made on the description of the particular interactions between PTFE and a counterpart material.

**Chapter 2** Considering the complexity of the loading experienced by the billet during the first step of the process, Finite Element (FE) simulation is required to describe the final properties of the material depending on the type of compounds, the geometry of the tool or the applied load for instance. A 3D mechanical model is to be identified, based on experimental characterization. The parameters of the Drucker-Prager/cap type elasto-plastic model are identified for the four studied compounds thanks to an original 3D compaction device. This compaction tool is presented in the first section. In the second section, the identification procedure of the Drucker-Prager/cap model parameters is detailed. The influence of the ambient temperature phase transition is characterized. An improvement of the model is proposed to account the non linearity induced by this phase transition and is implemented in the FE code ABAQUS®. Then material behaviors are compared. Finally a first validation of the model and its identification as well as a critical review of the technical of characterization are reported.

**Chapter 3** This chapters shows other experimental tests in order to validate the proposed constitutive equations. The materials are submitted to two different uniaxial tests. First experimental results obtained from the compaction and the ejection of the parts in a fully instrumented die are shown. To simulate the shaping of the green parts, an interaction model between the polymer and the tool is proposed. Then a comparison between the experimental results and the predictions of the Finite Element (FE) simulation is done. In a second part, the material is compacted in an original 'V' shaped tool, from an original idea of R.B. Canto from UFSCar. The die allows the measurement of the applied and transmitted force as well as the measurement of the displacement field inside the matrix by Digital Image Correlation (DIC). A routine is used to directly compare the experimental measurements and the results of the simulation.

**Chapter 4** After the previous validation of the constitutive law, our model is used to simulate the industrial process by FE simulation. The influence of different process parameters like the dimensions of the tool, the material or the loading path is studied.

**Chapter 5** Finally, as prospective attempts to connect the macroscopic behavior to the microstructural features of the material, some preliminary works have been performed and are here reported. To do so, first measurements of the crystalline texture of green parts compacted through different loading paths are made thanks to X-ray diffraction (XRD). The results are compared with the same measurements made on the sintered parts. Evolution of the volumes changes before and after sintering is also measured.

# Chapter 1

# PTFE and its pressing at room temperature

*In this chapter, the two main phenomena involved during the pressing of powders are described : the mechanical behavior of the powder under compaction loading and its interaction with the tool. First, the compaction of granular materials is presented based on a bibliographic approach. Then different ways to model the compaction step of the manufacturing process are reviewed. In the third part, the interactions of PTFE in contact with another material are discussed in relation with the low friction properties of PTFE, as this question is critical for the compaction process. Models usually developed for the description of the compaction of granular materials are described.*

## Sommaire

# 1 Compaction of powders

The general specificities of the PTFE powder have been presented in the introduction. Here, a detailed presentation of the behavior of this material under compaction loading is made.

## 1.1 Crawford *et al.* studies

In studies run by Crawford and co workers, the compaction of different polymeric powders, including PTFE resin, has been thoroughly studied experimentally ([Crawford *et al.*, 1979], [Crawford et Paul, 1980], [Crawford et Paul, 1981], [Crawford *et al.*, 1982], [Crawford, 1982], [Crawford et Sprevak, 1984]). Compacted samples were cut in half and hardness measurement were performed over the entire diametral cut surface of the sample ([Crawford *et al.*, 1979]). The results highlight the heterogeneities created inside the part and the complexity of the compaction behavior even for simple cylindrical geometry (figure 1.1).

A fully instrumented die was also developed to measure stresses at different locations: axial stresses at different points along the radius of the top and bottom pistons and transversal stresses along the radial surface of the mold ([Crawford et Paul, 1981]) (figure 1.2). Finally, the heterogeneous properties found in the green parts are linked to the variation of pressure caused by friction with the mold. The behavior of the compacted powders is different from one polymer to the next. The PTFE powder is distinct from the other polymers because of its particular density profile and stress distributions and its low friction coefficient ([Crawford et Paul, 1980], [Crawford et Paul, 1981]).

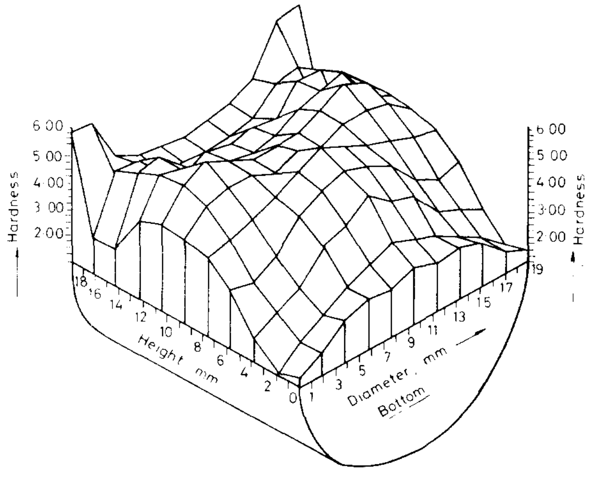

**Figure 1.1:** Map of the hardness distribution in polyvinylidene chloride after compaction at 200 MPa from [Crawford et Paul, 1981]

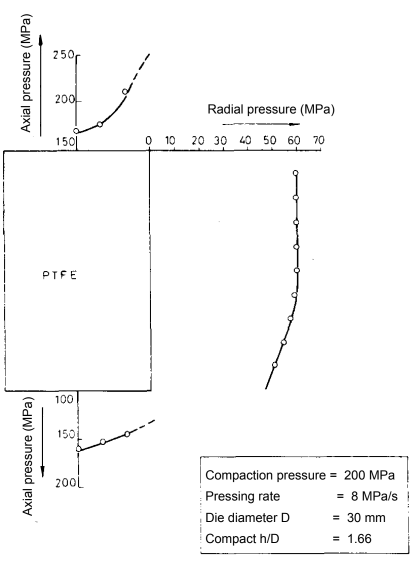

**Figure 1.2:** Measured stresses along the axial and radial directions during the compaction of PTFE powder from [Crawford et Paul, 1981]

## 1.2 From the particle point of view

A description of the phenomenon involved during the compaction at the scale of particles during compaction of polymeric powder is made for instance in [Crawford et Paul, 1982]. When the powder is poured inside a vertical tool, a more or less compacted and regular structure is established, depending on the shape of the particles, their size distribution and their interactions with their neighbors and the tool. Arching and bridging structures decrease the initial density of the material. In contrast, vibrations during the filling, as they break down such arches, may lead to higher densities.

The following compaction step may be partitioned in several substeps. First of all, when the piston enters in contact with the powder and starts its compression, particles move and rearrange. A very low level of pressure is required here as particles have enough room to move and rearrange to accommodate the applied displacement. The open and connected porosity allows for the free expulsion of air.

Then polymeric particles start to deform first elastically then plastically. Rearrangements by sliding of particles are still possible and particles are mainly submitted to compression loading. The area of contact between particles increases. Air may still flow out until isolated closed pores are formed. Then, it may be entrapped or the material may absorb part of the remaining air ([Meimon, 2000], [Baudet *et al.*, 2011], [Ebnesajjad, 2002]). Quick unloading may create local heterogeneous expansion generated by sudden depressurization which may lead to cracks.

## 1.3 Examples of parameters influencing the compaction behavior

Difference of behavior between powders may be explained by different parameters : the local behavior of the particles of course but also their shape, their size, their size distribution or their adhesion and friction. The influence of the particular shapes on the compaction behavior and the mechanical properties of the green part have been experimentally studied for different types of material like in [Poquillon *et al.*, 2002] (where compaction of two steel powders, one spherical and one with spongy morphology, are compared), in [Li et Puri, 1996] (for food powders with different morphologies), in [Galen et Zavaliangos, 2005] (with two pharmaceutical powders).

As highlighted in [Crawford et Paul, 1982] and [Bigg, 1977], polymeric powder compaction is different from other types of powder like ceramic or metallic ones. In [Crawford et Paul, 1982], it is found that small particles with irregular shapes are easier to compact and have a higher strength than particles with smooth and spherical surfaces or/and bigger particles. However, this is not systematic as illustrated with Ultra High Molecular Weight PolyEthylene (UHMWPE) and PolyEthylene (PE) powders. UHMWPE samples are easily compacted and are ejected without apparent failures, whereas the geometry of the particles is spherical and their size is of 400 $\mu$m, which is quite big compared to the other tested materials. On the other hand, the cohesion of PE powder, with an average size of 300 $\mu$m and smooth irregular surface, is too low, so it is not possible to eject a green part from the die without failure. In the case of the PE, some grades are compactible while others not. Polypropylene powders, even after a die compaction with an applied load of 700 MPa, stay in powdery state. This study does not focus on parameters like the size distribution of the particles and does not try to adapt the compaction process depending on the type of powder. But it highlights the huge variety of behaviors of polymeric powders whose compactability strongly depends on the variable physical and chemical properties.

The compaction behavior is also influenced by the addition of filler particles. Many studies have been made on the compaction of metallic powders (or model material like PMMA for hot compaction) reinforced with hard inclusions in cold or hot environment like in [Besson et Evans, 1992], [Bonnenfant *et al.*, 1998], [Kim *et al.*, 2003] or [Martin *et al.*, 2000]. As explained in [Bouvard, 2000], different microstructures are obtained after compaction of soft and hard particles compounds function of their shape and volume content. If the volume fraction exceeds a critical value (generally extimated to about 20%), percolation network may be set and prevent or slow down the densification of the material.

Note that in the cases cited hereinbefore, the soft particles of the matrix are relatively hard compared to other material like polymeric powders or compaction is performed at high temperature and the observed behaviors are not representative of cold pressing of filled polymeric powder. Less data are available on the compaction of composite powder for other types of material.

In [Pandeya et Puri, 2011], the influence of binder in pharmaceutical tablets is studied for low level of pressure ($<$10 MPa). The binder is added with volume fraction from 0, 5 to 10%. Adding binder delays the densification with respect to the applied pressure and the bulk modulus slightly increases. The effect on failure stress and shear modulus is not predominant here.

# 2 Mechanical behavior of the powder - existing modeling techniques

Now that the mechanical behavior of the powder during compaction has been illustrated through experimental observations, modeling techniques to predict this behavior are presented. Different types of model, with different approaches have been developed. They may be classified in two main categories: micro-mechanical models and phenomenological approaches.

## 2.1 Discrete micro-mechanical approaches

The micro-mechanical approach is based on the modeling of the interaction between particles at the local scale to address the macroscopic behavior of the material.

In [Fleck, 1995], a micro-mechanical model, (which extends a former one [Fleck *et al.*, 1992]) is presented. The model describes the behavior of randomly distributed pack of mono-sized spheres.The objective of the model is to compute a macroscopic response of the material as a function of the description of the contacts between each particles.

From a statistical analysis, the number of contacts per particle and the area of contacts as a function of density is estimated. The statistical distribution of the contact area, which varies under load, is included in the model and described by a second order tensor (fabric tensor). Their distribution reflects the stress anisotropy. Accounting for the plastic behavior of the inter particle interaction, the macroscopic stress-strain constitutive law is proposed. A macroscopic yield surface is described and its shape depends on the applied loading. It favorably compares with a Cam Clay surface in the case of the hydrostatic loading.

Based on the same approach, Sinka and Cocks ([Cocks et Sinka, 2007] and [Sinka et Cocks, 2007]) proposed a ‘simpler’ model. As experimentally shown in [Sinka *et al.*, 2001] for various metallic powders, iso density contours in the $(-\sigma_H, q)$ plane are not consistent with usual soil mechanics models for materials whose initial density and state cannot be precisely known. Thus, the authors proposed a more appropriate state variable which is related to the plastic work (or the complementary work) per unit of volume. The contours in that case are found to be smoother and without angular points. Here again, due to the rather strong hypotheses, this model is limited to few materials where the compaction results from the plastic deformation of the particles and to the case of simple loading paths without any friction effect.

Another approach consists of modeling each particles in a Finite Element code ([Chen *et al.*, 2007]). Each particle is meshed and has its own mechanical behavior. The interactions between the particles are implemented in the FE simulation. The calculations are long and cannot be reasonably extended to a large volume of particles. However the large deformation of the particles may be accurately described.

## 2.2 Phenomenological approaches

The majority of discrete element models address elastic cohesion less granular materials, but only few ones have been developed for powders composed of plastically deformed grains whose adhesion provides cohesion. Phenomenological continuum models appear as another interesting approach.

In phenomenological approaches, constitutive equations are given to describe the thermo mechanical behavior of the material under multiaxial loadings. To describe the state of the material, constitutive equations relate stress and strain tensors.

To better describe the observed deformation mechanisms, the invariants of the stress and strain tensors are commonly chosen. They may be written as:

- the first invariant, $\sigma_H$, which corresponds to the hydrostatic part of the Cauchy stress tensor $\underline{\underline{\sigma}}$:

$$\sigma_H = \frac{1}{3}\mathrm{tr}(\underline{\underline{\sigma}}) \tag{1.1}$$

- the second invariant, $q$ is defined from the partition of the stress tensor in hydrostatic and deviatoric parts, with $\underline{\underline{s}}$ the deviatoric part of the Cauchy stress tensor:

$$\underline{\underline{\sigma}} = \sigma_H \underline{\underline{I}} + \underline{\underline{s}} \tag{1.2}$$

  with $\underline{\underline{I}}$ the second order unit tensor. The equivalent deviatoric stress, $q$, is a scalar proportional to the norm of $\underline{\underline{\sigma}}$ :

$$q = \sqrt{\frac{3}{2}\underline{\underline{s}} : \underline{\underline{s}}} \tag{1.3}$$

- the third stress invariant, $r$, corresponds to

$$r = \sqrt[3]{\frac{9}{2}\underline{\underline{\sigma}} : \underline{\underline{\sigma}} : \underline{\underline{\sigma}}} \tag{1.4}$$

  whose contribution may conveniently expressed by the Lode angle defined by

$$\cos(\theta) = \left(\frac{r}{q}\right)^3 \tag{1.5}$$

In 1977, Gurson ([Gurson, 1977]) proposed to extend the classical elastoplastic model for ductile metal to take into account the damage induced by the nucleation and growth of spherical voids. The main (matrix) phase is described as an isotropic perfectly plastic and incompressible, which obeys the von Mises yield criterion. A flow rule is derived from an homogenization procedure when spherical voids are embedded in the medium. When the fraction of void tends to 0, the yield criterion tends to the von Mises yield criterion. The obtained yield criterion depends on the hydrostatic loading (contrary to former plastic models for metallic material).

The Gurson's model has been improved by the works of Tvergaard and Needleman (Gurson-Tvergaard-Needleman or GTN model)([Tvergaard, 1981], [Tvergaard, 1982], [Tvergaard et Needleman, 1984]). They introduced additional parameters $(q_1, q_2, q_3)$ and a damage variable $f^*$.

The yield surface of the GTN surface is equal to :

$$Y = \left(\frac{q}{\sigma_{YM}}\right)^2 + 2q_1 f^* \cosh\left(\frac{3}{2} q_2 \frac{\sigma_H}{\sigma_{YM}}\right) - (1 + q_3 {f^*}^2) = 0 \tag{1.6}$$

with the damage variable $f^*$ such as

$$f^*(f) = \begin{cases} f & \text{for } f \leqslant f_c \\ f_c + \frac{q_1^{-1} - f_c}{f_F - f_c}(f - f_c) & \text{for } f > f_c \end{cases} \tag{1.7}$$

where $f_c$ corresponds to the void ratio at which the void nucleation begins and $f_F$ denotes the final failure. The void ratio may be separated in two parts $\dot{f}^* = \dot{f}_{growth} + \dot{f}_{nucleation}$ to represent the void nucleation and growth.

The expression of the flow rule is

$$\dot{\varepsilon^{pl}} = \dot{\lambda} \frac{\delta Y}{\delta \underline{\underline{\sigma}}} = \dot{\lambda}\left(\frac{1}{3}\frac{\delta Y}{\delta \sigma_H}\underline{\underline{I}} + \frac{3}{2q}\frac{\delta Y}{\delta q}\underline{\underline{s}}\right) \tag{1.8}$$

One of the disadvantage of this model is the symmetrical behavior in tension and compression. In recent work, a solution is proposed by Guo et al [Guo *et al.*, 2008] where the matrix is pressure-sensitive and dilatant and supposed to follow a Drucker-Prager's yield criterion. The internal pressure in the voids is taken into account. The same approach is adopted in [Lin *et al.*, 2012] to model the mechanical behavior of ductile porous chalk.

However these models are not able to describe the behavior of materials with a high level of porosity and a low level of cohesion. These models are generally used for material with high cohesion like green part or partially sintered material where voids are closed and whose pore volume fraction is low. The use of this model makes sense for materials where the plastic deformation of the particles is predominant and the relative motion of the particles during their rearrangement may be neglected.

Based on the same homogenization concept of the behavior of a highly porous matrix, models are proposed to predict the influence of fillers added to the matrix. In [Bonnenfant *et al.*, 1998] for instance, the multi-scale schemes proposed by Hill

[Hill, 1965] and Hashin and Shtrikman [Hashin et Shtrikman, 1963] are used, depending on the size ratio of the fillers versus the particles of the matrix, to predict the densification behavior and an effective bulk modulus of the material.

### 2.2.1 Models derived from soil mechanics theory

Popular models to describe the behavior of a wide variety of granular and powder materials were initially developed in the field of soil mechanics.

The development of elastoplastic models dedicated to geomaterials starts with the Mohr-Coulomb criterion. It corresponds to a straight line in the normal stress $\sigma_n$ vs shear stress $\tau$ plane, parametrized by two basic quantities: the cohesion, $c$, and the internal friction angle, $\phi$, described in the equation 1.9. In the principal stress space, the criterion is a cone whose axis is the hydrostatic stress direction and whose orthogonal section is an irregular hexagon.

$$\tau = c - \sigma_n \tan\phi \tag{1.9}$$

The Drucker-Prager criterion ([Drucker D.C., 1952]) proposed a smoothed version (circular cone in the principal stress space) that can be seen as a generalization of the von Mises criterion where a linear dependance of the yield stress with the hydrostatic stress has been introduced.

Models, where the yield surface is closed in the $(-\sigma_H, q)$ plane, have been developed to describe both effects of shear loading and material consolidation, viz the volume shrinkage and the pore collapse under hydrostatic loading.

The Cam-Clay model (CC) or Cambridge model ([Roscoe *et al.*, 1958] and [Schofield et Wroth, 1968]) introduces the critical state concept. The material undergoes continuous hardening (decrease of volume $\mathrm{tr}(\dot{\varepsilon}) < 0$) or softening (increase of volume $\mathrm{tr}(\dot{\varepsilon}) > 0$) until the critical state is reached where additional loading produce flow without change of volume. This maximal deviatoric state is characterized by a critical straight line in the $(-\sigma_H, q)$ plane. The material is dilatant above the critical straight line ($q > -M\sigma_H$) and is consolidated below ($q < -M\sigma_H$). The yield state is described by an ellipse 'sliding' along the critical state line in the $(-\sigma_H, q)$ plane and its size depends on the hardening law (parametrized by the void ratio). The flow is associated (i.e. it obeys the normality rule, the plastic strain rate direction is normal to the yield surface). A cohesion parameter may be added to describe the behavior of the material in tension. The elastic part of the model is non linear.

The yield surface of the modified Cam-Clay (mCC) model is such as

$$f = \left(\frac{q}{M}\right)^2 + \sigma_H(\sigma_H - \sigma_c). \tag{1.10}$$

An other widely used model, which has been chosen in the study, is the Drucker-Prager/cap model (DP/c). The yield surface is composed of two parts, the shear failure surface and the consolidation surface. The shear failure surface comes from the Drucker-Prager model and controls the dilatancy of the material and its softening under mainly shear loading. In the $(-\sigma_H, q)$ plane, the slope of the straight line, $\tan\beta$, represents the internal friction of the material while the intercept of the $q$ axis corresponds to the cohesion $d$. The flow rule is generally non-associated and controlled by the dilation angle $\Psi$ such that associated flow corresponds to the coincidence of these two angles, $\Psi = \beta$. The shear failure line is closed by a consolidation surface as proposed by Dimaggio and Sandler [Dimaggio et Sandler, 1971] with an elliptical cap in the $(-\sigma_H, q)$ plane. The cap surface describes the volume shrinkage under compaction with mainly hydrostatic loads and whose position is dictated by a hardening law relating the hydrostatic stress to the volumetric plastic strain. The shape of the elliptical cap is monitored by a parameter $R$, ratio of the major to minor axis. The flow rule related to the cap surface is generally associated. A third transition surface to link the shear failure line and the cap surface may be added to the model.

Many versions of DP/c model with multiple yield surfaces have been developed. The Drucker-Prager line may be replaced by a more general curve or the surface may be cut off in the tension area or above the von Mises criterion for instance to better describe the experimental observations ([Chtourou *et al.*, 2002], [Coube et Riedel, 2000], [Han *et al.*, 2008]).

Both Cam Clay model and Drucker-Prager/cap model and their derived versions offer an accurate description of the behavior of cohesive powders from the early stage (in the powdery state) to the fully compacted state under various loading paths. This is shown for instance by [Tripodi *et al.*, 1995] where a Cam Clay model successfully describes the early stage of the compaction of wheat flour. Influence of others parameters like the temperature ([Brulin *et al.*, 2011]) or the amount of fillers ([Kim *et al.*, 2003] for low volume fraction) may be taken into account in the constitutive equations. These models may be used to describe the manufacturing process of many different materials :

- metallic ([Watson et Wert, 1993] aluminium powder (DP/c), [Shang *et al.*, 2011] steel powder (DP/c), [Guyoncourt *et al.*, 2001] ferrous and aluminum powders (elliptical model)),
- ceramic ([Brulin *et al.*, 2011] ramming mix (mCC), [Aydin *et al.*, 1996] (DP/c)),
- pharmaceutic ([Han *et al.*, 2008] (DP/c), [Wu *et al.*, 2005] (DP/c), [Cunningham *et al.*, 2004] (DP/c)),
- other organic powders ([Kamath et Puri, 1997] and [Tripodi *et al.*, 1995] wheat flour (mCC)).

## 2.3 Evolution of the parameters with the density

In early studies, parameters that describe the shape of the yield surface and elastic parameters were assumed constant. However, during their pressing, powder materials may undergo large transformations as they evolve from a powdery state with low cohesion and no elastic behavior, to a shaped green part endowed with enough cohesion to be handled. The elastic and plastic parameters have to evolve along the densification process to describe the different mechanical states of the material.

The shape of the consolidation surface changes during consolidation as shown by [Brochu et Turenne, 2004] who identified the consolidation surfaces of three metallic powders at different levels of density. From the pulverulent to the denser state, the higher the density, the more the deviatoric component facilitates densification. Therefore, the consolidation surface evolves to a higher aspect ratio.

In [Aubertin et Li, 2004], an inelastic criterion able to describe a wide range of mechanical behavior with a unique set of equations is proposed. The shape of the yield surface depends on the porosity and may reduce to the previous described models as it is described by a unique function.

**Table 1.1:** Example of evolution of the parameters as a function of the density (or equivalent state variables) in the litterature

| Study | Material | Cohesion $d$ | Friction coefficient $\beta$ | Cap parameter $R$ | Young's modulus $E$ | Poisson's ratio $\nu$ |
|---|---|---|---|---|---|---|
| [Cunningham *et al.*, 2004] | pharma. | 0 ↗ 9 MPa | 40° ↗ 70° | 0.5 ↗ 0.8 | 0 ↗9 MPa | 0.02↗ 0.31 |
| [Han *et al.*, 2008] | pharma. | 0 ↗ 16 MPa | 70° slight ↘ | 0.6 ↗ 1.6 – '$S'shape$ | 0 ↗ | ↗ |
| [Shang *et al.*, 2011] | metallic | 0 ↗ 25 MPa | slightly ↘ | ↗ | 10 ↗70 MPa | 0.18↘ 0.12 |
| [Coube et Riedel, 2000] | metallic | 0 ↗ 30 MPa | slight ↘ | 0.4 ↗ 0.9 – '$S'shape$ | $E(\rho,\sigma_H,q)$ * | constant |

In table 1.1, the evolution of different parameters as a function of the density or equivalent state variables for different materials is given. The same experimental characterization technique is used. Parameters are identified from classic uniaxial, diametral and die compression tests.

In [Coube et Riedel, 2000], $E$ follows a non linear law which depends on $-\sigma_H$ and $q$. $\nu$ is assumed to be constant. To better predict the appearance of cracks in multilevel die compacted powder, a dependance of $\beta$ and $d$ on both the volumetric and the deviatoric plastic strains is implemented. $\beta$ and $d$ decrease when the material is sheared. This evolution was not identified experimentally but led to a better prediction of crack nucleation in the sample, contrary to models only based on the volumetric plastic strain (and where the onset of cracking cannot be predicted).

Even for the same material and with the same measurement techniques, the evolution of some parameters of the elasto plastic Drucker-Prager/cap model are different. Cohesion and Young's modulus increase with density is consistent with a densification process but the evolution of other parameters appear less intuitive. A more extensive study of the evolution of the different parameters has to be carried out.

# 3 Adhesion and friction between the PTFE and contacting materials

To describe the compaction of powder, the modeling of the interaction between the powder and the die wall is necessary. From a more general viewpoint, interaction between two bodies is characterized by two phenomena : adhesion and friction.

When two surfaces are brought into contact, they interact through surface forces, with potentially attraction and repulsion forces depending on the nature of the surface and the surrounding medium. Chemical or physical bonds, promoting binding between contact points are formed or broken. This phenomenon, dependent on many parameters such as the chemical nature of the surfaces or the mechanical and rheological properties of surface material, is described as the adhesion. When a tangential force is exerted at a contact, the mechanical behavior of the resisting junction is what the friction consists of. If the tangential force overcomes the shear strength of the junction, the two surfaces may slip relatively to each other. A distinction is commonly made between the static friction (maximum tangential force that may be sustained before slip) and the dynamic one (in steady state sliding).

In the next part, the specificities of the interaction between PTFE and metal are presented.

## 3.1 Characterization of the interaction between PTFE and other materials

Particularly in polymer materials, contact and relative motion between polymer and a facing solid, is resisted by the deformation of junctions that may involve shear localization in the subsurface. When interfacial bonding is stronger than the cohesion of both contacting solids, a transfer of matter from the weaker to the harder counter solid may take place. Thereby, a consistent film may be formed that shields the soft polymer from the hard metallic asperities. This ‘third body’ acts as a self-lubricant and decreases the friction coefficient. Not all polymers may create such a coherent film, depending on their backbone flexibility, side chains, pendant groups, and crystallinity, the loading conditions and the nature of the contacting solid influence also the formation of the thin film. Lump debris may be formed instead and therefore, the interface properties are degraded. The nature, formation conditions and stability of this transfer film are intrinsically complex and it is impossible to present an exhaustive and fair overview.

However, PTFE is known as the polymer which forms the best transfer film in the shortest sliding distance. In [Makinson et Tabor, 1964], evidences for the creation of thin transfer film whose length is approximately equal to the slip distance are presented. A 200 $\AA$ thick transfer film is measured and is shown to display a highly oriented crystalline structure (figure 1.3 (a)).

In [Pooley et Tabor, 1972], it is observed that, for very small slip distances, the friction coefficient is high and then quickly drops to low values comparable to those measured by

[Makinson et Tabor, 1964]. To confirm the mechanisms involved at the interface, a pin is first rubbed on the surface in one direction. It is observed that a film of polymer remains on the disc. Then the pin is rubbed in the transversal direction. The friction coefficient starts at a high value before decreasing, like on the virgin surface. This may be explained by the fact that crystalline chains have to realign in the transverse direction before starting to slip on each other again.

Other measurements by XRD or situ surface plasmon resonance ([Biswas et Vijayan, 1992], [Krick *et al.*, 2013], [Sawyer *et al.*, 2014]) confirmed that on an extremely thin thickness, crystalline chains are oriented. The strong bond between the PTFE transfer film and the metal surface may be explained by van der Waals forces (as the main physical interaction) and the high conformability of the transfer film with the facing surface. So, right from the onset of slip, adhesion is high enough (as compared to the cohesion of the bulk) to cause cohesive failure (slip) in the near surface of the PTFE. Lumps of PTFE are transferred to the metal part. While the material is slipping, a thin film, strongly bonded and highly oriented, between 100-400 $\AA$ thickness, is laid on the contact surface. The helical chains tend to orient in the direction of the sliding movement. As the chains are oriented, they can easily and smoothly slip over each other. The layered structure of PTFE, enhances the shear and the slippage of the crystalline structure compared to classic spherulitic structure of other polymers (see on figure 1.3 (b) from [Biswas et Vijayan, 1992]). Evidence of such a phenomenon at the industrial scale is shown figure 1.3 with the formation of fibrils at the surface of the green part. The interaction is not any longer between PTFE and metal but between bulk PTFE and PTFE transferred film.

The friction is time and temperature sensitive and depends on the loading conditions and the nature of the counterpart (figure 1.4). In [Makinson et Tabor, 1964], a transition of the friction coefficient is found, depending on the temperature. At low temperature the friction coefficient is of the order of 0.1 while it drops to a smaller value, 0.07 when the temperature increases.

### 3.1.1 Influence of the fillers on the friction and wear properties

Fillers improve the material properties such as hardness, elastic modulus or creep. The prediction of the effect of fillers on wear is complex. When fillers are added, the wear resistance is increased if the fillers improve the bound between PTFE and contacting solid. But added particles may also create discontinuities on the formed transferred film, increase the roughness by abrasion, prevent the formation of the transfer film and so degrade the wear properties.

Thus a particular attention has been paid on the choice of types (size, geometry, chemical properties, hardness...) and amount of fillers as they may improve or degrade the tribological properties ([Tanaka et Kawakami, 1982], [Bahadur et Tabor, 1984], [Sawyer *et al.*, 2003], [Friedrich *et al.*, 2005]). Tanaka and Kawakami [Tanaka et Kawakami, 1982] suggest that filler particles inhibit large-scale destruction of the PTFE banded surface. For Lancaster [Lancaster, 1968], long fiber parti-

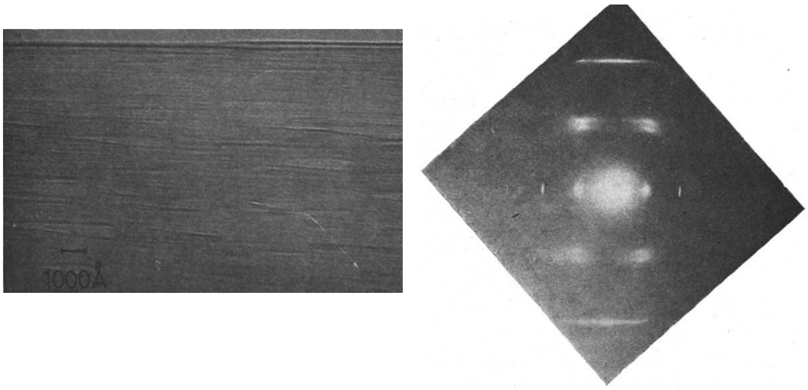

(a) Observation of the oriented chains at the sliding glass surface by electron micrograph observations (left) and XRD characterization of the highly oriented crystalline structure after sliding (right) from [Makinson et Tabor, 1964].

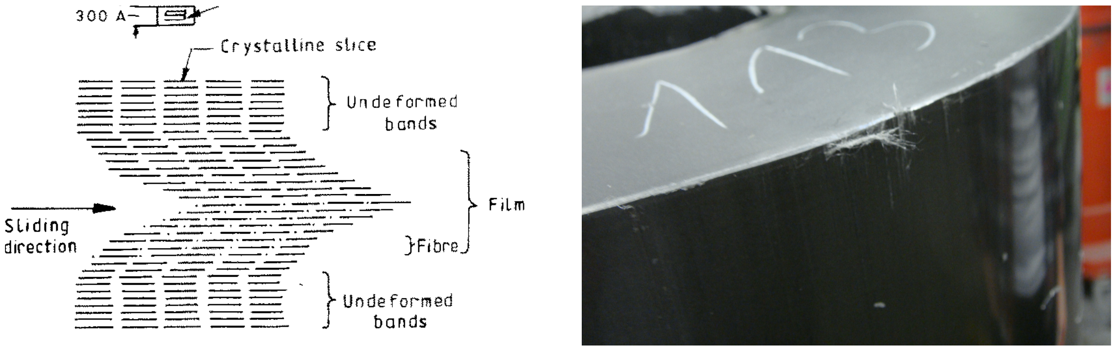

(b) Mechanism of formation of the transfer coherent film and of long fibrils from [Biswas et Vijayan, 1992], from Pooley and Tabor 1972.

(c) Observation of long fibrils at the end of the compaction step at the surface of the green part

**Figure 1.3:** Formation of oriented crystalline structure between the PTFE sample and the contacting part.

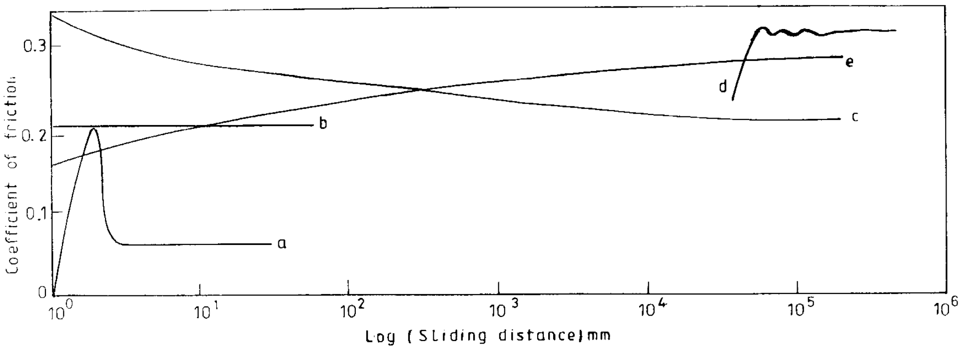

Fig. 2. Friction of PTFE. (a) Sphere on glass: speed, $10^{-6}$ m $s^{-1}$; load, 10 N; roughness, less than 0.1 $\mu$m c.l.a. (centre-line average); temperature, ambient; pressure, atmospheric [18]. (b) Sphere on glass: speed, $10^{-6}$ m $s^{-1}$; load, 10 N; roughness, greater than 0.1 $\mu$m c.l.a.; temperature, ambient; pressure, atmospheric [18]. (c) Pin on glass: speed, $3\times10^{-1}$ m $s^{-1}$; normal pressure, 19.62 MPa; temperature, ambient; pressure, $4\times10^{-5}$ mm Hg [17]. (d) Pin on steel: speed, $3\times10^{-1}$ m $s^{-1}$; normal pressure, 0.086 MPa; roughness, 0.3 $\mu$m c.l.a.; temperature, ambient; pressure, atmospheric [12]. (e) Pin on steel: speed, $1\times10^{-1}$ m $s^{-1}$; normal pressure, 2.8 MPa; roughness, 0.02 $\mu$m c.l.a.; temperature, ambient; pressure, atmospheric [7].

**Figure 1.4:** Evolution of the friction coefficient function of the sliding distance on different conditions (roughness, speed, normal load...) from [Biswas et Vijayan, 1992]

cles may support the loading. In [Sawyer *et al.*, 2003], it is shown that alumina nano particles on PTFE increase the wear without degrading the friction coefficient. The nano particles are not homogeneously distributed, they are spread at the surface of the 500 times bigger particles of PTFE. During sliding, islands of PTFE surrounded by fillers may prevent the formation of debris and thus allow for the formation of a transfer film.

## 3.2 Modeling of the interaction

The interaction between two surfaces in contact during their relative sliding is, as above discussed, still under investigation. Yet, some experimental observations give clues to model these phenomena.

In the widely used Coulomb's law, it is assumed that no slip occurs as long as the tangential force $\vec{T}$, is smaller than $\mu_0||\vec{N}||$ with $\mu_0$ a static friction coefficient and $\vec{N}$ the normal force. As soon as this limit is reached, relative motion is allowed, the surfaces may slip along each other and the tangential force is assumed proportional to the normal force with a ratio equal to a dynamic friction coefficient $\mu_d$. Models have been developed to justify this empirical law.

Models developed by Tabor and co-authors ([Bowden et Tabor, 1966]) are based on the idea that a surface is composed of asperities and craters whose topography may be described up to nanoscopic scale. When two surfaces come closer to each other, the highest asperities come into contact and form individual contact spots. The real contact area is equal to the sum of the area of contact of each touching asperities. And the coefficient of friction may be equal to the ratio between the real shear $\tau_r$ and the real pressure of contact $p_r$ which depend on the real area of contact and of the mechanical properties of the material. The estimation of this area is tricky as, if the micro roughness is taken into account (Archard type model), each contact is not a continuous surface but the sum of smaller discontinuous spots. The total area is named the ‘physical contact area’ and is much less than the real contact area.

Under loading, the area of contact changes. Asperities may be deformed elastically ([Greenwood et Williamson, 1966]), plastically ([Bowden et Tabor, 1966]), with or without viscous components depending on the nature of the couple of surfaces and the loading. In [Bowden et Tabor, 1966] model, the asperities of the harder surface is assumed to plough the softer one. When a tangential force is applied, a ploughing resistance is created which contributes to the friction force. The sum of the coefficients due to the adherence and the one due to the plough may justify the Coulomb law in a certain range of normal load, certain range of roughness and some material. [Greenwood et Williamson, 1966] model is based on the same idea but elastic deformation is assumed and specific hypotheses on the surface topography are made.

However Coulomb’s law is not applicable to all interaction conditions. In [Myshkin *et al.*, 2005], a literature review of the evolution of the friction coefficient function of the applied load for different polymers is proposed. It is highlighted that Coulomb’s law is not unconditionally true.

In many studies on die compaction of different types of powder, the interaction behavior between the powder and the tool is modeled thanks to a Coulomb friction coefficient.

Experimental procedures, based on instrumented œdometric dies, are developed to estimate friction coefficient material/tool during compaction test ([Briscoe et Rough, 1998] for ceramic powder and [Cunningham *et al.*, 2004] for pharmaceutical powders). To evaluate the friction coefficient at the interface in an œdometric tool, the Janssen and Walker model, initially developed to predict the stress/strain state of agricultural grains inside silo, is often used. It is based on a one dimension differential slice analysis and provides a semi-empirical analytical calculation of the stress transmission through the axis of compaction. It is assumed that the radial stress is proportional to the axial stress, $\sigma_{rad} = \kappa\sigma_z$, and that the contact at the wall follows the Coulomb law, $\tau_{rz} = \mu\sigma_{rad}$. By integrating the force balance equation in a slice along the height of the tool, if a stress $\Sigma_{Top}$ is applied on the top of the sample and the displacement is blocked on the bottom, the expression of the axial stress as a function of the height $z$ is:

$$\sigma_z(z) = \Sigma_{Top} \exp\left(-\frac{4\mu\kappa}{D}(H-z)\right) \tag{1.11}$$

This classical model highlights the exponential decrease of the axial load along the height of the tool, the consequence of which is a heterogeneous densification of the material.

In [Millet *et al.*, 2006] and [Rahmoun *et al.*, 2009], an improvement of the analytical solution of the Janssen model is given. The properties of the material, viz. the internal friction and the cohesion of the material are integrated in the model. A slip condition at the wall and a Mohr-Coulomb criteria is added to the model.

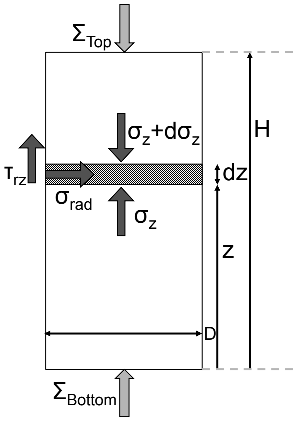

**Figure 1.5:** Differential slice analysis

In [Briscoe et Tabor, 1975], it was found that the shear strength of various polymeric films (included PTFE), sliding on a glass surfaces, is incrementally proportional to the normal applied pressure. Therefore, for polymers, authors proposed the following expression of the shear strength $\tau_r = \tau_0 + \alpha p_r$ with $\tau_0$ and $\alpha$ constants. In [Briscoe et Rough, 1998] the model is improved and takes into account the real area of contact at the interface to evaluate the tangential and normal stresses. Despite the ambition to propose a more realistic model, estimating the real contact area remains a fragile point of the analysis and additional information is needed to fit experimental data.

The identification of the interaction model and its modeling require a specific care for polymers like PTFE.

# Chapter 2

# 3D compaction device and experimental results

*In this second chapter, the procedure of identification of 3D constitutive law suitable to describe the behavior of PTFE powders under compaction is presented. The experimental characterization is made thanks to the original 3D compaction device, initially developed during the PhD study of R. Canto [Canto, 2007] and for which some further developments have been made to improve on the measurements. Different tests are performed in order to identify the parameters of a Drucker-Prager/cap type model, where the evolution of each parameter with the void ratio is identified. In addition to the soil mechanics model, the phase transition between phases II and IV has been taken into account. Indeed, this phase transformation takes place at ambient temperature and for a relatively low level of pressure, conditions that are often met in practice, and it gives rise to a significant volume expansion. Finally the model is implemented in the FE code Abaqus®. A first validation of the model is proposed and a critical analysis of the 3D compaction device is made.*

## Sommaire

# 1 Goal

As seen in the previous chapter, mechanical models have been developed to precisely describe the phenomena involved during the compaction of the powder and to predict the final properties of the obtained green parts. These models have to be identified and validated from experimental studies and to do so, experimental tools have been developed to describe the specific mechanical behavior of powder or grain based materials.

In the case of the PTFE powder compaction, three main difficulties have to be taken into account to characterize their mechanical behavior:

- the tricky definition of the initial state which is irreversibly modified by low loads;
- the large displacements to be imposed;
- the relatively high level of confinement stress, which can reach several tens MPa.

Thus, in order to identify the mechanical behavior of the PTFE powder under compaction, several loading paths are needed to investigate the whole $(-\sigma_H, q)$ space. Dedicated experimental tools, which fulfill the above cited constraints, have to be designed.

An original 3D compaction device was designed in the previous PhD study of Rodrigo B. Canto [Canto, 2007]. Improvements of the pressure sensors and of the displacement measurement were performed during the present study and are described in this chapter. The different loading paths and the obtained results are then presented, followed by a description of the identification procedure of the elasto-plastic model together with its constitutive parameters.

Finally a comparison between the experimental observations and the results obtained from the Finite Element simulation of the tests (based on the identified model) provides a validation of this first part of the proposed model.

# 2 Presentation of the true triaxial compaction device

Experimental tools dedicated to the study of powders and granular materials and their behavior under mainly compaction loading or shaping by pressing, have been developed.

**Commonly used experimental devices** Isostatic press ([Turner et Ashby, 1996]) and œdometric tools are commonly used either for mechanical characterization or for pre-compaction to endow the powder with some cohesion for further handling and processing. Both devices provide information on the compactability of the material.

To enrich the description of the behavior of the material, œdometric tools have been instrumented [Crawford et Paul, 1981, Guyoncourt *et al.*, 2001, Cunningham *et al.*, 2004, Burlion *et al.*, 2001]. The transmitted axial stress is measured to provide information on the interaction between the mold and the material. Evaluation of the radial stresses, by measuring the deformation of the matrix with strain gauges for instance, allows one to describe the loading path in the (-$\sigma_H, q$) plane at a given height. From those data, evolution of the elastic parameters, hardening law, and plasticity models may be identified [Guyoncourt *et al.*, 2001, Cunningham *et al.*, 2004, Shang *et al.*, 2011].

Let us stress that this simple test presents some limitation as it only partially describes the mechanical behavior of the material. Indeed, in industrial cases, due to the interaction with the tool, the geometry of the sample and the complexity of the behavior of the material, heterogeneous loading is applied through the compact, as discussed in chapter 1.

Other tests may be performed to investigate the cohesive part of the mechanical behavior, such as Brazilian test [Jonsën et Häggblad, 2007] (where the central diametral plane of the sample is in uniform and uniaxial tension) , shear test in Jenike shear cells [Jenike, 1964] and simple compression test [Coube et Riedel, 2000]. These tests are suited to green samples, ideally compacted thanks to hydrostatic loading. But even with these additional tests, parts of the ($\sigma_H, q$) plane remain to be investigated (figure 2.1).

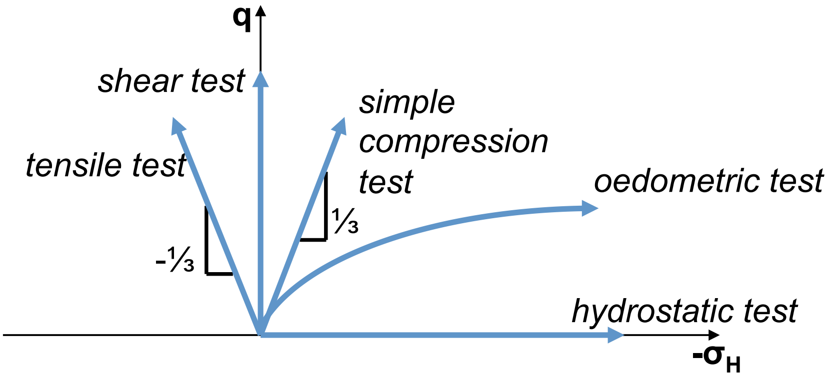

**Figure 2.1:** Summary of the loading paths in the ($-\sigma_H, q$) plane, usually performed to characterize powder materials. Let us stress that the œdometric path is not prescribed in the stress space but rather the strain one, and hence its representation is here schematic.

**Triaxial compaction devices** To overcome this problem, triaxial compaction devices allowing the application of complex loading paths in the hydrostatic/deviatoric plane have been developed.

They may be separated in two categories : the triaxial cells, initially devoted to the study of geomaterials and now widely used for the study of many types of materials; and the true 3D compaction devices.

In triaxial cells, a cylindrical sample, placed in an elastomeric bag, is surrounded by a fluid whose pressure is controlled. While it is submitted to a confining pressure, two plates located on the bottom and top ends of the sample apply an additional axial stress. By controlling the confining pressure and the axial stress, both deviatoric and hydrostatic parts of the stress can be modified. This way, all the intermediate loading states between the simple compression case and the hydrostatic one may be applied. The evolution of the strain tensor may be deduced from the displacement of the axial piston and the measurement of the variation of the volume of the sample. To avoid important errors in the measurement of volume change due to barreling effect, sophisticated devices with a direct measurement of the radial length of the sample have been developed like in [Dorémus *et al.*, 1995].

To allow the application of the same kind of complex loadings, true 3D compaction devices have been developed. The original idea was proposed by [Hambly, 1969] and developed by [Pearce, 1971]. The device is composed of six metallic blocks, placed in front of the six faces of a cubic sample, as described in figure 2.2. The blocks are arranged so that they may slide with respect to their neighbors as they are moving. The blocks are activated thanks to three perpendicular pistons.

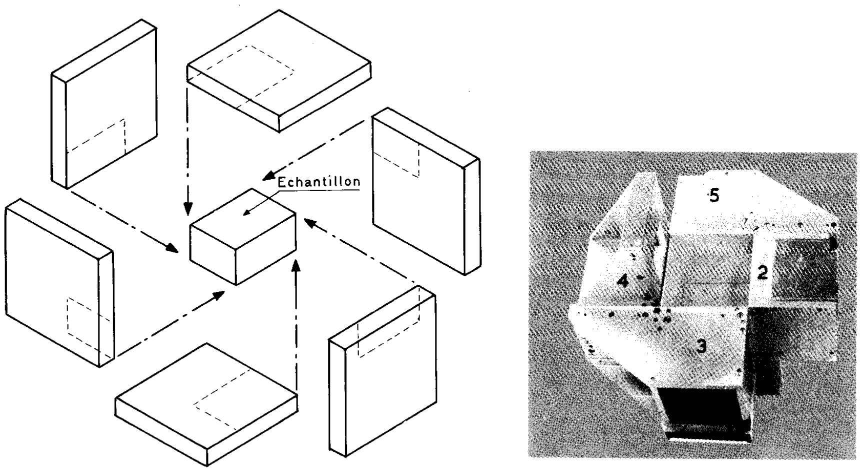

(a) Scheme of the device from [Pearce, 1972]

(b) Photography from [Pearce, 1972] of five of the six blocks of the device which are positioned to form a cavity for the tested sample.

**Figure 2.2:** Triaxial device proposed by Pearce [Pearce, 1971, Pearce, 1972]

Based on the same idea, the device proposed by [Shima et Mimura, 1986] for ceramic powders and improved by [Brown et Abou-Chedid, 1994] for metallic powders, is activated by a simple uniaxial machine as depicted in figure 2.3. The device is designed so that different ratios between the displacement in the vertical direction and the ones in the horizontal directions may be applied. However, it is not possible here to measure directly the radial displacement during the unloading step and only proportional loadings can be applied.

Others devices, activated thanks to six independent pistons have been developed and allow complex loadings with accurate measurement of the strain and stress responses, like in [Lanier, 1988] or [Kamath et Puri, 1997] (here, a flexible boundary type cubical triaxial tester is developed). In both cases, large displacements and complex loading paths ([Bouvard *et al.*, 1988]) with accurate measurement of the response of the material in each

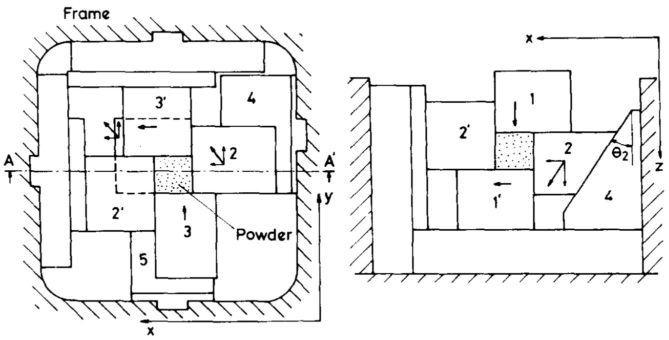

**Figure 2.3:** Triaxial device proposed by [Shima et Mimura, 1986], top and side views are respectively shown on the left and on the right. While the top block moves, the radial blocks are subjected to two translations : they are pushed down and, as they slide on tilted planes, they also move horizontally. The ratio between the two translations may be tuned by the angle of the tilted plane $\theta_2$ on the figure. Each block is equipped with a pressure sensor and the imposed displacements are geometrically related to that of the top piston.

principal directions. However, contrary to the stage described in [Shima et Mimura, 1986] or [Brown et Abou-Chedid, 1994], applied loads do not exceed 5 MPa.

**Design of a new true triaxial device for powder compaction** The main advantages of the 3D tool compared to triaxial cells are the possibilities to apply large displacements and to better control of the geometry of the sample. To meet the specific demands of materials such as the PTFE powder, where higher level of applied pressure and large displacements in non-proportional loading cases are required, an original 3D compaction tool, developed during the PhD thesis of Rodrigo B. Canto [Canto, 2007] and improved during the present study, has been used.

The 3D compaction device, inspired from the original device of Pearce ([Pearce, 1971]), is composed of six stainless steel blocks, as presented figure 2.4. The device is installed in the triaxial testing machine ASTREE, at the LMT-Cachan. This machine is composed of six independent actuators. The capacity of the horizontal actuators is of 100 kN, while the two vertical ones may reach 250 kN. The maximal amplitude of the displacement of the actuators is 250 mm. The actuators may be controlled independently in displacement or in force, enabling complex proportional or non-proportional loading paths.

Each block is placed in front of one actuator of the triaxial machine in contact through metallic platens. This allows the blocks to slide transversally while they are pushed in the axial direction by the actuator. An initial cavity of a maximum size of $50\times50\times75$ mm$^3$ offers the possibility to obtain after compression a sample size of $23\times23\times23$ mm$^3$.

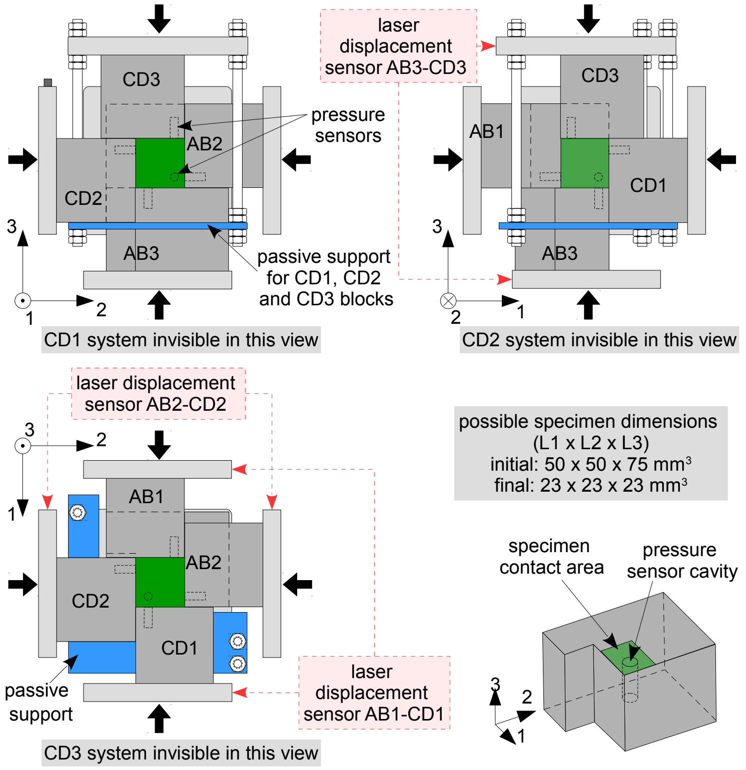

**Figure 2.4:** New triaxial device ([Canto *et al.*, a]). The blocks are placed in front of one face of a cube-shaped sample. Each block is positioned with respect to its neighbor blocks and the metallic platens so that they all may slide perpendicularly to the actuator. The passive support in blue allows to fill the initial cavity by holding the upper blocks. A particular care has been taken on the surface dressing of the functional surface to decrease the friction between elements.

# 3 Detailed information on the measurement techniques

A particular care has been exercised concerning the measurements of the stresses and the displacements experienced by the sample. To fully describe the strain and stress state of the material during the loading, the displacements and the stresses have to be measured in the three perpendicular directions. The difficulty to overcome here is the confinement of the sample.

## 3.1 Pressure measurement

Not to loose accuracy of the measurement, the stress sensors are directly in contact with the sample. A pressure sensor is embedded in each metallic block as described on figure 2.5. The sensors are located in the corners of the metallic block so that they are always in contact with the sample through the loading.

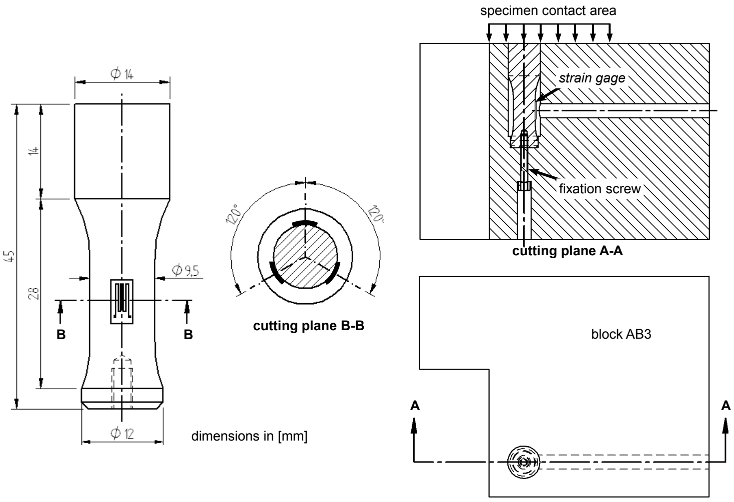

**Figure 2.5:** Pressure sensor and its position in block AB3 - [Canto, 2007]. One surface is locked inside the metallic block while the opposite surface is machined at the same time as the surface of the block to be precisely at the same level. A small gap between the cylindrical surface and the block allows the pin to slide freely.

This system, inspired from that developed for instance in [van Rooyen et Backofen, 1960] or [Guyoncourt *et al.*, 2001], is a cylindrical sample of 14 mm diameter with a reduction of section in the middle (section of 9.5 mm diameter), built in the same material as the metallic block. Three strain gauges of 120 Ω are equally distributed on the circumference of the part and enable the measurement of the average deformation, minimizing the possible parasite flexural component of the local deformation, and thus the measurement of the pressure applied on the sample in the direction of the axis of the sensor. These three strain gauges are connected through a half Wheatstone bridge to three others strain gauges which are glued on the free surface of the metallic block to correct the thermal deviation. The system is conditioned with a 2.0 V excitation voltage and amplified with a Signal Conditioning Amplifier model 2130 from Vishay Company. The maximal pressure applied on the sample is limited to 110 MPa not to overtake the elastic limit of the steel. Finally, the normal compression component in each perpendicular direction is measured twice, on each face of the cubic sample, through the principal directions of the system. The calibration of the pressure sensors are presented in appendix A.

## 3.2 Measurement of the displacements

### 3.2.1 Artefactual displacements of the triaxial machine

In the first experimental campaign of the present study, the displacements were directly measured thanks to the LVDT sensors embedded in the actuators of the triaxial machine, which enabled the position control of the machine. The LVDT sensors are at the end of the kinematic chain: this measurement does not take into account the stiffness of the whole actuator and of the 3D compaction device as well as the different plays between the parts of the kinematic chains, the consequence of which is a large overestimation of the displacement applied on the sample.

The difference of the displacements measured by the two actuators is shown in figure 2.6.

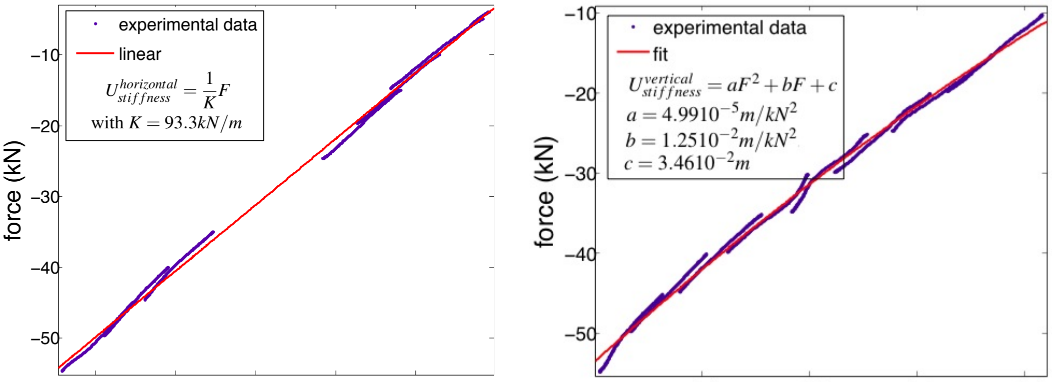

(a) horizontal axis (b) vertical axis

**Figure 2.6:** Stiffness of the axes of the triaxial testing machine coupled with two blocks of the 3D compaction device in two directions. A compression loading is applied on two blocks placed face to face on one axis of the triaxial machine. One of the two horizontal axes and the vertical one were tested. The second horizontal axis is supposed to have the same mechanical behavior as the other.

The error of position due to the stiffness of the machine cannot be neglected. To give an order of magnitude, a displacement of 0.5 mm is measured for an applied compression of 60 kN on each actuator for instance. From the expressions of the stiffness in each direction, presented figure 2.6, correction of the displacements may be done through the relationship :

$$U_{tot} = U_{sample} + U_{stiffness}(F). \tag{2.1}$$

with $U_{tot}$ the total displacement, $U_{sample}$ the displacement applied on the sample, $U_{stiffness}$ the one due to the stiffness of the kinematic chain of the triaxial machine and $F$ the force applied on the cubes.

But this calculation only gives an approximation of the correction of the measurement of the displacement. Indeed, it does not take into account the stiffness of the whole system and the interaction between the 3D compaction device and the machine.

Moreover, the LVDTs of the triaxial machine are embedded in the middle of the actuators and thus, are surrounded by oil of the hydraulic net. Because of the system of temperature regulation, the oil is subjected to cyclic and slow variations of temperature of few degrees Celsius, which induces a thermal dilation of the LVDTs' parts, up to 100 $\mu$m per actuator (which is consistent with an increase of 5°C in a steel bar of 1.5 m with a expansion coefficient of $13 \times 10^{-6}$/K) (figure 2.7).

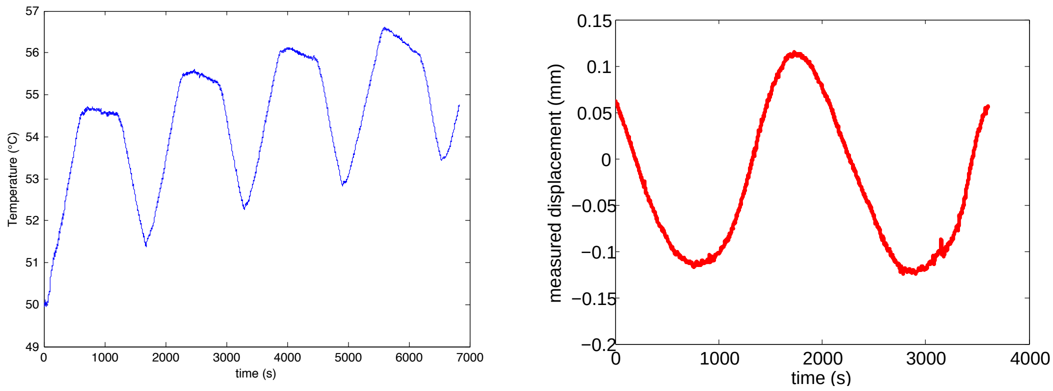

(a) Fluctuation of the temperature of the oil due to the aerotherm cooling system

(b) Evolution of the distance between two face to face actuators measured with a laser sensor as described in the next paragraph 3.2.2.

**Figure 2.7:** If the displacement speed is imposed to be null, as the LVDTs are in the control loop of the machine, fluctuations of the real position of the actuators are observed and are directly linked to the variation of temperature of the oil through the thermal dilation strain of the LVDTs.

Finally an external system of measurement of the displacements in the three perpendicular directions of the 3D compaction device has been set. To fulfill the constrains imposed by the confinement of the device and by the involved large displacements, instrumentation with laser displacement probes has been chosen.

### 3.2.2 Measurement of the displacements with laser sensors

The laser displacement probes LK-G 407 provided by Keyence have been selected. An accuracy of about 10 $\mu m$ is guaranteed. More details on the choice of the laser model and its characterization are given in appendix B.

Three laser probes and three corresponding targets are fastened to the platens in contact with the 3D compaction device and deported thanks to aluminum optical rails provided by CVI Melles Griot, to avoid any collision problem, as shown figure 2.8. A particular attention is paid to the alignment of laser probes and targets.

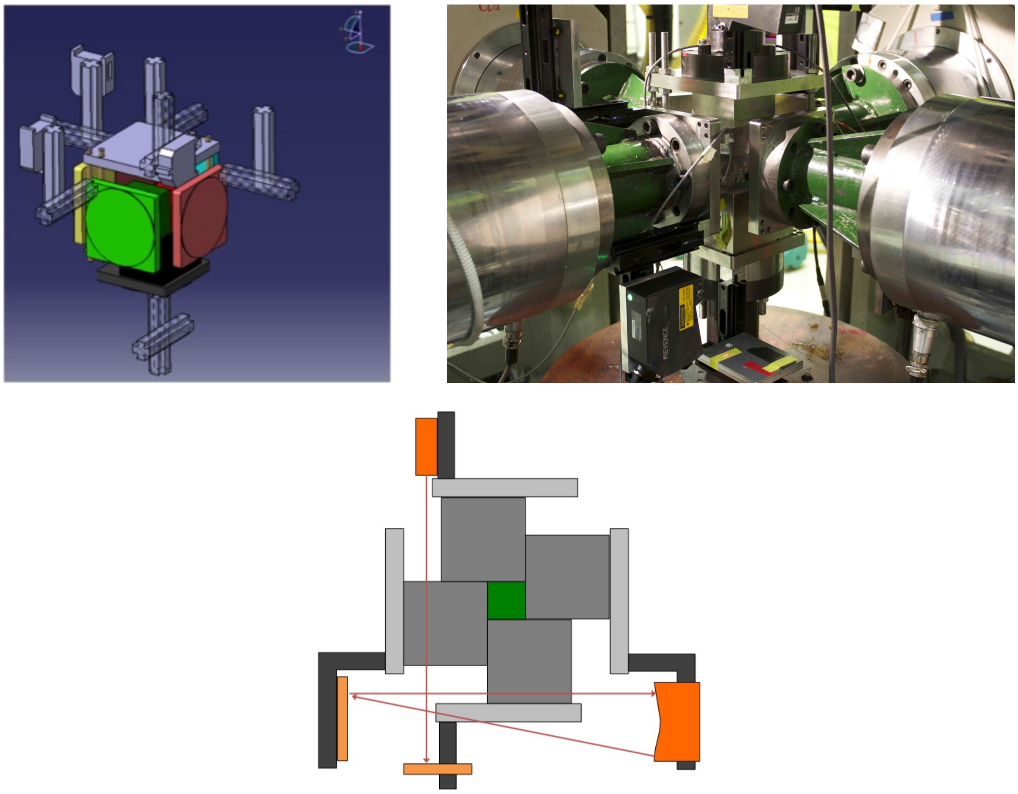

**Figure 2.8:** Laser probes and targets set on the 3D compaction device. Each axis is instrumented.

Moreover the temperature of the oil is followed during the test to make sure that it does not reach exceeding high values (that would be detrimental to the control of the applied displacement). The variations are slow compared to the time needed to complete the test (less than 5 min).

Before the beginning of the test, the initial cavity is calibrated by compacting a polyoximethylene (POM) cube of side length of 45.3 mm under hydrostatic loading up to 5 MPa. This ensures a proper contact between the blocks and the sample. The position of the laser is set to zero to record the initial dimensions of the cavity in each directions. Once the POM sample is taken out of the device and the blocks are moved on the calibrated position. The top block CD3 is removed to open the cavity and the powder is poured inside the formed mold. The block is finally placed back to close the cavity and the test may start. This way, despite the fluctuation of measurement of the LVDT, the initial size of the sample is accurately reproduced from one test to the other.

This procedure is more accurate than the one developed by [Canto, 2007] but the desired displacement loading is not exactly followed and tests involving long hold times (such as relaxation) are not possible. Ideally, the feedback loop should be done on the measurements made by the laser probes. However, considering the complexity and the risk of such a control loop (risk of obstruction of the laser beam, speckle default as explained in the annex B for instance) and because of a lack of time, this solution has not been implemented during this study.

Figure 2.9 is an illustration of the resulting displacements and its consequence on the identification of the mechanical behavior of the material. The benefit of the measurement the displacement with laser probes is clearly established.

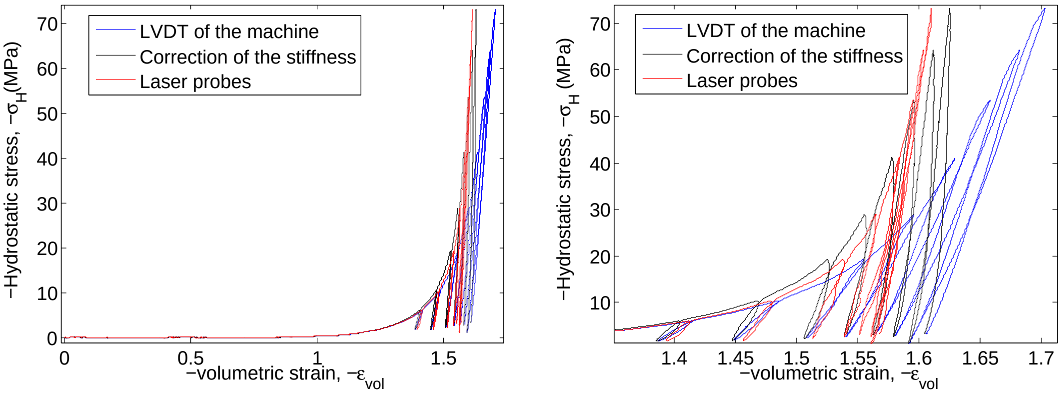

(a) Measurement (b) Zoom on the loading/unloading steps

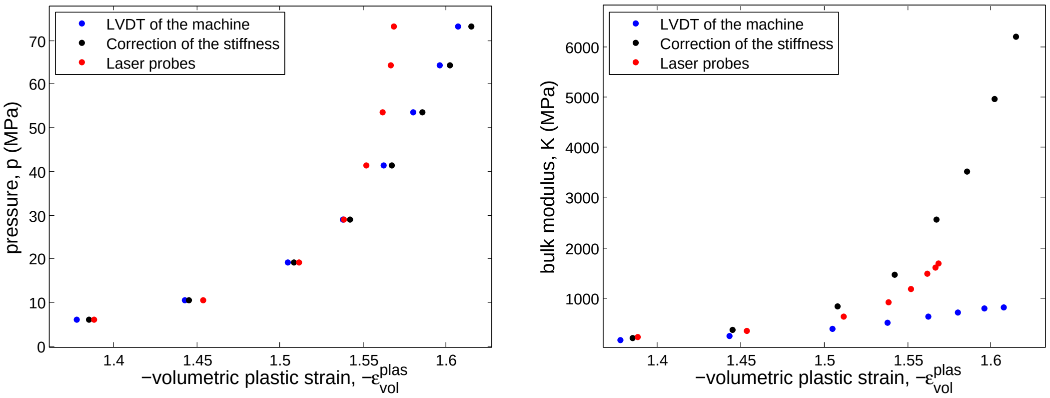

(c) Identification of the hardening law of the cap (d) Identification of the evolution of the bulk modulus K

**Figure 2.9:** Comparison of the displacement measurements with the LVDT of the machine with and without correction of the measured stiffness or with the laser displacement probes. An hydrostatic test is run with successive loading and unloading steps.

# 4 Identification of the parameters of the model

## 4.1 Drucker-Prager/cap model

As explained in the previous chapter, both elasto-plastic models Cam Clay and Drucker-Prager/cap are suitable to describe the behavior of cohesive powders. These two models have their own merits. Although the Cam Clay model offers some simplicity (e.g. it obeys the normality rule) it may lead to compaction failure, and for this reason we did not retain it. In contrast, the Drucker-Prager model is somehow more involved, (it has an associated flow rule only along the cap surface, while it may violate the normality rule along the Drucker-Prager cone). It is also more versatile in the evolution of the yield surface as needed to comply with the experimental data obtained with the PTFE powders, as will be shown in the following chapter. For these reasons, we were led to choose this latter constitutive framework in the sequel.

The precise model used for the study is based on the implementation that has been included in the Finite Element software Abaqus [Hibbit *et al.*, 2011]. A detailed presentation is made in the following section. Considering the large transformations involved in the pressing of the material, large-displacement effects are included in the model using the NLGEOM option implemented in Abaqus. Elements are formulated in the current configuration using current nodal positions and may thus distort from their original shapes as the deformation increases. The logarithmic expression of the deformation is used. True Cauchy stresses are calculated. In a first stage, the viscous behavior of the material is not taken into account. Finally, the anisotropy of the material is not accounted for in the Drucker-Prager/cap model and thus the material remains isotropic. We will see later that this assumption is not quite appropriate, but the introduction of an anisotropy in the plasticity law would require a considerable investment in time and effort with presumably a lot of difficulties to ascribe decent values to the large number of additional constitutive parameters required.

To describe the elasto-plastic model, the strain rate is decomposed in an elastic part $d\underline{\underline{\varepsilon}}^{elas}$ and a plastic part $d\underline{\underline{\varepsilon}}^{plas}$ such as

$$d\underline{\underline{\varepsilon}} = d\underline{\underline{\varepsilon}}^{elas} + d\underline{\underline{\varepsilon}}^{plas} \tag{2.2}$$

The strain tensor may be separated in deviatoric part $\underline{\underline{\mathbf{e_d}}}$ and an volumetric part $\varepsilon_{vol}\underline{\underline{\mathbf{I}}}$ such as

$$\underline{\underline{\varepsilon}} = \frac{1}{3}\varepsilon_{vol}\underline{\underline{\mathbf{I}}} + \underline{\underline{\mathbf{e_d}}} \tag{2.3}$$

where

$$\varepsilon_{vol} = \mathrm{tr}(\underline{\underline{\varepsilon}}) \tag{2.4}$$

The contribution of the deviatoric part of the strain is summed up in an equivalent deviatoric scalar $\varepsilon_{dev}$

$$\varepsilon_{dev} = \sqrt{\frac{2}{3}\underline{\underline{e_d}} : \underline{\underline{e_d}}} \tag{2.5}$$

### 4.1.1 Description of the state of the material

Here, the state of the material is assumed to be only dependent on the void ratio $e$. It is defined as the ratio of the volume of void in the material $V_{void}$ on the volume of the solid part of the material $V_{solid}$.

$$e = \frac{V_{void}}{V_{solid}} \tag{2.6}$$

The void ratio $e$ is equivalent and directly linked to the porosity $n$ by

$$n = \frac{V_{void}}{V_{total}} = \frac{V_{void}}{V_{solid} + V_{void}} = \frac{e}{e+1} \tag{2.7}$$

From the experimental tests, the final and initial mass $m$ and volume of the sample $V$ are measurable. The void ratio and its evolution through the test are indirectly deduced from the measured variation of volume. Indeed if reversible volumetric strain is neglected, the evolution of the state variable $e$ is directly related to the evolution of the volumetric plastic strain, $\varepsilon_{vol}^{plas} = \ln(V/V_0)$, and the initial void ratio of the loose powder, $e_p$, so that (from equation 2.6)

$$d\varepsilon_{vol}^{plas} = \frac{dV_{void}}{V} = \frac{de}{e+1} \tag{2.8}$$

By integration from the initial state described by the initial void ratio of the loose powder, $e_p$

$$\varepsilon_{vol}^{plas} = \int_{e_p}^{e} \frac{de}{e+1} = \ln \frac{1+e}{1+e_p} \tag{2.9}$$

Then

$$e = (1+e_p)\exp(\varepsilon_{vol}^{plas}) - 1 \tag{2.10}$$

As the initial state of the material is highly variable from a sample to the other and difficult to characterized because of the fluffy nature of the powders, the state of reference chosen here is the fully compacted material, without any porosities. Thus, the state of the material may be defined as a function of its critical state for which $e = 0$ with

$$\varepsilon_{crit} - \varepsilon_{vol}^{plas} = \ln\left(\frac{1}{1+e}\right) \tag{2.11}$$

Based on the assumption that the elastic part of the deformations may be negligible, all these quantities may be easily linked to each other.

The density is simply defined as $m/V$, where the elastic part of the deformation is included.

### 4.1.2 Linear isotropic elasticity model

The elastic part is described by a linear isotropic elastic model. The stress tensor is linked to the strain tensor following the Hooke's law :

$$\underline{\underline{\sigma}} = \left(K - \frac{2G}{3}\right)\varepsilon_{vol}^{elas}\underline{\underline{I}} + 2G\underline{\underline{\varepsilon}}^{elas} \tag{2.12}$$

with $G$ the shear modulus and $K$ the bulk modulus.

### 4.1.3 Plastic part of the model

As explained in the previous chapter 1, the yield surface of the Drucker-Prager cap model is written as a function of the two invariants of the stress tensor, the hydrostatic part of the stress tensor $-\sigma_H$ and the equivalent deviatoric stress $q$.

It consists of two parts: the shear failure surface, which is closed by the second part, viz. the consolidation part or cap surface (figure 2.10).

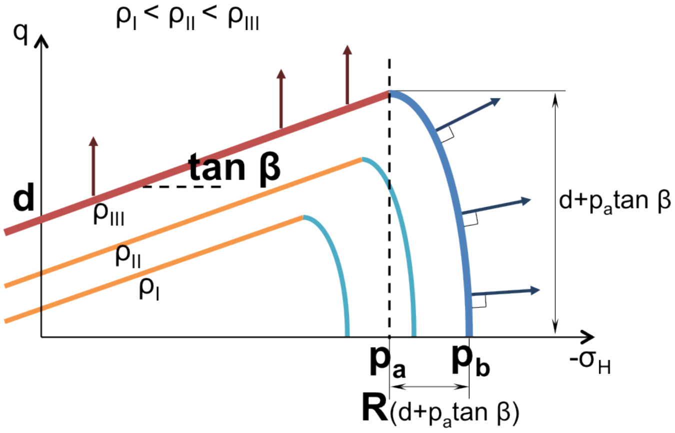

**Figure 2.10:** Scheme of the Drucker-Prager/cap yield surface

**Shear failure surface** In the $(-\sigma_H, q)$ plane, the Drucker-Prager yield criterion is described by a line whose slope $\tan(\beta)$ corresponds to the internal friction of the material and whose shear axis-intercept corresponds to the cohesion of the material $d$ under pure shear loading (figure 2.10).

Therefore, the expression of the shear failure surface in the $(-\sigma_H, q)$ plane is :

$$F_s = q - (-\sigma_H)\tan\beta - d = 0 \tag{2.13}$$

In Abaqus, the non-associated flow of the shear failure surface is implemented through the definition of the plastic potential, $G_s$, which is described as an ellipse

$$G_s = \sqrt{((p_a - (-\sigma_H))\tan\beta)^2 + q^2} \tag{2.14}$$

The plastic strain rate is derived from the flow rule

$$\underline{\underline{\dot{\varepsilon}}}^{plas} = \dot{\lambda}\frac{\partial G_s}{\partial \underline{\underline{\sigma}}} \tag{2.15}$$

with $\dot{\lambda}$ the multiplicator.

In [Canto *et al.*, 2009], simple compression tests were made on square based bar samples of PTFE, compacted in an isostatic press at different levels of density. Thanks to DIC, the displacement field of the sample is measured. In the $(-\sigma_H, q)$ plane, the loading path followed during this test is a line which passes through the origin with a slope of 3. If the loading is high enough, the Drucker-Prager shear failure surface is reached. When data are observed in the hydrostatic-deviatoric strain plane $(-\varepsilon_{vol}, \varepsilon_{dev})$, it is shown that once the yield surface of the material is reached, the volumetric component of the strain rate is null while its deviatoric part increases (figure 2.11). Thus the plastic flow is non-associated and seems to be vertical in the $(-\sigma_H, q)$ plane in the case of PTFE green part. Which, with a low internal friction coefficient, as it will be showed in this chapter, is actually very close (though not strictly identical) to the equation 2.14 of the plastic flow.

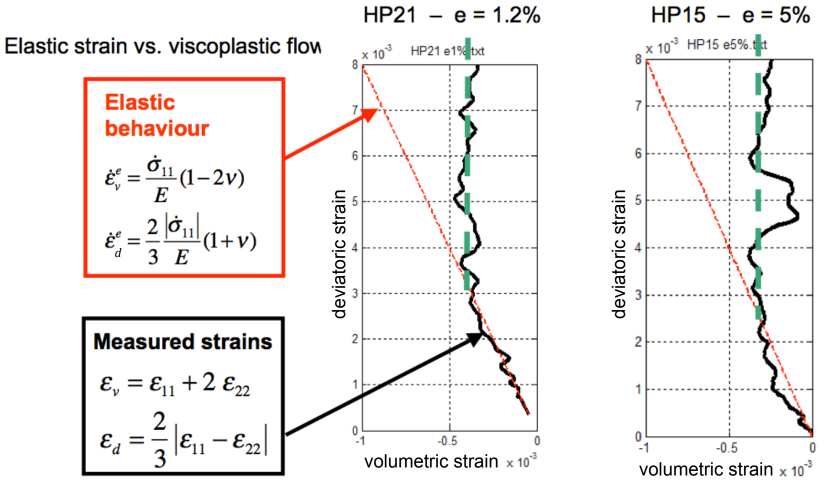

**Figure 2.11:** Results of simple compression tests on two PTFE green parts with different levels of density - The plastic flow is non associated in the Drucker-Prager part of the model - from [Canto *et al.*, 2009]

**Cap surface** The yield domain is closed by a cap surface. This consolidation part is described in the $(-\sigma_H, q)$ domain by an elliptical curve, crossing the hydrostatic stress axis in $p_b$ (in blue on figure 2.10). The center of the ellipse is at the point $(p_a, 0)$. The shape of the cap is monitored by the parameter $R$.

As proposed in Abaqus, the yield surface may be closed by a transition region that links the Drucker-Prager line and the elliptical cap to ensure a smooth link between the two areas. In our case, considering the parameters measured in the next section and after checking that the transition region has no influence on the results of the simulations, no transition surface is implemented. The apex of the elliptical cap is coincident with the Drucker-Prager line in $(p_a, tan(\beta)p_a + d)$.

Here, the assumption of the associated plastic flow is made.

So, to sum up, the cap yield surface is described by the equation

$$F_c = 0 = \sqrt{(-\sigma_H - p_a)^2 + (Rq)^2} - R(d + p_a \tan\beta) \tag{2.16}$$

with

$$p_a = \frac{p_b + Rd}{1 + R\tan\beta} \tag{2.17}$$

The plastic flow in the cap area is defined from the plastic potential $G_c$ which for the cap (and only for this part) can be chosen to be $F_c$ associated flow rule and the plastic strain rate is derived from the associated flow rule

$$\dot{\underline{\underline{\varepsilon}}}^{plas} = \dot{\lambda}\frac{\partial G_c}{\partial \underline{\underline{\sigma}}} = \dot{\lambda}\frac{\partial F_c}{\partial \underline{\underline{\sigma}}} \tag{2.18}$$

The position of the cap depends on the density of the material. Let us note that the yield surface is continuous but may have a discontinuous derivative at the intersection between the shear and the cap surfaces. However, the plastic potential does not lead to discontinuous gradients with our chosen two potential. While the material is compacted under mainly hydrostatic loading, its density increases, the air between particles is expelled (at least in part) and PTFE particles are brought to intimate contact. To reach a given density, a level of hydrostatic stress is required. This is described by a hardening law linking the hydrostatic stress $p_b = -\sigma_H$ for which $q = 0$ and the volumetric plastic strain $\varepsilon_{vol}^{plas}$.

$$p_b = f(\varepsilon_{vol}^{plas}) \tag{2.19}$$

### 4.1.4 Evolution of the base model

To the based version of the model proposed in Abaqus, two main improvements of the model are added in this study :

- the evolution of the parameters of the model as a function of the void ratio, based on the experimental results ;
- the modeling of the first order phase transition that appears in the range of temperature and pressure considered here.

These two points and the procedure of identification of the model are presented in the following section.

### 4.1.5 Initial state of the material

For lowest density, a small loading induces a high deformation of the sample (as illustrated in the figure 2.12). The initial state of the material is highly variable from a sample to the other and difficult to characterize because of the fluffy nature of the powder. The material has very low resistance to compaction and shear. Identification of the constitutive law is difficult due to the limitation of the accuracy of the pressure sensors and some hypotheses have to be made. The hardening of the powder occurs as soon as a loading is applied. The cohesion of the powder is null and the elastic parameters are small compared to the one identified for the fully compacted material.

To overcome the difficulty to describe properties of the powder, the fully compacted material, for which the void ratio is null, is chosen as state of reference. At this stage, the hardening law, the elastic parameters and the cohesion tend to asymptotic values. The state of the material is described thanks to the void ratio instead of the volumetric strain whose definition depends on the initial state of the sample.

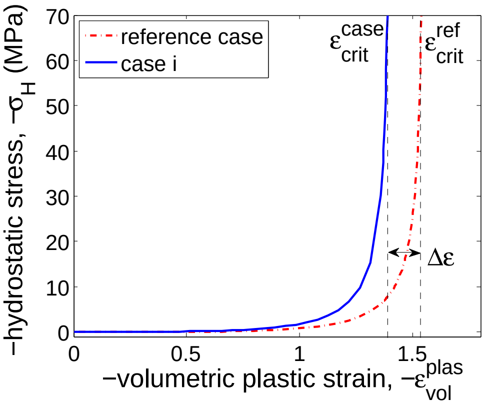

**Figure 2.12:** For high void ratio, a small loading induces a large variation of volume. The uncertainty on the initial state of the powder is high.

## 4.2 Procedure of parameter identification

### 4.2.1 Consolidation part - hardening law - description of the densification of the material

First of all, the consolidation part of the mechanical behavior of the material is studied. The hardening law of the consolidation part of the model is described as the evolution of the hydrostatic yield stress (i.e. the parameter $p_b$ figure 2.10) as a function of the volumetric plastic strain. It is identified from the hydrostatic test with successive loading/unloading steps, performed in the 3D compaction device. The experimental data obtained for the virgin PTFE is shown in figure 2.13.

At the end of each unloading step, the hydrostatic stress is smaller than 5 MPa so that the elastic recovery of the material is assumed to be complete. The plastic part of

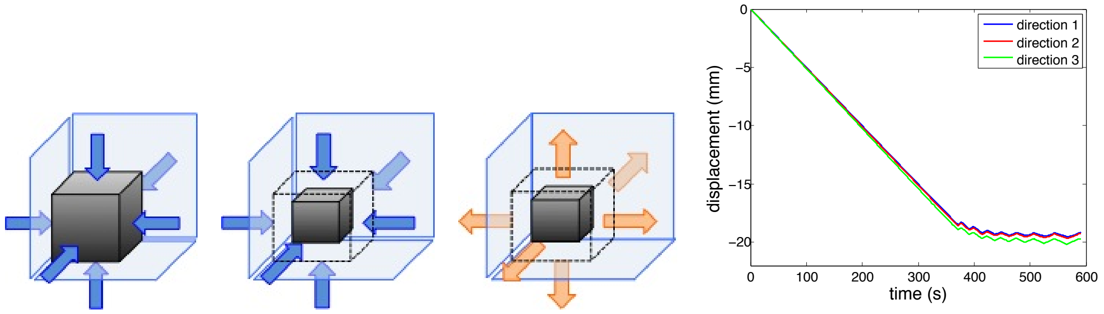

(a) Initial state (b) Loading (c) Unloading (d) Measured displacements in the three directions

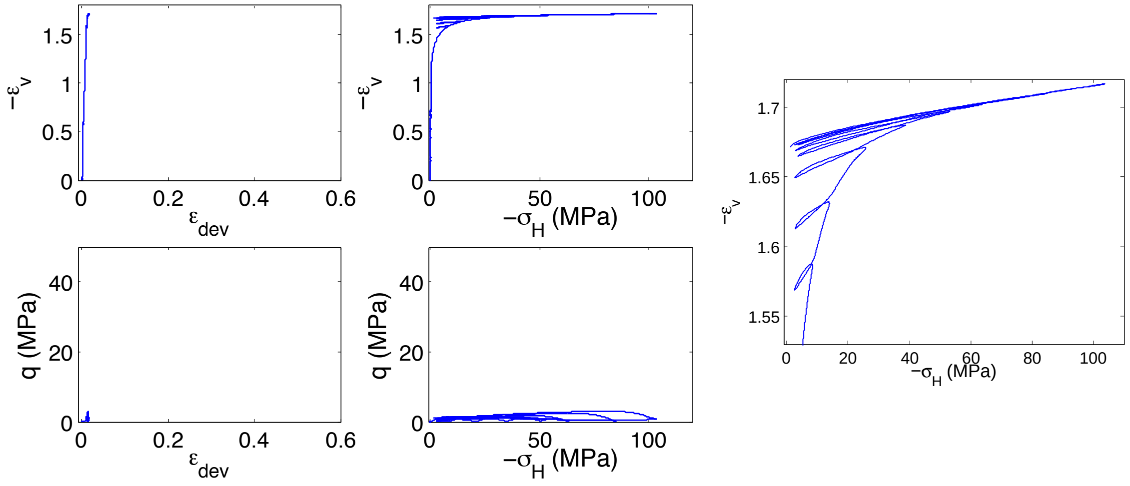

(e) Experimental results

(f) Zoom on the unloading steps in the volumetric strain vs hydrostatic stress plane

**Figure 2.13:** Hydrostatic test with successive unloading steps at increasing levels of hydrostatic stress - The same displacements are applied in the three directions - The volumetric strain increases while the deviatoric strain remains small - a small variation of the deviatoric part is mainly imputed to the non symmetry of the actuators of the machine - virgin PTFE

the volumetric strain is directly given by the measured minimum volumetric strain. The hydrostatic stress required to reach this level of plasticity is equal to the maximal stress reached before the beginning of the unloading.

The evolution of the hardening law, as required in Abaqus, is described, as proposed in [Frachon, 2002], by

$$p_b = a.\left(\ln\left(\frac{b\varepsilon_{crit}}{\varepsilon_{crit} - \varepsilon_{vol}^{plas}}\right)\right)^n \tag{2.20}$$

with $a$, $b$ and $n$ positive constants and $b > 1$. It is easy to observed that the maximum volumetric compaction is $\varepsilon_{crit} = \varepsilon_{vol}^{plas}(e_p = 0)$, the asymptotic volumetric plastic strain corresponding to a dense material for which the void ratio $e$ tends to zero as defined in the above section. The algebraic expression is illustrated in figure 2.14.

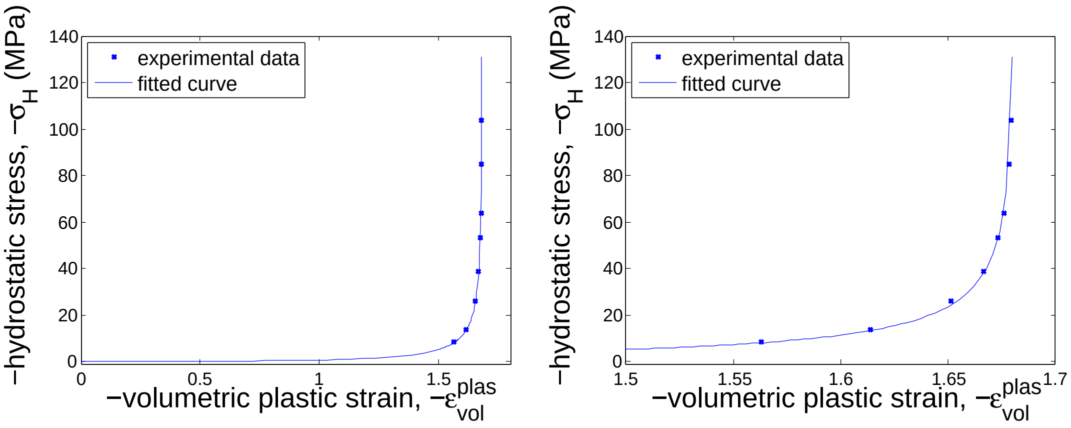

(a) Evolution of the hydrostatic stress as a function of the volumetric plastic strain

(b) Zoom on the high pressure area

**Figure 2.14:** Fit of the experimental hardening curve - virgin PTFE

The expression 2.20 of the hardening law describes the main steps of the compaction. Indeed, during the first stage of the pressing, large displacements occur with negligible applied stress as the main action is to expel the air. Particles may rearrange easily. When the cohesion in the material increases and bonds between particles become tighter, stress starts to increase until reaching an asymptotic vertical limit at $\varepsilon_{crit}$. The voids are then closed, and the density of the material tends to the absolute PTFE density, $\rho_{crit}$ (figure 2.15).

The absolute density of the different compounds studied here are measured by helium pycnometry. The measurements are made on 5 g of material at 21°C and are presented table 2.1. The favorable comparison between these measured values and the value of density extrapolated from the data obtained in the 3D compaction device indicates that the critical state (where $e = 0$) is well estimated.

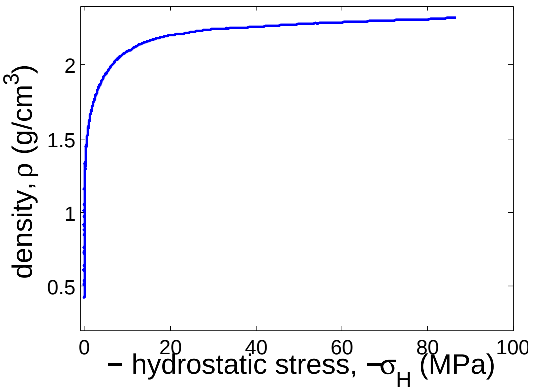

**Figure 2.15:** Evolution of the density as a function of the hydrostatic stress - virgin PTFE

**Table 2.1:** Validation of the identification of the density by comparison of the absolute densities measured by helium pycnometry the one identified from the hydrostatic test.

| Material | Absolute density (g/cm$^3$) | |
|---|---|---|
| | He pycnometry | hydrostatic test |
| virgin PTFE | 2.26 | 2.27 |
| PTFE + filler 1 | 2.23 | 2.19 |
| PTFE + filler 2 | 2.02 | 2.017 |

### 4.2.2 Identification of the elastic parameters

The identification of the evolution of the elastic properties with the void ratio, based on experimental tests made in the 3D compaction tool, is presented in this part.

The bulk modulus $K$ and the shear modulus $G$ are chosen to describe the elastic behavior of the material. This way, stress and strain quantities are directly linked with

$$\sigma_H = K\varepsilon_{vol}^{elas} \qquad \text{and} \qquad q = 3G\varepsilon_{dev}^{elas} \tag{2.21}$$

Based on the previous hydrostatic test with successive loading/unloading steps, the value of the bulk modulus $K$ is identified as the slope of curve in the $(-\varepsilon_{vol}, -\sigma_H)$ plane at the beginning of the unloading step. The evolution of $K$ as a function of the void ratio, identified in the previous step, in the case of the virgin PTFE, is presented figure 2.16.

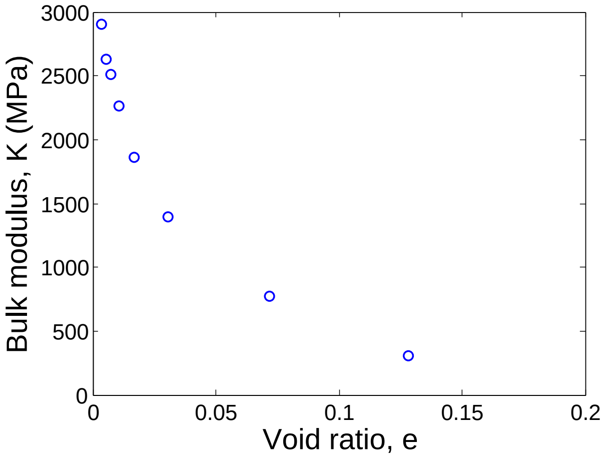

**Figure 2.16:** Evolution of the bulk modulus $K$ as a function of the void ratio $e$, deduced from the hydrostatic test. As expected the elastic stiffness of the material increases while the resin is pressed - virgin PTFE.

Hysteresis loops appear during the loading/unloading steps 2.13, because of dissipation mainly caused by viscoelasticity effects resulting from the polymer viscosity, as well as the permeation of the air out of the compacted volume. However the viscosity of the elastic part is assumed to be negligible here. The same test has been performed at different strain rates. The observed differences are within the measurement uncertainties and hence no specific micro structural information may be derived (figure 2.17) in the range of the tested applied speeds, allowed by the capacities of the triaxial machine (thermal problem, maximal speed of the actuators).

The 3D compaction device makes it possible to investigate various complex loading paths in the $(-\sigma_H,q)$ plane. In 'isodensity' tests (figure 4.2.2), after a monotonic hydrostatic displacement loading, the volume is kept constant while the deviatoric part of the strain is increased. During the second stage, the displacement in one direction is increased while it is decreased in the other two directions, twice slower, so that the material

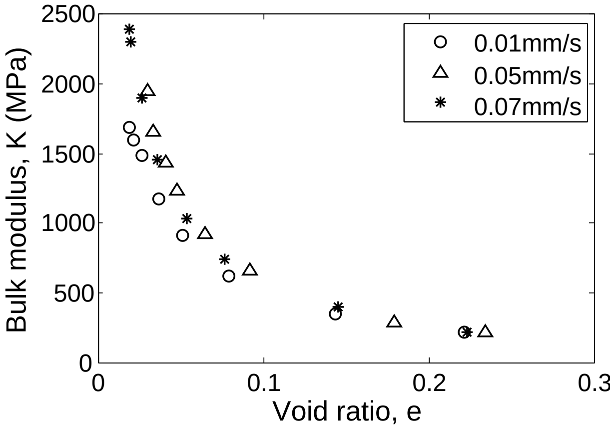

**Figure 2.17:** Evolution of the bulk modulus as a function of the void ratio - influence of the strain rate. No influence of the strain rate could be seen here - PTFE + filler 1

is sheared at a constant volume. The increase of strain is finally imposed so that

$$\Delta\underline{\underline{\varepsilon}} = \begin{pmatrix} \Delta\varepsilon & 0 & 0 \\ 0 & -\frac{1}{2}\Delta\varepsilon & 0 \\ 0 & 0 & -\frac{1}{2}\Delta\varepsilon \end{pmatrix} \tag{2.22}$$

in order to have,

$$\mathrm{tr}(\Delta\underline{\underline{\varepsilon}}) = \Delta\varepsilon_{vol} = 0 \tag{2.23}$$

The shear modulus $G$ may be straightforwardly identified as 3 times the slope of the curve in the $(\varepsilon_{dev}, q)$ plane, in the elastic regime, at the beginning of the isodensity step. The same test is performed with different levels of hydrostatic stress during the first pressing step so that the evolution of the shear modulus as a function of the void ratio is measured as shown in figure 2.19.

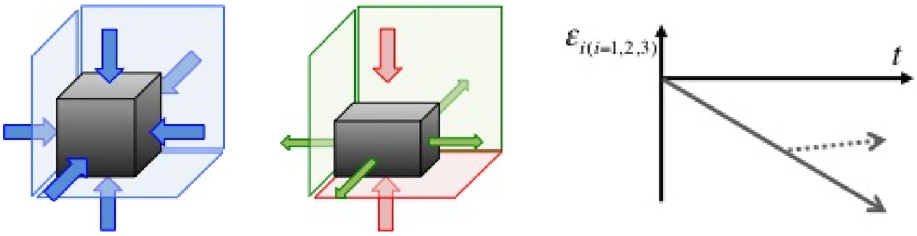

(a) Hydrostatic loading

(b) Isodensity loading

(c) Imposed strain in the 3 directions

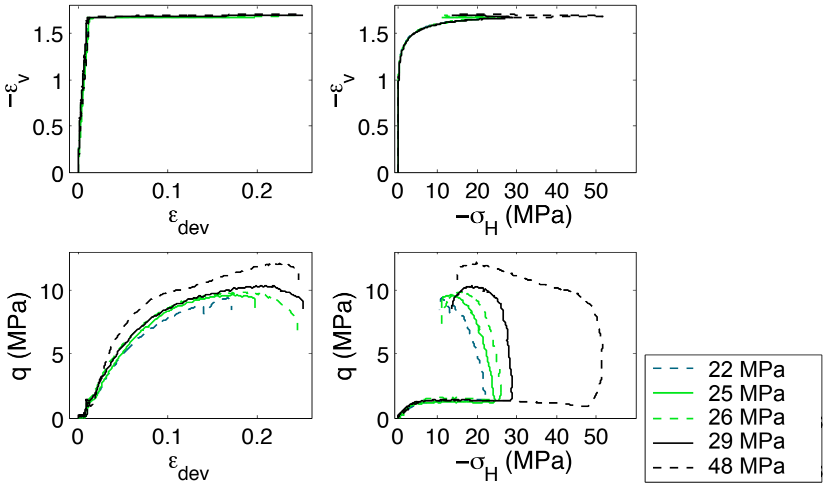

(d) Isodensity tests at different level of hydrostatic loading - virgin PTFE

**Figure 2.18:** Displacement controlled isodensity test in 3D compaction device - during the second part of the test, the volume is kept constant.

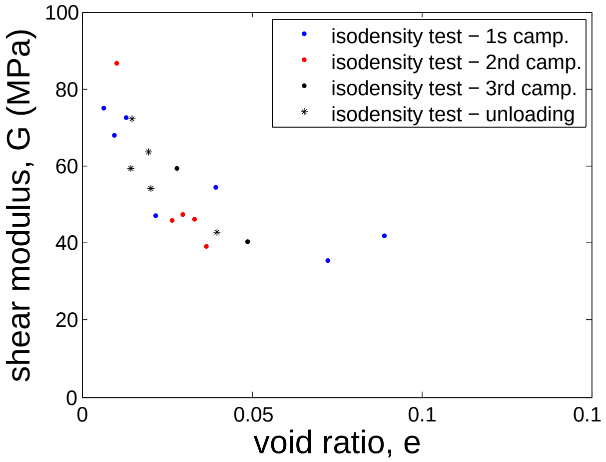

**Figure 2.19:** Evolution of the shear modulus $G$ as a function of the void ratio $e$ - virgin PTFE - The uncertainty on $G$ is higher than the one on $K$, several series of tests have been performed.

One may argue that hardening may occur right from the beginning of the isodensity step. To validate this point, another series of tests have been done. After the hydrostatic loading and before the isodensity step, the hydrostatic stress is released by a few MPa to ensure to be inside the yield surface. The shear modulus $G$ is identified the same way and no significant difference of results is observed between the two types of tests as shown in figure 2.20. The differences are of the order of magnitude of the uncertainties as shown figure 2.19.

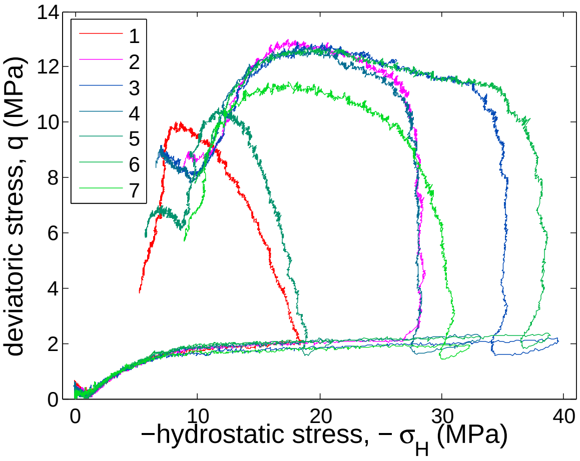

**Figure 2.20:** Isodensity test preceded by unloading hydrostatic step - tests 1 and 2 are isodensity tests without unloading step. The procedure of identification is validated.

The evolution of the elastic parameters, viz the bulk modulus $K$ and the shear modulus $G$, as a function of the void ratio is described as

$$K(e) = K_p + (K_{crit} - K_p)\,(1+e)^{-a_K} \tag{2.24}$$

$$G(e) = G_p + (G_{crit} - G_p)\,(1+e)^{-a_G} \tag{2.25}$$

with $K_p$ and $G_p$ the values of the bulk modulus and the shear modulus respectively of the powder at the initial state, $K_{crit}$ and $G_{crit}$ the elastic parameters of the densified bulk material for which $e = 0$ and $a_K$ and $a_G$ are two exponents. Both bulk and shear moduli $K_p$ and $G_p$ can be chosen arbitrary small compared to the one of the bulk material $K_{crit}$ and $G_{crit}$. The parameters $a_K$ and $a_G$ characterize the more or less rapid increase of the moduli with compaction. The increasing is faster for the hydrostatic part of the behavior than for the deviatoric part.

The associated engineer moduli $E$ and $\nu$, calculated from the relationship

$$E = \frac{9KG}{3K+G} \qquad \text{and} \qquad \nu = \frac{3K-2G}{2(3K+G)} \tag{2.26}$$

are presented figure 2.21 At the critical state, $\nu$ tends to 0.5 which is consistent with the fact that the material is closer to the bulk PTFE material that is quasi incompressible.

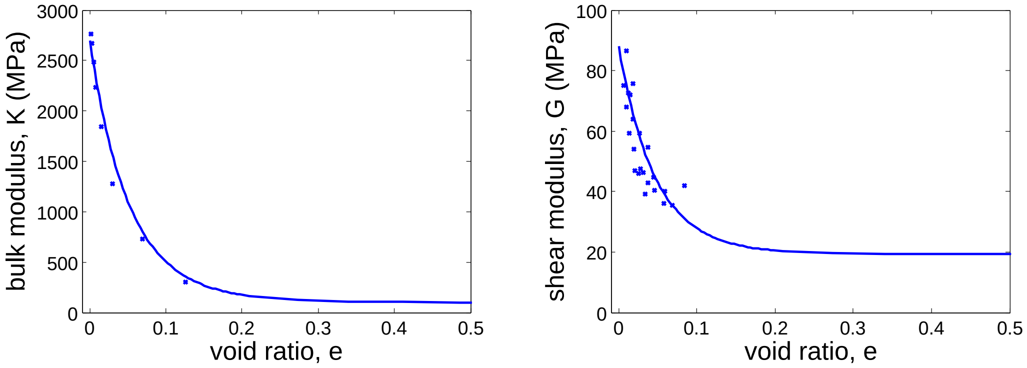

(a) Bulk modulus *K* (b) Shear modulus *G*

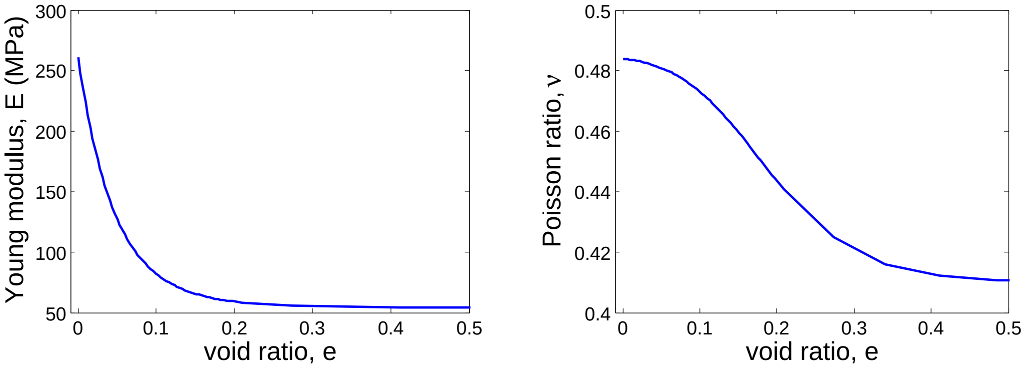

(c) Young's modulus, *E* (d) Poisson's ratio, ν

**Figure 2.21:** Evolution of the elastic parameters and their fitted curves - virgin PTFE

### 4.2.3 Characterization of the cohesion part

In two tests, the material may reach its shear failure surface :

- hydrostatic test followed by 'isodensity' test,
- hydrostatic test followed by 'isopressure' test.

For the so-called 'isopressure' test, which is force-controlled, all the samples are compacted with the same void ratio at the end of the hydrostatic loading, as the first hydrostatic load is similar for all the tests. Then the hydrostatic pressure is decreased to a given value, before the 'isopressure' loading starts. As shown figure 2.22, the forces are controlled so that the pressure remains almost constant while the deviatoric strain increases. The offset yield points at 0.2% strain are measured for each level of pressure. These points define the shear failure surface for a hydrostatic pressure $p_b$ of $\sim$70 MPa. They may be fitted with a line whose slope is equal to the tangent of the internal friction angle of the material $\tan(\beta)$ (figure 2.23).

It is found to be small and equal to 0.06, which is in agreement with the physical properties of the PTFE described in the introduction. This parameter is assumed to be constant. Considering the low sensitivity of the angle during the simulation of the industrial process and its low value, no effort has been made to characterize the evolution of the internal friction with the void ratio.

Once the value of the slope of the Drucker-Prager line is known, the cohesion of the material $d$ may be identified. Both 'isopressure' tests and 'isodensity' tests performed at different level of density allow for the identification of the cohesion.

During 'isodensity' tests, while the material is sheared after the consolidation step, the deviatoric stress increased while the hydrostatic stress slightly decreases. Indeed, as seen in other materials ([Brochu et Turenne, 2004], [Watson et Wert, 1993]), a reasonable deviatoric component in the loading makes the compaction of the material easier. Thus, as the volume is kept constant, the hydrostatic component of the stress tensor is decreased. However, if the shear component is too large as compared to the combined effects of the cohesion and the internal friction of the material, the material fails. The failure is characterized by a quick decrease of the hydrostatic stress and the much slower increase of the deviatoric stress.

The cohesion is identified in the $(\varepsilon_{dev}, q)$ plane as shown figure 2.24. The deviatoric stress is equal to $q^d = \tan\beta(-\sigma_H^d) + d$ where $-\sigma_H^d$ is the value of the hydrostatic stress at the same time. As the internal friction angle $\beta$ has been previously measured, the cohesion $d$ and its evolution as a function of the density of the material may be directly deduced.

Figure 2.25 shows the evolution of the cohesion $d$ as a function of the hydrostatic stress $p_b$. As expected, the cohesion of the material increases with the densification of the material. Note that low values of confinement pressure followed by isodensity test were difficult to achieve. The initial value of this cohesion is assumed to be close to zero in the initial powder state. The cohesion is described as a power-law of the solid volume fraction

$$d(e) = a_d\,(1+e)^{-b_d} \tag{2.27}$$

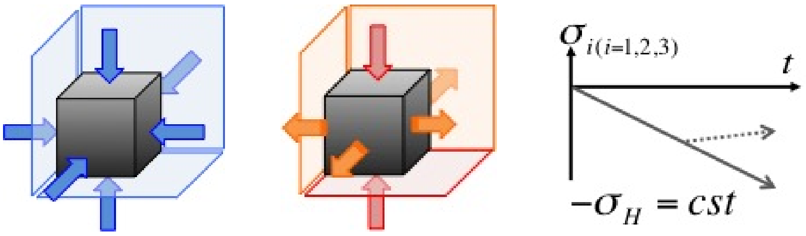

(a) Hydrostatic loading

(b) Isopressure loading

(c) Imposed stress in the 3 directions

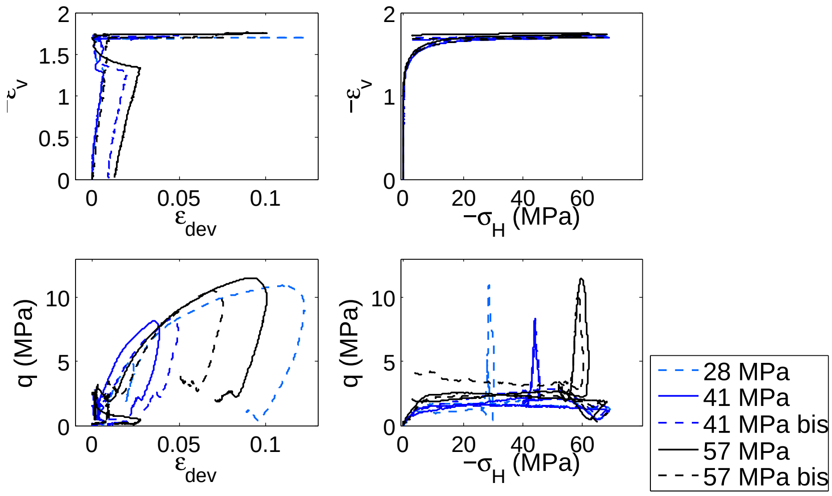

(d) Isopressure tests at different level of hydrostatic loading

**Figure 2.22:** Force controlled 'isopressure' tests in 3D compaction device. For the first stage of the hydrostatic loading, displacement are applied until a sufficient level of stress is reached to control the loading in force. Once the switch is made, the same force is applied in the three directions. The sample is compacted to a maximal hydrostatic stress and unloaded. Then during the second part of the test, the hydrostatic stress is kept constant while the deviatoric stress increased by decreasing the forces equally in two directions and increasing the force in the third one, twice as much.

with $a_d$ the maximal cohesion at the asymptotic state and $b_d$ the exponent. The cohesion is close to zero for large values of void ratio $e$ and increases up to the maximal cohesion at the asymptotic state. Considering the limitation of the implemented model in Abaqus, no hardening of the Drucker-Prager surface as a function of the shear component is taken into account. The behavior would not be realistic under tension where the strength is known to be much lower.

### 4.2.4 Characterization of the consolidation part of the model

Up to this point, the Drucker-Prager line has been characterized as well as the position of the consolidation surface (the hardening law associated to the consolidation mechanism,

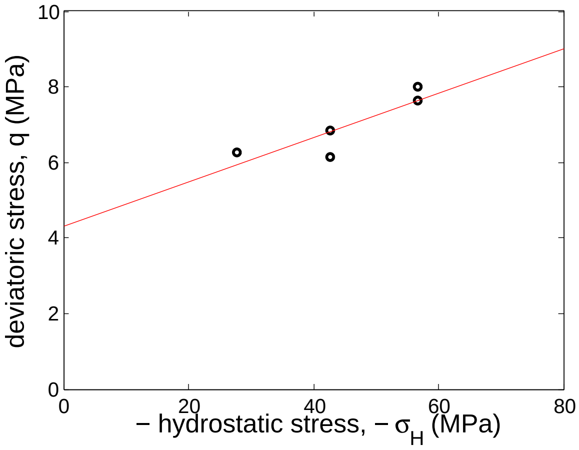

**Figure 2.23:** Identification of the internal friction coefficient tan β - for virgin PTFE initially hydrostatically compacted at 70 MPa

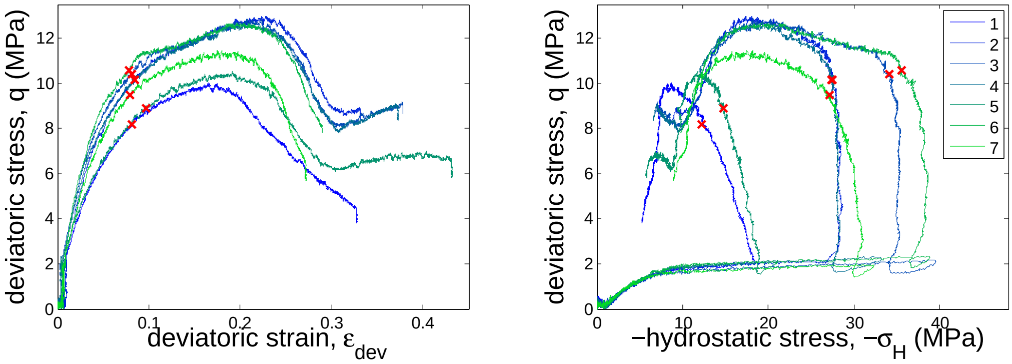

(a) First step - identification in the $(\varepsilon_{dev}, q)$ plane

(b) Corresponding hydrostatic stress

**Figure 2.24:** Identification of the cohesion *d* of the material

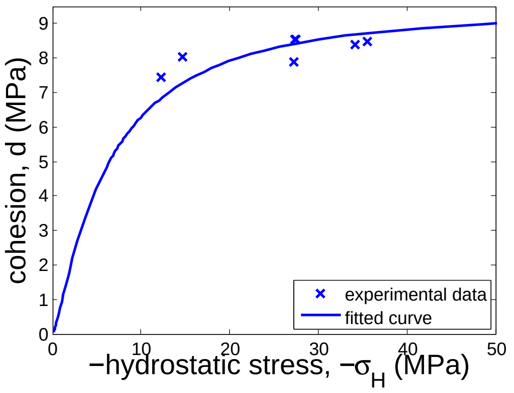

**Figure 2.25:** Evolution of the cohesion $d$ respect to the hydrostatic stress $p_b$

identified from the hydrostatic test). The evolution of the parameter $R$ as a function of the void ratio is identified from the response of the material along a 'three rate' type test where the applied displacement rates in each direction are constant and $\dot{\varepsilon}_1 = x\dot{\varepsilon}_3$ and $\dot{\varepsilon}_1 = y\dot{\varepsilon}_2$ (figure 4.2.4). For computational reasons, the ratio $p_a/p_b$ which always satisfies $0 < p_a/p_b < 1$, is preferred as an unknown to be identified as compared to the quantities $R$ or $p_a$. These quantities are linked through the equation 2.17. The range of the void ratio $e$ is divided in several intervals $e_{i-i+1}$. First the value of the ratio $p_a/p_b$ is assumed to be constant. A first FE simulation of the 'three rate' test on an element of volume (as described section 7.2) is made. By comparison of the experimental data with the FE results, the values of the ratio $p_a/p_b$ on each interval $e_{i-i+1}$ are adjusted to minimized the error. The FE computations are iterated, the results are compared to the experimental data and the parameters are adjusted by dichotomy at each iteration until the error between the response of the material and the simulation of the test is less than 10%. The piecewise-defined function of the ratio $p_a/p_b$ as function of the void ratio $e$ may be then fitted with a continuous function. Results for virgin PTFE are shown in figure 2.27.

With this last step, the identification procedure has been presented exhaustively. In the following it will be used to characterize the different powders.

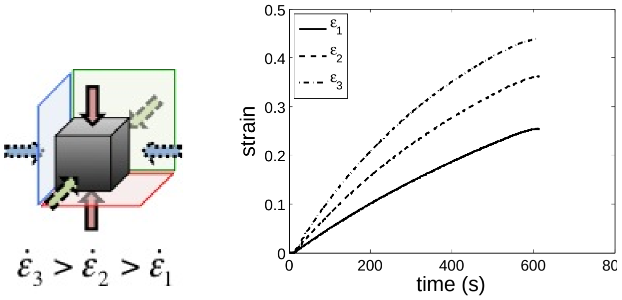

(a) ‘three rate’ loading

(b) Imposed strain in the three directions

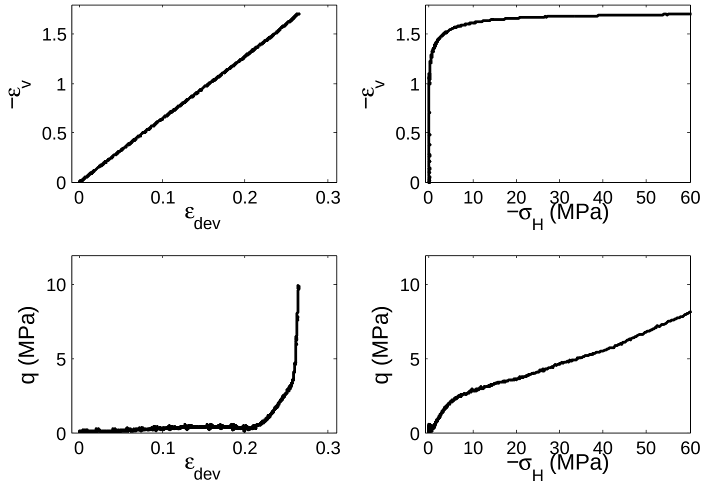

(c) Experimental results

**Figure 2.26:** Displacement controlled ‘three rate’ test in the 3D compaction device. The displacements are imposed in each direction with different monotonic rates.

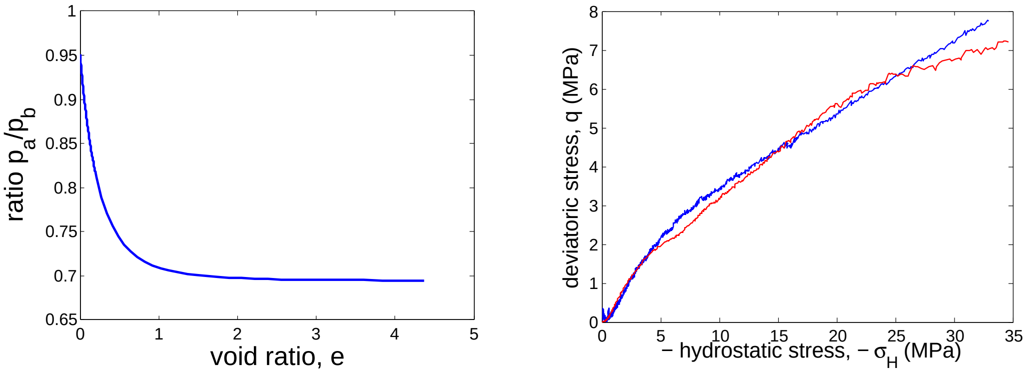

(a) Evolution of the ratio $p_a/p_b$

(b) Comparison of the experimental data and the FE simulation of the ‘three rate’ test.

**Figure 2.27:** Identification of the shape of the cap surface.

# 5 Phase transition

## 5.1 Description of the phenomenon

During the unloading and reloading steps, a non-linear behavior is observed (see for instance the evolution of $\sigma_H$ vs. $\varepsilon_{vol}$ during the hydrostatic test shown in figure 2.13). This may be explained in cohesive materials like clay or non-cohesive materials like glass beads, by the modification of the area of contact between particles with the applied loading. In the case of PTFE, the ambient phase transition, described in the introduction 2, has to be taken into account and contributes to this non linearity.

Indeed, it is argued here that the crystalline phase transition has a strong influence on the mechanical properties of PTFE ([Rae et Brown, 2005], [Brown et Dattelbaum, 2005], [Blumm *et al.*, 2010]). The influence of the phase transition (II to IV and IV to I) is observed on the evolution of the elastic parameters and the failure stress. The fracture mode brutally goes from brittle with coalescence of micro voids in phase II to ductile fracture with localization in fibril up to 1 $\mu m$ in diameter and several mm length for phases IV and I.

The phase transition II-IV has an influence on the interactions between the particles of PTFE and with other materials. It is found that the blending of PTFE material with other particles is easier below 19°C while the transmission of load during the compaction is less efficient than at higher temperature. The compaction of the compounds is always made above 19°C ([Ebnesajjad, 2002]).

The phase transition causes a significant change in the volume of the crystal and so of the bulk material. From phase II to phase IV, an increase of the volume of 1.8% is commonly measured for sintered material with a crystalline fraction of 50-60%w ([Ebnesajjad, 2002], [Quinn Jr *et al.*, 1951], [Kirby, 1956], [Blumm *et al.*, 2010]).

In [Eby et Sinnott, 1961], it is shown that the rate of the phase transition and the level of variation of the parameters linked to this phase transition depends on the crystallinity. The transition extends on a wider range of temperature for nascent PTFE than for sintered material.

Phase change may also occur varying the pressure in isothermal conditions. In [Beecroft et Swenson, 1959], at 27.8°C, a volume change due to the II-IV transition occurs at 65 MPa and is estimated to amount to 0.5%. The volume change is found to be higher at 20°C and atmospheric pressure and equal to $\sim$0.8%. [Brown *et al.*, 2007] shows that the phase transition may occur at a lower level of pressure if a shear loading is added.

## 5.2 DSC measurement

In order to characterize these phase transitions, at first, Differential Scanning Calorimetry (DSC) analyses of the three compounds were carried out on samples of approximately 15 mg of the as received powders using a Setafram DSC 131.

As expected and described in the literature (for instance on nascent PTFE in [Canto *et al.*, 2011]), two first peaks appear at around 19.5°C and 28°C (figure 2.28) which correspond to the phase transitions at ambient temperature between the phases II and IV and the phases IV and I. Then a third peak arises and reaches its maximum at the temperature of 340°C, which corresponds to the melting of the nascent crystalline phase. When the material is cooled down, the re crystallization of the material occurs at a lower temperature than the melting one, viz 317°C. The material is partially crystallized ([Canto *et al.*, 2011]).

A particular attention is paid to the characterization of the ambient temperature transition phase. In a second test, the raw material is heated up with a rate of 5°C/min from -40°C to no more than 100°C so that the nascent crystalline phase does not start to melt. The sample is then cooled down with a rate of -5°C/min to the minimum temperature reachable by the testing device. Results are presented in figure 2.29.

During the cooling, the same peaks are observable but the transition temperatures are lowered, especially for the main IV-II transition.The integrated area of both peaks during cooling is 30% smaller than the same peaks during heating.

The influence of the fillers is analyzed (figure 2.30). The temperature of the phase transition are not changed by adding fillers to the PTFE powder. However, the area of all the peaks are smaller, which may be partly explained by the smaller amount of PTFE in filled samples. Interactions between the fillers and the PTFE particles may also explain these differences.

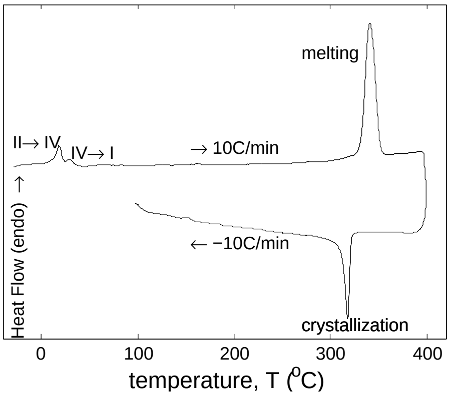

**Figure 2.28:** DSC of the virgin PTFE powder from -40°C to 400°C. The sample is cooled down to -40°C, heating up to 400°C with a rate of 10°C/min, maintained at the maximal temperature during 5 minutes, and finally cooled down with a rate of 10°C/min. Because of the limitation of the machine, the initial temperature of -40°C could not be reached at the end of the cooling step, keeping the same rate of decrease of the temperature.

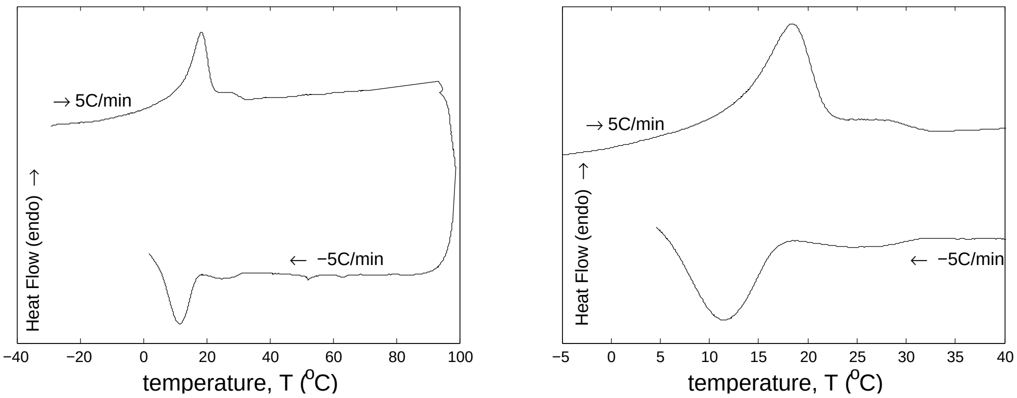

(a) DSC of the virgin PTFE powder from -40°C to 100°C

(b) Zoom on the phase transition area

**Figure 2.29:** DSC with heating up and cooling down without reaching the melting temperature

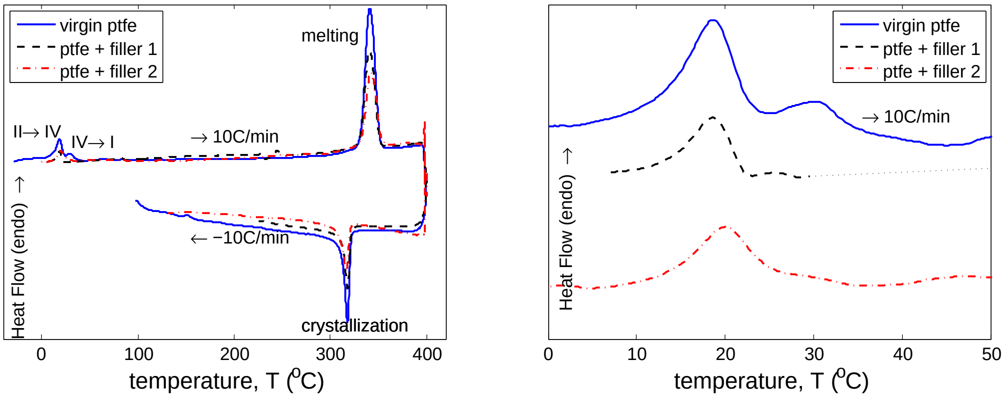

(a) DSC of the three compounds from -40°C to 400°C

(b) Zoom on the phase transition area at ambient temperature

**Figure 2.30:** Influence of the fillers. The same thermal loading is applied on each sample.

## 5.3 Thermal tests

A sample compacted in an œdometric tool with a rectangular base of 35×35 mm$^2$ section is subjected to a thermal loading between 7°C and 36°C. The sample is placed in a climatic chamber and lies on a glass plate. Once the desired temperature is reached, a minimum waiting time of 90 min allows the temperature to become homogeneous, and an equilibrium state reached in the sample. The sample is first cooled from 35°C to 7°C and then heated to 36°C. A random speckle pattern was previously sprayed on the sample and pictures are acquired at the end of each stabilization period of applied constant temperatures. Using DIC (see 6.2.2), displacement fields at the surface of the sample are measured. The deformation field is homogeneous at the surface of the sample and almost equal in both directions. Between 7°C and 35°C, the evolution of the deformation with temperature is non linear as shown figure 2.31 and the increase of deformation is equal to 0.6%. This value is in good agreement with what is reported in the literature ([Quinn Jr *et al.*, 1951], [Kirby, 1956], [Blumm *et al.*, 2010]). The deformations at 35°C before the cooling and the ones after the heating from 7°C to 36°C are almost equal (the difference is less than 5% which may also be caused by the difference of temperature and the error of measurement of the displacements).

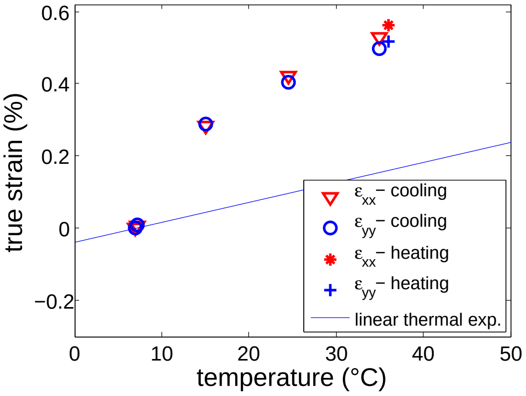

**Figure 2.31:** Averaged measured deformations at the surface of the sample (standard deviation less than 0.03%) vs temperature. The line has a slope equal to the thermal expansion coefficient at the reference temperature $T_{ref} = 5°C$ and corresponds to the thermal expansion that the sample would exhibit without phase change.

## 5.4 Mechanical tests

Figure 2.32 shows details of the loading/unloading hydrostatic test in the volumetric strain vs. hydrostatic stress plane presented earlier. For better representation, only few loading/unloading loops are represented. Neglecting the non linearity due to the viscosity of the material, an elastic recovery would follow the dash lines. This is the case for the first unloading step. But above 10 MPa, the gap between the linear fit is almost zero up to a critical pressure where the difference starts to highly increased. This gap is plotted for each unloading step 2.33. The final value of the gap tends to a mean value equal to $6.10^{-3} \pm 0.23$ (figure 2.33). This value is consistent with the estimation of the volume change due to phase change from phase IV to phase II. The observed non-linearity may be reasonably and partly explained by a progressive phase change induced by an increase of hydrostatic stress.

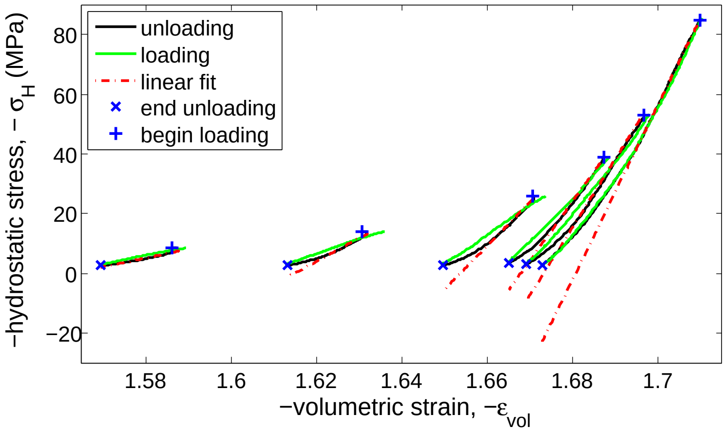

**Figure 2.32:** Loading/Unloading steps of hydrostatic test. The black lines are for the unloading steps up to the local minimum point (x), the green ones for the re loading step up to the local maximal pressure (+). The fit of the linear part of the curve at the beginning of the unloading is plotted with dash lines. The slope of these lines corresponds to the bulk modulus $K$ of the material at a given void ratio.

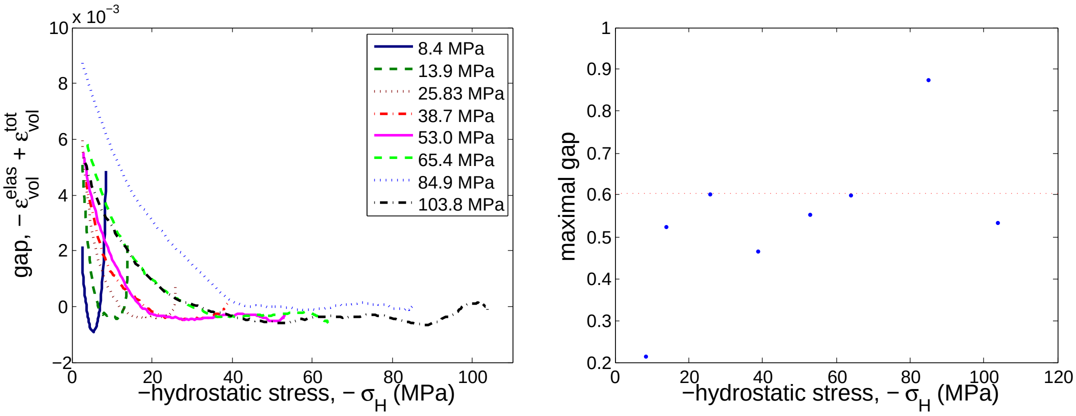

(a) Difference between the total volumetric strain and the elastic strain at different level of pressure during the compaction

(b) The maximal difference, at the end of the unloading is plotted as a function of the maximal applied pressure of each loop. Above 10 MPa, the difference may be considered as constant and tends to ∼0.6%.

**Figure 2.33:** Evolution of the volume change superimposed to the linear elastic recovery

## 5.5 Modeling

Here, a constitutive modeling is proposed to describe the II-IV phase transition.

Two striking observations can be made that distinguish the above discussed phase transitions from other simple ‘textbook’ phase transitions :

1. they are spread over a significant range of temperatures ;
2. they may display a very large hysteresis.

The second (2) obviously does not fit in the classical description of equilibrium thermodynamics. An explanation based on nucleation phenomena is not satisfactory when addressing non monotonous loading, even if parameter tuning may provide good fits when enough freedom is left for simple paths. One difficulty comes from the fact that energy barriers between different states exceed by far the thermal energy level $kT$ (with $k$ the Boltzmann’s constant) and hence one cannot consider the system as exploring its phase space due to thermal agitation, and hence it cannot reach a proper equilibrium.

Our interpretation is that intrinsically temperature $T$ and stress (pressure $p$) are coupled. Residual stresses may initially be responsible for an effective apparent distribution of transition temperatures. Indeed, residual stresses come in addition to the macroscopically imposed stress, and the $p-T$ coupling can easily convert stress into a temperature offset. This phenomenon may explain the first reported point (1) if the temperature width of the macroscopic transition is read as the statistical distribution of local transition temperatures. Moreover, the phase transition is locally very anisometric (the helix conformation of PTFE is not simply a change of volume, as lateral and longitudinal strains are not equal). Such a local transition cannot be kinematically compatible with the neighboring elements unless all crystallized domains have the very same orientation (and no residual stress). Similarly, a heterogeneous residual stress distribution would also generate incompatibilities even for pure volumetric transformations as different element of volumes do not change their conformation simultaneously. Incompatibility is resolved through the development of elastic stress, itself influencing the transition point and hence a transition locally may impede or promote the neighboring phase transformation. This phenomenon may give rise to strong hysteretic effects. Its theoretical description is however a formidable task and we are not aware of any convincing approach to account for it, in spite of the fact that such non-equilibrium transition is quite common in solid mechanics.

The phase transition is spread over more than 10°C at atmospheric pressure and several MPa in isothermal conditions without a significant hysteresis when cycling. A simple linear mapping from temperature to pressure is used. The conversion factor $\alpha_{pT}$ cannot be else than the slope of the transition line in the $p-T$ plane (figure 3). Now, the remaining task is to model the distribution of effective transition temperatures, $d_{trans}(T)$, (that can be read in calorimetric measurement, in figure 2.29), or its cumulative version $D_{trans}(T) = \int_{T_{start}}^{T} d_{trans}(T')dT'$ which can be accessed in dilatometric measurements (such as shown in figure 2.31) (up to a scale factor which is the asymptotic strain after the transition) or isothermal mechanical loading (figure 2.33).

The distribution of effective transition as a function of the temperature is described by

$$d_{trans} = \frac{ab\exp(-a(T-\delta T))}{(1+b\exp(-a(T-\delta T)))^2} \tag{2.28}$$

The expression of the cumulative version of the distribution is

$$D_{trans} = \frac{1}{1+b\exp(-a(T-\delta T))} \tag{2.29}$$

with $a$, $b$ and $\delta T$, constant values. Thus, the heat flow $W$ during calorimetric measurement, such as in figure 2.29, may be expressed such as

$$W = C_w d_{trans} \tag{2.30}$$

with $C_w$ a constant. Note that the maximum of heat flow is reached at the temperature $\Delta T = \delta T - 1/a\ln(1/b)$.

The expression of the deformation during the heating of the sample, $\varepsilon_{th}$ is the sum of the linear thermal expansion, whose thermal coefficient is $\alpha_{th}$, and the deformation caused by the phase transformation

$$\varepsilon_{th} = \varepsilon_{crist} D_{trans} + \alpha_{th}(T - T_{ref}) \tag{2.31}$$

with $\varepsilon_{crist}$ the total variation of volume due to the phase transition.

The pressure and the temperature are linked by the conversion factor $\alpha_{pT}$. Thus the expression of the cumulative distribution $D_{trans}$ as a function of the pressure in isothermal loading is

$$D_{trans}(p) = \frac{1}{1+b\exp(-\frac{a}{\alpha_{pT}}(p-\delta p))} \tag{2.32}$$

with $\delta p = \delta T/\alpha_{pT} - (1/a)\ln(1/b)(1 - 1/\alpha_{pT})$. Finally, at constant temperature, the phase change strain $\varepsilon_{trans}(p)$ is equal to

$$\varepsilon_{trans} = \varepsilon_{crist} D_{trans}(p). \tag{2.33}$$

And the total strain would be equal to the sum of the elastic, plastic and transformation strains

$$\varepsilon = \varepsilon_{elas} + \varepsilon_{plas} + \varepsilon_{trans} \tag{2.34}$$

The identified parameters are given in the table 2.2 and the comparison between the experimental data and the model are shown in the figure 2.34.

**Table 2.2:** Identified parameters

| | |
|---|---|
| Conversion factor $\alpha_{pT}$ (MPa.K$^{-1}$) | 3.7 |
| $a$ | 0.635 |
| $b$ | 7.0 |
| Temperature $\delta T$ (˚C) | 8.34 |
| Total phase change deformation $\varepsilon_{crist}$ (%) | 0.6 |

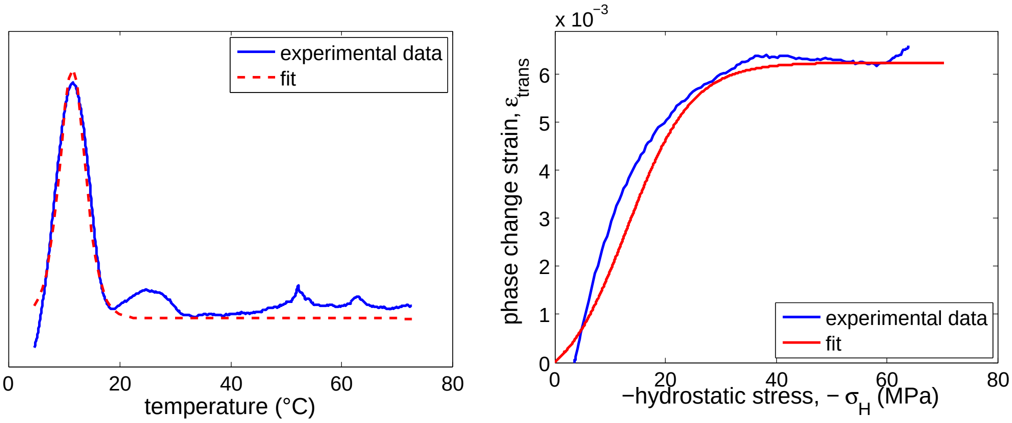

(a) Modeling of phase transition IV-II during DSC test

(b) Modeling of the deformation caused by phase transition during isothermal hydrostatic loading. The experimental curve corresponds to the gap $\varepsilon_{vol}^{tot} - \varepsilon_{vol}^{elas}$ as shown figure 2.33a. where a maximal stress of 65 MPa is applied before the unloading step.

**Figure 2.34:** Comparison between the experimental data and the identified model of the phase transition for tests at atmospheric pressure and tests at ambient temperature.

The comparison of the two models, with or without adding the phase change model to the elasto-plastic constitutive equations is presented figure 2.35. The improvement of the model is obvious. This phase change describes the major part of the observed non linearity that appears above 20 MPa of hydrostatic loading and cannot be neglected.

To improve the model, additional experimental tests may be done. DSC and dilatometry tests at difference rate of thermal loading and with both cooling and heating stages may allow to better characterized the irreversible aspect of the phase transformation and its dependance on time. As shown in [Brown *et al.*, 2007], the phase change also depends on the amount of shear loading. Additional loading unloading tests like 'isopressure' or 'isodensity' tests, where the hydrostatic part of the loading is kept constant, should help to characterize the influence of shear.

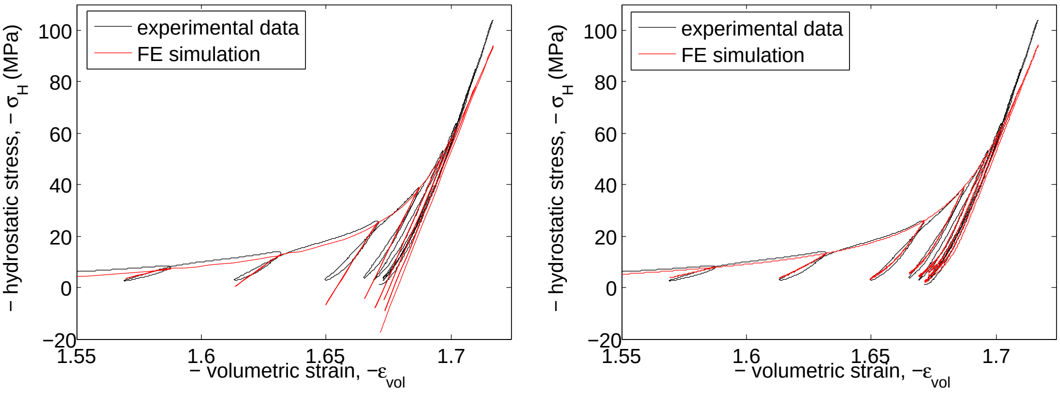

(a) Simulation without the phase transition model (b) Simulation with the phase transition model

**Figure 2.35:** Comparison of the model with and without taking into account of the phase change II-IV. Finite Element simulation of the hydrostatic test with successive loading/unloading steps - The hydrostatic stress is plotted as a function of the volumetric strain.

# 6 Comparison between the four compounds

The four materials studied in the frame of this PhD study are submitted to the same experimental tests and to the same identification procedure described hereinbefore. In this section, their mechanical properties are compared.

**Comparison between two virgin PTFE powders** Firstly, the differences between the virgin PTFE, which is a fine cut resin, and the free flow pelletized resin PTFE B are examined. Both materials have the same chemical properties (same nascent crystallinity fraction). The main difference comes from the treatment of the polymer after the polymerization as explained in the introduction .

In [Rae et Dattelbaum, 2004] and [Rae et Brown, 2005], the mechanical behavior of two types of sintered PTFE samples under compression and tension respectively is also investigated. PTFE 7A and PTFE 7C from Dupont, whose main difference in raw powder material is the size and the shape of the particles, are compared. PTFE 7C has smaller particles 28 $\mu m$ with elongated and irregular shape (ratio 20:1). The evolution of the behavior with strain rate and temperature is similar, except that the failure stress in tension is $\sim$20% higher for PTFE 7C and the stiffness is slightly higher in compression. But no comparison is made on the behavior of the green parts.

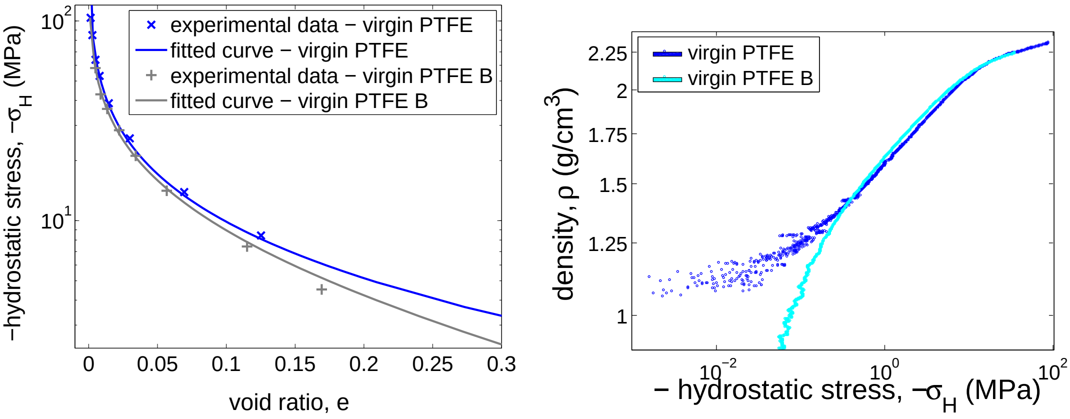

(a) Evolution of the hydrostatic stress as a function of the void ratio

(b) Evolution of the density as a function of the hydrostatic stress while the material is submitted to hydrostatic loading

**Figure 2.36:** Comparison of the hardening of the two virgin PTFE powders. The initial densities are different but the hardening law are superimposed for the two virgin PTFE powders and for a void ratio close to zero (for pressing up to 100 MPa, see figure 2.36), the final density of the two PTFE powders is equal.

The initial density of the loose powders are notably different. The initial density of the fine cut powder is around 0.42 g/cm$^3$ and is highly variable depending on the condition of preparation like the handling, the temperature or the humidity. The initial density of the free flowing powder is much more reproductible with a value of 0.9 g/cm$^3$. However, the specific gravity of the the two powders is almost equal (2.26 g/cm$^3$ for virgin PTFE and 2.25 g/cm$^3$ for virgin PTFE B) (figure 2.36 (b)). Finally, the pelletization of the fine resin acts as a ‘pre compaction’ of the PTFE fine particles. The initial density is higher for the pelletized resin compared to the fine cut resin but as soon as a sufficient level of density is reached in the fine cut resin sample, the densification is similar for both powders (figures 2.36). The evolution of the bulk modulus $K$ as a function of the void ratio $e$ is also similar in both cases (figure 2.37).

However, their behavior under shear is different. Surfactants are used for the granulation process to separate the particles. They are normally evaporated. However, remaining

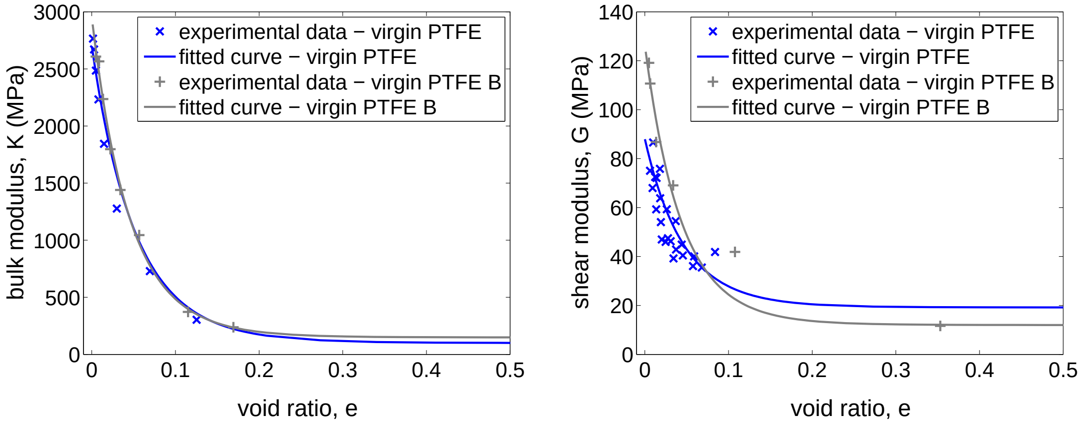

(a) Evolution of the bulk modulus $K$ as a function of the void ratio $e$

(b) Evolution of the shear modulus $G$ as a function of the void ratio $e$

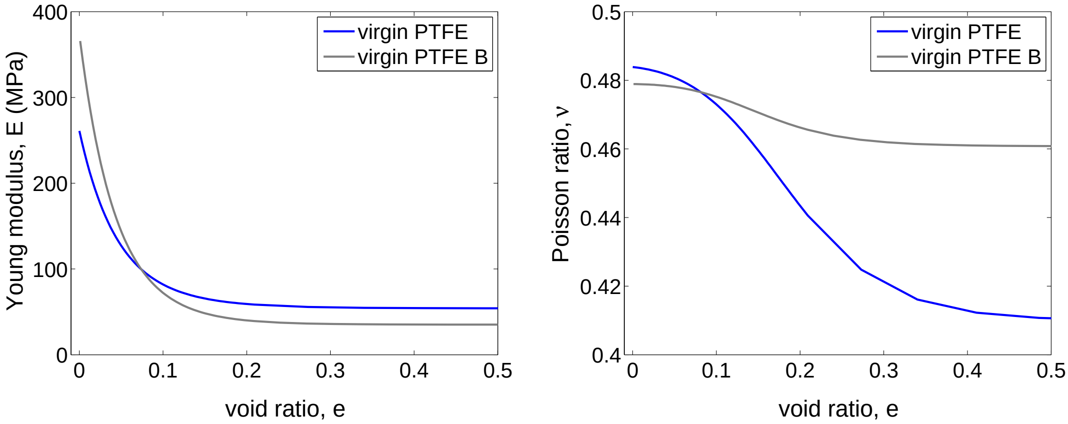

(c) Evolution of the Young's modulus $E$ as a function of the void ratio $e$

(d) Evolution of the Poisson's ratio $\nu$ as a function of the void ratio $e$

**Figure 2.37:** Comparison between the two virgin PTFE powders - Elastic parameters

amount of surfactant at the surface of the pellets may explain the poorer cohesion of the pelletized compacted powder.

Thus the internal friction coefficient of the fine cut resin, equal to 3.4°, is lower than the one of the pelletized resin, equal to 5.1°. The build up of strong cohesion between the pellets is more difficult than for the fine cut resin.

**Influence of the fillers** The influence of the fillers added to the virgin PTFE powder is also analyzed. The initial density of the filled materials is close to the density of the virgin powder. However, as the specific gravity of the fillers are different from the one of the PTFE, the final densities are different and depends of the amount of fillers (table 2.3). The densification curve for filled material is different from the one of virgin PTFE (figures 2.39). The filled compounds require a higher amount of work to be pressed. Note that the behaviors of both filled materials are similar.

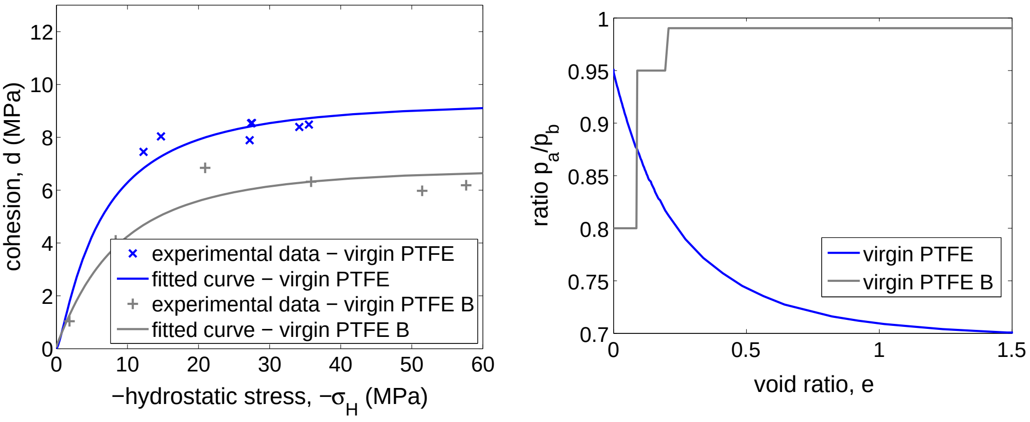

(a) Evolution of the cohesion as a function of the hydrostatic stress which describes the position of the cap, $p_b$

(b) Evolution of the ratio of the $p_a/p_b$

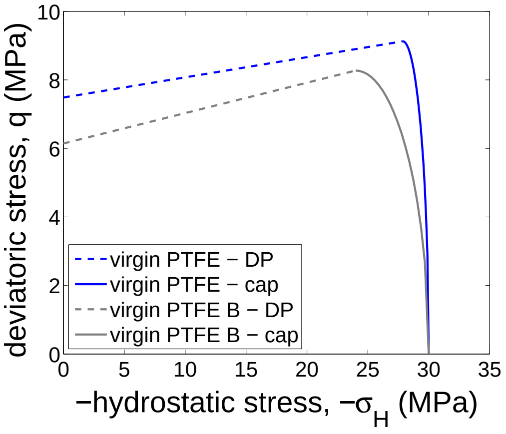

(c) Shape of the yield surface for an hydrostatic stress of 30 MPa

**Figure 2.38:** Comparison between the two virgin PTFE - Drucker-Prager/cap surface

The level of the bulk modulus $K$ is a little higher when fillers are added but its evolution as a function of the void ratio is close for the three compounds (figure a.2.40). On the other hand, the influence of the fillers on the mechanical behavior the compounds is particularly significant under shear. The shear modulus $G$ is higher (figure b.2.40) as well as the cohesion (figure a.2.41). Fillers are added, among others things, to improve the shear strength of the PTFE. The internal friction angle is higher but is increased by the fillers in a smaller range; 5.4° for the compound with filler 1 and 4.6° for the compound with filler 2 compared to 3.4° for the virgin PTFE (figure c.2.41). Here again, this is consistent with the properties found in the finished material (see 1).

The influence of both fillers on the behavior under shear is not exactly the same. In the case of the PTFE+filler 2, the round semi crystalline polymeric fillers have approximately the same size and the same geometry as the PTFE particles but a higher strength. This

**Table 2.3:** Densities - The initial density is equal to the average density measured at the end of the filling of the 3D compaction tool. This initial density is, like for virgin PTFE, highly variable. The final densities are directly linked to the amount of fillers and their own specific gravity.

| Material | Initial density (g/cm$^3$) | Final density (g/cm$^3$) (pycnometry He) |
|---|---|---|
| virgin PTFE | 0.42 | 2.26 |
| PTFE + filler 1 | 0.44 | 2.23 |
| PTFE + filler 2 | 0.43 | 2.02 |

is consistent with the fact that the cohesion and the shear modulus are increased (figures 2.40 and 2.41). Moreover, apart from the amplitude, the evolution of the shear modulus is similar in PTFE+filler 2 and virgin PTFE as if the average elastic modulus were increased without other effects caused by the interaction of the particles for instance. The same observation is made on the shape of the yield surface (figure 2.41). This is not the case for the material filled with particles 1. The evolution of the shear modulus with the void ratio is faster in this case (figure b 2.40). The effect of the deviatoric part of the loading on the consolidation surface of the yield domain is more important (figure 2.41). But in this case, the geometry and the properties of this inorganic filler are completely different from the ones of polymeric particles.

The detail of the identified parameters of the Drucker-Prager/cap model are given in appendix C.

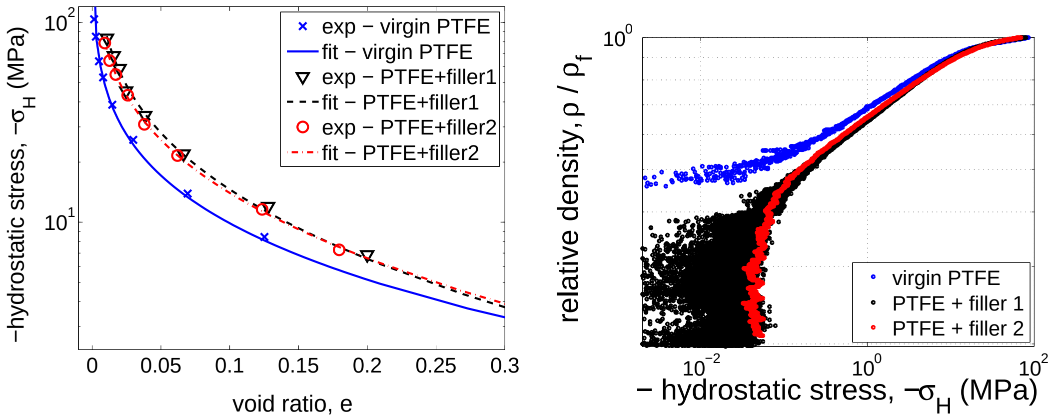

(a) Evolution of the hydrostatic stress as a function of the void ratio identified from hydrostatic tests with successive loading/unloading steps

(b) Evolution of the relative density (ratio of the actual density over the final density for $e$=0) as a function of the hydrostatic stress. The evolution of the density is similar for both filled compounds but stiffer than for virgin PTFE.

**Figure 2.39:** Hardening law - Influence of the fillers. To reach the same void ratio a higher level of stress has to be applied on the filled compound.

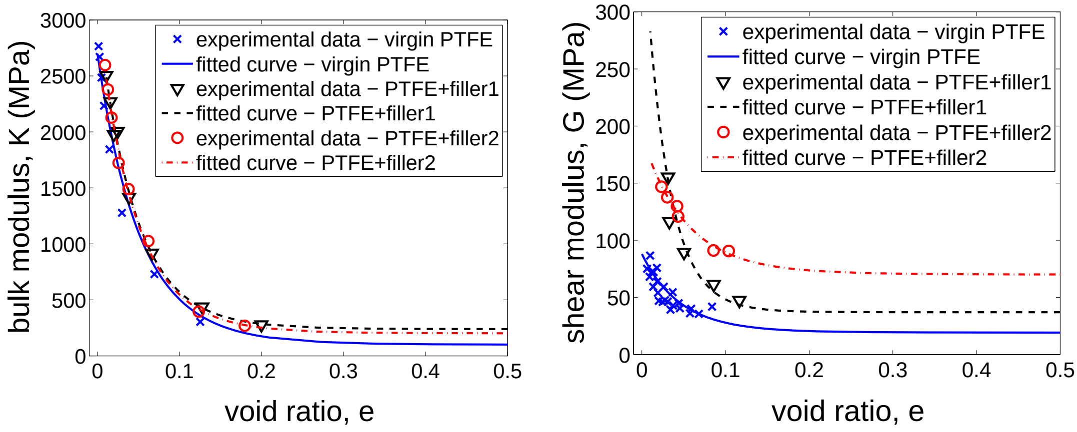

(a) Evolution of the bulk modulus as a function $K$ of the void ratio $e$

(b) Evolution of the shear modulus $G$ as a function of the void ratio $e$

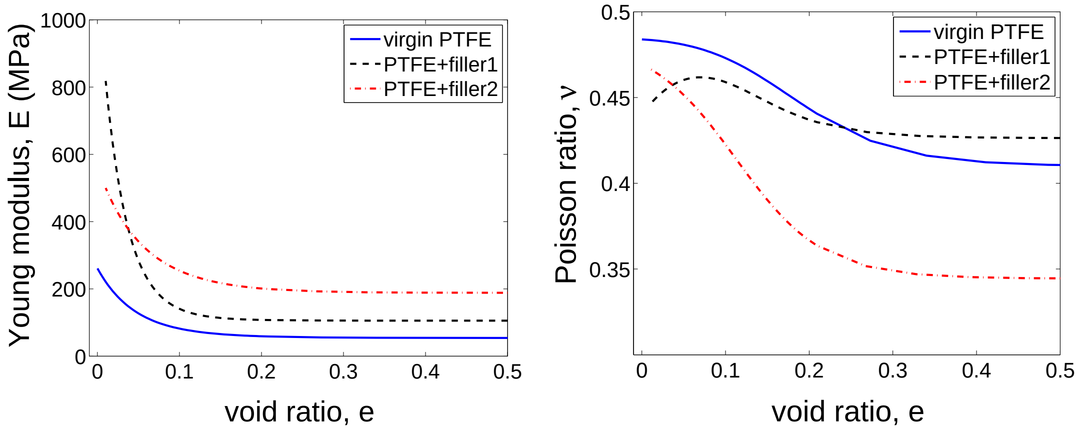

(c) Evolution of the Young's modulus $E$ as a function of the void ratio $e$

(d) Evolution of the Poisson's ratio $\nu$ as a function of the void ratio $e$

**Figure 2.40:** Elastic properties - Comparison of the three compounds.

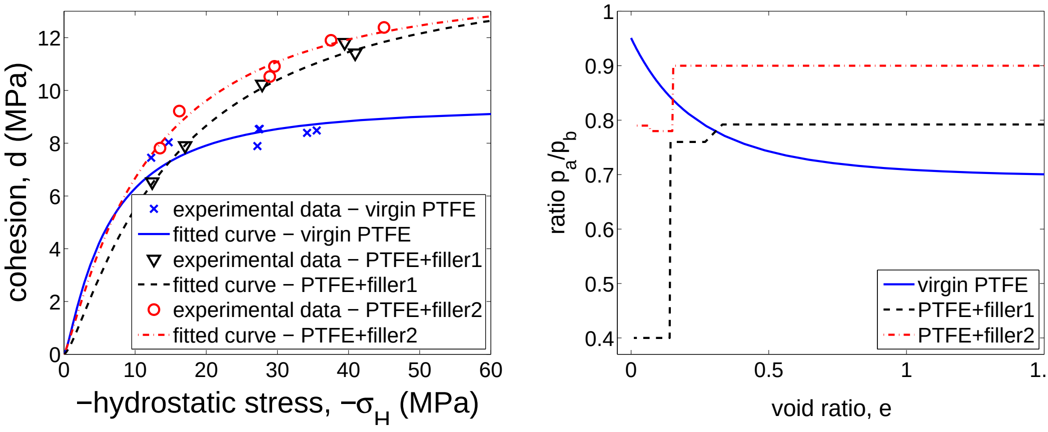

(a) Evolution of the cohesion as a function of the position of the cap, $p_b$

(b) Evolution of the ratio $p_b/p_a$

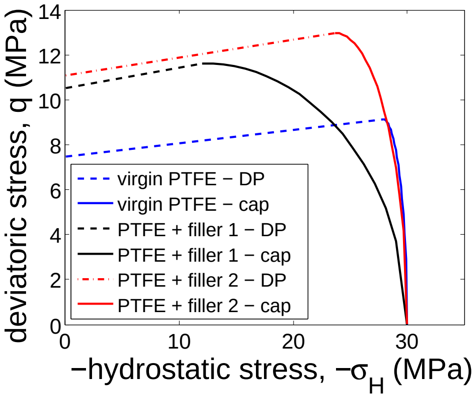

(c) Shape of the yield surface at the position of the cap $p_b$=30 MPa

**Figure 2.41:** Parameters of the yield surface. Comparison of the three compounds.

# 7 Finite Element simulation

## 7.1 Implementation in Abaqus

To predict the mechanical behavior of the compounds during their pressing and the final state of the green part at the end of the industrial pressing, the Finite Element code Abaqus® was chosen. The Drucker-Prager/cap model proposed in Abaqus is modified to be suited to the studied PTFE.

The dependance of the parameters of the Drucker-Prager/cap yield surface and of the elastic parameters is defined thanks to the subroutine USDFLD. With the utility routine GETVRM, volumetric plastic strain $\varepsilon_{vol}^{plas}$ variable is defined for each integration point and equal to the sum of the plastic strain components in the three principal directions. A compaction may starts from various states as the initial void ratio of the powder is not well defined. The value of reference $\varepsilon_{crit}^{ref}$, is adjusted to take into account the variation of the initial state. If the reference state for which $e$=0 is not known, $\varepsilon_{crit}^{case\_i}$ is shifted such as

$$\varepsilon_{crit}^{case\_i} = \varepsilon_{crit}^{ref} + \ln\left(\frac{\rho_p^{case\_i}}{\rho_p^{ref}}\right) = \varepsilon_{crit}^{ref} + \Delta\varepsilon \tag{2.35}$$

with $\rho_p^{ref}$ and $\rho_p^{case\_i}$ the initial densities of the reference and the actual case respectively. In secondary code (matlab, excel...), the parameters of the model are previously computed as a function of the volumetric plastic strain $\varepsilon_{vol}^{plas}$ and the constant $\Delta\varepsilon$ which describes the initial state of the material.

In Abaqus, a linear interpolation between each value of the parameters corresponding to successive densities is made and at each increment, the model parameters are updated as a function of the computed volumetric plastic strain $\varepsilon_{vol}^{plas}$ calculated at the previous step.

The phase transition phenomenon is also implemented in Abaqus, using the UEXPAN subroutine which allows to define an increment of strain depending on the variables of the calculation. At each increment and each integration point, based on the value of the hydrostatic stress computed at each integration point thanks to the USDFLD subroutine, the volumetric phase strain $\varepsilon_{trans}$ is evaluated with the equation 2.32. This increment of deformation is added to the total strain as it would be done for a thermal expansion strain. The calculation is made under Abaqus/Standard. The phase change incremental strain is computed through an explicit scheme. A sufficiently small increment of time is carefully chosen for convergence.

## 7.2 Simulation vs. experimental results – 1st validation

### 7.2.1 Simplified Finite Element simulation

First FE simulations are made to check the implementation of the model and to roughly validate the identification of the model. These simulations are also performed to refine the identification as for the ratio that defines the shape of the cap surface. The FE simulations are performed on a cubical shaped sample assuming perfect boundary conditions (no friction) between the powder and the 3D device. The measured displacements obtained with the laser sensors are directly applied on the three directions of the cube in the case of tests with imposed displacements. The initial sample is a cube of 45.35cm side with the same initial density measured experimentally. Computed stresses in the principal directions are then compared to the experimental data (figure 2.42, 2.43, 2.44).

Note that once the shear failure surface is reached, like in ‘isodensity’ tests, the material follows the DP surface as it is implemented in Abaqus. This is not realistic but is out of the scope of the modeling of the mechanical behavior of the material in the studied application.

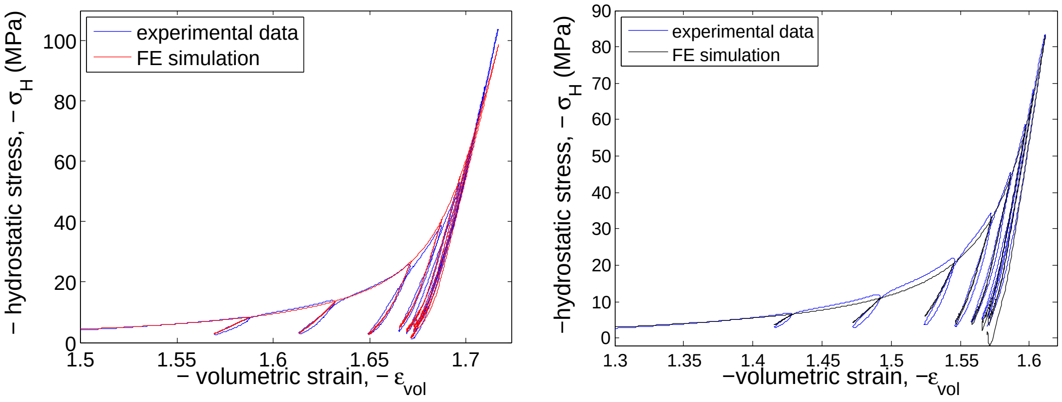

(a) virgin PTFE (b) virgin PTFE + filler 1

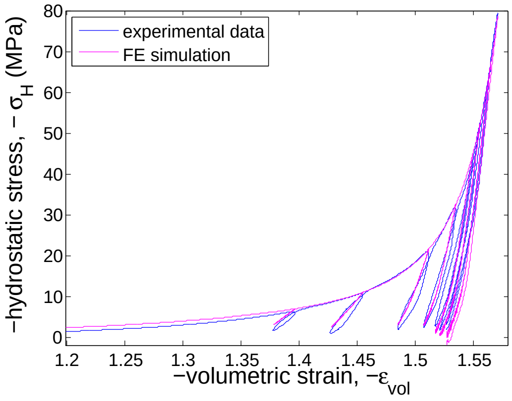

(c) virgin PTFE + filler 2

**Figure 2.42:** FE simulation of a loading/unloading hydrostatic test - simplified simulation - thanks the modeling of the phase change, the non linearity during the unloading steps is well described for the three materials.

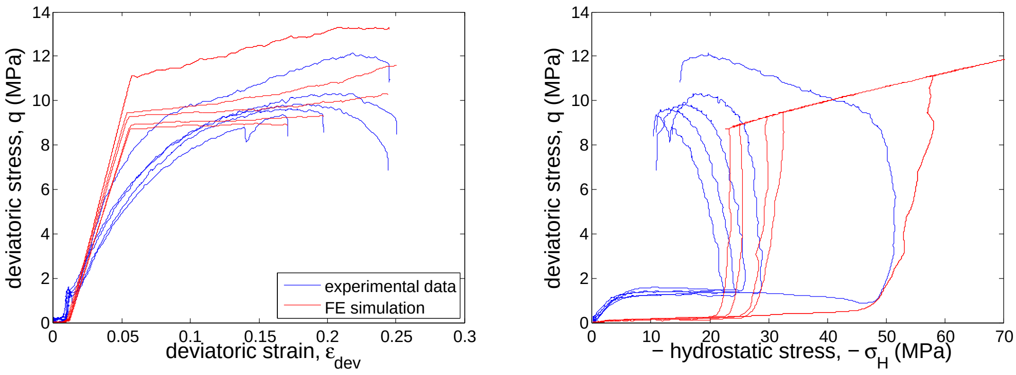

(a) Deviatoric strain stress plane - virgin PTFE (b) Stresses plane - virgin PTFE

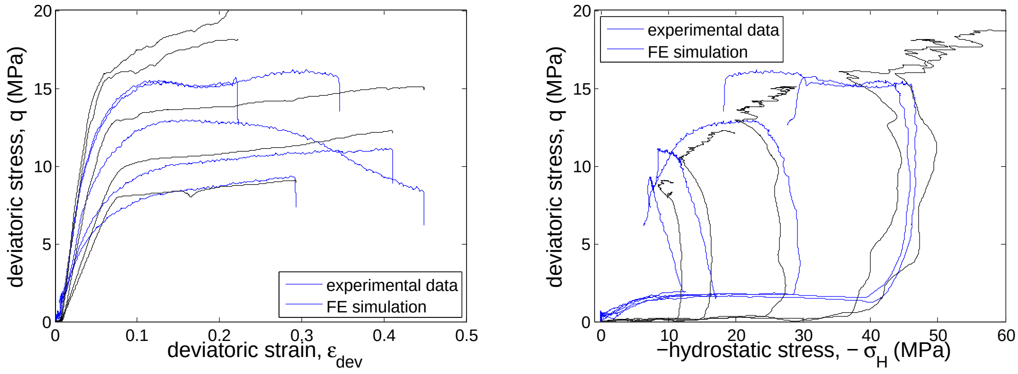

(c) Deviatoric strain stress plane - PTFE+filler1 (d) Stresses plane - PTFE+filler1

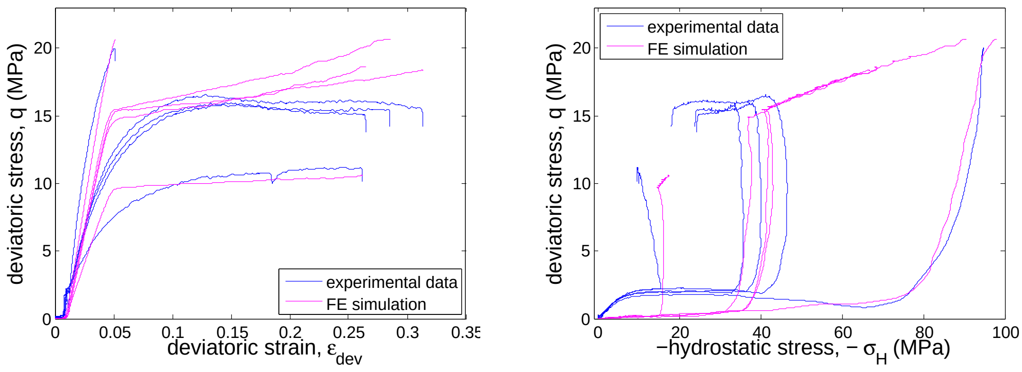

(e) Deviatoric strain stress plane - PTFE+filler2 (f) Stresses plane - PTFE+filler2

**Figure 2.43:** FE simulation of isodensity tests - simplified simulation - The evolution of the elastic part as a function the density is well described (beginning of the slope in the deviatoric stress strain plane). The evolution of the cohesion with the density is good as the DP surface is reached to the good level of deviatoric stress. The increase of the deviatoric stress in the $(-\sigma_H, q)$ plane is well described for the filled materials and is a little bit poorer for the virgin PTFE powder.

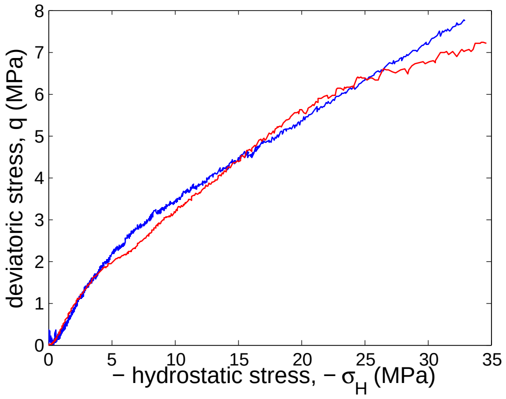

(a) Stresses plane - virgin PTFE

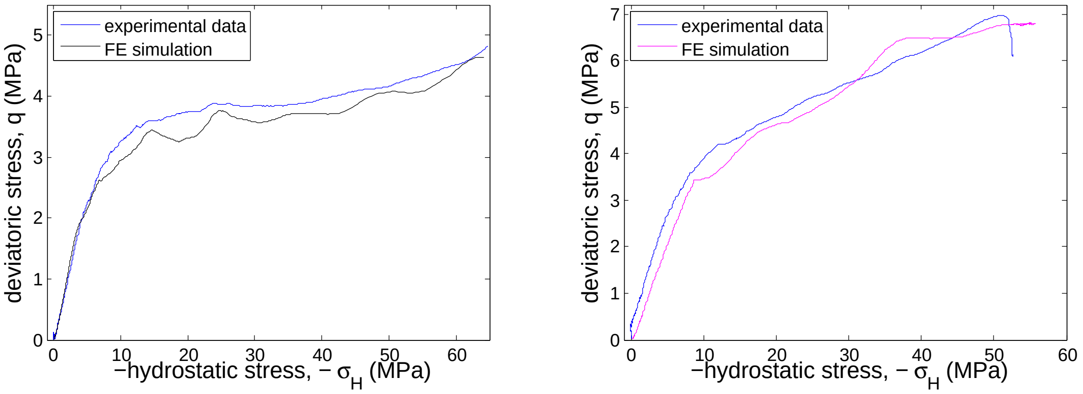

(b) Stresses plane - PTFE+filler1 (c) Stresses plane - PTFE+filler2

**Figure 2.44:** FE simulation of ‘three rate’ test - simplified simulation - The evolution of the deviatoric and hydrostatic stresses in the case of ‘three rate’ loading is faithful for the three compounds.

## 7.3 Finite Element simulation of the 3D compaction device

The hypothesis of homogeneous state assumed for the identification of the parameters is convenient but not exact. In [Yi et Puri, 2013], the local stresses are measured inside a sample submitted to a hydrostatic loading thanks to a cubical triaxial tester. They are found to be not homogeneous inside the material. The 3D compaction tool used here is different but present also some defects. Indeed, interactions between the sample and the 3D compaction device induce heterogeneities of loading and ‘parasite’ loadings in the sample. The transverse motions of the metallic cubes of the 3D compaction device coupled with the non negligible friction interactions between the compacted material and the tool, create an additional shear loading in the sample, even if hydrostatic loading is applied. A rotation is induced inside the specimen. This additional shear component of the loading and its inhomogeneity have been also observed on cubical plastered samples compacted in the same 3D compaction tool ([Bouterf, 2014]) and is clearly identifiable as shown with the external and tomographic observations of a ‘striped’ PTFE based sample figure 2.45.

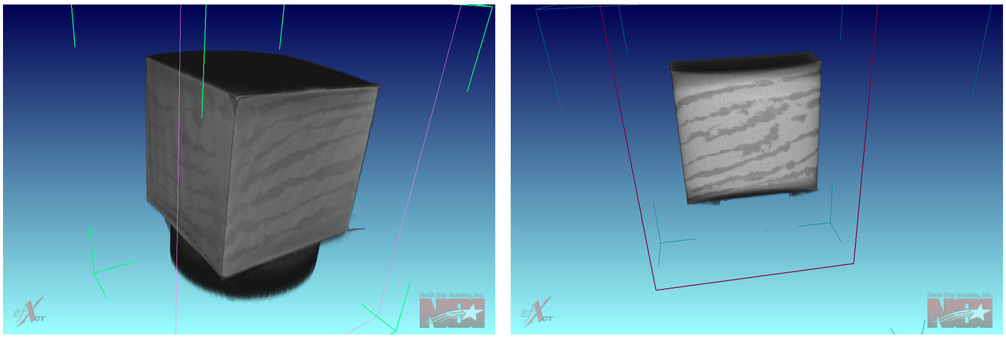

(a) External view of the sample

(b) Cut view of the sample through one of the middle vertical plans

**Figure 2.45:** Tomographic observation of sample compacted through hydrostatic loading in the 3D compaction tool. The sample has been prepared by filling the initial cavity of the tool by successive horizontal layers of virgin PTFE and PTFE+filler1. A contrast is thus created on tomographic observations and the iso-displacement line may be observed inside the sample. The rotation created by friction along the cube faces is clearly visible.

Moreover, the deformation of the sample is deduced from the measurement of the distance between two metallic blocks positioned face to face. The deformation of the metallic blocks as well as the interaction between each other is neglected.

To understand and estimate the influence of the imperfections of the compaction device on the experimental data and the identification of the parameters of the model, a complete simulation of the system 3D compaction device coupled with a sample is proposed (figure 2.46). The displacements or the forces are applied on the external surfaces of the metallic blocks. The blocks are free to slide in the transverse directions, which is conditioned by the displacement of the neighbors blocks. The six metallic blocks have an isotropic elastic behavior with a Young's modulus of 200 GPa and a Poisson's ratio of 0.3. The interaction between the material and the tool is based on the interaction model described in the next chapter 2. The augmented Lagrange normal contact and Coulomb friction with a coefficient of 0.1 is chosen to model the interaction between the metallic blocks of the compaction device.

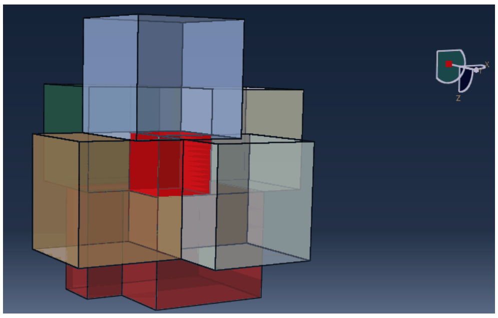

**Figure 2.46:** FE simulation of the whole 3D compaction device. The metallic blocks of the 3D compaction device are translucent to allow to see the PTFE sample in red in the middle of the device, in its initial state.

### 7.3.1 Analysis of the FE simulation

As observed on the 'striped' sample, the same transverse displacement inside the material, caused by the rotation motion of the compaction device, is simulated (figure 2.47). An heterogeneous stress and strain state inside the sample results from this defect, combined with the stress alteration created by the friction (figure b.2.47). During this test, the deviatoric component of the load is not null, mainly because of the non symmetry of the actuators of the triaxial machine ASTREE. An additional heterogeneous deviatoric strain, created by the interactions with the 3D compaction device, is added thereto.

However, the desired loading is approximately reached and the heterogeneities of loading inside the part are acceptable as shown figure 2.48.

In the case of tests which involve high shearing loading like 'isodensity' test, a more heterogeneous state loading results from the imperfection of the test. Figure 2.49, the strain-stress state of some elements on one of the diagonals of the sample, from one corner to the centre part, is presented. The isodensity parts of the loading are overlay in colored lines. The isodensity loading, viz. the constant volume, is nowhere really followed during the isodensity tests. Even if the hydrostatic stress is relatively constant in the material, the deviatoric strain is very heterogeneous. Nevertheless, identification of the shear modulus from the average quantities remains close to the identified value from the experimental data (in this case a shear modulus of 65 MPa is found compared to 68.3 MPa for the identification from the experimental data and considering a homogeneous state).

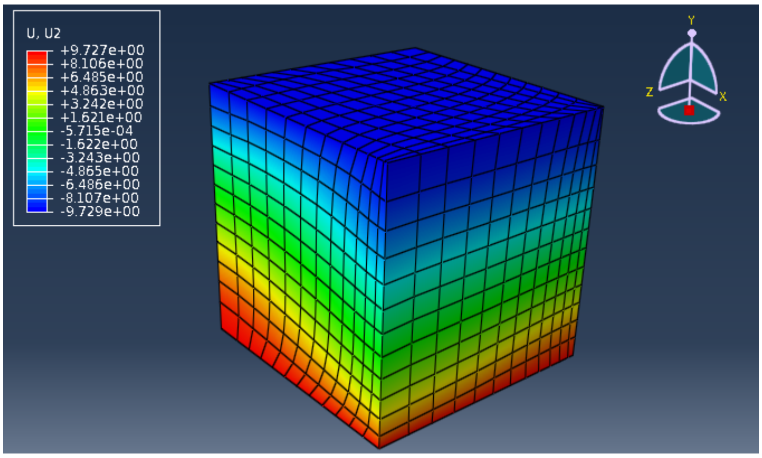

(a) Displacement field in the Y direction after a variation of volume of -167% and an increase of hydrostatic stress of around 90 MPa

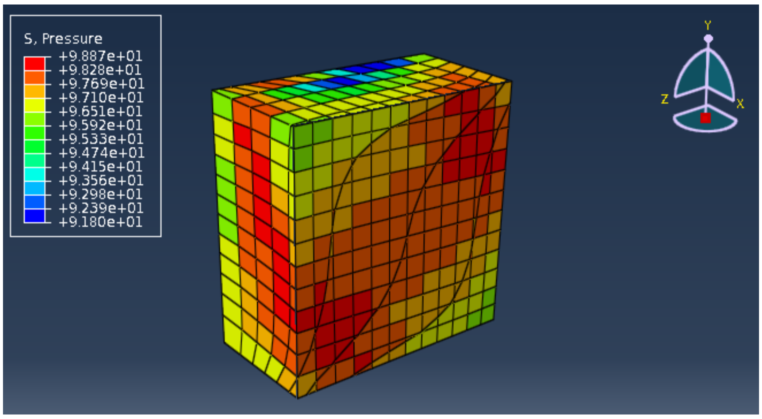

(b) Hydrostatic stress field in one half of the sample

**Figure 2.47:** Displacement and stress field inside the sample submitted to hydrostatic loading.

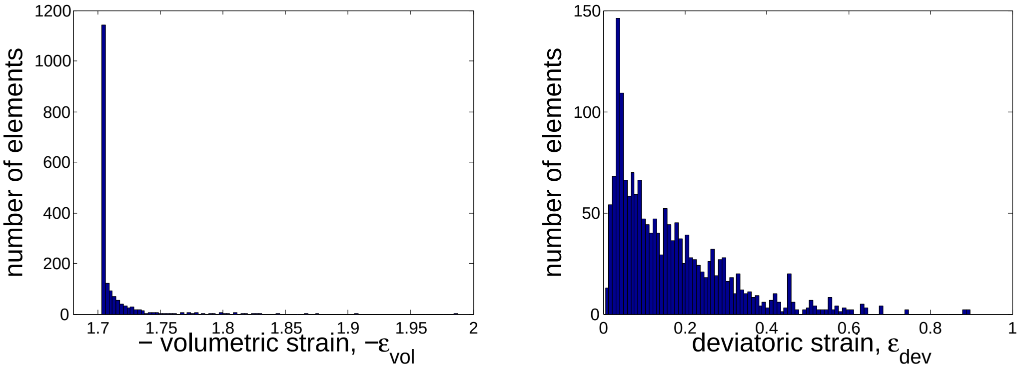

(a) Histogram of the volumetric strain components of each integration points of the sample

(b) Histogram of the deviatoric strain components of each integration points of the sample

**Figure 2.48:** Volumetric and deviatoric strains in the sample under the maximal measured hydrostatic stress of 90 MPa - A gradient of loading in noticed but remains low as the distribution of the volumetric strain is narrow. A deviatoric component of the strain exists but its average value remains low compared to the volumetric strain.

To conclude, even if the 3D compaction set up presents some weakness and deviation from an ideal test, which induce an heterogeneous loading of the sample, the identification of the parameters based on the average measurements of the displacement and pressure quantities appears reliable. Presumably, the low coefficient of friction of PTFE is very instrumental to reach this positive conclusion.

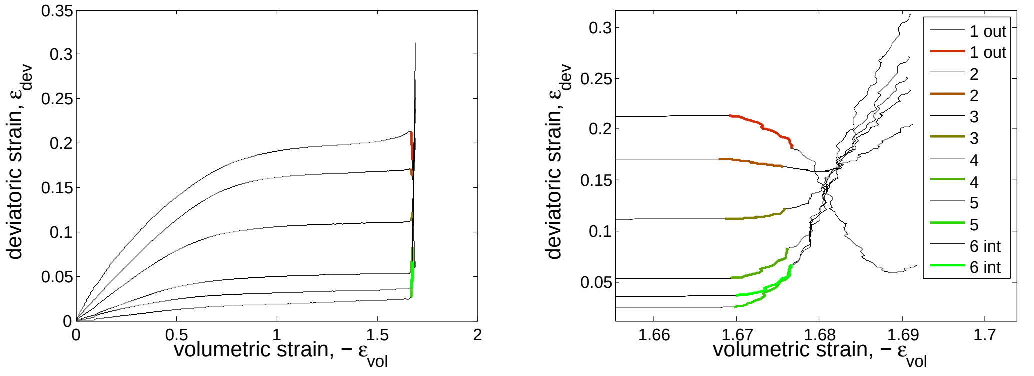

(a) applied load (b) zoom on the isodensity part of the loading

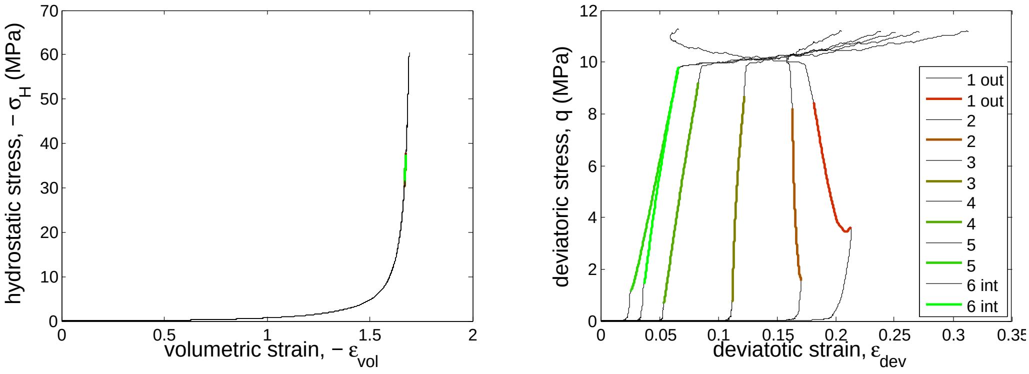

(c) response of the material - hydrostatic strain-stress plane (d) response of the material - deviatoric strain-stress plane

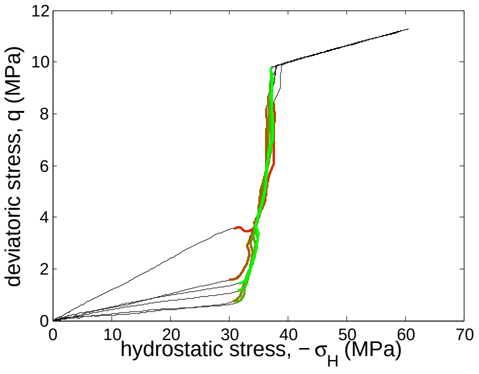

(e) response of the material - hydrostatic-deviatoric stresses plane

**Figure 2.49:** Stress-strain state of elements on one of the diagonals of the sample from outer to inner part of the sample

# 8 Conclusion

The 3D compaction tool allows to applied complex loadings to PTFE samples. Besides the above cited imperfections of the device, identification of the powder constitutive parameters during its pressing is possible. The parameters of the Drucker-Prager/cap model as a function of the void ratio are identified for four different compounds. The influence of the size and shape of the particles are evidenced as well as the role of two types of fillers.

The viscous behavior of the PTFE sample has been characterized thanks to relaxation stage after œdometric loading. Several tests at different loading rates and different level of maximal applied stress are made. The influence of the void ratio on the response of the material is evidence. An hyperbolic sine creep law is identified whose parameters are a function of the void ratio (figure D.3). All the results are presented in appendix D. Unfortunately, the implementation of the model in Abaqus does not allow us to implement such a behavior (limitation of the creep component to too small values).

A first comparison between the model and the experimental data has been reported and seems satisfactory. But this validation is based on the tests used for the identification, and hence further work would strengthen this identification. A further consolidation of this identification is the purpose of the next chapter.

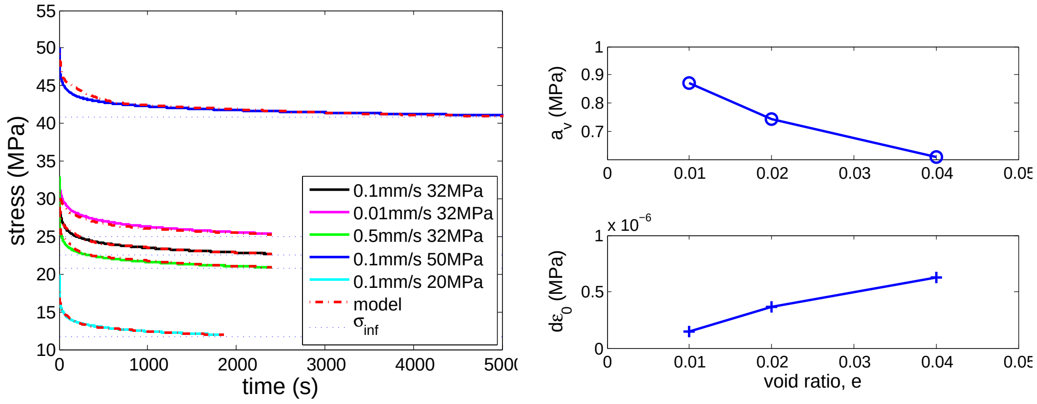

(a) Comparison between the experimental results and the identified analytical solution

(b) Identified parameters and their evolution with the void ratio - *m* is set to 0.75

**Figure 2.50:** Identification of the viscous part of the elasto-viscoplastic model from œdometric tests followed by relaxation steps.

# Chapter 3

# Uniaxial compaction tools

*The purpose of this chapter is the model validation at the scale of laboratory tests. Two compaction tools are used :*

- *The first one is an œdometric tool where applied and transmitted axial and radial stresses are measured during compaction. A modeling of the interaction between the mold and the powder is proposed.*
- *The second one, hereafter called 'V-tool', developed from an original idea of R.B. Canto from UFSCar, has a complex geometry that allows different loading paths. It is possible to measure the displacement field inside the mold by DIC and to perform a direct comparison with the simulated displacement* fields.

## Sommaire

# 1 Instrumented œdometric tool

## 1.1 Presentation of the tool

Saint-Gobain CREE (Centre de Recherches et d'Etudes Europeen) generously allowed us to use the œdometric tool presented in this section. The tool is composed of a cylindrical die whose dimensions are given figure 3.1. Two adjusted pistons enable the compaction of the sample from top and bottom. The top piston is linked to the actuator of the uniaxial compaction machine.

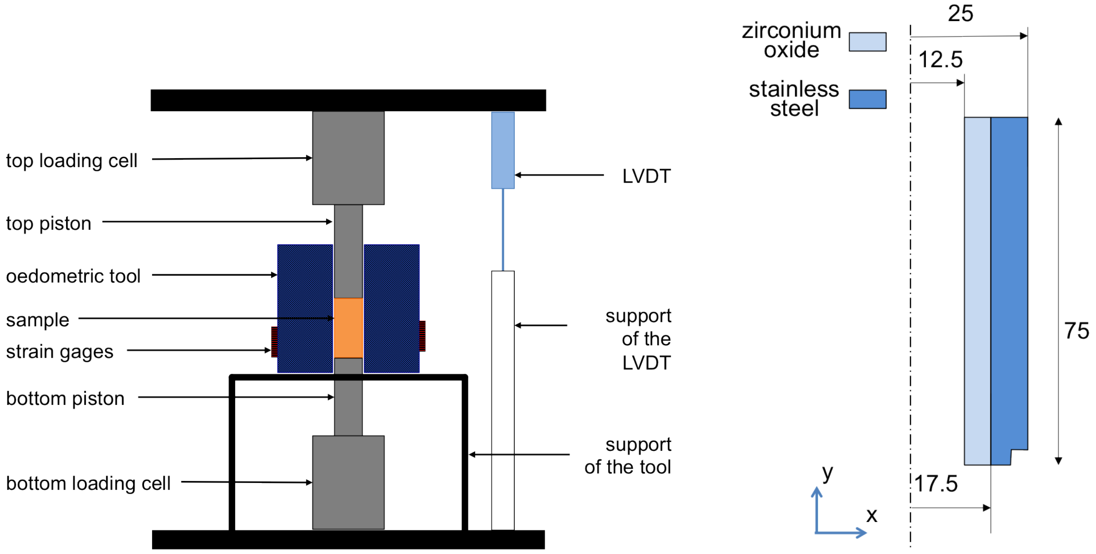

(a) Scheme of the œdometric tool and its instrumentation. The tool also enables double side compaction (although it was not used here because of the insufficient wall shear stress).

(b) Scheme of the section of the die (dimensions in mm)

**Figure 3.1:** Instrumented œdometric tool. As the tool was initially designed for ceramic material, the external part of the mold is made of stainless steel while the inner part is made of zirconium oxide.

During the test, both transmitted and applied stresses are measured by the bottom loading cell with a capacity of 100 kN and the top one with a capacity of 50 kN. The tool is equipped with eight strain gauges which are glued on the external surface of the tool. They are placed at eight different heights on the bottom part of the tool, centered on the position of the sample at the end of the compaction. The thickness of the wall of the tool was designed to remain in the elastic domain while deformation are large enough to be measurable. As the tool is composed of two different materials, a simulation of the matrix under loading was made to estimate its stiffness as a function of the height of the sample (data from J. Brulin, CREE). The radial stress may then be deduced from the measured deformation of the matrix. Sensors are not accurate enough to distinguish

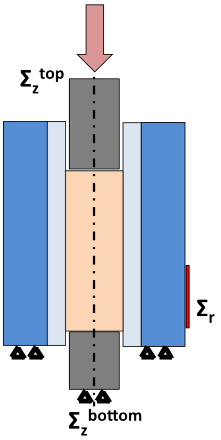

**Figure 3.2:** Scheme of the measured stresses

the small variation of radial stress along the height of the sample. The radial stress is thus assumed to be constant and is equal to the average of all the measured radial stresses with an error of less than 10%. Figure 3.2, a schematic drawing of the measurable data is reported.

The height of the sample is deduced from the displacement of the top piston. An LVDT is installed between the movable crossbar and the bottom plateau of the machine as described figure 3.1. Part of the deformation of the system, mainly the deformations of the loading cells, the pistons and the junctions between them, are not excluded from the measurement of the LVDT. To have an accurate measurement of the displacement, the stiffness of the whole system as a function of the loading was estimated. The two pistons were put into contact and the displacement given by the LVDT of the machine was recorded while the applied force is increased (data from J. Brulin, CREE). The correction of the displacement is given by a third order polynomial, as a function of the applied stress. Figure 3.3 shows the contribution of this correction on the measurement of the sample height. At zero load, at the end of the test, a gap of 0.2 mm between the raw displacement and the corrected displacement is observed. The zero of the LVDT of the machine is made bringing the two pistons in contact. The effect of the stiffness appears also here and the same correction of the displacement has to be applied. This type of correction allows to have a better estimate of the displacement but is not as accurate as a direct measurement, particularly for high level of stress.

## 1.2 Compaction step

### 1.2.1 Description of the test and of the measured data

Œdometric compaction test with successive loading and unloading steps are performed. Displacements are imposed with a velocity of 0.05 mm.s$^{-1}$. The evolution of the average density of the sample is directly deduced from the mass of the sample and its volume. Fig-

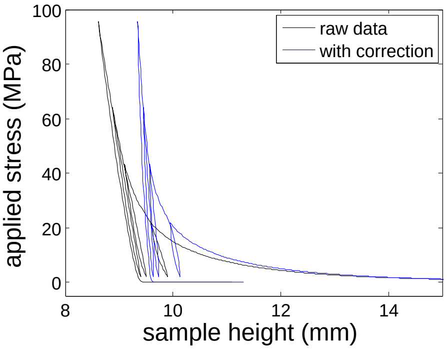

**Figure 3.3:** Correction of the measured displacement taking into account the stiffness of the system

ure 3.4 illustrates the results obtained during the compaction of two samples of 10.4 g of virgin PTFE pressed with the same loading. The error of repeatability of the measurement is less than 2% for stresses higher than 1.5 MPa.

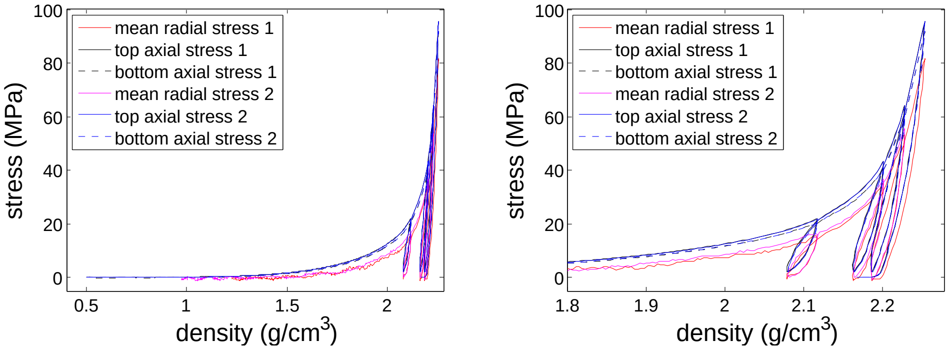

(a) whole test

(b) zoom on the end on the end of the test

**Figure 3.4:** Loading-unloading œdometric tests on virgin PTFE - measurement of the top, bottom and radial stresses as a function of the density.

As the difference between the applied stress and the transmitted stress is small, the assumption of an homogeneous stress state inside the sample does not involve large errors in the description of the sample during the test. Based on this assumption and knowing both axial and radial stresses, the hydrostatic and deviatoric stresses may be calculated

$$-\sigma_H = \frac{\Sigma_z + 2\Sigma_r}{3} \tag{3.1}$$

$$q = |\Sigma_z - \Sigma_r| \tag{3.2}$$

The experimental results shown in the previous figure 3.4 are shown in the $(-\sigma_H, q)$ plane figure 3.7. For the virgin PTFE, loading and unloading are almost superimposed.

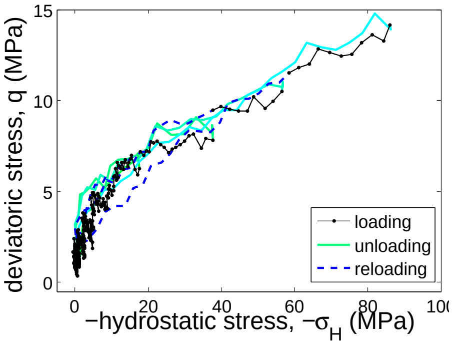

**Figure 3.5:** Œdometric test in the $(-\sigma_H, q)$ plane. Loading, unloading and reloading up to the stress reached before the beginning of the previous unloading, are plotted.

### 1.2.2 Influence of the fillers

First observations of the data are in good agreement with the experimental results obtained with the 3D compaction device, as described in the previous chapter 2.

Figure 3.6, the evolution of the density as a function of the average applied stress $\Sigma_z^{applied}$ is presented for the three studied materials. Similarly to hydrostatic pressing, the applied stress required to reach a given relative density is higher when fillers are added.

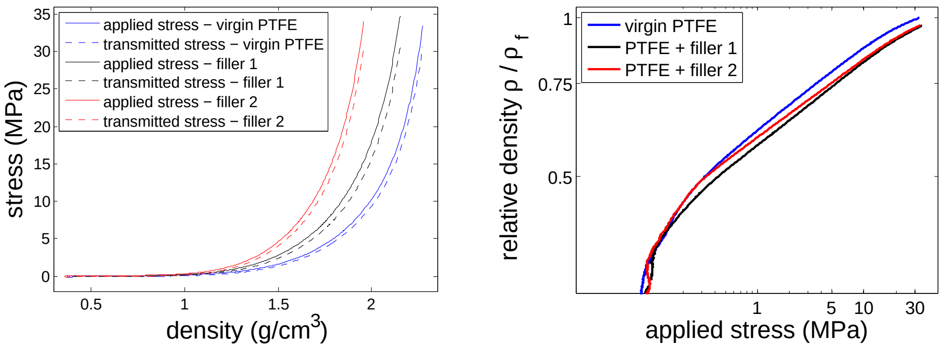

(a) Evolution of the applied and transmitted stresses as a function of the density

(b) Relative density as a function of the stress

**Figure 3.6:** Œdometric test - Influence of the fillers on the densification

The hydrostatic and deviatoric stresses are plotted in the $(-\sigma_H, q)$ plane (figure 3.7) in the case of the œdometric test and are compared to the results of the 'three rate' tests performed in the 3D compaction device (chapter 2) figure 3.8. Here again, levels of the deviatoric stress for a given applied hydrostatic stress is lower for the compound with fillers than for the virgin powder.

Figures 3.9, the ratio of transmitted over applied stress is plotted as a function of the

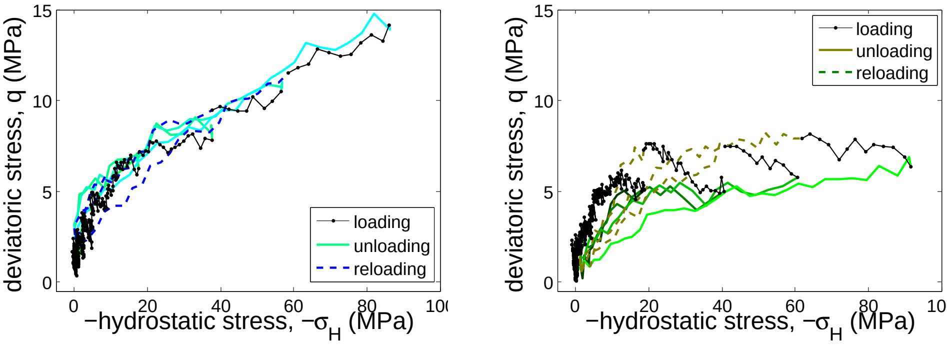

(a) virgin PTFE (b) PTFE + filler 1

**Figure 3.7:** Results of the œdometric test presented in the $(-\sigma_H, q)$ plane - influence of the fillers

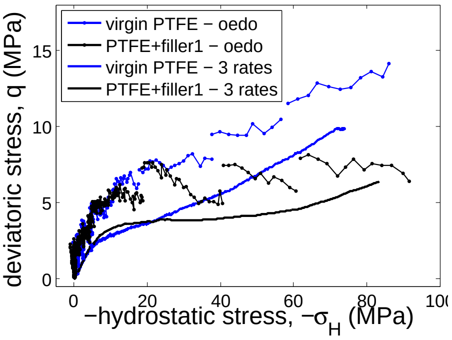

**Figure 3.8:** 'Tree rate' loading performed with the 3D compaction tool and œdometric loading obtained with the instrumented die matrix (where only the loading steps are represented)

density or the applied top stress. Note that the measurement is highly repeatable as the three curves corresponding to the pressing of the PTFE filled with filler 1 and obtained during three different tests are almost superimposed. The ratio is low at the first stage of the compaction and increases up to a constant value as the applied stress increases. This ratio increases with the formation of a transfer film between the PTFE and the side of the wall. When fillers are added, the ratio decreases consistently with the higher internal friction coefficient and the measured higher level of radial stress.

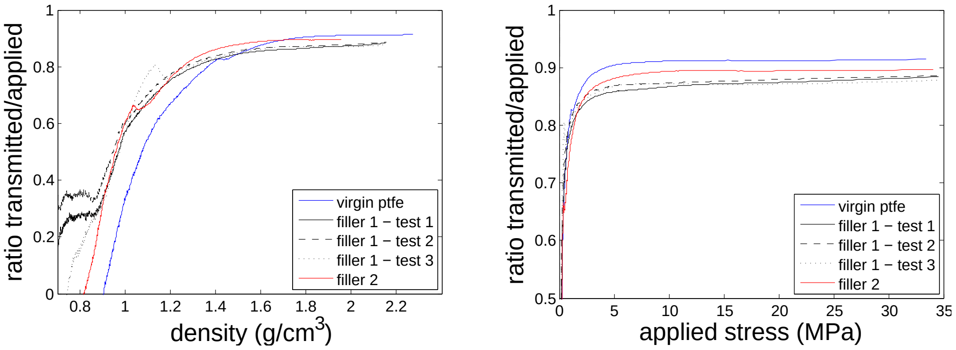

(a) Evolution of the transmitted stress with the density

(b) Evolution of the transmitted stress with the applied stess

**Figure 3.9:** Evolution of the ratio of transmitted versus applied stress — comparison between the three compounds

# 2 Simulation of the œdometric compaction - Focus on the modeling of the interactions between the tool and the material

Friction between the tool and the powder is not negligible and has to be added to the behavior of the bulk material. As explained in chapter 1, interaction of PTFE with a hard surface is characterized by the adhesion of the polymer at contact followed by the transfer of a coherent film. Modeling approaches usually developed for metallic, ceramic or pharmaceutical powders are not adapted here as this specific phenomenon is involved.

A simple proposition of the modeling may be :

- the adhesion of the PTFE on the wall is established right from the beginning. This adhesion impedes any tangential motion of the PTFE with respect to the tool surface. The non-smooth character of this condition makes it inconvenient for a numerical implementation. To mimic this behavior, a very high friction coefficient is implemented $\mu_{adh}$
$$\tau_{contact} = \mu_{adh} p_{contact} \tag{3.3}$$
- As soon as cohesion is reached $\tau_{contact} = d$, wall slip is possible and it is assumed that incrementally a Coulomb law is encountered and
$$\tau_{contact} = \mu_{PTFE}(p_{contact} + \sigma_{adh}) \tag{3.4}$$
- Then, this interaction may be seen as a PTFE-PTFE contact, between the PTFE transfer film and the bulk material. Thus the incremental friction coefficient should be nothing but the internal friction coefficient $\mu_{PTFE} = \tan\beta$ of the material.

In the Finite Element code, a smooth interpolation between the stick regime (described with a large coefficient of friction), (3.3) and the slip regime (3.5) is implemented. A convenient form is an equivalent friction coefficient $\mu$

$$\mu = \frac{\mu_{adh} - \mu_{PTFE}}{2}\left(1 - \tanh\left(a\left(p_{hardening} - \frac{d(\varepsilon_{vol}^{plas})}{\mu_{adh}}\right)\right)\right) + \mu_{PTFE} \tag{3.5}$$

with $d$ the cohesion of the bulk material, which is a function of the density of the material. $a$ is a constant which tunes the decrease of the friction coefficient, its value is high and constant for all the materials. $p_{hardening}$ is computed from the contact pressure for each interface element. It is equal to the maximal contact pressure reached by each element during the test. This way, once the transfer film is created, it does not disappear, as the direction of loading does not change during the pressing. The evolution of the law for different levels of density is illustrated in the figure 3.10. Let us emphasize that the interface friction is treated here exactly as the bulk constitutive law, but in a situation where the activated plastic strain is along a particular direction (that of slip) and all along

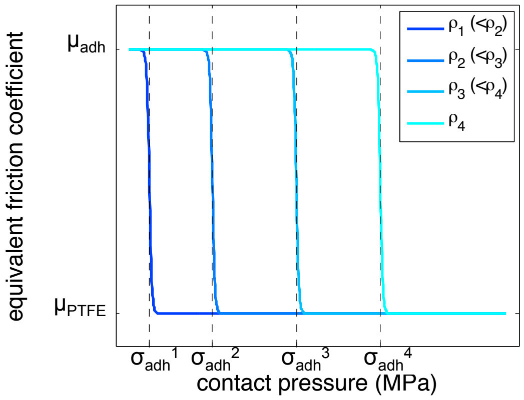

**Figure 3.10:** Illustration of the modeling of the interaction between PTFE and hard surface.

a prescribed interface. This gives rise to a non trivial friction law yet without the difficulty to identify another constitutive law and with a sound physical basis.

With this approach, all the parameters of the interaction may be described as a function of the parameters of the bulk material, identified in chapter 2. The main advantages are that no additional parameters need to be identified and that the model take into account the properties of each compounds and their evolution with respect to their density.

# 3 Simulation of the compaction step

## 3.1 Parameters of the simulation

In order to validate the model of the bulk material and of the interaction of the PTFE with the mold, simulations of the different œdometric tests are made and compared to the experimental results.

The parameters and hypothesis made for the simulation are listed below:

- the initial state of the material is defined as an initial homogeneous density;
- the die and the piston are assumed to be rigid bodies ;
- the system is assumed to be and remain axisymmetric.

The initial configuration of the FE simulation of the die compaction is shown in figure 3.11.

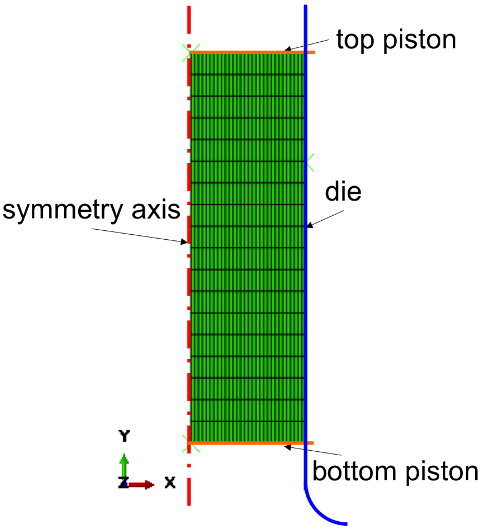

**Figure 3.11:** Initial configuration of the simulation of the œdometric test. The curved line at the bottom of the rigid die enables a smooth loss of contact between the tool and the material during the ejection step.

## 3.2 Results of the simulation

### 3.2.1 Compaction step

FE results are analyzed the same way as the experimental measurements, i.e. the average axial stresses applied by the pistons and the average radial stress of the mold are plotted. Mean deviatoric and hydrostatic stresses are calculated with the equations 3.2 so that the same quantities are compared. Figure 3.12, the three measurable stresses are plotted as a function of the density of the sample. A good agreement between the experimental and the simulation results is observed. An error of only 4% is made on the estimation of the final height of the sample. The loops that may be due to viscous effect and mechanical plays of the compaction tool, are obviously not described in this simulation. The ratio between the applied stress and the radial one is well described as shown in figure 3.13. In figure 3.14, the data are plotted in the $(-\sigma_H, q)$ plane. The simulated stress of the loading steps is in good agreement with the experimental data all over the test, except for the highest level of pressure where the simulated deviatoric stress is a little underestimated as compared to the experimental measurement.

For PTFE+filler 1, the loading steps are well described by the simulation as shown in figure 3.15. However, the simulation of the unloading steps appears to be unrealistic. The slope of the experimental unloading curves is non linear and much lower in the experiment than in the simulation at the beginning of the unloading steps. The experimental slopes of the second parts of the unloading steps are comparable to the constant slope of the simulated curve. However, the unloading is not well described here by the simulation.

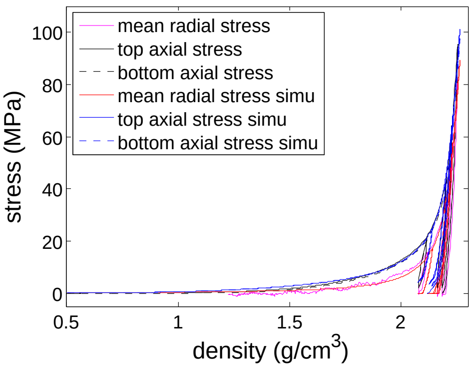

(a) Evolution of the applied and transmitted axial stresses and of the radial stress as a function of the density

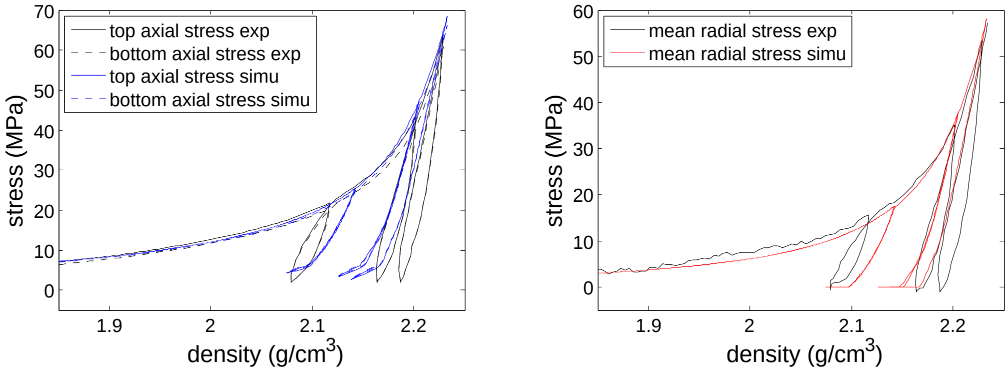

(b) Top and bottom stresses as a function of the density - zoom on the end of the test

(c) Radial stress as a function of the density - zoom on the end of the test

**Figure 3.12:** Comparison between the experimental results and the simulation - virgin PTFE

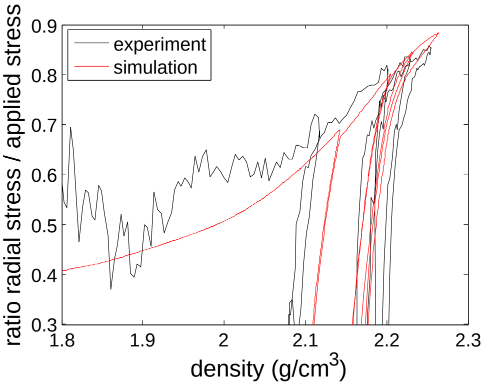

**Figure 3.13:** Ratio of the radial stress over the applied stress during the compaction - virgin PTFE.

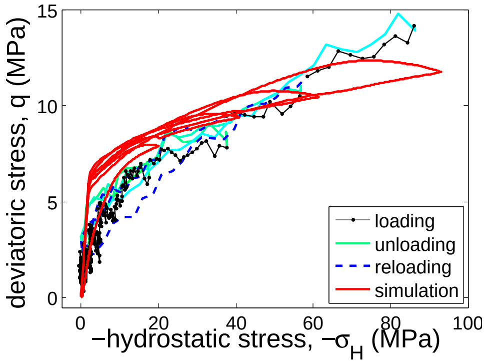

**Figure 3.14:** Evolution of the stresses in the $(-\sigma_H, q)$ plane - virgin PTFE.

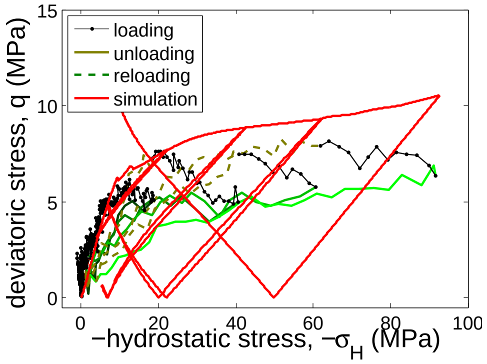

**Figure 3.15:** Evolution of the stresses in the $(-\sigma_H, q)$ plane - virgin PTFE + filler 1.

### 3.2.2 Interaction

Figure 3.16, the ratio of the transmitted over the applied stress obtained from the simulation is compared with the experimental data for the three compounds. The transmitted stress is higher in the simulation than in the experiment for the three materials. Hypotheses made for the simulation like no friction between the mold and the pistons and rigidity of the mold may explain this difference. Let us note however that the trends and the ranking between the three materials are well described by the simulations.

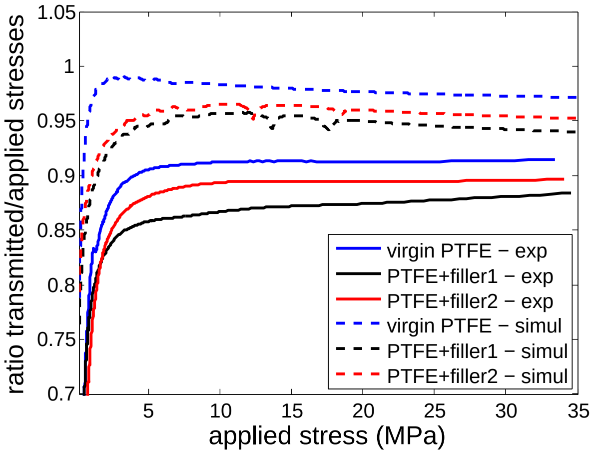

**Figure 3.16:** Comparison between the simulation and the experimental result - ratio of the transmitted stress versus the applied stress for the three compounds.

# 4 Ejection step

During the unloading step, the elastic component is partially relaxed. The radial stress induced by the plastic part of the mechanical behavior is still present and a residual radial stress may persist. An axial load is required to eject the part from the mold.

In [Briscoe et Rough, 1998], measurement of the ejection force is done in the case of samples of ceramic alumina powder. In the case of a lubricated compaction, once the piston is in contact with the sample, the ejection force reaches a plateau or slightly decreases when the entire sample is moving along the tool axis. As the sample starts exiting, this stress decreases. The level of the first plateau depends on the aspect ratio and on the level of compaction stress. A linear relationship between the aspect ratio and the maximal ejection stress is observed. This is consistent with the fact that this stress is proportional to the area of contact. Concerning the influence of the compaction stress, the higher the compaction stress, the higher the maximal ejection stress and a power law relationship is found to account for their dependence. However, the higher the compaction stress, the faster the decrease of the ejection step in the second stage of the ejection.

### 4.0.3 Description of the experimental test

As schematically depicted in figure 3.17, to measure the ejection force, dedicated tests are run.

During the ejection, the displacement is applied with a rate of 0.05 mm/s and the force applied by the actuator is recorded. A loading cell with a capacity of 50 kN is used. Then, the final diameter of the part is measured. Depending on the material or the level of the maximal applied stress, in some cases, the elastic recovery is large enough so that the part is no longer in contact with the tool at the end of the unloading step. The table 3.1 summarizes the final diameter for the different tests. The results are presented in figure 3.18.

**Table 3.1:** Final diameter of the parts after the compaction and the ejection from the tool

| Material | Test | $\Sigma_{max}^{top}$ (MPa) | Final diameter (mm) | simulation |
|---|---|---|---|---|
| virgin PTFE | loading/unloading 1 | 100 | 24.85 | 24.74 |
| | loading/unloading 2 | 100 | 24.85 | |
| | loading/unloading 3 | 100 | 24.84 | |
| | simple loading | 34 | 24.93 | 24.64 |
| PTFE + filler 1 | loading/unloading 1 | 100 | 25.00 | |
| | loading/unloading 2 | 100 | 24.99 | |
| | loading/unloading 3 | 100 | 25.00 | |
| | simple loading 1 | 34 | 25.04 | 25.02 |
| | simple loading 2 | 34 | 25.04 | |
| | simple loading 3 | 51 | 25.01 | 25.13 |
| | simple loading 4 | 51 | 25.01 | |
| | simple loading 5 | 81 | 24.99 | 25.22 |
| PTFE + filler 2 | loading/unloading 1 | 100 | 24.98 | |
| | loading/unloading 2 | 100 | 24.97 | |
| | loading/unloading 3 | 100 | 24.98 | |
| | loading/unloading 4 | 100 | 24.97 | |
| | simple loading 1 | 34 | 25.03 | |

Thus, it is found that for this geometry, for the three compounds, the higher the maximal applied stress during the compaction step, the higher the recovery. The equilibrium between the radial stress and the elastic recovery appears to be different depending on the material. For virgin PTFE, whatever the applied stress is, the recovery is so high that the diameter of the part becomes smaller than the inner diameter of the tool. When fillers are added the ejection force becomes strictly positive but also decreases with the compaction pressure (figure 3.17.b). The ejection force is smaller for PTFE+filler 2 than for PTFE+filler 1 (figure 3.17.c). Whatever the maximal applied stress during the compaction

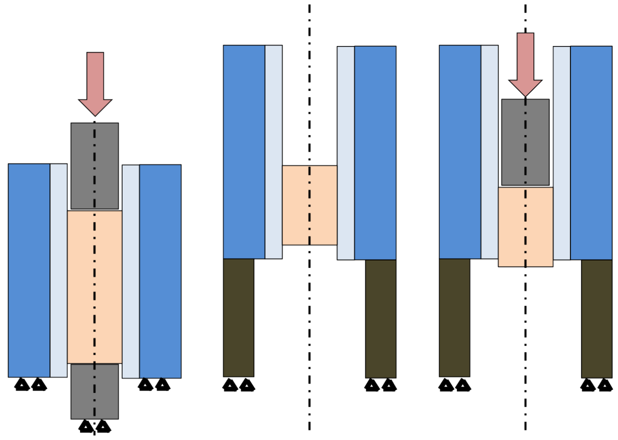

(a) Steps of the ejection test : the sample is compacted and unloaded. the matrix is raised on a metallic cylinder so that the lower punch is no longer in contact with the sample. Then a displacement is applied on the upper punch. When the contact between the sample and the punch is set, the axial force increases up to a global slippage of the sample in the chamber. The sample slides inside the tool. The measured stress is almost constant until the sample exits out of the die. The stress decreases with an almost constant slope until the sample is fully ejected from the die.

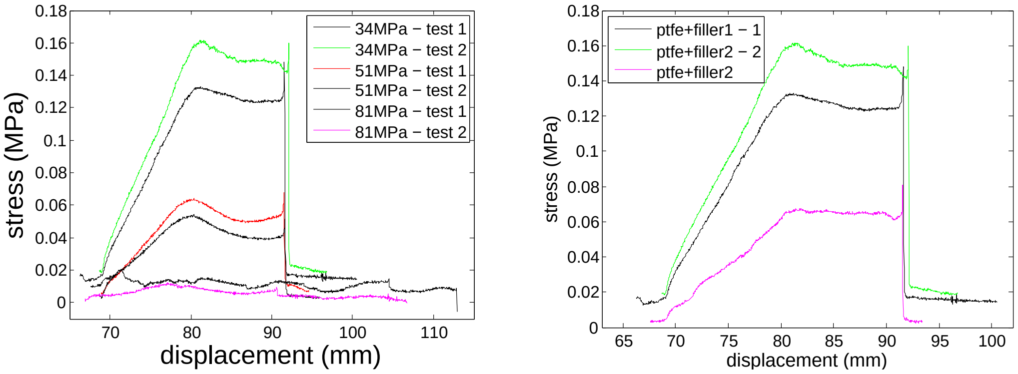

(b) The piston moves from the top to the bottom (so from right to left on the curve). Influence of the maximal applied stress used for the compaction step - PTFE + filler 1

(c) Here the maximal applied stress for the compaction is 34 MPa - Influence of the fillers

**Figure 3.17:** Ejection tests - Ejection force as a function of the applied displacement - In the case of the virgin PTFE, at the end of the unloading, the diameter of the part is smaller than that of the tool and no ejection is required.

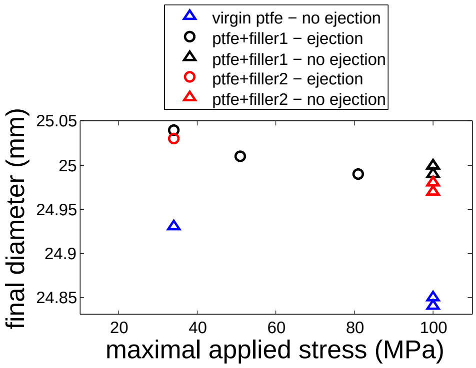

**Figure 3.18:** Influence of the maximal applied load during the compaction and of the type of material on the final diameter of the part and the ejection step

is, the final diameter is always higher for PTFE+filler 2 than for PTFE+filler 1 than for virgin PTFE.

The opposite trend for the evolution of the elastic recovery and the ejection force with respect to the maximal applied stress is observed compared to the results obtained for ceramic powder in [Briscoe et Rough, 1998]. It is also the case for the prediction of the simulations as shown in table 3.1 and figure 3.19. Note that the higher level of force in the simulation may be also explained by the rigidity of the mold, but that does not explain the different ranking.

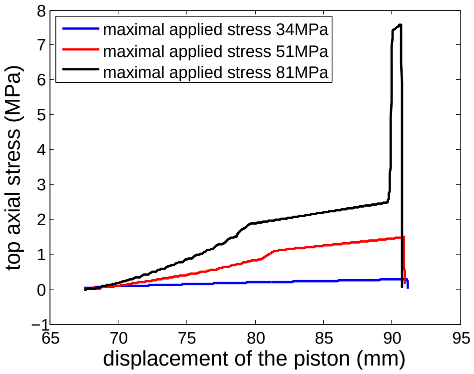

**Figure 3.19:** Simulation of the ejection step - Influence of the maximal applied stress used for the compaction step - PTFE + filler 1

In Rolland et al. 2012, a Lode dependence is implemented in a model based on a Cam Clay type model to see if its omission in the description of the mechanical behavior could explain discrepancies observed by co-authors between the experimental measurements and the simulation results (which over-predict the ejection forces and the residual stresses). This study concludes that no influence of the third invariant is observed during the compaction. Indeed, apart from the friction effect, most of the loading and the deformation are axial. Differences are observed during the ejection step. But no difference more than 10% decrease in the radial stress during the ejection step are observed.

Using the model implemented in Abaqus where the third invariant may be taken into account, setting its influence to the extreme value compatible with a convex yield surface, did not produce any significant influence on the PTFE compaction results. Hence, the omission of Lode parameter is not the cause of the observed discrepancy.

It can be speculated that anisotropy of the material developed during the compaction is a possible cause of these differences of behavior.

# 5 Anisotropy - bibliographic review

The majority of models developed to describe the behavior of powder materials are based on a single state variable equal or equivalent to the porosity. It is commonly admitted that for monotonic loadings, isotropic model are sufficient to describe the behavior of the material. Anisotropic aspects have to be taken into account only for complex non proportional cyclic loading. However, even for simpler loadings, this is not always sufficient to describe the behavior of the material which may depend on other state variables.

As explained in the introduction, anisotropy of the sintered PTFE, induced by the compaction step has been proven. But no tests on the green part are made.

Experimental evidence of anisotropy of the green parts after die compaction may be found for different types of material in the literature like in [Li et Puri, 1996] (glass beads and fibers, wheat flour and potato starch), [Frachon, 2002] (metallic powders), [Galen et Zavaliangos, 2005] (metallic and pharmaceutical powders). Fibers or non-equiaxed particles exhibit high level of anisotropy whereas this effect is less visible for irregular shaped particles (like wheat flour). For irregular shaped particles, no preferential direction of contact is created. For ductile particles like metallic powders, the deformation of the particles is higher in the direction of compaction than in the radial one and may explain the different levels of tensile strength and elastic parameters with respect to the direction of compaction ([Frachon, 2002]).

As described in [Fleck, 1995], the state of the material and more precisely the shape of the yield surface may depend on the history of the loading path. In [Frachon, 2002] for metallic grain or in [Radjai et Roux, 1995], [Radjai *et al.*, 1999] and [Roux et Radjaï, 2002] for perfectly rigid particles, a second order ‘fabric’ tensor is introduced to describe the preferred direction of the normal contact and the anisotropy of the material.

In spite of the possible relevance of anisotropy for the description of the compacted PTFE, we did not investigate the point further, although this seems a very interesting direction to investigate.

# 6 ‘V’ tool

The experimental set up has been designed and made in collaboration with the team of Rodrigo B. Canto from the DEMA laboratory in UFSCAR, Brazil. The set up of the tool and the different measurement and acquisition tools were made in the frame of the internship of third year of license of Caiuã C. Melo at the LMT Cachan, partly under my supervision ().

## 6.1 Presentation of the tool

**Design of the tool** This compaction tool has been designed for two main purposes:

- it has been designed with a ‘complex’ and variable shape in order to test the material along different and various loading paths. The rectangular section of the tool may be more or less reduced. This way, a gradient of hydrostatic and shear strain is obtained through the sample;

- besides the measurement of the displacement of the piston and of the applied and transmitted axial stresses, the complete displacement field of one of the surface of the sample inside the tool is measured thanks to DIC. Images are taken through a glass plate which replaces one of the original metallic plates of the mold.

**Geometry of the tool** The geometry of the tool is illustrated in figure 3.20. The cavity is 54 mm wide and 20 mm thick so that the gradient of displacement in the thickness of the tool induced by the friction between the wall and the powder is negligible. Hypothesis of plane strain may be done. The upper part of the compaction tool is rectangular while the section of the bottom part is more or less reduced. Different wedges can be mounted on the device, allowing for exploring different geometries. Three different values of the angle between the horizontal plane and the tilted part of the mold have been fabricated $65^\circ$, $75^\circ$ and $85^\circ$, where the $85^\circ$ position is closer to a classical $90^\circ$ angle rectangular œdometric mold.

The front plate of the tool is movable and may be replaced by a glass plate. A thermal tempered glass plate of 10 mm thick is chosen here. An applied axial stress of approximately 15 MPa may be reached before breaking the glass.

**Applied loading** Tests are performed in the electromechanical testing machine Instron-5882. A displacement with a rate of 0.05 mm/s is imposed to the top piston. Successive loading and unloading steps at different levels of axial stress are programmed.

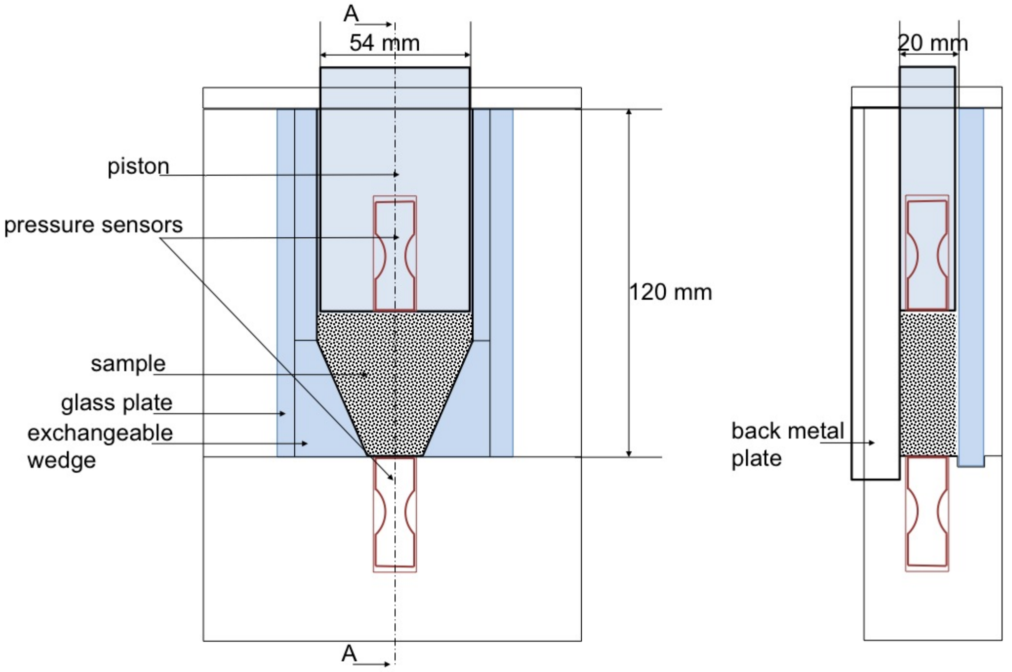

**Figure 3.20:** Scheme of the 'V' tool - Front view on the left side and A-A cross section on the right side

## 6.2 Instrumentation of the tool

### 6.2.1 Stress measurement

In order to follow the evolution of the stress of the sample, two pressure sensors are installed inside the piston and in the bottom part of the mold, so that they are directly in contact with the upper and bottom surfaces of the sample. They are similar to the ones presented in chapter 2 and used in the 3D compaction tool. Strain gauges are included in a Wheatstone bridge Vishay model 2120B. Acquisition of the signal is made through National Instruments acquisition device thanks to the interface developed under the software LabVIEW. The pressure sensors are calibrated following the same technique as depicted in appendix B.

### 6.2.2 DIC and displacement field measurement

**DIC technique** Digital Image Correlation (DIC) is a widely used measurement technique, initially developed by [Chu *et al.*, 1985], that allows to obtain the displacement field of one face of a loaded sample from pictures taken during a test. The displacement field is determined on a region of interest (ROI).

Two images are compared: an image of reference $f$, usually taken when the sample is free of any loading, and a deformed image $g$, taken when the sample is subjected to a given loading. Each picture is described by the texture of its gray level. If the conservation of the gray levels is assumed, it may be written that, in each point of the ROI with coordinates $\mathbf{x}$ at the reference state

$$f(\mathbf{x}) = g(\mathbf{x}+\mathbf{u}(\mathbf{x})) \tag{3.6}$$

where $\mathbf{u}(\mathbf{x})$ is the unknown displacement field to be measured. To determine $\mathbf{u}(\mathbf{x})$, the squared differences over the ROI is minimized

$$\Phi_c^2 = \int_{ROI} (g(\mathbf{x}+\mathbf{u}(\mathbf{x})) - f(\mathbf{x}))^2 d\mathbf{x} \tag{3.7}$$

Two approaches may be adopted. The first one, developed by [Chu *et al.*, 1985], is the local DIC. The image is decomposed in independent zones of interest (ZOI) of typical size from 16×16 pixels to 64×64 pixels. Each ZOI of reference is compared to its neighbors in the deformed image in order to minimize the above equation. The interpolation of the estimated displacements at the center of each ZOI leads to the displacement field of the ROI.

In the second approach, the so-called global DIC ([Hild et Roux, 2012] ), the displacement field is projected on a suited basis, like finite element shape functions. The displacement $\mathbf{u}$ is then expressed as

$$\mathbf{u}(\mathbf{x}) = \Sigma_{\alpha=i}^{2} \Sigma_{i=1}^{n} a_{\alpha i} N_i(\mathbf{x}) \mathbf{e}_\alpha \tag{3.8}$$

with $a_{\alpha i}$ the unknowns, $N_i$ the shape functions and $\mathbf{e}_\alpha$ the unit vector in direction $\alpha$.

The problem is solved iteratively, where each correction is obtained from a linearization of the objective function $\Phi^2$, leading to the system

$$[\mathbf{M}]\{\delta\mathbf{a}^{n+1}\} = \{\mathbf{b}^n\} \tag{3.9}$$

with $[\mathbf{M}]$ the correlation matrix, $\{\delta\mathbf{a}^{n+1}\}$ the unknown correction vector of the amplitudes $a$, $\{\mathbf{b}^n\}$ the second member of the equation.

In the regularized global DIC method ([Tomičević *et al.*, 2013]), the uncertainty of the measurement is decreased. A mechanical regularization is added to enforce the mechanical admissibility of the displacement field. Equilibrium equation based on linear elasticity is introduced

$$[\mathbf{K}]\{\mathbf{u}\} = \{\mathbf{F}\} \tag{3.10}$$

with $[\mathbf{K}]$ the stiffness matrix and $\{\mathbf{F}\}$ the vector of nodal forces. Now, the expression to minimize is

$$(1+\omega_m+\omega_e)\Phi_t^2 = \Phi_c^2 + \omega_m \Phi_m^2 + \omega_e \Phi_e^2 \tag{3.11}$$

with $\Phi_m^2$ the mechanical function to be vanished in the inner part of the ROI

$$\Phi_m^2 = \{\mathbf{u}\}^t [\mathbf{K}]^t [\mathbf{K}] \{\mathbf{u}\} \tag{3.12}$$

and $\Phi_e^2$ the equivalent expression for nodes at the edge of the ROI. $\omega_m$ and $\omega_e$ are parameters to weight the contribution of each part of the equation thereby defining the fourth power of the ‘regularization’ length. Regularization with an elastic kernel does not mean that one assumes a linear elastic behavior to hold, but rather it is a penalty term that allows to have smooth variation of the displacement field yet without prejudice to rigid body motion possibly affecting the displacement. This allows to deal with arbitrarily fine mesh and introduces a lower length scale that is more physical than a given shape function.

Here the regularized global DIC based on unstructured three-noded triangles, Correli T3 is used. An average element size of around 100 pixels is defined to construct the mesh over the Region of Interest (ROI). The initial size of the element takes into account the final size of the elements, highly reduced due to the large displacements experienced by the sample, and the resolution of the images. A slightly larger regularization length is chosen. For each pictures $i$, a first calculation is performed where the reference image is the previous picture $i-1$. This first results allows to initialize the computation of the second step, where the image of reference is the first image of the series for $i=0$.

**Experimental set up** A Canon 60D camera with a lens of 100 mm focal length is placed in front of the glass plate as shown in figure 3.22. To avoid any damage on the camera in case of breaking of the glass, a tempered glass is used as a protection. Pictures are acquired every 5 s.

**Figure 3.21:** V tool inside the testing machine and with the picture acquisition set up

**Preparation of the sample** Samples are prepared in two steps. First, the back part of the tool is removed and the tool is laid down such that the glass surface is face down. A first thin layer of mix of filled ‘black’ PTFE powder and virgin PTFE powder is uniformly poured on the glass surface of the mold. The two powders were previously gently mixed so that a grey level texture with a random speckle pattern and a characteristic length of few pixels is created. Then, the tested powder is poured to fill in the mold.

The final distance of compaction is limited here by the reduction of section of the mold. In order to reach a sufficient level of compaction, a more important volume of powder as compared to the volume of the die needs to be compacted. To overcome this problem, a metallic extension of the mold, with the same section as the die, is aligned and fastened on top of it. The powder is pre-compacted up to the top surface of the mold and the extension is removed.

For the virgin PTFE, 81.2 g of powder is poured in the case of the tool in the ‘65°’ configuration, 85.5 g in the ‘85°’ configuration.

**Overview of the tests** In figure 3.22, pictures taken at the beginning of the tests of the samples corresponding to the different geometries of the tool, are presented. In figures 3.22, the initial state of the sample and the compacted ones respectively are presented.

(a) 85°

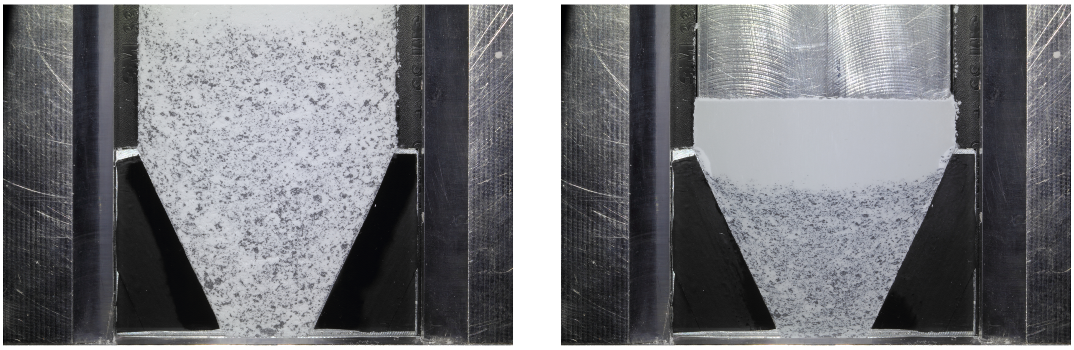

(b) 65° - Initial state (c) 65° - Final state

**Figure 3.22:** Pictures of the sample before the compaction for two different geometries and sample at the end of the loading in the case of the ‘65°’ configuration

# 7 Presentation of the results

## 7.1 Stress vs displacement curves

Two tests are presented and analyzed here. The tests are performed on virgin PTFE and the two configurations ‘65°’ and ‘85°’ are considered, which are respectively denoted 65° test and 85° test. In figure 3.23, the applied displacement on the piston is plotted as a function of time. The stresses measured by the internal pressure sensors from the top and bottom sides as a function of the displacement imposed by the actuator are also shown in the same figure.

From these curves, it may be seen that the transmitted stress, $\sigma_{bot}$ is smaller than the applied stress, $\sigma_{top}$. This is caused by the friction between the tool and the mold and the geometry of the tool. Indeed in the case of 85° test, close to an œdometric compaction, stresses are almost equal in agreement with the results presented in the first part of this chapter. In the case of 65° test, part of the axial force is supported by the tilted lower part of the mold. Thus the bottom stress inside the material is smaller. The differences between both tests are a first illustration of the variety of applied loading paths.

In both cases, the unloading steps are not linear, which is reminiscent of the observations made in previous tests and interpreted as reflecting a phase transformation.

## 7.2 DIC analyses

In the four next figures, 3.24, 3.25, 3.26 and 3.27, displacement fields in the vertical and horizontal directions for selected steps are presented. Note that the displacement fields are plotted on the reference geometry (Lagrangian displacement field). They are expressed in mm. As could be seen figure 3.22, because of the filling technique, it is not possible to create a texture through the whole length of the sample. The displacement field of only half of the sample may be analyzed. This is consistent with the fact that the maximal displacement measured by DIC is half the displacement imposed by the actuator. From these pictures, it may be seen that the applied loading is almost symmetrical. Comparing both tests, the 65° tool creates an additional gradient of displacement due to the shape of the cavity (as seen from the curvature of the iso displacement lines in the $U_x$ field).

From the displacement fields, strain components may be deduced and particularly the volumetric and deviatoric part of the strain tensor. Figure 3.28, results are presented for the steps at the maximal applied load for both considered tests. This illustrates the heterogeneity of the applied loading path inside the tool, which is more important in the case of the 65° test, as expected.

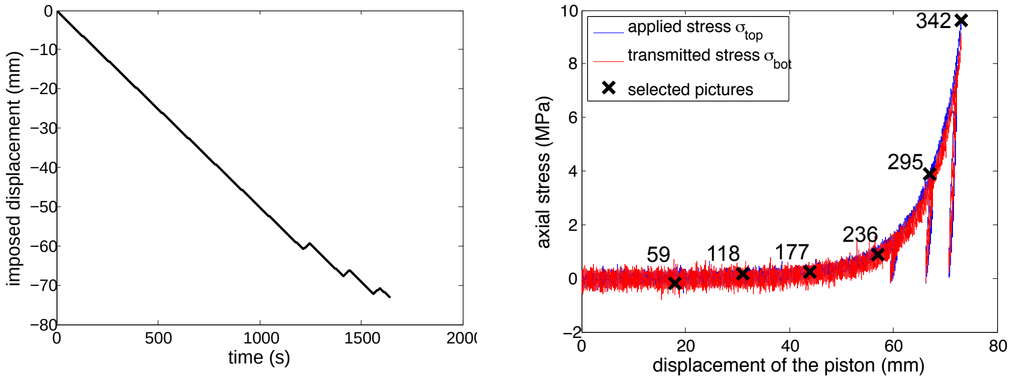

(a) Applied loading - 85° test (b) Displacement - stress response - 85° test

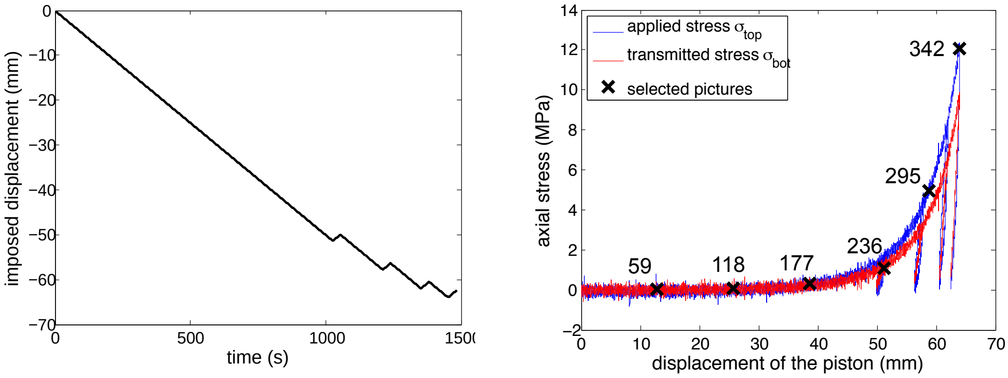

(c) Applied loading - 65° test (d) Displacement - stress response - 65° test

**Figure 3.23:** Figures a and c show the applied displacement by the actuator as a function of time is presented for 85° test and 65° respectively. In figures b and d, the associated stress vs displacement repsonses are plotted. Both applied and transmitted axial stresses are presented. Black crosses indicate when the pictures presented in the next parts were acquired.

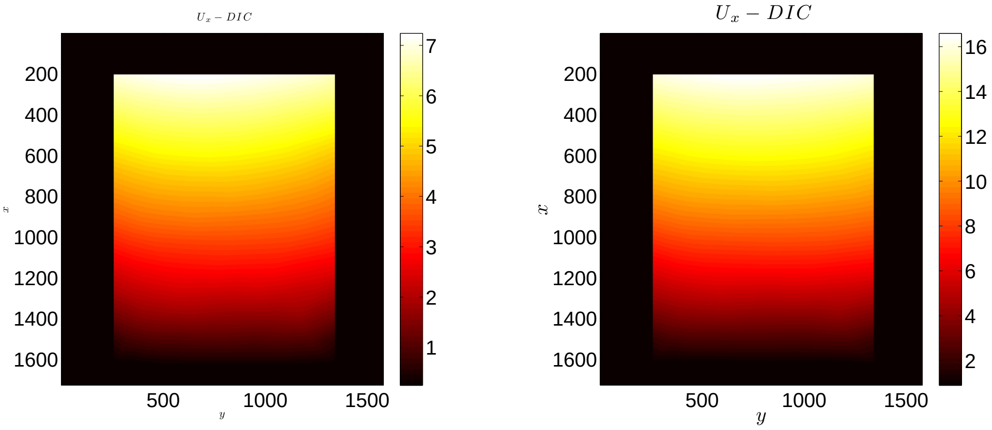

(a) Step 59 (b) Step 118

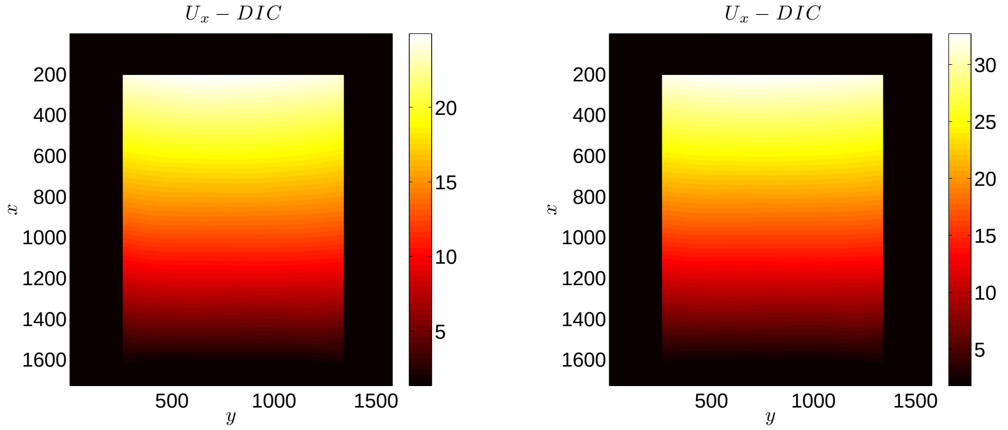

(c) Step 177 (d) Step 236

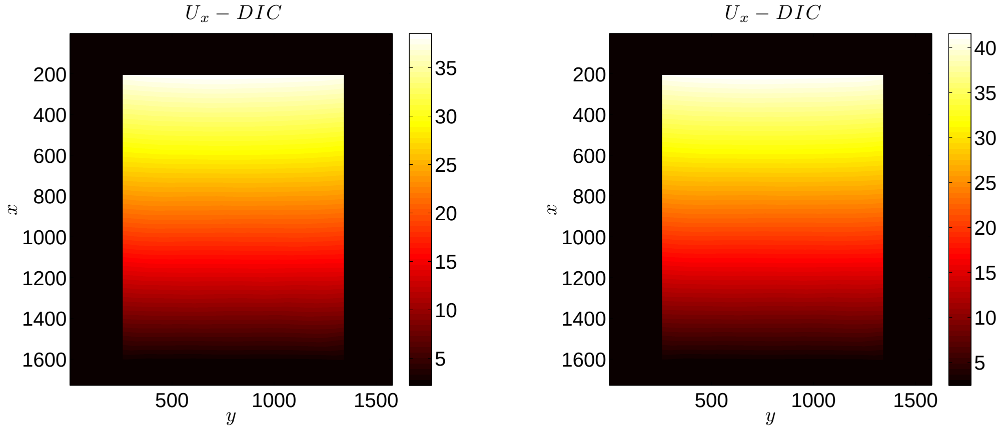

(e) Step 295 (f) Step 342

**Figure 3.24:** Displacement field along the direction $x$ - 85° test

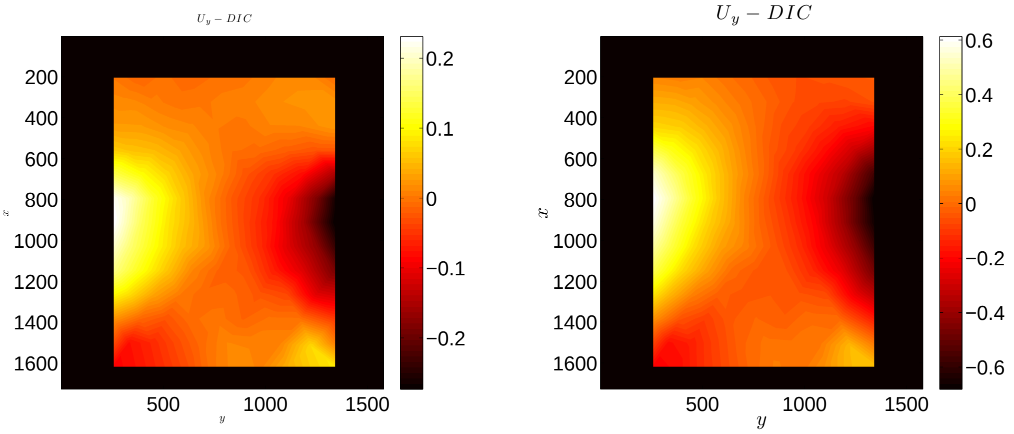

(a) Step 59 (b) Step 118

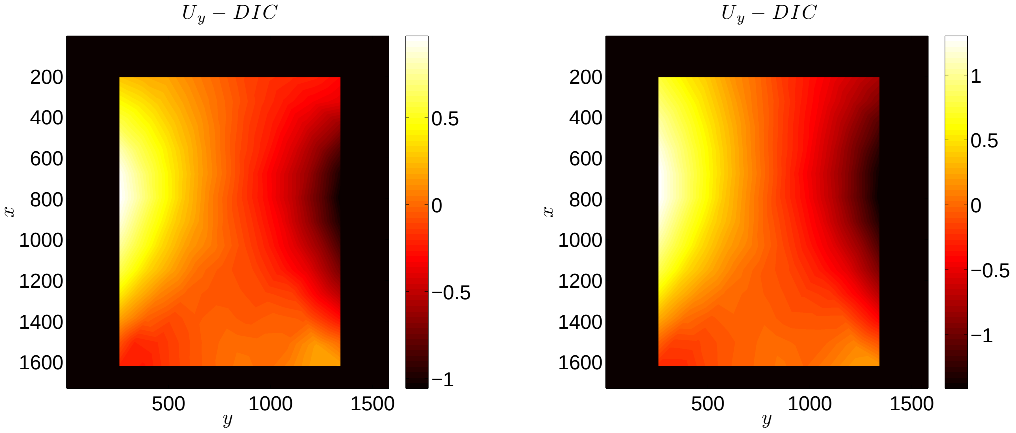

(c) Step 177 (d) Step 236

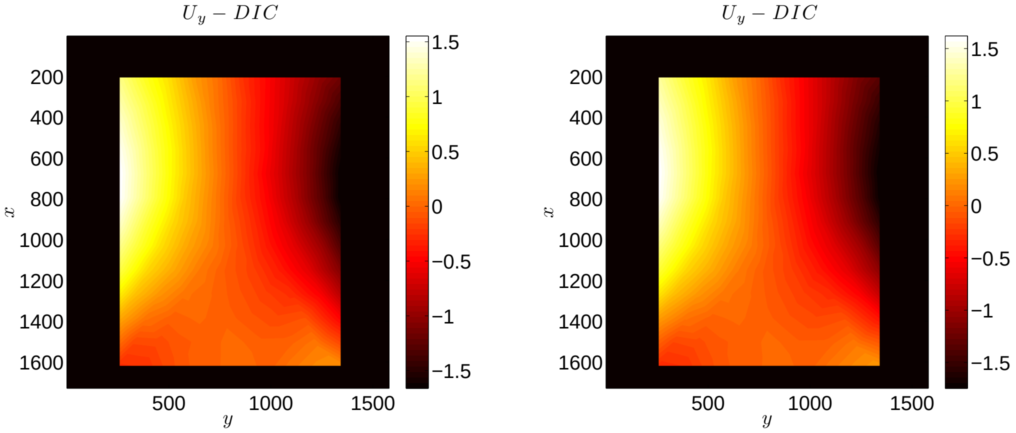

(e) Step 295 (f) Step 342

**Figure 3.25:** Displacement field along the direction $y$ - 85° test

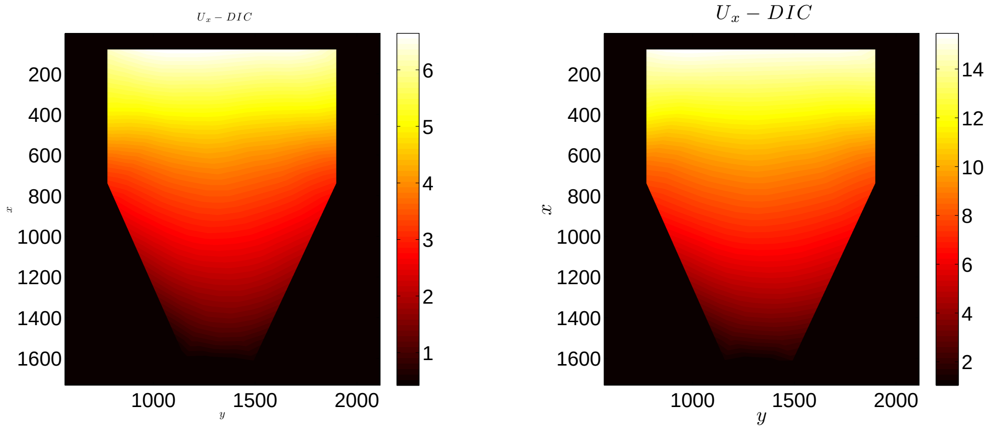

(a) Step 59 (b) Step 118

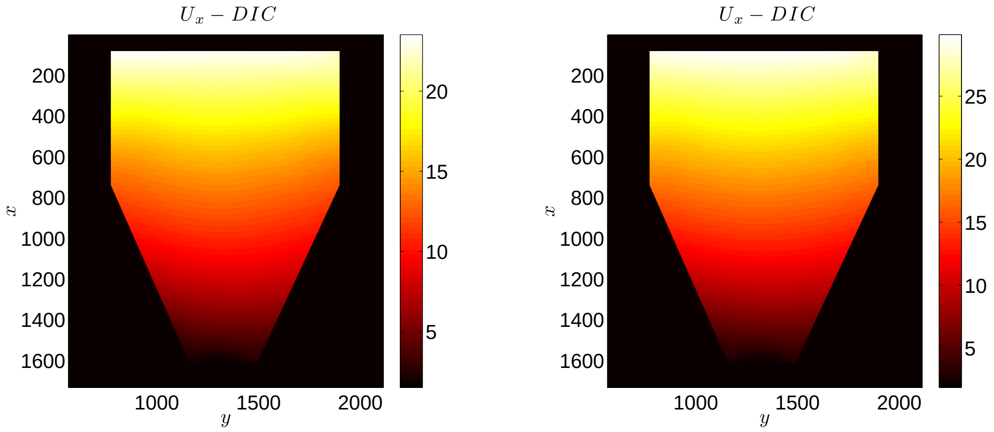

(c) Step 177 (d) Step 236

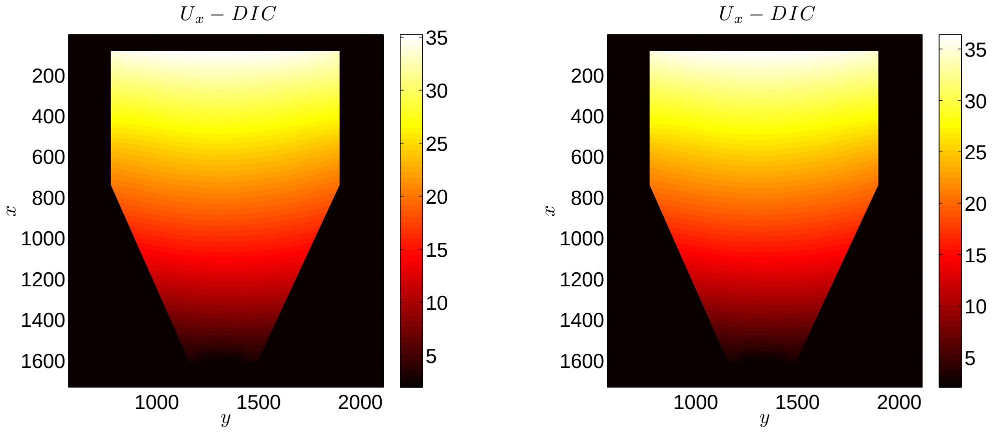

(e) Step 295 (f) Step 342

**Figure 3.26:** Displacement field along the direction $x$ - 65° test

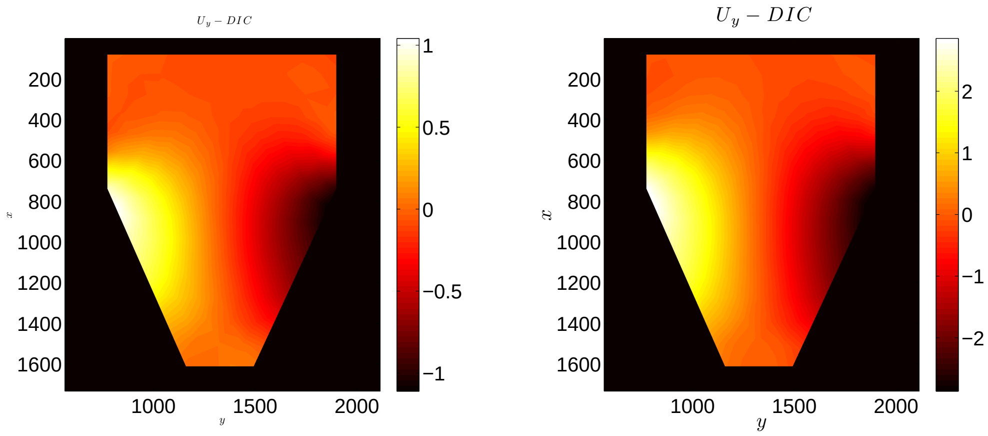

(a) Step 59 (b) Step 118

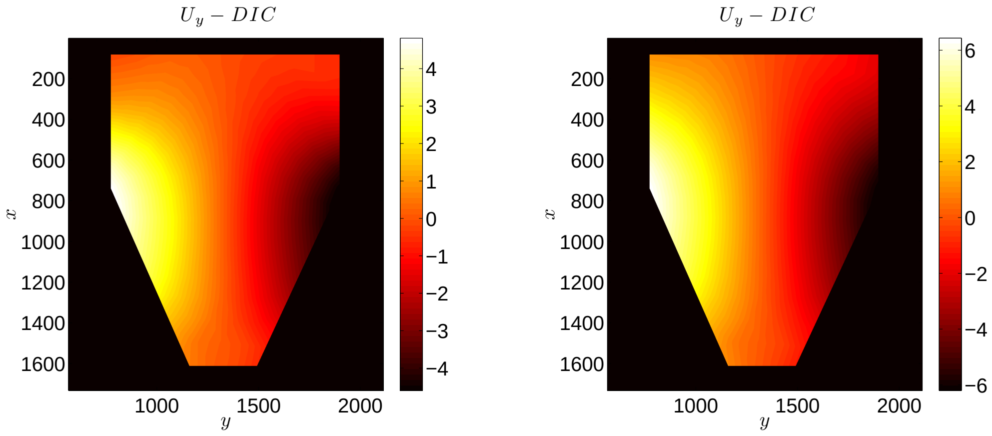

(c) Step 177 (d) Step 236

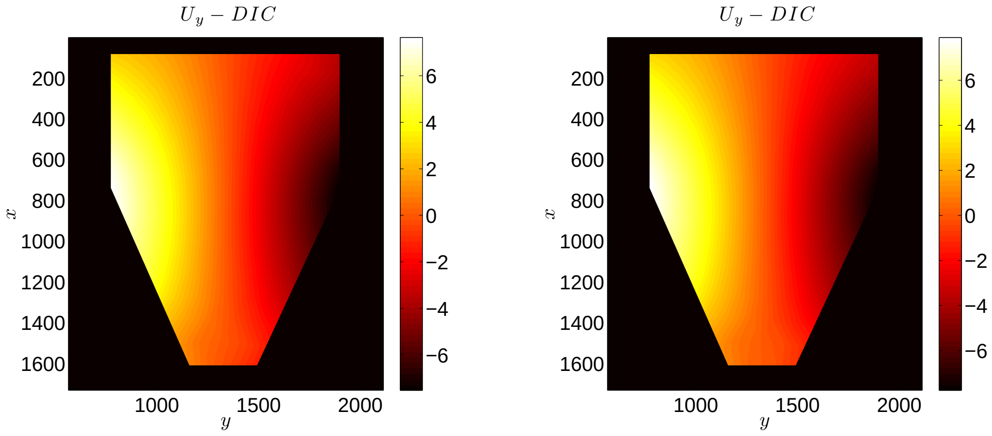

(e) Step 295 (f) Step 342

**Figure 3.27:** Displacement field along the direction $y$ - 65° test

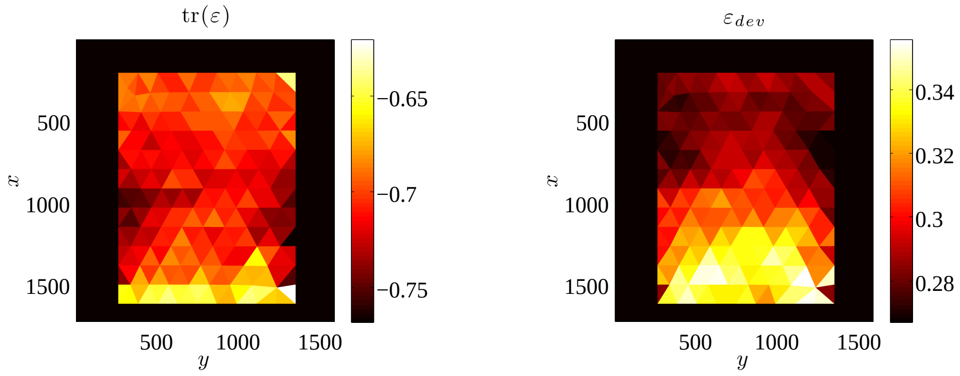

(a) Volumetric strain - 85° test

(b) Deviatoric strain - 85° test

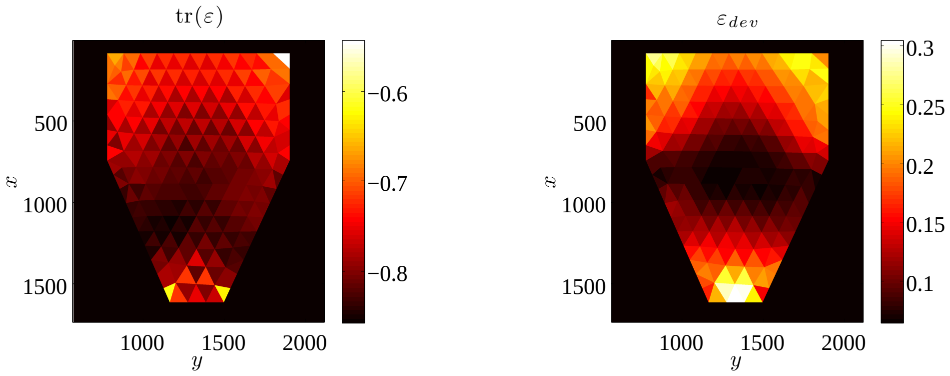

(c) Volumetric strain - 65° test

(d) Deviatoric strain - 65° test

**Figure 3.28:** Volumetric and deviatoric strain fields at the maximal applied loading for tests 85° and 65°.

# 8 Simulation vs. experimental results - $3^{rd}$ validation

## 8.1 Comparison with the DIC measurements

As compared to the ‘classical’ comparison between measured and computed stresses, a richer analysis may be done. Indeed, here the computed displacement field is directly compared to the displacement field obtained from the DIC analyses. To do so, the same mesh as the one used for the DIC, is built in the FE code Abaqus. To this mesh, the constitutive equations of the material is associated. For each step (i.e. for each pictures), the displacements, measured by DIC, $U_{corr}^{edge}$ at the edges of the region of interest are imposed to the edges of the mesh in the FE simulation in both directions $x$ and $y$. Once the computation is completed, node displacements $U_{simu}$ are recorded at each node and directly compared to the displacements $U_{corr}$.

Note that, in the case of our material which is almost incompressible in its asymptotic state and which is subjected to high deformations, using T3 elements leads to locking effect and errors of computation as explained in [Hibbit *et al.*, 2011]. Quadratic elements CPE6MH are used to avoid this problem.

The error $Er$ made in the simulation as compared to the DIC measurement is defined as

$$Er = \frac{\sqrt{(U_{simu}^{x} - U_{corr}^{x})^2 + (U_{simu}^{y} - U_{corr}^{y})^2}}{\sqrt{{U_{corr}^{x}}^2 + {U_{corr}^{y}}^2}} \tag{3.13}$$

It is plotted for the different steps presented in figures 3.29 and 3.30.

In figure 3.31, the average error over the region of interest of the simulation calculation is plotted for each step as compared to the experimental displacement field. At the beginning, error is higher and decreases to a value below 3% and 5% for tests 65° and 85° respectively.

Error is generally higher in the bottom half part of the sample as it may be seen figures 3.30 and 3.29. This may come from a two sources of error :

- the model is not accurate enough to describe the behavior of the material for low density. Some improvements have to be done as explained in chapter 2. The characterization of the behavior of the fluffy powder is difficult considering the large displacements associated to the low level of resulting stresses.

- the initial density of the material, after the powder has been poured inside the mold may be not homogeneous. This difference of state may explain why the error decreases as the density increases and the initial variation of density tends to be erased. This expression of the error tends to increase the estimation for displacements close to zero.

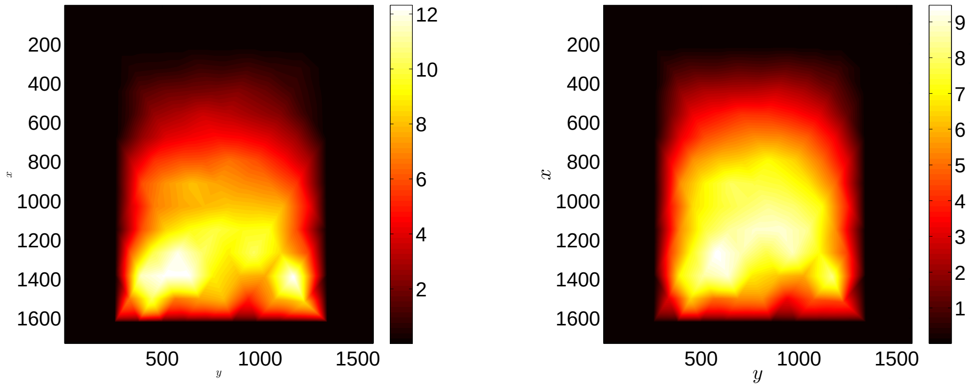

(a) Step 59 (b) Step 118

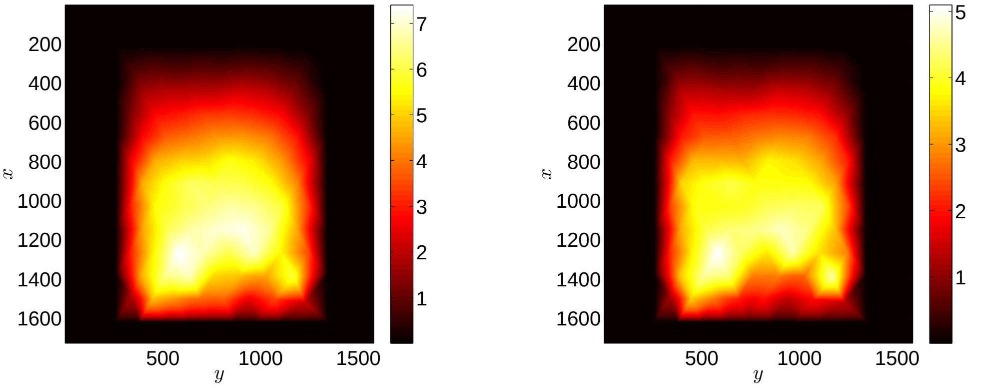

(c) Step 177 (d) Step 236

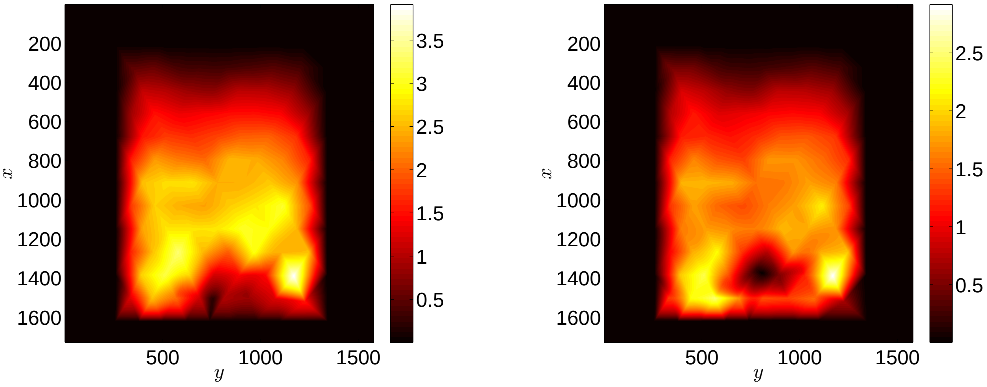

(e) Step 295 (f) Step 342

**Figure 3.29:** Error in % - 85° test

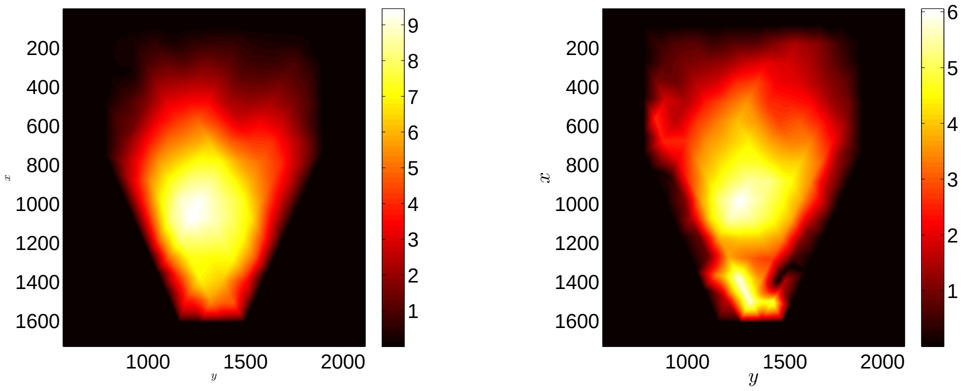

(a) Step 59 (b) Step 118

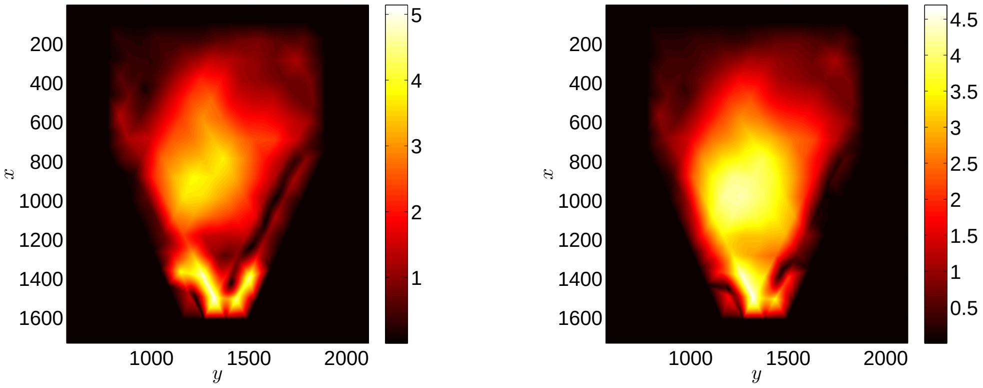

(c) Step 177 (d) Step 236

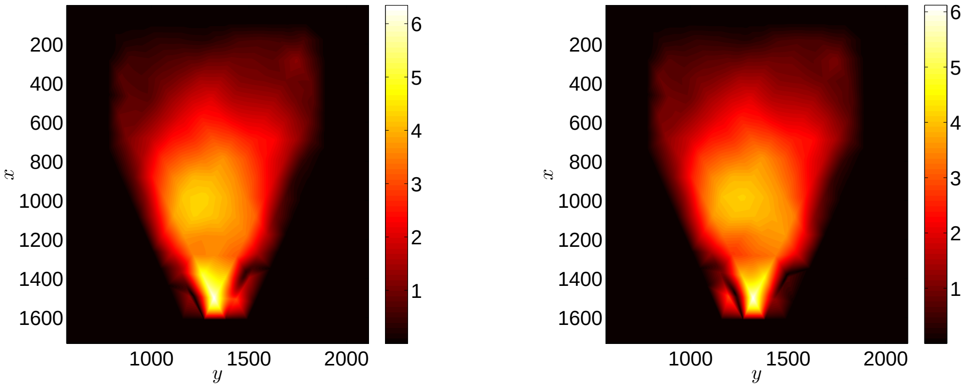

(e) Step 295 (f) Step 342

**Figure 3.30:** Error in % - 65° test

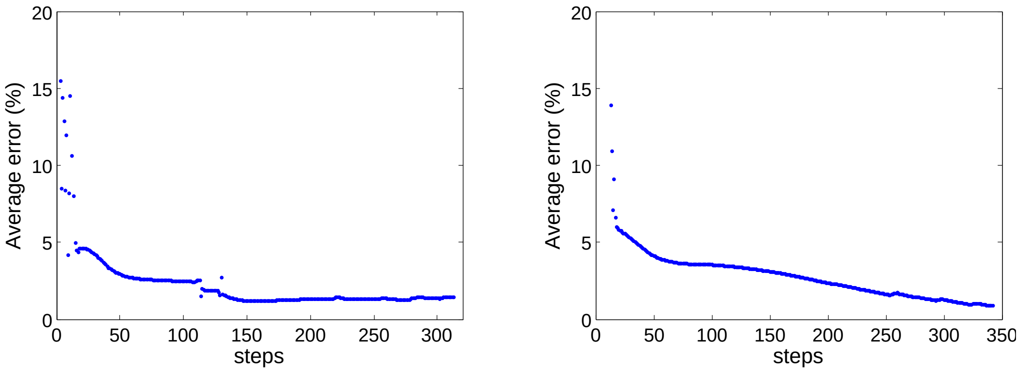

(a) 65° test - mean error 2.92%

(b) 85° test - mean error 4.6%

**Figure 3.31:** Average error over the analyzed field for each step of the test

## 8.2 Comparison with the stress measurements

In figure 3.32, stresses computed on the elements in the middle of the bottom and top edges of the sample (which corresponds to the position of the pressure sensor in the bottom case and which is in the central axis of the top pressure sensor for the second case) are compared to the experimental measurements. Results are here again in good agreement even if the uncertainty on the initial density may highly influence the results. The difference between bottom and top stresses are higher in the case of 65° test than in the case of 85° test. Thus the difference of behavior with respect to the type of geometry of the tool is well described. As for the displacements, the error is higher at the beginning of the test. One may speculate that the same reasons may be put forward to account for the discrepancy.

Note that because the top piston is not in contact with the top of the analyzed area, the simulated top stress is lower than the measured applied top stress, but higher than the bottom stress. Particularly in the case of 65° test, this is consistent with the fact that the top edge of the analyzed meshed area is approximately at the half length of the whole sample.

# 9 Conclusion and perspectives

This original tool allows the measurement of the applied and transmitted stresses and of the whole displacement field of the sample during its compaction. The variable geometry of the tool enables the application of different loading paths to obtain a different amount of shear strain depending on location.

Simulations of the tests are directly compared to the stresses and displacements measurements. The comparison on a complex loading is globally good. An average error of

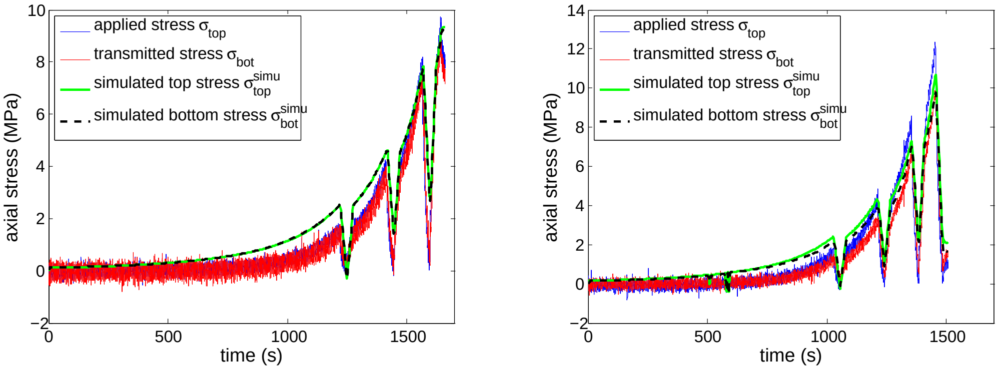

(a) Stresses - 85° test (b) Stresses - 65° test

**Figure 3.32:** Comparison of simulated and experimental axial stresses for 85° and 65° tests.

less than 5% on the displacement fields is measured for both tested geometries.

This $3^{rd}$ validation is satisfactory even if some points need to be improved : the description of the behavior of the material for low density inherits from the preparation state which is difficult to be made homogeneous and impacts the density inside the tool, at the end of the filling.

With the help of Florent Mathieu, an inverse identification procedure has been adapted to this test and this complex material model. This procedure is based on the FEMU (Finite Element Model Updating) technique described in [Gras, 2012] and [Mathieu, 2013]. This iterative procedure consists of minimizing the gap between the simulation and the experimental data (measured force and displacement) by modifying the parameters of the model which have to be identified. Tests have been done to develop a procedure of identification of the Drucker-Prager/cap model of the PTFE based materials from these tests. However, mainly because of the uncertainty of the initial state of the material which is completely dependent on the mechanical behavior of the powder material, no satisfactory results have been obtained. More robust experimental and identification procedures need to be developed.

In situ X-ray radiography observations coupled to DIC on the radiographies could solve this problem. In situ visualization are done thanks to X-ray radiographic and tomographic apparatus, in studies such as those of [Colliat-Dangus *et al.*, 1988] on compacted sands or more recently of [Lachambre *et al.*, 2013] where microsphere porosities and their deformations of syntactic foams are observed during hydrostatic loading. Here, post-loading observations are performed as shown in figure 3.33. The tool has also been modified to allow this measurement replacing the metal back plate by a plastic plate. Design of a new tool, dedicated to the behavior of these tested PTFE powders will also help the identification procedure.

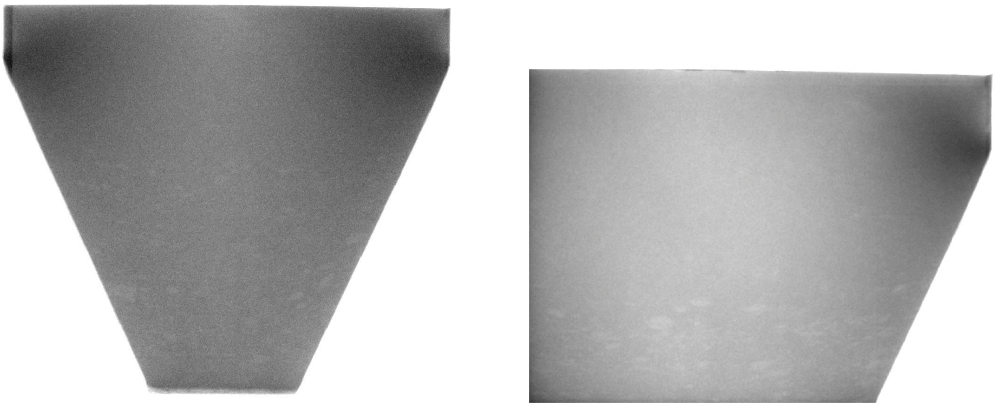

(a) Compacted sample (b) Zoom on one of the corners

**Figure 3.33:** Radiograhic observations of compacted PTFE samples in V tool - As the thickness of the sample is constant, the grey level is linked to the density of the material. Non uniform density is clearly observed here.

# Chapter 4

# Simulation of the industrial process

*In the first part of this chapter, simulations of the PTFE billet compaction at the industrial plant scale are compared to available process data. The model may be considered as validated, and hence reliable for this range of conditions. Then different characteristics of the process such as the loading path, the geometry of the tool and the type of material are studied as well as their influence on the obtained green parts.*

## Sommaire

# 1 Validation of the model at the industrial scale

## 1.1 Presentation of the test

Data obtained from a medium scale press were provided by the industrial partner. A hollow cylindrical billet with a wall thickness of several tens centimeters and a final height between 6 to 8 times higher is pressed. This part is obtained thanks to a cylindrical œdometric tool, the mantel, inside which a cylindrical mandrel is centered, as illustrated in figure 4.1. It is compacted with a hydraulic double effect press. Displacement or force may be imposed from both top and bottom sides of the part through two pistons. Record of the axial displacements and forces is possible. However, note that the measurement of the displacement is not as accurate as in the previous experimental results. No external displacement sensors are available, no measurement of the stiffness of the system was possible in order to get over the error caused by the stiffness of the tool and the actuators. Moreover the initial state of the material is not well known as the powder is pre-compacted ‘by hand’ before the beginning of the test to completely fill the mold. Considering these two aspects, data have to be considered with caution.

However, data of several trials performed on PTFE+filler 1 with different loading conditions are accessible and comparison with FE simulation results is an essential validation of the proposed model required for its use.

For confidentiality reasons, force, displacement and dimensions of the part are normalized. Displacements and stresses are normalized by the maximal displacement and the maximal level of stress respectively. In figure 4.2, the typical histories and responses of the material in the uniaxial direction from top and bottom sides are shown. After the filling of the mold, the material is first compacted from one side. While the top piston is being locked in displacement, an imposed displacement is applied from the bottom until a sufficient level of stress is reached to allow the control in force (until point A). When the desired level of first pre-compaction force is reached (point B), the part is unloaded (point C). In a second stage, namely the main compaction, the part is loaded from both sides by controlling the force (point E to F) . Finally applied stress is set back to zero (point G to H) and the billet is ejected from the tool.

Compaction from both sides enhances the homogeneity of the density of the material through the height. Due to the low density of the powder. And hence its very low stiffness, and the limitation of the equipment (range of measurement and control) double effect compaction is not possible right from the beginning, and a pre-compression step is first applied.

## 1.2 Comparison between the experimental data and the simulation - medium scale

To validate the proposed model on a larger scale, available experimental data are compared with the FE simulation results. The same assumptions as for the simulation of the œdometric tool in chapter 3 are made. In figure 4.3, the evolution of the density with the

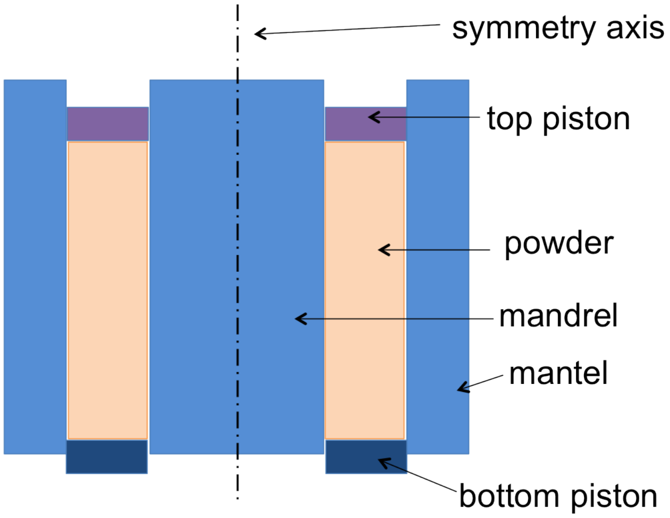

**Figure 4.1:** Schematic representation of the geometry of the tool, filled with a compound

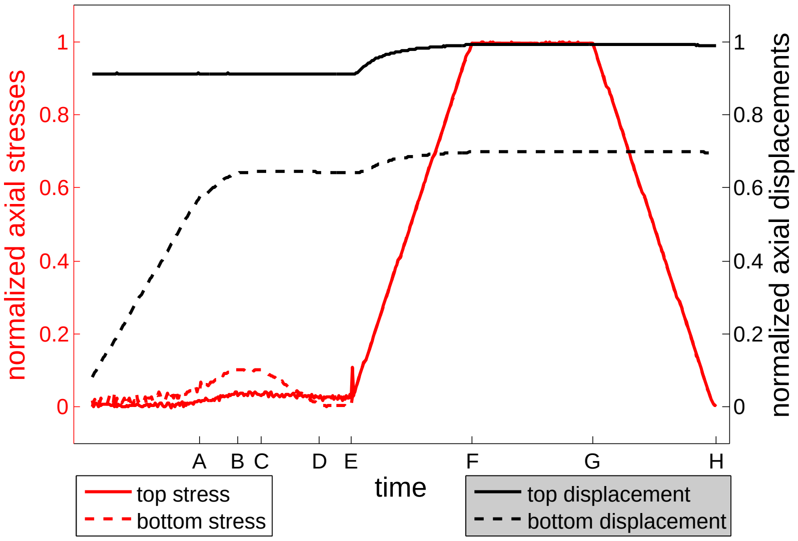

**Figure 4.2:** Stress and displacement loading path.

average axial stress is compared. Up to 60% of the maximal applied stress, the simulation result is superimposed on the experimental curve. Then, a gap appears which may be attributed to a measurement error of the displacement during the experimental test (the stiffness of the tool is not taken into account as explainedabove). A 3.35% error is made on the prediction of the final height of the part.

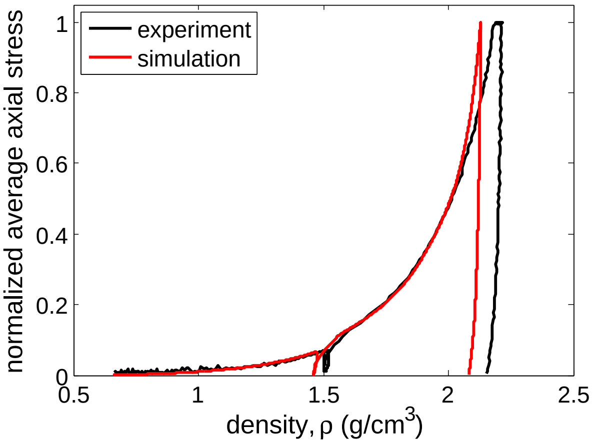

**Figure 4.3:** Comparison between the experimental data and the results of the simulation - evolution of the density with the average applied stress

Here again, except at the beginning of the loading where the measurement uncertainty is higher, the trend and the transmitted over the applied stress ratio during the pre-compaction or displacement during the main compaction are well described (figure 4.4). The evolution of the piston displacements from both sides as a function of the applied forces is also in good agreement with the experimental data even if the same gap as described in figure 4.3 is observed. Thus, it may be concluded that the elasto-plasticity model combined with the friction model, which affects the transmission of the load through the tool, is consistent with the observed phenomena on large scale.

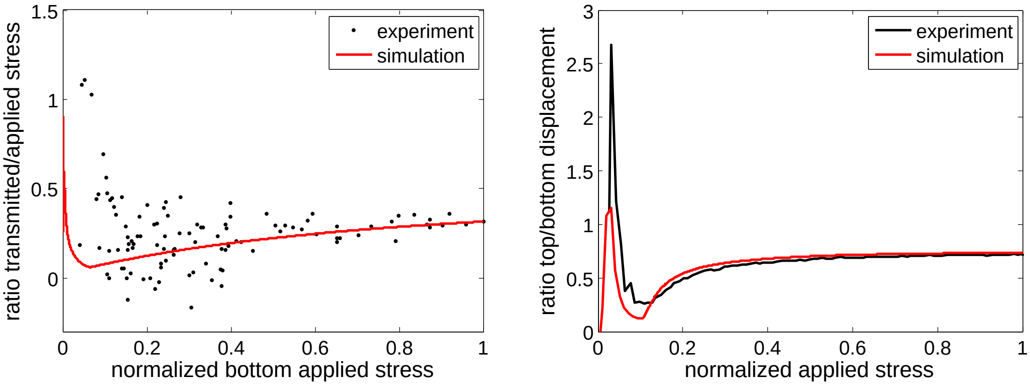

(a) Ratio between the top and the bottom stresses during the pre-compaction (displacement imposed from one side)

(b) Ratio between the top and the bottom displacements during the main compaction (same force imposed from both sides)

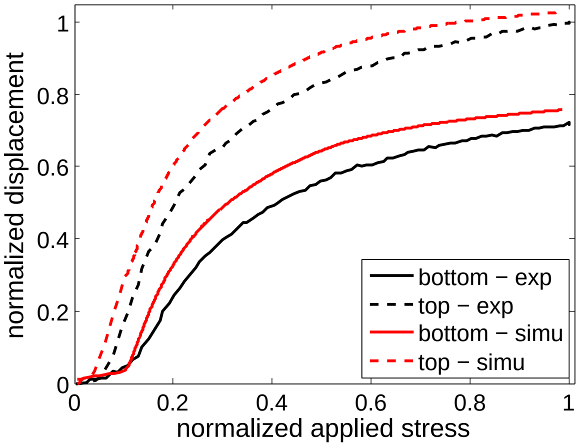

(c) Evolution of the displacements from the top and the bottom sides as a function of the applied stress

**Figure 4.4:** Comparison between the experimental data and the results of the simulation for medium scale tool - Focus on the differences of evolution of the displacements and the stresses from top and bottom sides.

## 1.3 Validation of the simulation at the industrial scale

### 1.3.1 The industrial parts

Figure 4.5, the geometry of the four industrial tools studied here are depicted. The above presented medium scale press is a reduced model of the industrial tool 2 preserving the ratio of internal to external diameters. As for the medium scale tool, a pre-compaction step, where the part is compacted from one side, is followed by a main compaction with a double effect pressing.

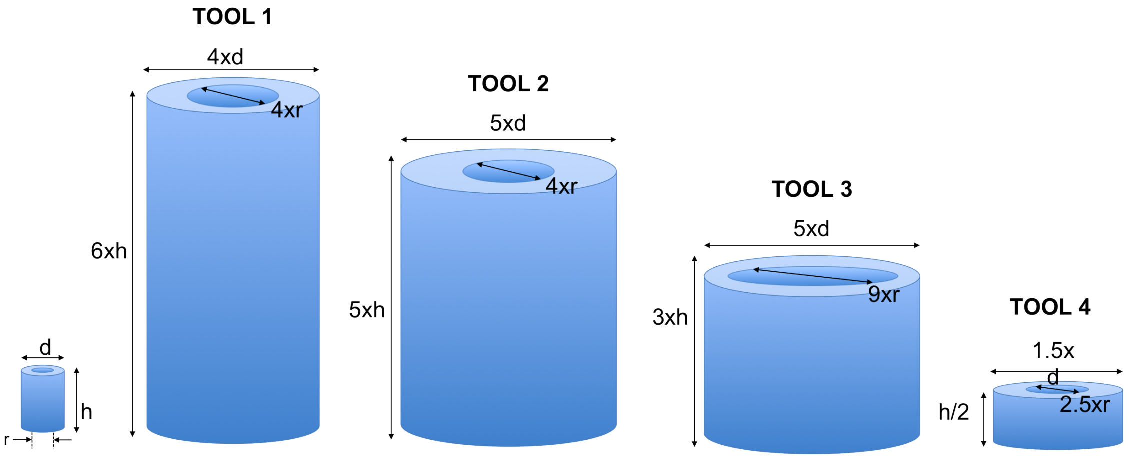

**Figure 4.5:** Geometry of the four industrial tools, compared to the medium scale tool (on the left)

### 1.3.2 Validation - comparison with the dimensions at the end of the two compaction steps

In the case of the industrial process, less experimental data are available due to the difficulty of instrumentation of the production line. However, the height of the billet at the end of the tool filling, at the end of the pre-compression step and of the main compaction step was measured for some billets. In table 4.1, comparison with the simulation results is reported for two tools and two materials. Displacements are normalized as a function of the initial height of the part. Standard deviations, as compared to the mean value, are given. At the end of the pre-compression the error is higher than the uncertainty of the measurement but acceptable. The prediction of the final height is considered satisfactory.

**Table 4.1:** Comparison of the height of the billet from the process and from the simulation. Measurement at the end of the pre-compaction step and of the main compaction. Results are normalized by the final height of the part.

| | TOOL | Material | Initial height | standard deviation (%) | Height after the pre compression | standard deviation (%) | Height at the end of the main step | standard deviation (%) | number of tests |
|---|---|---|---|---|---|---|---|---|---|
| Process | 2 | PTFE | 3,11 | 0,87 | 1,29 | 3,70 | 1 | 0,24 | 3 |
| Simulation | | | 3,13 | | 1,41 | | 1 | | |
| Difference (%) | | | -0,68 | | -9,07 | | 0 | | |
| | | | | | | | | | |
| Process | 1 | PTFE | 3,84 | NA | 1,24 | NA | 1 | NA | 1 |
| Simulation | | | 3,68 | | 1,23 | | 1 | | |
| Difference (%) | | | 4,20 | | 0,76 | | 0 | | |
| | | | | | | | | | |
| Process | 2 | PTFE+filler A | 3,15 | NA | 1,34 | NA | 1 | NA | 1 |
| Simulation | | | 3,17 | | 1,41 | | 1 | | |
| Difference (%) | | | -0,47 | | -5,28 | | 0 | | |
| | | | | | | | | | |
| Process | 1 | PTFE+filler A | 3,59 | 4,01 | 1,20 | 1,05 | 1 | 0,41 | 40 |
| Simulation | | | 3,58 | | 1,35 | | 1 | | |
| Difference (%) | | | 0,17 | | -12,24 | | 0 | | |

# 2 Influence of the process parameters

## 2.1 Influence of the double effect loading

The advantages of the double effect compaction is highlighted when looking at the density profile in the PTFE sample. In figure 4.6, the profile of density through the height of the billet, at mid-thickness, is followed from the end of the pre-compaction step to the end of the main compaction. At the end of the pre-compaction, a high gradient of density exists in the part due to the simple compaction. Part of the pressure exerted by the piston head is screened by wall friction. The bottom side is more compacted than the upper side. This inhomogeneity is corrected by the double effect compaction. As soon as the stress is applied from the top, the density of the loose part increases while the average density of the material goes up as shown in figure 4.6. Note that the gradient in the transverse direction and its variation through the height of the billet is negligible as compared to the gradient in the axial direction. Map of the deviatoric and volumetric part of the strain and stress tensors may be also observed both at the end of the pre-compression (figure 4.7) and of the main compression (figure 4.8). The benefit of the double effect compaction is highlighted by the better homogeneity of the loading inside the part after the main compression as compared to the state reached at the end of the pre-compression step. The applied pressure and thus the volumetric strain are smaller in the middle section of the part at the end of the main compaction step, due to the reduction in the compression stress caused by friction effect. The inhomogeneity of the deviatoric loading is decreased during the second stage of the loading but still non negligible. These data will be useful to link the sintering and compaction processes and to predict the final state of the part.

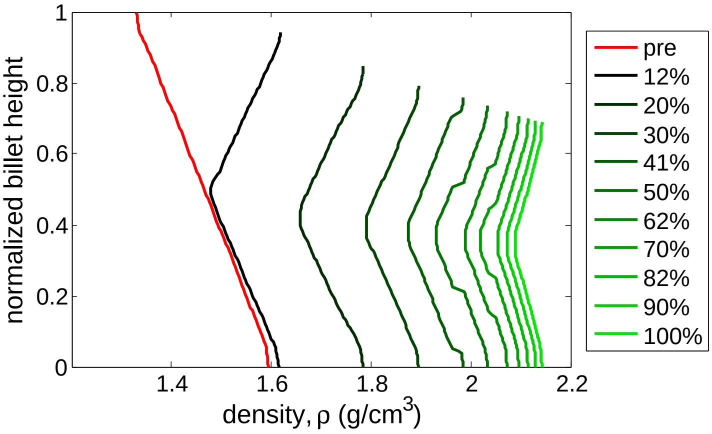

**Figure 4.6:** Evolution of the density field through the height of the billet as a function of the loading path. The density profiles are plotted for percentages of the maximal applied stress.

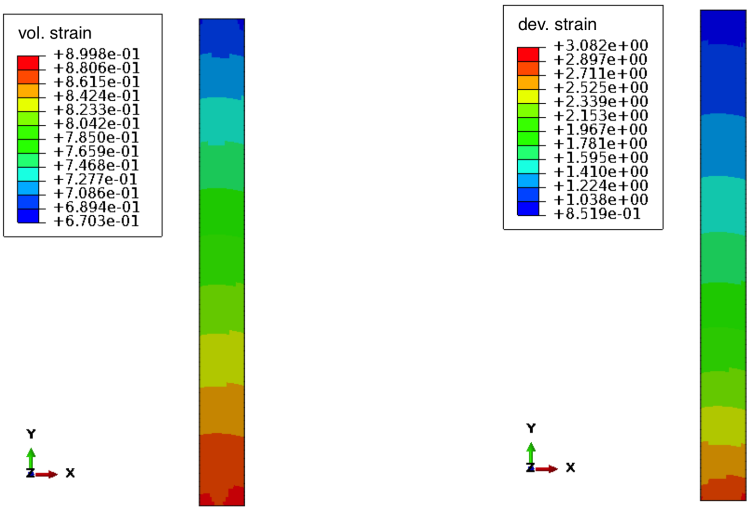

(a) Plastic volumetric strain (b) Plastic deviatoric strain

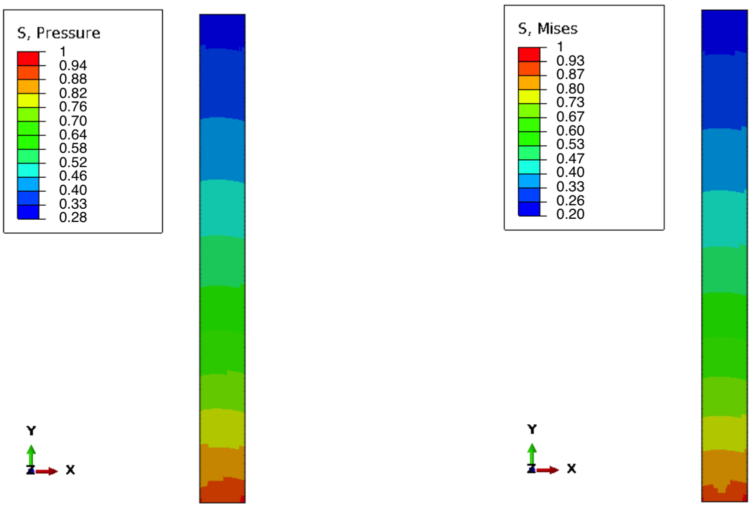

(c) Hydrostatic stress (d) Deviatoric stress

**Figure 4.7:** Map of the components of the stress and strain fields - End of the pre-compaction step

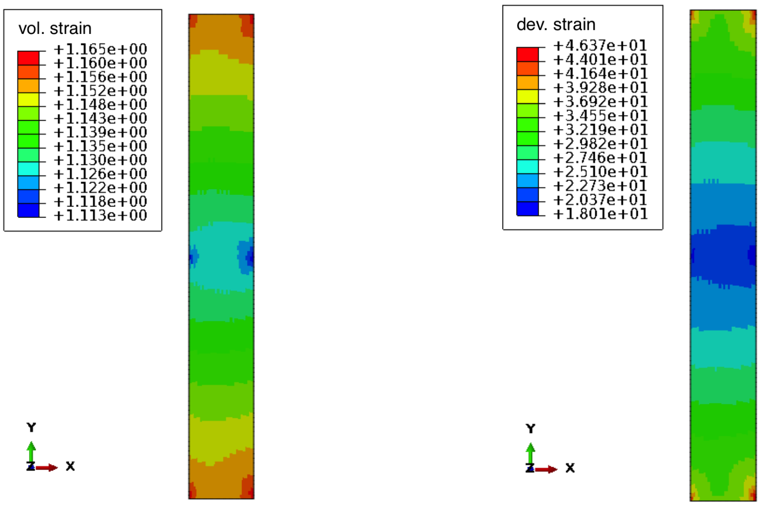

(a) Plastic volumetric strain (b) Plastic deviatoric strain

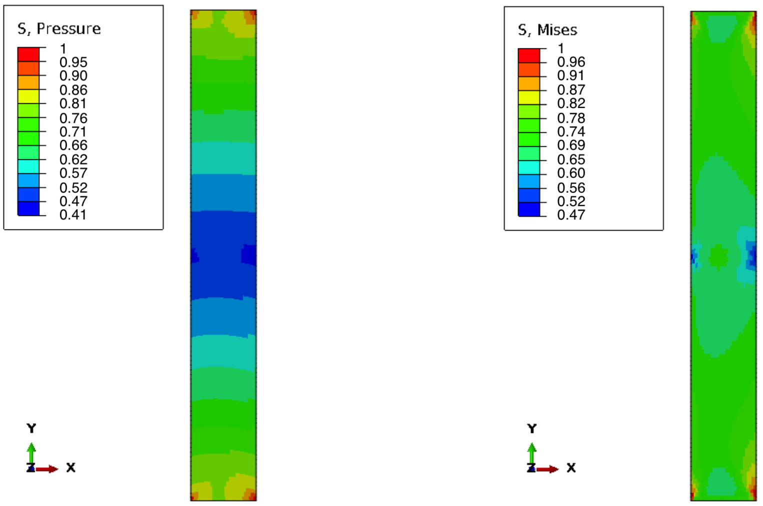

(c) Hydrostatic stress (d) Deviatoric stress

**Figure 4.8:** Map of the components of the stress and strain fields - End of the main compaction step

## 2.2 Influence of the loading path

The level of the maximal stress applied during the first pre-compaction has to be high enough to allow for higher stresses without servo-control problems but not too high so that the gradient of density at the end of the pre-compression may be ‘erased’ by the double effect main compaction.

Figure 4.9 presents the three different applied loading paths where the maximal level of applied stresses during the pre-compression and the main compaction are changed. The corresponding evolution of the density as a function of the average axial stress is shown. As expected, the higher the final stress, the higher the average final density (test C). It may also be concluded that if the level of the pre-compaction is too high, the final gradient of density may be drastically increased as shown by the results obtained for test B as compared to the profile obtained with test A. The profile of the loading path A seems to be the best choice to obtain the most homogeneous part.

Applying simultaneously the same stress from top and bottom sides does not compact the same way as applying a load from one side at a time. In figure 4.10, the loading is first applied from the top at a percentage of the maximal final stress. Then the maximal loading is applied from the opposite side. Here, the gradient of the final density profile is minimum if the same stress is applied for both steps of the compaction.

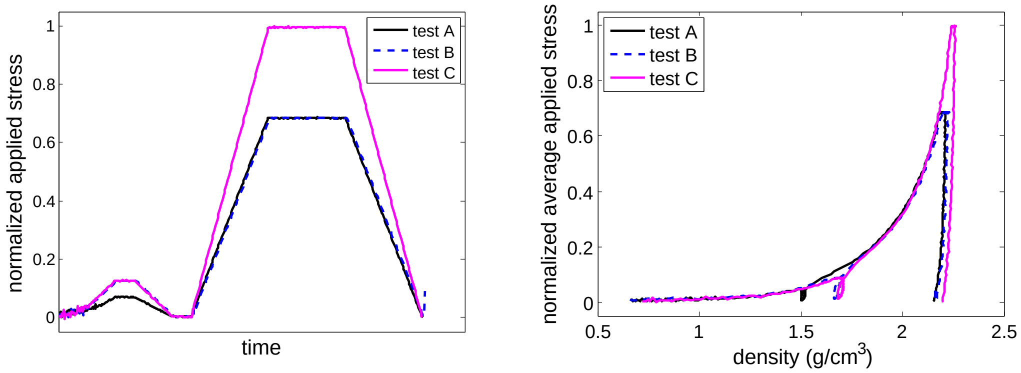

(a) Three studied loading cases

(b) Evolution of the stress versus the density

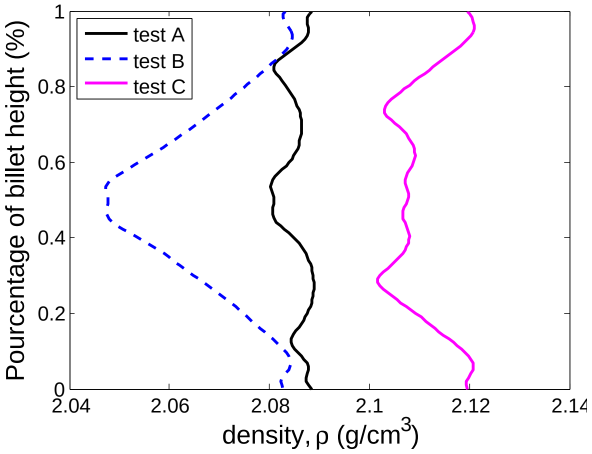

(c) Final profiles of density though the middle part of the wall

**Figure 4.9:** Influence of the level of the pre-compression stress with respect to the maximal applied stress of the main compaction. If the level of the pre-compression stress is too high as compared to the one of the main compaction, the homogeneity of density of the part is degraded.

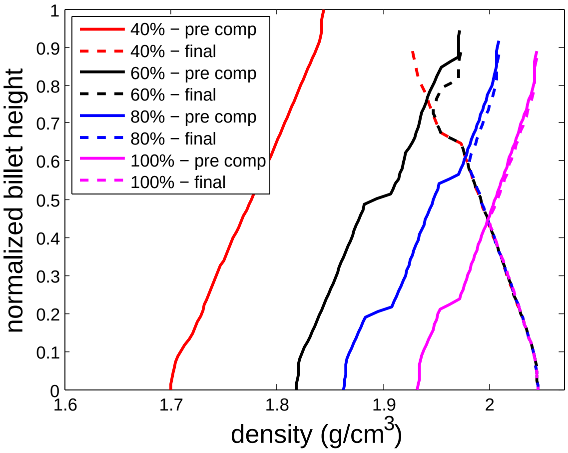

**Figure 4.10:** Here, the load is applied on one side at a time while the displacement is locked on the opposite side on tool 4. The density profile after the first loading step and at the end of the process are plotted. The influence of the percentage of applied compression during the first loading step is observed. It appears that the smaller gradient of density is achieved when the same stress is applied from the top and the bottom sides. But pre-compressions at 40 or 60% of maximal loading are almost equivalent to a simple effect compaction for PTFE+filler 1.

## 2.3 Influence of the geometry

**Is the scale up deemed satisfactory ?** When a replica of a process is made at a smaller size, the question of the representativity of the reduced model is raised. Figure 4.11, the final density profiles for tools 1 and 2 and the corresponding results obtained with medium size tool where the same loading paths (level of applied stresses) are applied on the same material (PTFE+filler1), are compared. Even if the same trends are observed when comparing tests A and C and tools 2 and 1 respectively (increase of the density and higher level of heterogeneity of density), the scale up is less representative in the case of the tool 1 where the mold dimensions are not an exact rescaling of the medium scale tool.

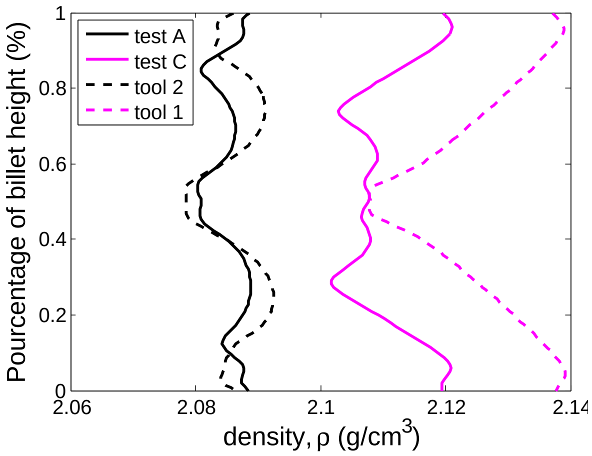

**Figure 4.11:** Comparison of the final density profile for process tools 1 and 2 and for medium scale parts obtained with profile A and C (A correspond to the loading paths of tool 2 and C to the loading path of tool 1)

**Comparison between tools 2 and 3** Figure 4.12, the density profiles obtained with the three tools are compared. The billet thickness in tool 3 is more than two times smaller to allow a better homogeneity of the temperature during the sintering step. This reduction of the section of the billet leads to a similar gradient of density as compared to tool 2 (figure 4.12). But stress and strain fields seen by the material during the compaction 4.13 are different. The average level of the deviatoric parts is higher. This may also have an incidence on the behavior of the specimen during the sintering step and on the properties of the final product.

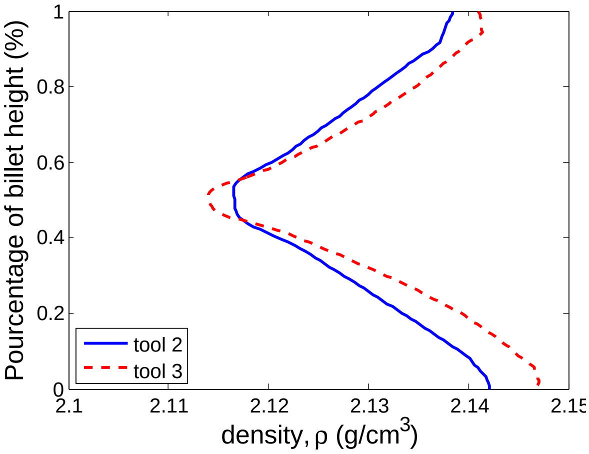

**Figure 4.12:** Comparison of the final density profile for tools 2 and 3. A similar gradient of density is obtained even if the geometry are different - virgin PTFE

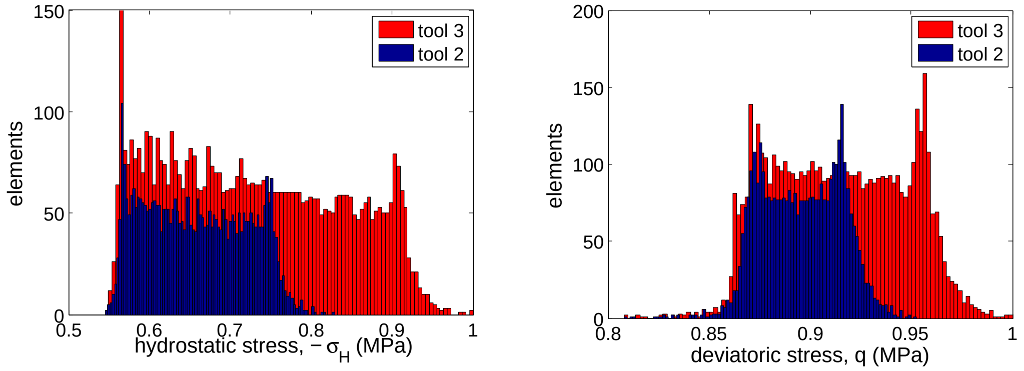

(a) Distribution of the hydrostatic stress through the section

(b) Distribution of the deviatoric stress through the section

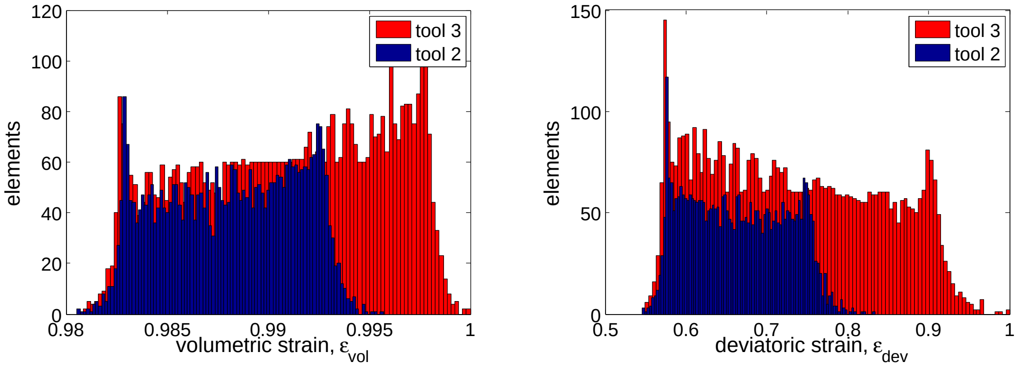

(c) Distribution of the volumetric strain through the section

(d) Distribution of the deviatoric strain through the section

**Figure 4.13:** Distribution of the stress and strain components through the section for tools 2 and 3 at the maximal loading stress.

## 2.4 Influence of the type of material

The loading path and the geometry have to be adapted to each material. Indeed, the benefit of the double side compaction highly depends on the type of material. To illustrate this point, we consider PTFE with different fillers in tool 4, and compaction on one side at a time. In figure 4.14, the final profiles of density through the height of the billet for both studied materials are compared. In the case of PTFE+filler 2, the gradient of density is almost twice smaller for the double side compaction as compared to single side compaction. The difference is not so important in the case of the PTFE+filler 1 material with the same compaction parameters.

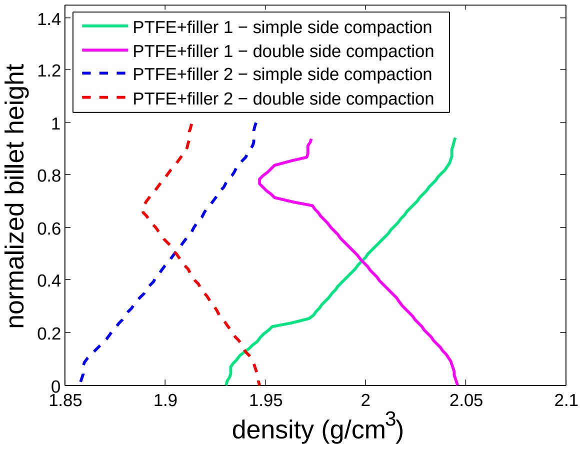

**Figure 4.14:** Final density profile, influence of the loading and the type of filler.

To conclude, the industrial process can be reproduced. Results are consistent. They are shown to be very dependent on the material, the billet geometry and the loading path (in particular homogeneity which is essential). Thus, a faithful and trustworthy modeling approach is the way to optimize the compaction process and tool geometry avoiding the very expensive ‘trials and errors’ route to progress.

# Chapter 5

# First links to the final properties of the billets

*In order to better understand the link between the compaction step and the properties obtained at the end of the sintering, XRD measurements are made on samples compacted through different loadings, before and after thermal treatment. Only qualitative observation may be done but a crystalline texture is visible and may be linked to the compaction load. This preferential crystalline orientation is also present in sintered samples.*

## Sommaire

In order to better understand the influence of the compaction step on the sintering stage in the process and on the final properties of the billet, as described in the introduction , XRD measurements are performed on both green and sintered parts, previously subjected to different compaction loadings. Indeed, mechanical loading may induce deformation and reorganization of the crystalline structure as observed in sintered PTFE samples in studies such as those of [Speerschneider et Li, 1963], [Wecker *et al.*, 1972] or [Young, 1975].

The experimental results of the following section were obtained during the Master 2 internship of Anna Trauth, student of the Master MAGIS within of a franco-german double degree with ENSAM Paristech and Karlsruher Institut für Technologie.

# 1 Variation of volume during the sintering step

Samples have been compacted through different loading paths as listed in table 5.1. For each case, two samples are made with the same loading path. One of the two samples is sintered and all the sintered samples have received the same thermal treatment, which is undisclosed here for confidentiality.

The influence of the green body void ratio on the density variation during sintering is shown in figure 5.1. After sintering, the crystalline volume fraction is lower than in the green part (or in the powder as the crystalline ratio is assumed not to be modified in this loading range) and thus the specific gravity of the material is lower. The initial crystalline ratio of the PTFE powder may never be reached again. All samples have received the same thermal treatment, and thus their final crystalline ratio is the same and, as voids close, the density is almost equal in each sample. Note that this means very different levels of deformation from one sample to the other. In the case of samples with heterogeneous density, this may lead to incompatible deformations and thereby high level of residual stresses.

In figure 5.2, measured length variations in all directions of the same samples are presented. The length variation is directly linked to the applied loading during the precompression step. Anisotropic deformations are measured on PTFE samples previously compacted under œdometric loading, whereas for samples compacted under hydrostatic loading, deformations are isotropic. The same trend as in [Canto *et al.*, 2011] is observed in the case of œdometric test. There is a small discrepancy between the two types of powder, which may be caused by the difference of geometry of the sample (a smaller die with a higher ratio between the height and the transverse dimensions is used in the case of PTFE B) and of thermal treatment. The larger the difference of applied loading in each direction, the higher the deformation anisotropy during sintering, as illustrated by the comparison between ‘œdometric’ samples and ‘three rate’ sample.

Anisotropy in compacted sample may be caused by geometrical effects, like for elongated particles which align in a preferential direction during compaction as shown in [Galen et Zavaliangos, 2005] or [Li et Puri, 1996] or in the case of ductile spherical particles which deform more in the direction of compaction ([Frachon, 2002]). In these studies, anisotropic behavior is evidenced and directly linked to the compaction loading.

Here, the geometry and the size of the particles of the fine cut resin and the pelletized one are very different while the influence of the compaction step on the anisotropy of the deformation during the sintering are similar. Geometry alone cannot be the principal reason for the anisotropy of the material.

**Table 5.1:** Compacted samples with various levels of final density and subjected to different loading cases. Two samples are tested for each compaction experiment out of which one is sintered.

| legend | type of loading | level of applied stress (MPa) |
|---|---|---|
| 16.3 | œdometric - 35 mm side square base die | 16.3 |
| 24.5 | œdometric - 35 mm side square base die | 24.5 |
| 32.7 | œdometric - 35 mm side square base die | 32.7 |
| 40.8 | œdometric - 35 mm side square base die | 40.8 |
| 49.0 | œdometric - 35 mm side square base die | 49.0 |
| three rate | ‘three rate’ loading applied in 3D compaction device | 31 |
| hydro | hydrostatic loading applied in 3D compaction device | 100 |

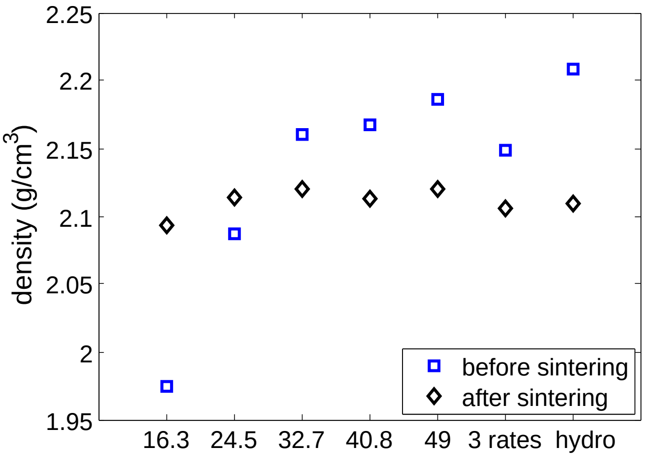

**Figure 5.1:** Comparison of the densities before and after sintering. The influence of the density of the green part is highlighted by comparing œdometric samples compacted with various level of applied stress (the legend is detailed in the table 5.1).

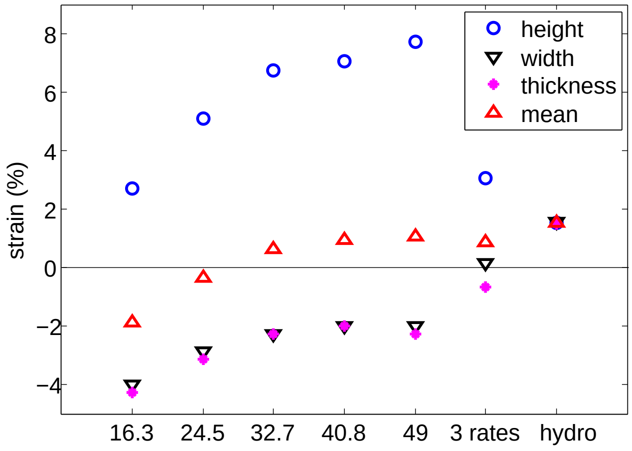

**Figure 5.2:** Length variations in the three directions after sintering. In the case of a sample compacted with a hydrostatic loading, the strains in each directions after sintering are equal. The sample may be considered as isotropic green part and remains isotropic after the sintering treatment. In the case of samples compacted with non isostatic loadings, the strains are anisotropic.

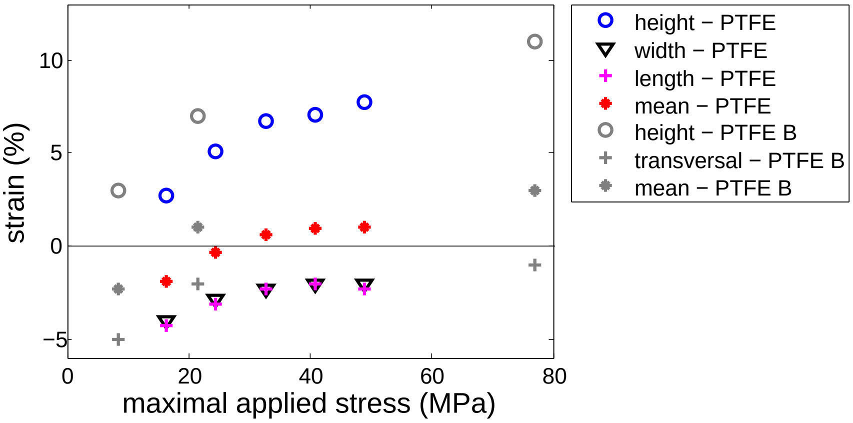

**Figure 5.3:** Strains at the end of the sintering step of samples compacted through œdometric loading at different level of maximal stress - Comparison between PTFE and PTFE B samples (from [Canto *et al.*, 2011])

# 2 XRD measurements

## 2.1 General overview

In contact with a material, X-rays induce an elastic displacement of the cloud of electrons with respect to the nucleus of the atom. Because of these induced oscillations, electro magnetic beams (with the same frequency) are scattered, which is referred to as the Rayleigh scattering. In the case of a crystalline lattice, at some specific angular orientations of the incident beam, scattered beams add up constructively to form a diffraction peak. Diffraction is obtained if the Bragg's law is followed :

$$2d_{hkl}\sin(\theta) = n\lambda \tag{5.1}$$

with $d_{hkl}$ lattice spacing between two scattering planes defined by Miller indices $hkl$, $\theta$ the Bragg's angle defined between the incident beam and the diffracting crystalline plane, $n$ an integer number and $\lambda$ the wavelength of the incident beam, as illustrated figure 5.4.

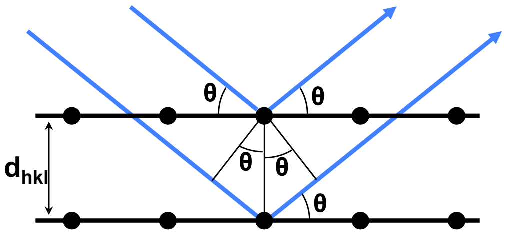

**Figure 5.4:** Bragg's law - Constructive interference occurs when beams approach a crystalline solid.

When a monochromatic X-ray beam hits a sample, a scattered signal may be measured and a diffraction pattern where the intensity of the signal is plotted as function of the angular position $2\theta$ is obtained. Semi-crystalline polymers consist of periodic arranged micro structure, the crystallite, and disordered or amorphous area. In this case, the diffraction pattern appears as a sum of (1) sharp peaks, which corresponds to the coherent diffraction of the crystalline structure, of (2) an amorphous halo, caused by the scattering of entangled macromolecular chains, and of (3) a non coherent scattering background. From this diffraction pattern, different informations may be deduced.

**Crystalline structure** The angular position of the sharp peaks is directly linked to the structure of the crystalline phase through the Bragg's law (equation 5.1). In the case of an hexagonal lattice, which is that of PTFE at ambient temperature and free of any mechanical loading (phase IV), the distance between the different diffracting planes is deduced from

$$d_{hkl} = \frac{a}{\sqrt{\frac{4}{3}(h^2+k^2+hk)+l^2\frac{a^2}{c^2}}} \tag{5.2}$$

where $a$ is the length of one edge of the hexagonal basis, $a$=0.566 nm and $c$, the length to complete one twist to the helical structure, $c$=1.95 nm ([Brown *et al.*, 2007]) and $h$, $k$ and $l$ the Miller indices, which reference the planes of the structure. The main diffracting planes of PTFE in phase IV are depicted on figure 5.5 (from [Brown *et al.*, 2008]). The theoretical positions of the peaks for Kα and Kβ radiations, which correspond to the different lattice planes, are listed table 5.2 (from [Cullity et Stock, 2001]).

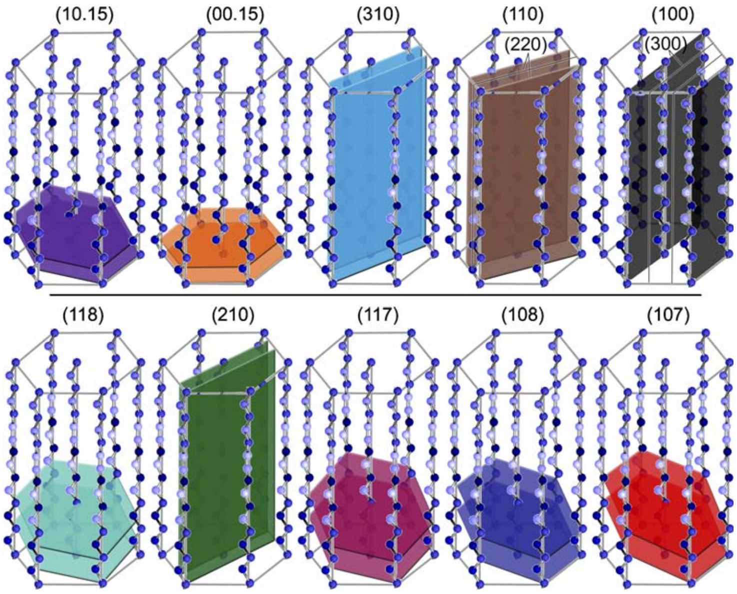

**Figure 5.5:** Principal diffracting planes of PTFE in phase IV, from [Brown *et al.*, 2008]

**Amorphous halo** In PTFE, a first amorphous halo is superimposed to the first (100) peak. A second amorphous halo appears around $2\theta=40°$ ([Lebedev *et al.*, 2010]). The crystalline ratio of a semi-crystalline material may be related to the ratio between the integrated part of the diffraction signal due to the crystalline phase and the integrated intensity of the whole signal ( [Hermans et Weidinger, 1961]). The relationship between intensity and ratio is identified from measurements of samples with different crystalline ratio. Several samples with various levels of crystallinity are required to scale the rule and thus precisely determined the shape of the amorphous halos.

**Orientation of the crystalline phase** In the case of an isotropic sample, the orientation of the crystalline structure is randomly distributed. Consequently, whatever the orientation of the incident angle, the diffracting pattern is the same. Now, if the material is textured, crystal lattice has preferred orientation and more or less planes diffract according to the orientation of the incident angle with respect to the orientation of the

**Table 5.2:** Theoretical position of the main diffracting peaks for PTFE in conformation IV - for cobalt target material used for the X-ray source (wavelength of 1.79$Å$)

| h | k | l | n | $d_{hkl}$ ($Å$) | 2θ - Kα (°) | 2θ - Kβ (°) |
|---|---|---|---|---|---|---|
| 1 | 0 | 0 | 1 | 4,90 | 21,03 | 19,03 |
| 1 | 0 | 0 | 2 | 4,90 | 42,81 | 36,62 |
| 1 | 0 | 0 | 3 | 4,90 | 66,38 | 59,47 |
| 1 | 1 | 0 | 1 | 2,83 | 36,85 | 33,28 |
| 1 | 1 | 0 | 2 | 2,83 | 78,42 | 69,88 |
| 1 | 0 | 7 | 1 | 2,42 | 43,35 | 39,10 |
| 1 | 1 | 7 | 1 | 1,99 | 53,56 | 48,18 |
| 1 | 0 | 8 | 1 | 2,18 | 48,39 | 43,59 |
| 1 | 1 | 8 | 1 | 1,85 | 57,94 | 52,05 |
| 2 | 1 | 0 | 1 | 1,85 | 57,74 | 51,88 |
| 3 | 1 | 0 | 1 | 1,36 | 82,29 | 73,18 |
| 0 | 0 | 15 | 1 | 1,30 | 86,95 | 77,13 |
| 1 | 0 | 15 | 1 | 1,26 | 90,77 | 80,32 |

sample. The orientation function of Hermans [Hermans *et al.*, 1948], initially developed for cellulose fibers, allows to quantify the degree of orientation of a sample.

This work is a first approach to the characterization of the crystalline texture of the green body and its evolution after the sintering step. A qualitative point of view is adopted, the main goal is to prove the presence of a crystalline texture induced by the compaction loading. The development of a specific experimental set up is presented in the next section.

## 2.2 Experimental set up

**Description of the diffractometer and experimental parameters** The X-ray diffractometer, available at the LMT-Cachan, was used. In the X-ray tube, the target material of the source is Cobalt material (the wavelength of the Kα ray is of 1.789Å). The angle of incidence of the source may be set through the upper goniometer and is equal here to the minimum value of 40°. Diffracted rays are measured thanks to the curved detector, INEL CPS 180, which has a radius of curvature of 180 mm and is divided into 4096 detector elements. Thus a large range of angular detection is covered (2θ range=120°).

The sample preparation from green PTFE compacts for transmission measurement is not possible here considering the available tools (circular saw, diamond saw, jet water cutting). It was not possible to machine thin enough sample with constant depth without damaging the material. So even if observation in reflection limits the range of observation, this second option is chosen. Transmission measurements are possible for sample of no more than 1 mm. The thickness of investigation in reflexion is thus estimated to be

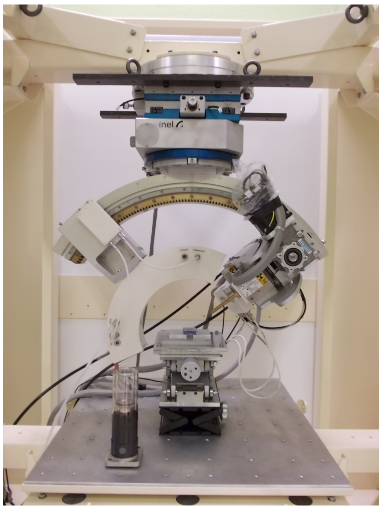

**Figure 5.6:** Picture of the diffractometer at the LMT-Cachan

between 0.2 - 0.25 mm.

To be able to measure the diffracted signal at small angles (the diffracted beam corresponding to the (100) plane remains inside the specimen as illustrated figure 5.7), the sample is tilted with an angle of 25° from the horizontal planes along the Y axis and placed close to the collimator so that the incident beam has a grazing incidence with respect to the surface of the material.

Considering that the purpose of the study is to characterize the texture of the material, it is commonly recommended to choose a large collimator so that the beam reaches several crystallites. On the other hand, at low angle of incidence, small diameter is preferred to avoid divergence of the beam. Finally a medium collimator is chosen with a diameter of 1 mm.

The parameters of the X-ray source are set to 30 kV and 30 mA with an acquisition time of 3 min to avoid any saturation effect.

**Calibration procedure** A specific procedure of calibration has been developed which is adapted to the non standard position of the sample. In a first trial, iron powder is placed on tilted plane, at the defined distance from the collimator and the detector as set for the PTFE samples (figure 5.7). Four diffracted peaks may be identified for the calibration after the scattered background being removed. However, no information is available for small angles with iron powder (the same problem is also encountered with titanium powder). To overcome the problem and to validate the procedure set in the laboratory, XRD tests on an ‘œdometric’ virgin PTFE green part are made on another device, a 4-axis X’Pert goniometer available at the laboratory PIMM, ENSAM Paritech (we are grateful to Olivier Zanellato for his kind and efficient assistance). Here, the sample can be positioned in the rotational center of the apparatus and thus the set up is completely calibrated. The velocity of the punctual sensor is set to 0,1°/20 sec and the

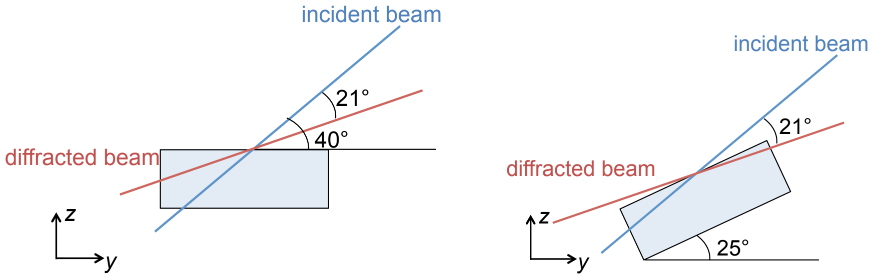

(a) Standard configuration - it is not possible to observe the first diffraction peak as the diffracted beam enters the sample

(b) 'Tilted' configuration with an angle of 25° from the direction of the incident beam

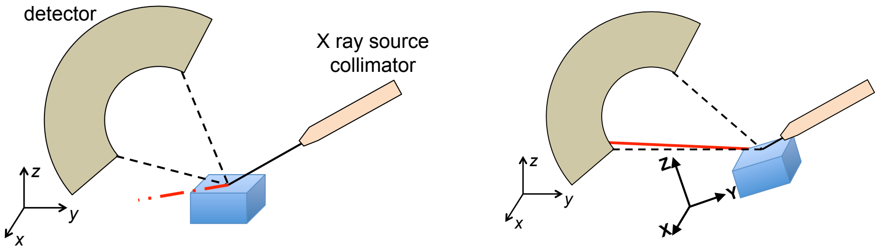

(c) Position of the sample at the geometrical center with respect to the sensor and the source - Standard configuration

(d) Current configuration - the sample is placed close to the collimator

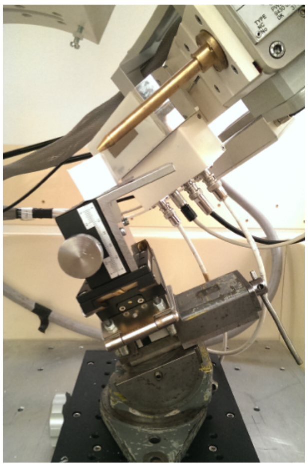

(e) Picture of the collimator and the positioned sample

**Figure 5.7:** Experimental configuration for XDR measurement.

diffractogram is scanned in the range of 2θ = 10° - 80°. With copper as target material (with a wavelength $\lambda = 1,54\AA$), the theoretical diffraction angles for PTFE (table 5.2) are favorably compared to the experimental values. This curve is now exploited, in addition to the identified peaks of the iron powder, to calibrate the experimental diffractogram obtained from the apparatus in LMT-Cachan. The obtained curves are shown in figure 5.8.

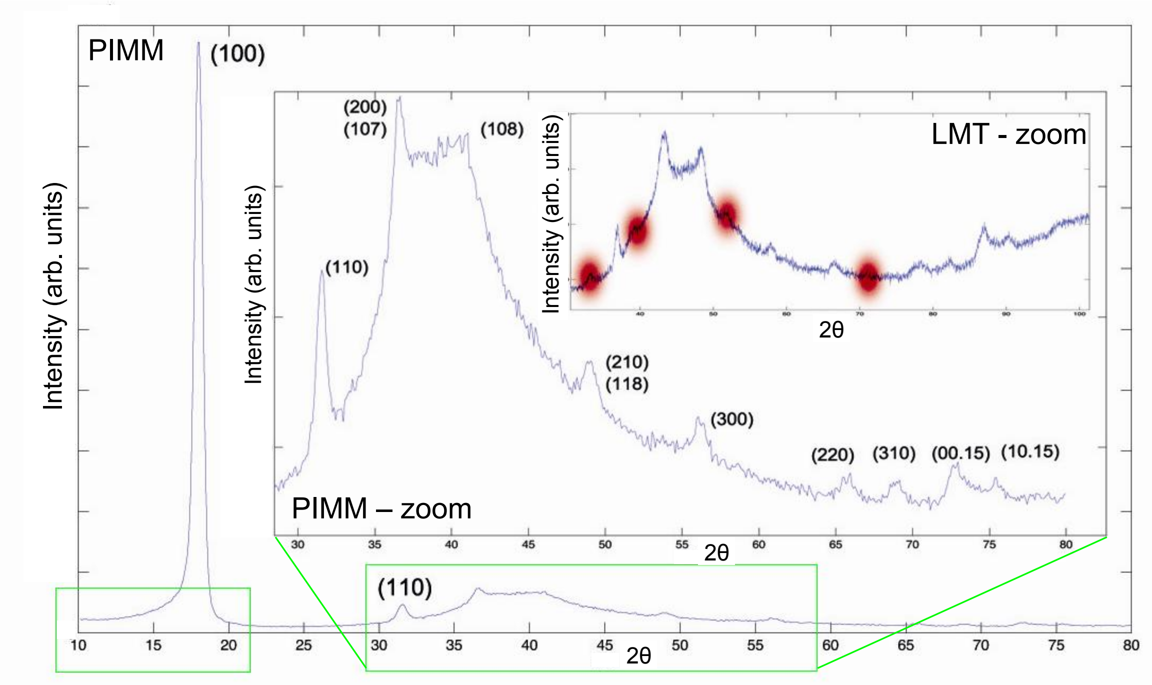

**Figure 5.8:** Indexing of the peaks with the Miller indices of the diffracting planes and comparison of the diffractograms obtained on both apparatus. The amorphous halos are marked in green. The Kβ radiations (highlighted in red) on the data from the diffractometer at the LMT-Cachan are visible as no monochromator is used. They are consistent with the theoretical values (table 5.2).

**Set up to measure the texture of the material** In order to characterize the crystalline texture, various rotations of the sample with respect to the incident beam are selected. As the sample is not placed in standard configuration, the automatic goniometer of the diffractometer cannot be used here. A dedicated rotation device has been set in order to apply a rotation keeping a constant distance from the sample to the collimator (figure 5.7). The coordinate system (X,Y,Z) is attached to the sample as presented figure 5.9. Because of the limited range of observation of small angles, rotation about the X axis is limited and does not enable texture analysis. Finally, rotations about the Y axis, with an amplitude of -40° to 40° to avoid distortion of the signal, and about the Z axis with no limitation in amplitude are possible.

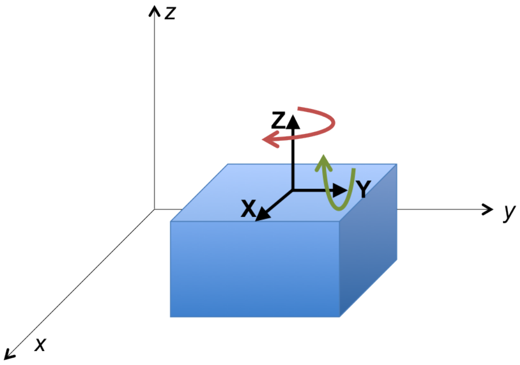

**Figure 5.9:** Rotations for the texture analysis

## 2.3 Approach

Because of the limitations induced by the properties of the PTFE and the diffractometer, partial pole figures may be constructed and allow for a qualitative characterization of the texture and its evolution respect to the compaction loading and the sintering treatment.

**Choice of the observed experimental data** Three rotations about the Z axis equal to $\omega_z$=0°, 45° and 90° coupled to 5 rotations about the Y axis equal to $\omega_y$=0°, 10°, 20°, 30° and 40° are performed. The symmetry of the results for negative values, particularly for the rotation about the Y axis, is verified.

To characterize the crystalline orientation of the lamellar crystallite, two planes are required. Not enough information is available concerning the amorphous halo around 40° (figure 5.8). So, as the amplitude and the shape of the halo is not known, it is not possible to extract with a sufficient level of accuracy the peaks in the range of 30 to 60°. Finally, peaks outside the area are chosen for this analysis. The principal peak around 21° (with Cobalt radiation) associated to the (100) plane and the peak around 87°, associated to the (00 15) plane which is almost basal, are considered here.

**Integrated intensity of the diffraction peaks** Integrated intensity of both peaks is calculated from their fitted curve. As proposed by Heuvel et al. [Heuvel *et al.*, 1976] and used by other authors such as [Marcellan, 2003] for PA66, a modified Lorentzian function, usually named Pearson VII, is chosen to fit the peaks

$$I(x) = \frac{I_0}{\left(1 + \left(\frac{x-x_0}{\Delta 2\theta}\right)^2 \left(2^{1/m} - 1\right)\right)^m} \tag{5.3}$$

with $I_0$ the intensity of the peak, $x_0$ the center position, $\Delta 2\theta$ the width at half maximum of the peak and $m$ a shape parameter, such as the curve tends to a Gaussian function when $m$ tends to the infinity and is equal to a Lorentz function if $m = 1$.

The non coherent background has to be uncorrelated from the peak signal. In the case of the (100) peak, the baseline is fitted with a third order polynomial function. For the part of the diffractogram behind the amorphous halo, the curve is initially fitted with a second order polynomial and subtracted to the fitted baseline to remove parts of the peaks whose variations are too large to be described by a second order polynomial. Parameters of the second order polynomial are adjusted until the baseline is fitted and uncorrelated from the contribution of the crystalline peaks.

Once the background is removed, (100) peaks are directly fitted with the function 5.3 with a parameter $m$ equal to 2. (00 15) peak is partially superimposed with the (10 15) peak. Both peaks are fitted simultaneously with the sum of two Pearson IV functions respectively centered on the position of each peak and with a parameter $m$ equal to 100.

**Choice of the presentation of the results** Experimental results are presented on Wulff's diagram after stereographic projection as illustrated in the figure 5.10 (raw data are also given in appendix E).

To map the Wulff's diagram, data are fitted with spherical harmonics. They are written in polar coordinates, as function of the angles $\theta$ and $\phi$ and are based on series of spherical harmonics.

$$f(\theta,\phi) = \Sigma_{l=0}^{\infty}\Sigma_{m=-l}^{l} C_l^m . Y_l^m(\theta,\phi) \tag{5.4}$$

where the spherical harmonic functions are written

$$Y_l^m(\theta,\phi) = \sqrt{\frac{2(l-m)!}{(l+m)!}} P_l^m(\cos\theta) e^{im\phi} \tag{5.5}$$

and the $P_l^m$ are Legendre's polynomials

$$P_l^m(x) = \frac{(-1)^m}{2^l l!}(1-x)^{m/2} \frac{\delta^{l+m}}{\delta x^{l+m}} \left((x^2-1)^l\right) \tag{5.6}$$

with $C_l^m$ coefficient, $l$ the degree and $m$ the azimuth order. An order of $l$=3 is considered to fit the available data. This treatment is made thanks to the MATLAB functions *getsh.m* and *leastsquaressht.m* developed by Archontis Politis.

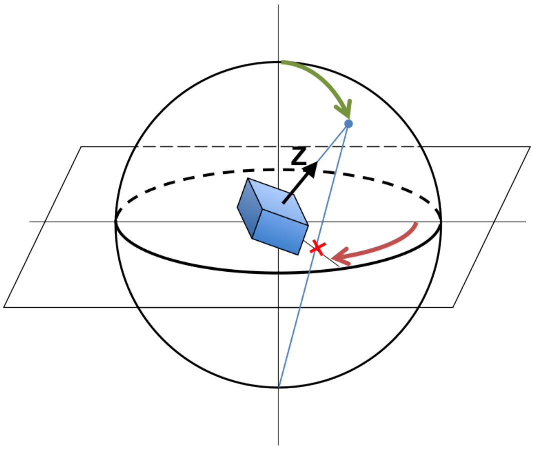

(a) Stereographic projection - the red arrow corresponds to the rotation through Z axis imposed to the sample and the green arrow to the rotation through Y axis

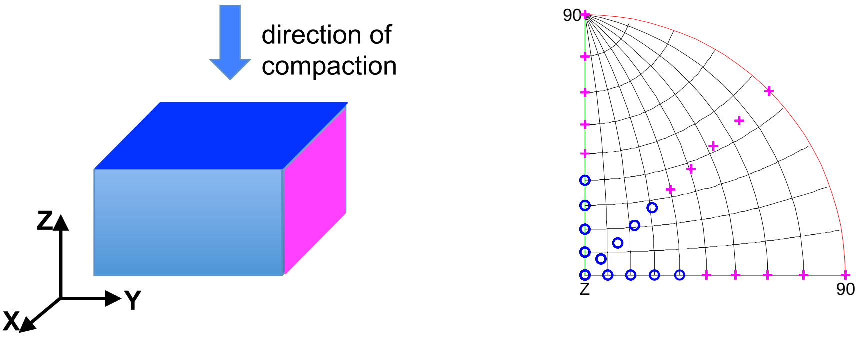

(b) Orientation of the axis as function of the direction of compaction

(c) First quarter of Wulff's diagram - Position of the measured points - blue circles are for face with normal parallel to the direction of compaction - magenta crosses are for face transverse to the direction of compaction

**Figure 5.10:** Representation of the experimental results - Stereographic projection

**Choice of the reference state** The as received PTFE powder is chosen as the reference pattern to evaluate the texture of the samples. The powder is placed in a PMMA blind hole of 20 mm and subjected to the previously described experimental tests. Obtained curves are presented figure 5.11. Integrated intensity of the (100) and (00 15) peaks are shown in figure 5.12. The powder may be considered as isotropic as the variation of the intensity is of the order of magnitude of the acquisition uncertainty (commonly considered equal to the square root of the measured intensity, Poisson's law). The average values of the integrated intensity of the (100) and (00 15) peaks are fixed and used to normalize the measured intensity as presented in figure 5.13. Results are also presented on Wulff's diagram in figure 5.13.

The density of the powder is 3 to 5 times smaller than the density of the compacted samples. This difference of density implies that fewer crystallites diffract in the case of the powder than in the case of green parts. The level of intensity for the same conditions of acquisition is smaller than for the material in its powder state. Comparison between the average intensity of each peak of the powder and the average intensity of each peak of the a sample compacted with an hydrostatic loading up to 100 MPa, assumed to be isotropic, gives a constant ratio $r_I = I_{powder}/I_{green} = 0.55$. This ratio is further considered fixed and multiplied with the average integrated intensity of the powder to normalize the subsequent measured intensities.

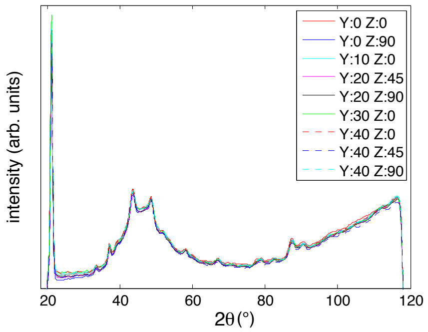

(a) Whole diffractogram

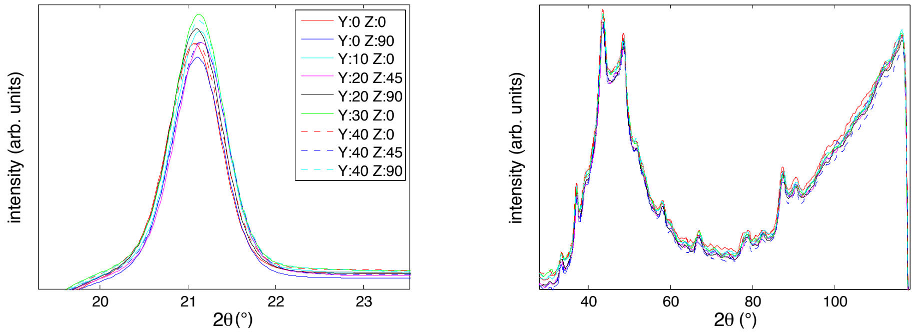

(b) Zoom on the principal peak (100)

(c) Zoom on the other peaks

**Figure 5.11:** Diffractogram for each tested position of the virgin powder.

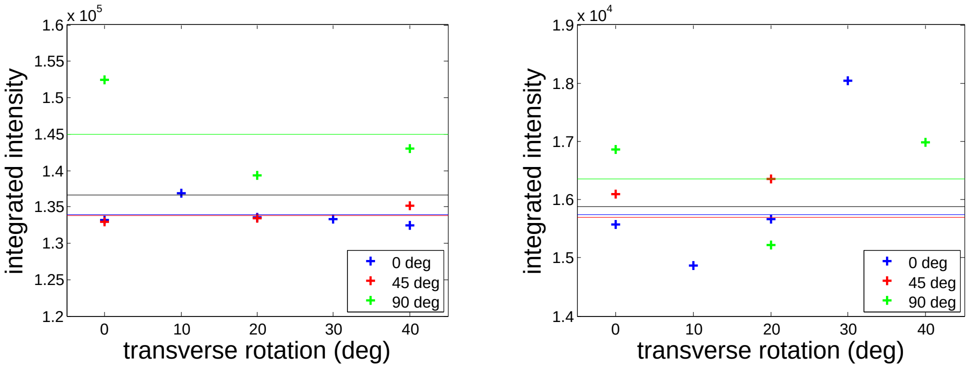

(a) Powder - (100)

(b) Powder - (00 15)

**Figure 5.12:** Integrated intensity - Powder - The variations of the intensities measured at different angular position may be considered as negligible with respect to the measurement uncertainty.

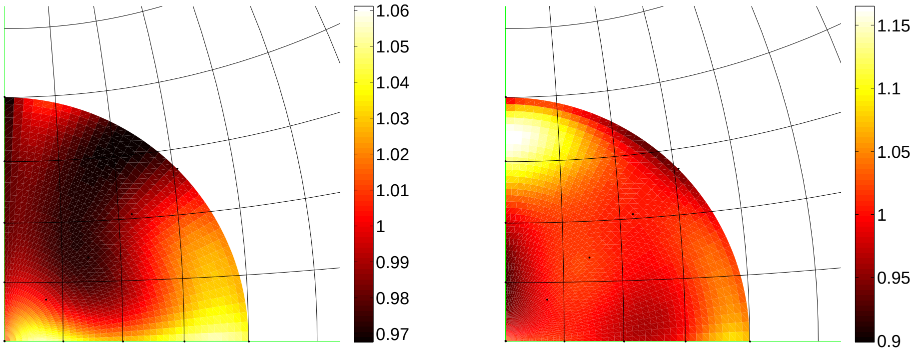

(a) Powder - (100)

(b) Powder - (00 15)

**Figure 5.13:** Wulff's Diagram - Relative intensity associated to the (100) and (00 15) peaks - Powder - The relative intensities are approximately equal to unity whatever the angular position, which reflects the isotropy of the powder. Note that for the ease of presentation, zoom on the area of interest is shown.

# 3 Analysis of the crystalline texture

## 3.1 Influence of shear on the crystalline texture of green parts

Samples, which have encountered different levels of deviatoric stress, are tested. Here the rotation along Z axis, $\omega_z$, is fixed and a rotation along Y axis, $\omega_y$, from 0 to 40° is performed. In figure 5.14, three samples are compared:

- a green part compacted through hydrostatic loading thanks to the 3D compaction tool in the ASTREE triaxial machine;
- a green part subjected to an ‘isodensity’ test in the same tool;
- a green part obtained by ‘biaxial extrusion’ of the powder.

For the last sample, the loading is not very well defined but the powder has been subjected to a high level of shear, extruded through a small gap of around 1 mm thick.

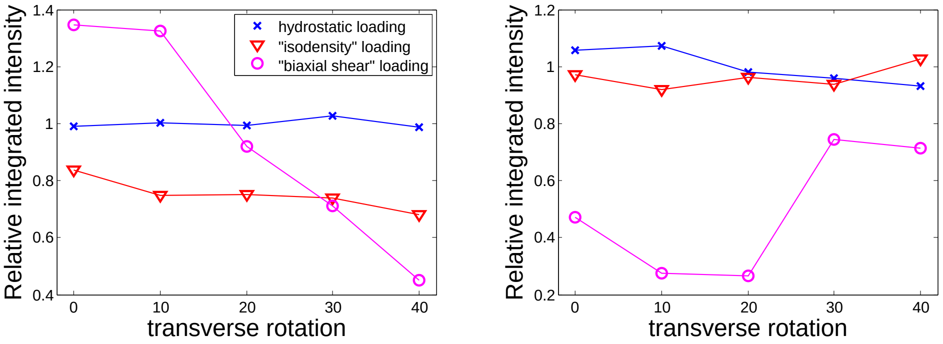

(a) Crystalline (100) plane (b) Crystalline (00 15) plane

**Figure 5.14:** Influence of shear loading on the crystalline texture. The external surfaces of the samples are tested in the three loading cases. Here, the time of acquisition is 7 min. The reference curve is obtained from the virgin powder subjected to the same conditions.

Sample compacted with hydrostatic loading may be considered as isotropic, considering the low fluctuation around unity of the data associated to the (100) and (00 15) planes. However, the variation of relative intensity is increased with the level of shear. If an isotropic orientation through the direction perpendicular to the ‘plane’ of extrusion is assumed and data obtained in the range of 0-40° are extrapolated to the area from 40 to 90 ° in order to have a consistent repartition of the crystallite (the integration through the domain of the relative integrated density has to be always equal to unity), it may be concluded that the majority of the (100) crystalline planes are parallel to the sample plane and that majority of the (00 15) crystalline planes are perpendicular to the same plane. That means that the hexagonal structure, and thus the crystallites, is oriented through a preferred direction as shown in figure 5.15.

For the ‘isodensity’ loading, the same trend is observed for the evolution of the integrated intensity with respect to the rotation but at a lower level.

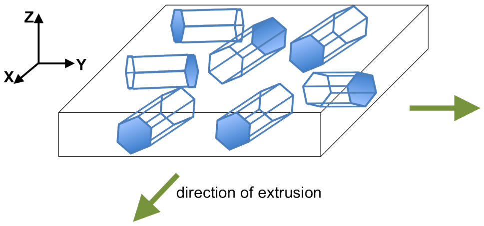

(a) Preferred orientation

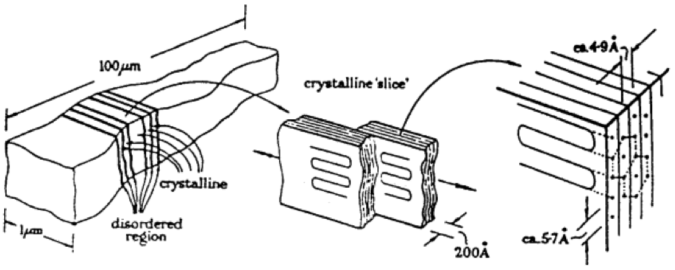

(b) Scheme of the PTFE structure from [Ebnesajjad, 2002] to remind the crystalline structure of PTFE

**Figure 5.15:** Preferred orientation of the crystallite in ‘biaxial shear’ sample.

## 3.2 Green parts compacted with an œdometric loading

Focus is now made on an œdometric sample compacted in a die with square section of 35 mm side. 45 g of powder are pressed with a maximal stress of 32.7 MPa at a displacement rate of 0.1 mm/s. Here, three surfaces are observed (figure 5.16):

- the upper surface, perpendicular to the direction of compaction, in contact with the piston;
- one of the exterior surfaces, whose normal is transversal to the direction of compaction, in contact with the die;
- a cut through the bulk. In the following we will denote this face of observation as ‘transversal bulk’. It is parallel to the previous one and obtained by cutting in half the sample by jet water (with the grateful help of Bruno Rondy and his team from 2R Industries). This technic allows to obtain a flat and perpendicular surface while the impact on the crystalline structure is minimized.

Experimental results, interpolated thanks to spherical harmonic functions as described in the previous section, are shown in the figure 5.17. Note that the accuracy of the measurements only allowes qualitative interpretation of the crystalline orientation.

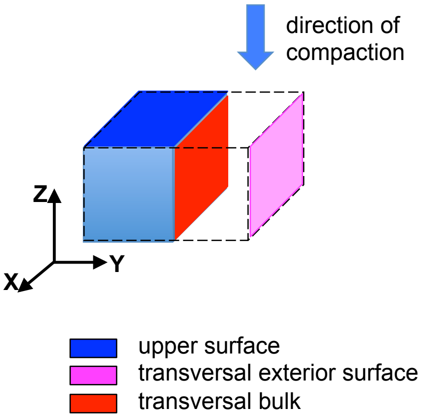

**Figure 5.16:** Observed surfaces of the sample compacted via œdometric loading

- **Upper surface (figures 5.17.a and .b)**: the relative integrated intensities for (100) and (00 15) planes seem to be independent from the rotation through the direction of compaction. The average level of intensity for (00 15) plane is relatively low. The intensity for (100) plane substantially decreases with the angle of rotation about the Y axis, $\omega_y$. These three points may lead to the conclusion that majority of the axes of the hexagonal structures are parallel to the surface. Thus, texture is not as high as for the 'sheared' sample, but the majority of the lamellar crystallite may be oriented perpendicularly to the surface of the upper face.

- **Transversal exterior surface (figures 5.17.c and .d)**: the average level of the intensity of the (100) plane is larger than 1. This means that the majority of the (100) planes are parallel to the surface of the mold. The intensity for $\omega_z = 90^\circ$ decreases with $\omega_y$ whereas it is the opposite trend for the directions $\omega_z = 0^\circ$ and $45^\circ$. Less (100) axes are perpendicular to the direction of compaction. More crystallite tends to align through the direction of compaction.

- **Transversal bulk (figures 5.17.e and .f)**: The intensities related to (100) and (00 15) planes are both closer to 1 compared to the other phases. A majority of (00 15) planes are parallel to the surface or perpendicular to the direction of compaction. It may be concluded that the majority of the crystallites is oriented perpendicularly to the direction of compaction here.

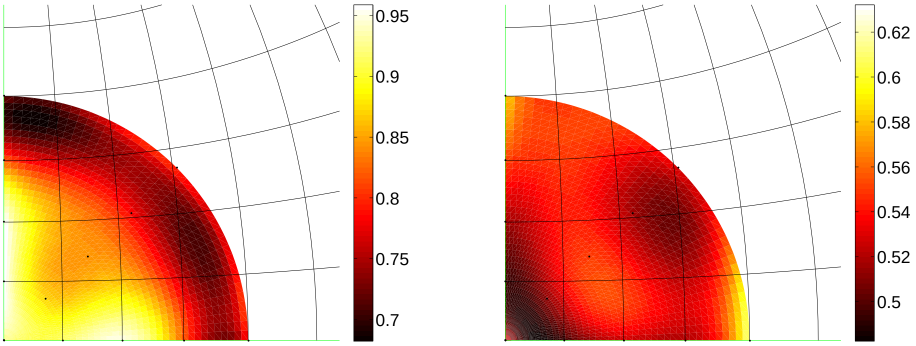

(a) upper surface - (100) - zoom (b) upper surface - (00 15) - zoom

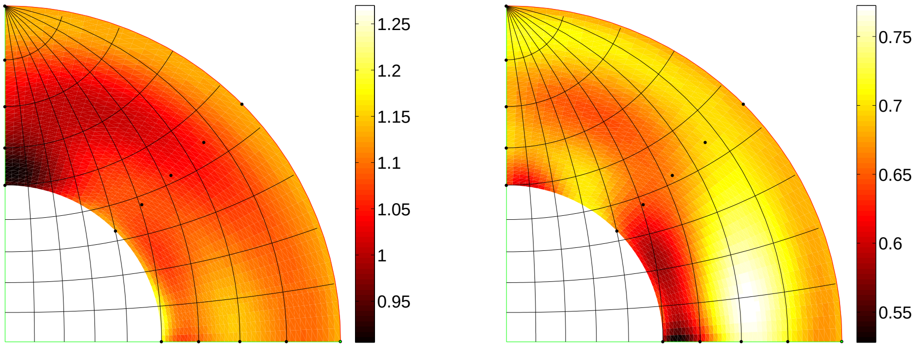

(c) transversal exterior surface - (100) (d) transversal exterior surface - (00 15)

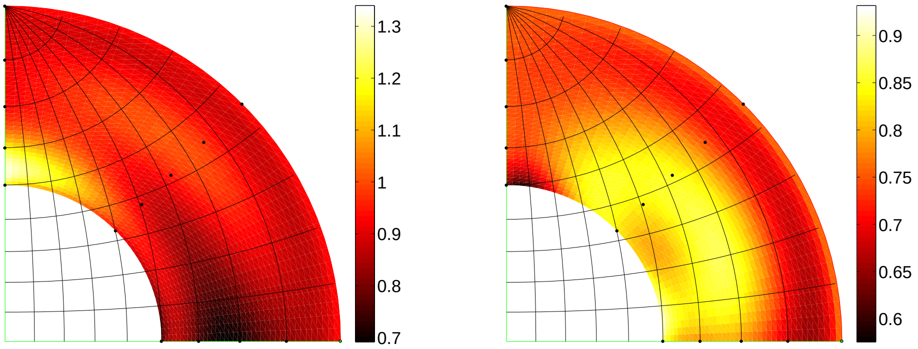

(e) transversal bulk - (100) (f) transversal bulk - (00 15)

**Figure 5.17:** Wulff's diagram - relative integrated intensities corresponding to (100) and (00 15) planes on the three different surfaces - œdometric sample compacted with a maximal applied stress of 32.7 MPa at a displacement rate of 0.1 mm/s

Figure 5.18 summarizes the deduced conclusions from the analysis of the pole figures. The preferred crystalline orientation are schematically represented. Let us stress that the experimental information on the crystalline texture is not complete. Moreover the sample is not fully textured, only the most probable orientations are represented.

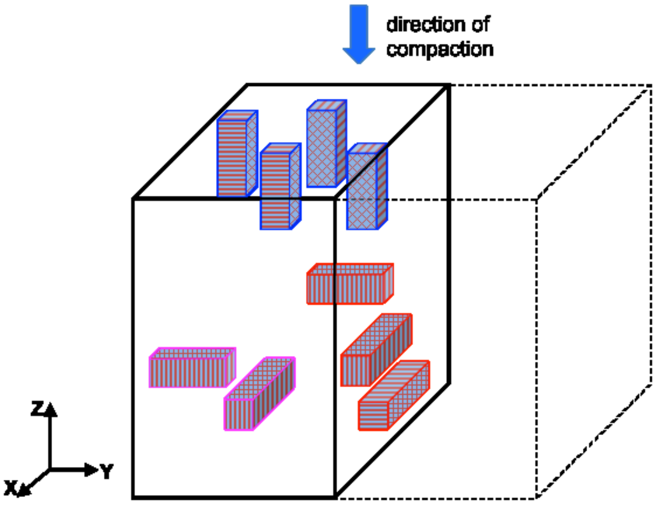

**Figure 5.18:** Schematic representation of the proposed preferred crystalline orientation on the upper surface (blue crystallites), the exterior surface (pink crystallites) and the transversal bulk (red crystallites)

## 3.3 Influence of the sintering step - comparison of the samples before and after sintering

An œdometric sample, compacted in the same conditions than the specimen studied in the previous section and sintered is tested and analyzed with the same procedure.

In figure 5.19, diffractograms representative of the diffraction of the material before the sintering step and after are compared. First of all, the crystalline structure seems to be unchanged. The peaks may be indexed the same way and one recovers the amorphous halos. Distinct patterns between the external surfaces and the inside of the sample are observed. The ratio between the intensity of the principal peak and the amorphous part of the pattern is higher for the exterior surface than for the inner one and is equivalent to the ratio found for the green sample. This is consistent with data found in the literature ([Rae et Dattelbaum, 2004]). A skin effect appears as chains on the external surface are free to align along the external surface. Crystallinity is less hindered than in the bulk. Note that measuring the crystalline ratio from the exterior surface of a sample overestimates the crystalline fraction because of this particular texture. For the inner surface of the sample, the ratio between the principal peaks and area around the amorphous halo (around 40°)

is smaller after the sintering than before. This is consistent with a smaller crystalline rate after the thermal treatment.

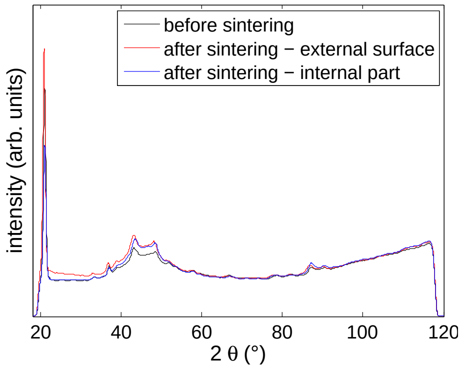

(a) Diffractogram pattern

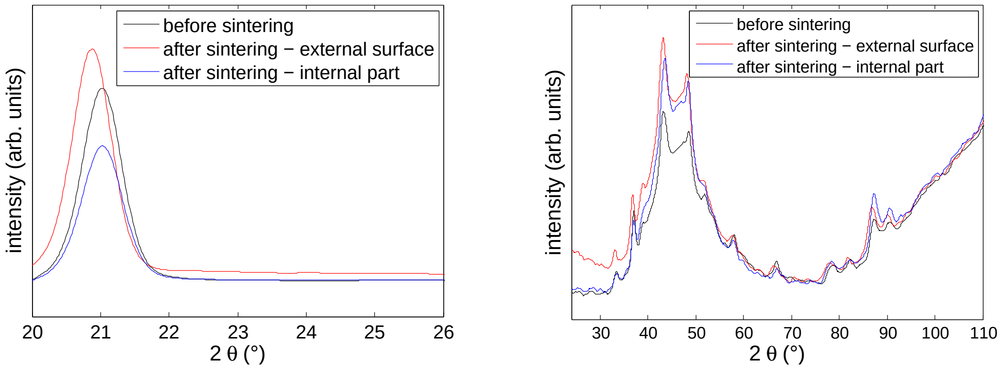

(b) Zoom on the principal peak

(c) Zoom on the second part of the diffractogram

**Figure 5.19:** Comparison between diffractogram patterns obtained before and after the sintering step on œdometric samples. After the sintering step, measurements made on the surface and in the bulk of the material reveal different.

The integrated intensity of each peak is also compared to the intensity measured for the powder. To take into account the decrease of crystallinity after the thermal treatment, the ratio of the crystalline fraction of the sintered sample to the non sintered one is multiplied by the density ratio between the powder and the green part. Relative integrated intensities measured on the three faces of the sintered œdometric sample are presented on Wulff's diagram figure 5.20. Note that here again, trends are reproducible from a sample to the other but levels of intensity are not accurate enough to allow for quantitative analysis. However preliminary conclusions may be proposed :

- **Upper surface (figures 5.20.a and .b**: first, the high intensity observed at $\omega_z = 45^\circ$ is not necessarily meaningful as it is not observed for other sintered samples. This point aside, the sintered sample shares with the green sample most of the above reported observations. Crystallites seem to be oriented the same way before and after the thermal treatment.

- **Transversal exterior surface (figures 5.20.c and .d**: a very high intensity related to (100) plane and a much lower one for (00 15) is measured. Then the intensity of (100) plane decreases as a function of $\omega_z$ while it increases for (00 15) plane. The crystallites seem to be aligned in the same preferred orientation as for the pre-compacted sample and the texture seems to be enhanced when the material is sintered.
- **Transversal bulk (figures 5.20.e and .f**: The decrease of the intensity diffracted by the (00 15) planes when the sample is tilted about the Y axis and the high intensity for $\omega_z = 0^\circ$ indicate that a majority of the basal planes is parallel to the surface of the material. This observation is strengthened by the opposite trend observed on the intensities diffracted by the (100) plane. The axis of the crystallites, defined as the axis through the larger dimension, is preferably oriented parallel to the surface of the inner surface, but it is not possible to conclude on a preferential direction with respect to the direction of compaction. Note that here the surface has been cut with a circular saw that may change the crystalline orientation of the part more than with the water jet technic.

To conclude, even if more measurements are required to better characterize the crystalline texture of PTFE samples, it seems that the initial texture induced by the œdometric loading is not erased by the sintering step as the same trends are observed before and after the sintering step.

Two other samples, compacted with a maximal applied stress of 40 MPa or a displacement rate of 1 mm/s, are partially characterized (presented in appendix E). Only measurements on the upper surface have been performed. No significant differences are observed with respect to the above presented sample.

These first data have to be confirmed by subsequent measurements but they give first clues to describe the mechanisms involved in the compaction of PTFE powder at the level of crystalline structure and their influence on the sintering step.

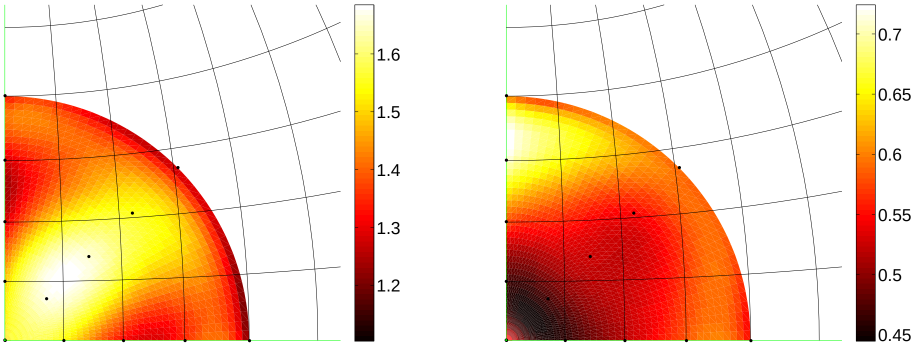

(a) upper surface - (100) - zoom (b) upper surface - (00 15) - zoom

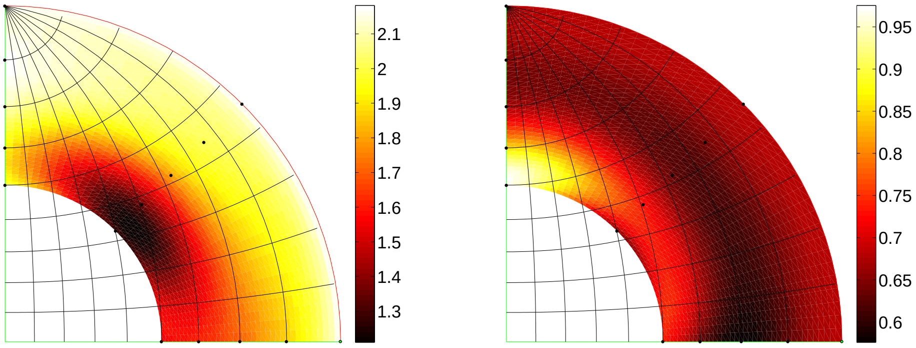

(c) transversal exterior surface - (100) (d) transversal exterior surface - (00 15)

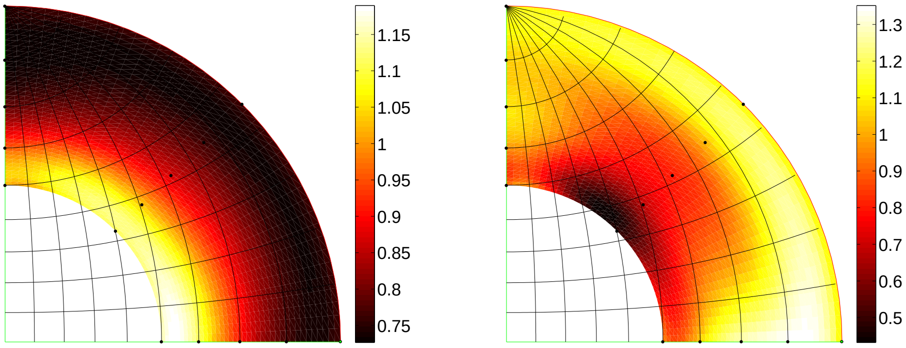

(e) transversal interior surface - (100) (f) transversal interior surface - (00 15)

**Figure 5.20:** Wulff's diagram - relative integrated intensities corresponding to (100) and (00 15) planes on the three different surfaces - Sintered œdometric sample compacted with a maximal applied stress of 32.7 MPa at a displacement rate of 0.1 mm/s

# Conclusion

The aim of this work was to propose a modeling of the mechanical behavior of PTFE powders during their industrial pressing in big billets in order to be able to predict the properties of the obtained green parts and to have a reliable tool to optimize the parameters of the process. PTFE is an original polymer with many unique properties and dedicated manufacturing processes which have not been well documented in the literature as compared to other polymers. In this work, we tackled different aspects of the problem to fulfill the objectives of this study.

In a first part, the characterization of the mechanical behavior of the PTFE powder is proposed. In the industrial context, complex loadings are applied to the material, from mostly hydrostatic pressing to simple shear near the wall of the mold. To predict such behavior and the associated properties of the material thanks to FE simulation, the Drucker-Prager/cap model has been chosen. It offers the possibility to describe the behavior of the material and the evolution of its properties from the low density powder, whose definition is tricky due to its high sensitivity to preparation and low loading, to the fully compacted material, the reference state, for which the void ratio is null. Large deformations and relatively high stresses may be reached in the part. All the parameters of the model and their evolution with the void ratio are identified. The influence of the size of the particles and the compounding with fillers is investigated by the characterization of four different powders. In addition to the elastoplastic model, a phase transformation in the crystalline structure at ambient temperature under pressure is experimentally characterized, modeled and implemented in the FE code.

To identify the parameters of the model, an original 3D compaction tool, installed in the triaxial machine ASTREE, allows for the application of complex loading paths from which the properties of the material and their evolution with the void ratio may be identified. Instrumentation is added to accurately measure the large dimension variation of the sample while it is adapted to the narrow available space. The triaxial device has some weaknesses : because of the interaction between the mold and the sample, a rotational movement inside the tested sample is induced. FE simulations of the whole device during test on PTFE sample shows that parameters identification can nevertheless be extracted reliably.

After the description of the behavior of the bulk material, the interaction of the PTFE with a metallic counterpart is modeled. The PTFE is known for being the polymer that forms the best transfer film in the shortest sliding distance. Thus the interaction between the PTFE and the contacting material is seen as a friction between the PTFE transfer film and the bulk PTFE, characterized by the internal friction coefficient of the Drucker-Prager line once the cohesion of the material is reached. No additional parameter needs to be identified.

A particular attention is paid on the validation of the identified model. The proposed model is validated through different tests and at different scales. An original compaction device, namely ‘V tool’, has been developed to apply complex loading paths thanks to a section reduction of the die, to measure the applied and transmitted stresses and to follow the internal displacement field of the powder during its compaction thanks to DIC. A good agreement is found between the experimental results and the FE simulation, where complete displacement field may be compared. Compactions in a classical instrumented circular œdometric compaction tool are also performed. The comparison of the experimental data with the simulation is satisfactory for the loading part of the tests but the limitations of the model are highlighted with the results obtained during the unloading and the ejection of the parts. These differences of behavior are suggested to result from the anisotropy of the material that appears during the uniaxial compaction and that is not accounted for. The compaction is well described but if a loading is applied in another direction than the direction of compaction, anisotropy should be taken into account. Further the model is also validated at the scale of the industrial part where good agreements are found between the available data and the simulation during the compression step. The up scaling is good. Note that additional measurement on the industrial part could provide useful data to complete the validation (measurement of the gradient of density, detection of the cracks, measurement of the residual stresses, of the elastic properties of the material...) even if non destructive experimental technics such as ultrasound are difficult to set and that the difficulty to machine green part render characterization tests uneasy.

Finally the first links between the compaction and the next steps of the industrial process are observed. Variation of the dimensions after sintering of samples which were compacted through different loading paths, confirms the influence of the anisotropy created during the compaction step on the sintering and the final properties. To explain this phenomenon, XRD measurements are made on green parts and sintered samples. The creation of a crystalline texture in œdometric samples and its preservation after the sintering step is evidenced.

The present work provides a reliable description of the behavior of the material during its pressing. Prediction of the properties of the green part as a function of the geometry of the tool and the loading path and depending on the type of material is now possible, which allows the optimization of the process respect to these parameters.

Some points are discussed but not deeply investigated although they would deserve it:

- more accurate loadings (for ‘isopressure’ and ‘isodensity’ tests for instance) and more complex paths would be possible by setting the control loop of the triaxial machine based on the pressure sensors and the laser displacement probes. This will require some experimental development to prevent any security and damage risks.

- the dependence on time of the behavior of the PTFE powder has been highlighted and a visco plastic law has been identified. More complex tests could be done to make the distinction between the viscosity of the PTFE itself and the effect of the escape of the air (compaction in airtight tool; several relaxation steps (after outgazing, the material is loaded again and relaxed, assuming that less or no air is present during the second relaxation step); evidence of the outflow of air if size effects are visible). This is required to optimize the relaxation step and the rate of loading of the industrial process.

- the dependence on the rate of loading of the crystalline phase change should also be characterized. Thermal (DSC, dilatometry) and mechanical tests at different speeds should be performed. Additional cyclic loadings will give more information on the irreversibility. XRD measurements under loading could also help to better characterize this phenomenon. The influence of the crystalline content and the anisotropy would be an interesting point to focus on.

- the importance of the anisotropy of the behavior of the material (particularly for the description of the ejection step) has been evidenced. But it will require an additional considerable amount of effort to be taken into account in the modeling of the compaction stage. Firstly, the anisotropy should be accurately characterized: œdometric followed by hydrostatic loading/unloading or ‘isodensity’ loading/unloading tests with a modification of the direction of the increase of the displacement for instance could be done in the 3D compaction tool. To do so, a modification of the geometry of the triaxial device or the design of an external œdometric tool would be required in order to test big enough anisotropic samples. Depending on the level of the anisotropy and its evolution as a function of the void ratio, new 3D constitutive laws could be implemented.

The ‘V tool’ offers interesting perspectives. An inverse identification procedure has been adapted to this test and the complex material model but it still needs some development. The main barrier is the non-homogeneous initial state of the material after filling of the mold. More robust experimental and identification procedures need to be developed. In situ X-ray radiography observations coupled to DIC could help to solve this problem.

The next obvious step of this study will be the study of the sintering of the PTFE green part, for which the same strategy could be followed: experimental characterization of the thermo-physico-mechanical coupling which takes place during the thermal expansion, the melt and the re crystallization of the material; modeling of these different phenomena; validation at the industrial scale after implementation in FE code. This will be the subject of a next PhD study.

# Appendix A

# Calibration of the pressure sensors

Each block is calibrated independently under an uniaxial compression machine (figure A.1). The link between the applied stress σ and the strain gauge signal $U$ may be easily calculated : $U = k.\sigma.\frac{S_2}{S_1}.\frac{1}{E}$ with $k$ the factor of amplification signal of the Wheastone bridge equal to $\sim$1600, $S_1$ the section of the reduced part of the sample, $S_2$ the section of the upper part of the sensor, $E$ the Young's modulus of the steel equal 180MPa for soft steel. The factor of amplification and the reduction of section of the pressure sensor are chosen to optimize the range of the strain gauge signal in volts compared to the range of measured stresses. At 100 MPa, a signal of 2 V in recored.

Figure A.2 provides an example of the chosen results for the calibration of the block CD3. The measured gain of each blocks is given in figure A.2.b.

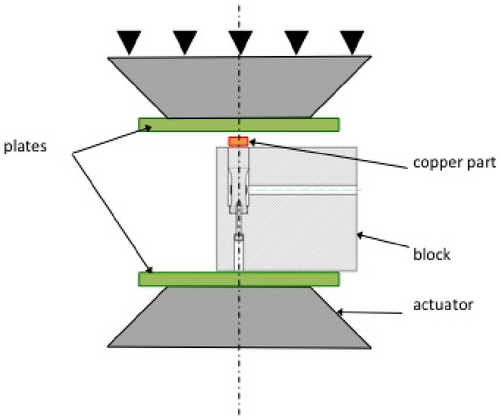

**Figure A.1:** Pressure sensor calibration set up. A uniaxial compression loading, with successive loading/unloading, is applied while the signal of the strain gauge is recorded. To apply a uniform force on the sensor, a cylindrical copper part slightly smaller than the pressure sensor is placed in front of it. Copper was chosen not to damage the block during the loading.

Note that the reponse of the pressure sensors presents a slight hysteresis which may be mainly attributed to frictional contacts inside the system, caused for instance by accumulation of dust inside the gap between the pin and the block. To quantify the influence

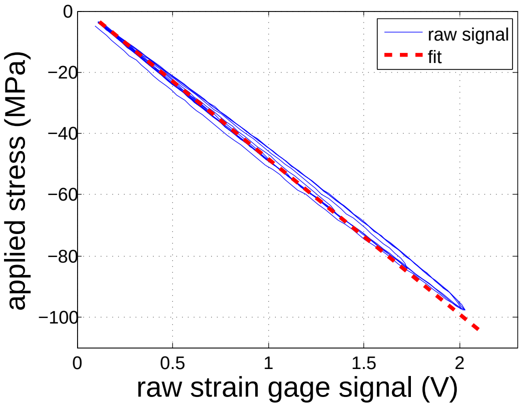

(a) Pressure sensor calibration - calibration of the pressure sensor of the CD3 block

| block | gain (MPa/V) | standard deviation |
|---|---|---|
| AB1 | 52.152 | 1.26 |
| CD1 | 50.899 | 1.39 |
| AB2 | 52.091 | 0.74 |
| CD2 | 53.246 | 1.12 |
| AB3 | 51.959 | 1.20 |
| CD3 | 50.600 | 1.01 |

(b) Gain of the pressure sensors after calibration

**Figure A.2:** Results of the calibration of the pressure sensors

of this hysteric behavior of the pressure sensors on the experimental results of the 3D compaction tests, the hysteresis behavior of each pressure sensor is simulated as shown figure A.3.a, by adding a Coulomb friction component. Then, the reponse of the material where the hysteric behavior of the pressure sensors is taken into account is compared to an ideal behavior (where a constant gain of the pressure sensors) is assumed. One example is given figure A.3.b where the two results are compared in the case of an hydrostatic test with successive loading/unloading in the $(-\varepsilon_{vol}, -\sigma_H)$ plane. The difference on the measured stresses with the two simulations of the pressure sensors behavior is less than 0.7%. This bias of the pressure sensor is finally assumed to be negligible.

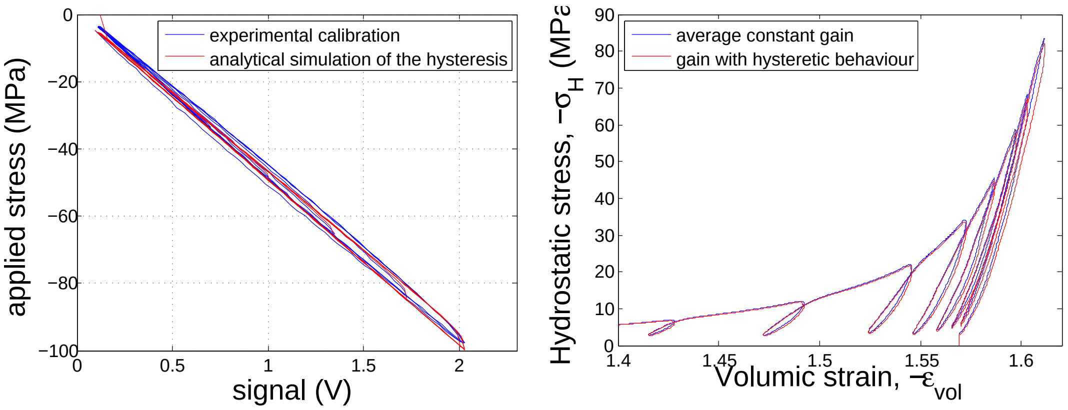

(a) simulation on one of the pressure sensor

(b) hydrostatic test - zoom on the loading/unloading steps

**Figure A.3:** Simulation of the hysteresis and influence of the phenomenon on the hydrostatic stress measured during an hydrostatic test

# Appendix B

# Choice of the laser probes and validation of the specification

To accurately measure the displacements along the three perpendicular directions, taking into account the bulk of the device and the risk of collision, an accuracy of few microns is required on a measured range of 50mm and a mean distance of the order of magnitude of 1m. Two types of lasers, supplied by Keyence, seem to fulfill the required specifications, namely :

- LK-G 402
- LK-G 407

The specifications given by the manufacturer are :

| | |
|---|---|
| Light source | Red semiconducteur laser / wave length 655nm |
| Reference distance | 400mm |
| Measurement range | ±100mm |
| Repeatability of the measure | 0,2$\mu$m (at the reference distance) |

**Table B.1:** Specifications given by the supplier

The size and the shape of the laser beam are the only difference in the specifications, from the supplier's point of view. At the focal distance, the diameter of the spot for the first laser, LK-G 402, is small : 290 $\mu$m. It allows to make accurate measurement in narrow spaces or on very small targets. The spot of the second model, LK-G 407, is rectangular and bigger: 290 $\mu$m $\times$ 8300 $\mu$m at the reference distance.

The accuracy given by the manufacturer is measured in a very specific case. A ceramic target, said to be "perfect" (in terms of planarity, roughness, absence of particular reflexion) is placed at the reference distance. The measurement of the distance is done several time and thus the accuracy of the measurement of 0.2 $\mu$m corresponds to the repeatability of the measurement.

The specifications of the laser probes were also tested in our laboratory. In our case, the roughness of the targets, metal plats, was measured and was found to be smaller than

10 $\mu$m, which is recommended to limit bright reflexions and so to allow a good scattering of the light. The planarity default was negligible. The parallelism between the target and the laser probe was carefully checked. The relative displacement between the laser probe and the target was monitored thanks to a linear micrometric stage. Displacements of several cm were applied around the reference distance.

| | |
|---|---|
| Initial distance from the target | 400 mm |
| Measure range | ±10 V from +40 mm to −20 mm |
| Averaging | 4 |
| Sampling rate | 200 $\mu$s |

**Table B.2:** Parameters used

An uncertainty less than 5 $\mu$m was obtained, which is much higher than the 0.2 $\mu m$ accuracy claimed by the manufacturer but which is acceptable, regarding the conditions of testing.

However, during a compaction test, it is not always possible to preserve these ‘ideal’ conditions as translation and rotation motion can occur. It was observed that measurement uncertainty was far above the needed one (figure B.1 ).

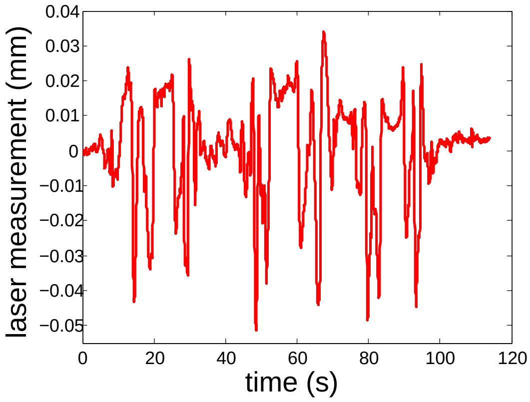

**Figure B.1:** The distance between the target and the probe laser is fixed. The target is translated along its plane, normal to the direction of the beam laser.

This problem is also described by [Muralikrishnan *et al.*, 2012]. Indeed, if the roughness of the target surface is small, a speckle phenomenon appears which strongly degrades the accuracy of the measurement.

This problem is pronounced for the first model LK-G 402 (small spot) but is strongly reduced using the second probe laser with a larger and rectangular spot, LK-G 407. A larger spot may average the ‘parasitic’ diffractions and the accuracy of the measurement is increased. To check this assumption, the two laser sensors were tested simultaneously while they reached the same point of a target. They were set on the same stage and slightly tilted so that the two spots were superimposed on the target. (Figure B.2 ). A specific setting was used to avoid problem of interference between both signals.

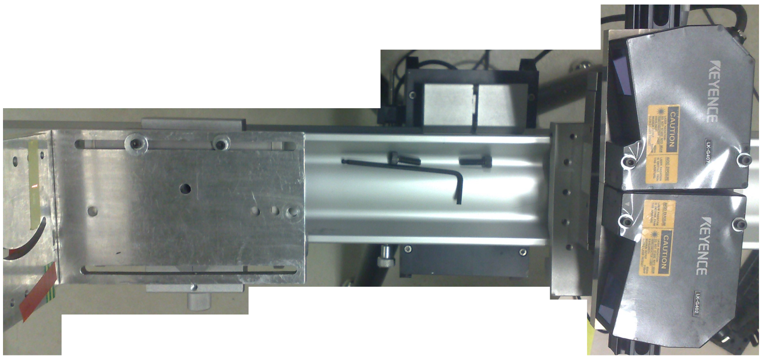

**Figure B.2:** Setting to compare the specifications of the two sensors

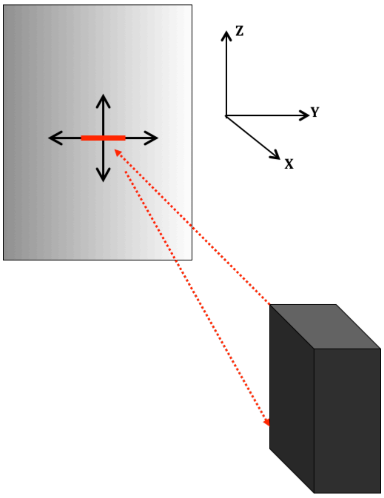

**Figure B.3:** Translation of the target along the length of the spot, the Y axis, or along its width, the Z axis.

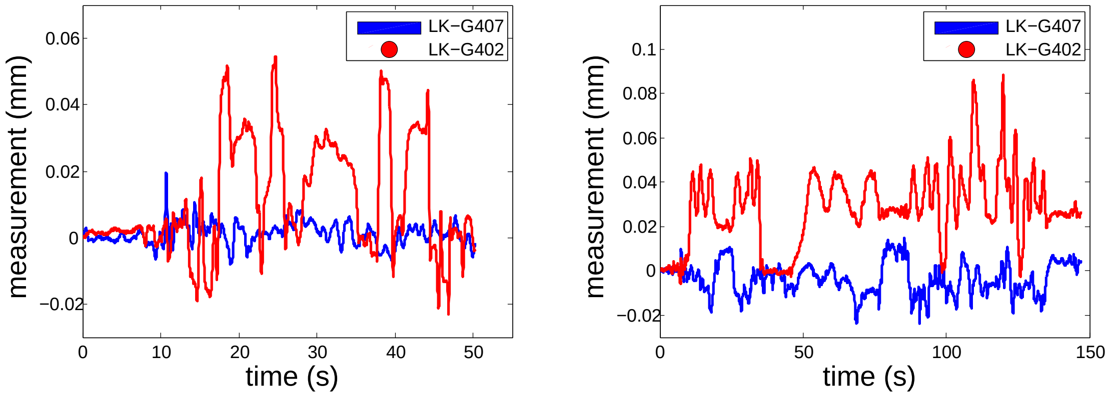

(a) Direction Y (b) Direction Z

**Figure B.4:** Measurement of the displacement for the two types of laser sensors - In plane translation of the target in the Y direction and the Z direction

The distance between the laser probes and the target was fixed and translations were imposed in the plan of the target ( Figure B.3 ). It appears that the noise of the measure with the LK-G-407 probes are smaller than with the LK-G-402 model. So it reveals less sensitive to the translation and rotation of the target induced by the movement of the actors in ASTREE. This second model is selected.

Note that, since our study, the supplier has changed the specifications of the LK-G-402. To date, the repeatability of the measurement is now given for 2$\mu$m.

# Appendix C

# Parameters of the Drucker-Prager/cap model

**Table C.1:** parameters of the virgin PTFE

| | | | |
|---|---|---|---|
| hardening | a | 0.2736 | MPa |
| | b | 1.564 | |
| | $\varepsilon_{crit}$ | -1.681 | |
| | n | 2.991 | |
| bulk modulus | $K_p$ | 100 | MPa |
| | $K_{crit}$ | 2700 | MPa |
| | $a_K$ | 19.5 | |
| shear modulus | $G_p$ | 19.19 | MPa |
| | $G_{crit}$ | 88.01 | MPa |
| | $a_G$ | 21.79 | |
| angle of internal friction coefficient | $\beta$ | 3.4 | ° |
| cohesion | $a_d$ | 9.16 | MPa |
| | $b_d$ | 4.212 | |
| ratio $p_a/p_b = r_a(1+e)^{-r_b} + r_c$ | $r_a$ | 0.2563 | |
| | $r_b$ | 4.134 | |
| | $r_c$ | 0.6947 | |

**Table C.2:** parameters of the virgin PTFE + filler 1

| | | | |
|---|---|---|---|
| hardening | a | 0.6176 | MPa |
| | b | 1.0 | |
| | $\varepsilon_{crit}$ | -1.589 | |
| | n | 3.057 | |
| bulk modulus | $K_p$ | 238.7 | MPa |
| | $K_{crit}$ | 3114 | MPa |
| | $a_K$ | 22.62 | |
| shear modulus | $G_p$ | 37 | MPa |
| | $G_{crit}$ | 390.1 | MPa |
| | $a_G$ | 36.18 | |
| angle of internal friction coefficient | $\beta$ | 5.4 | ° |
| cohesion | $a_d$ | 14.58 | MPa |
| | $b_d$ | 7.275 | |
| ratio $p_a/p_b$ | defined by piece, see figure 2.41 | | |

**Table C.3:** parameters of the virgin PTFE + filler 2

| | | | |
|---|---|---|---|
| hardening | a | 0.7614 | MPa |
| | b | 1.0 | |
| | $\varepsilon_{crit}$ | -1.549 | |
| | n | 2.84 | |
| bulk modulus | $K_p$ | 201.6 | MPa |
| | $K_{crit}$ | 3068 | MPa |
| | $a_K$ | 22.2 | |
| shear modulus | $G_p$ | 45.56 | MPa |
| | $G_{crit}$ | 204.4 | MPa |
| | $a_G$ | 17 | |
| angle of internal friction coefficient | $\beta$ | 4.5 | ° |
| cohesion | $a_d$ | 13.93 | MPa |
| | $b_d$ | 7.0 | |
| ratio $p_a/p_b$ | defined by piece, see figure 2.41 | | |

**Table C.4:** parameters of the virgin PTFE B

| | | | |
|---|---|---|---|
| hardening | a | 1.451 | MPa |
| | b | 1.0 | |
| | $\varepsilon_{crit}$ | -0.919 | |
| | n | 2.224 | |
| bulk modulus | $K_p$ | 149.1 | MPa |
| | $K_{crit}$ | 2951 | MPa |
| | $a_K$ | 22.25 | |
| shear modulus | $G_p$ | 12.01 | MPa |
| | $G_{crit}$ | 126.3 | MPa |
| | $a_G$ | 23.26 | |
| angle of internal friction coefficient | $\beta$ | 5.1 | ° |
| cohesion | $a_d$ | 6.811 | MPa |
| | $b_d$ | 5.56 | |
| ratio $p_a/p_b$ | defined by piece, see figure 2.38 | | |

# Appendix D

# Experimental characterization and modeling of the viscous behavior

Considering the limitation of the triaxial machine ASTREE (thermal drift) and the material limitation (time available and cost-in-use), characterization of the time dependent behavior of the material was not done with the 3D compaction tool.

In [Canto *et al.*, b], the viscous part of the elasto-viscoplastic model for PTFE green part is identified from the simple compression at different strain rates of green isostatic samples. Rectangular based PTFE samples are made of pelletized virgin PTFE B and shaped by isostatic pressing with different void ratio. The deformation of the material is measured by Digital image Correlation (DIC) (see 6.2.2).

For fine cut powders (virgin PTFE and filled compounds), it is not possible to obtain isostatic samples by hydrostatic pressing suitable for simple compression. Indeed the obtained samples have an irregular shape and a high surface roughness which cannot be rectified without damaging the material and with enough accuracy.

It is proposed here to identify the viscous behavior thanks to œdometric tests at different levels of maximal density and different imposed displacement rates, followed by relaxation step (figures D.1 and D.2). Contrary to the tests performed in [Canto *et al.*, b], the viscous part of the consolidation part of the yield surface is investigated and the effect of the escape of the air is included in the measurement.

With regard to the experimental results, it may be concluded that the behavior of the material during the compaction step is not sensitive to the displacement rate in the studied range (one decade) (figure D.1).

The relaxation appears to be dependent on the level of void ratio of the material and on the imposed displacement rate of the previous loading step. A viscous model of the consolidation plastic part of the model is proposed here and identified from the relaxation step. The viscous part of the stress $\sigma_v$ during the relaxation is defined as $\sigma_v = \sigma(t) - \sigma_\infty$, with $\sigma_\infty$ the asymptotic (long time) stress.

The total strain is defined as a partition of the elastic strain, $\varepsilon_{elas}$ and of the viscoplastic strain $\varepsilon_{vp}$, $\varepsilon = \varepsilon_{elas} + \varepsilon_{vp}$. During relaxation, the total strain rate is nul and hence

$$\dot{\varepsilon}_{vp} = -\dot{\varepsilon}_{elas} = -\frac{\dot{\sigma}}{E} \tag{D.1}$$

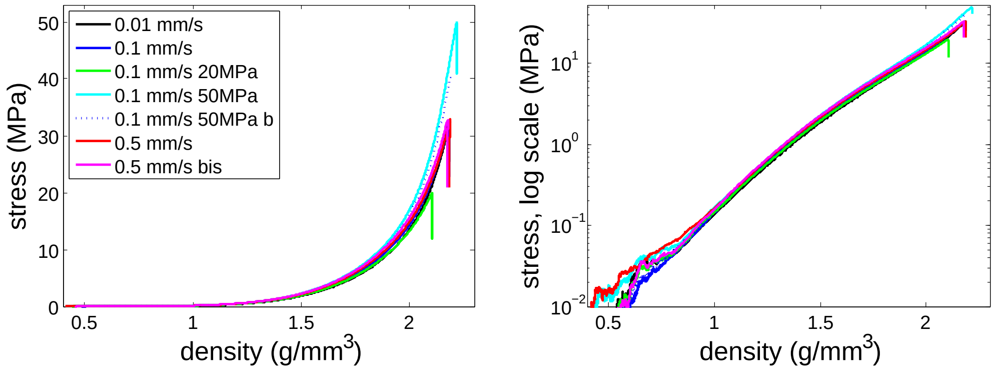

(a) Evolution of the stress as a function of the density

(b) Plot in semi logarithmic scale

**Figure D.1:** Comparison of the evolution of the axial stress respect to the density during œdometric loading as a function of the displacement rate. Samples of 45g of virgin PTFE powder are compacted in a die with a rectangular base of 35×35 mm$^2$ section, at different level of maximal applied stresses and different displacement rates. No effect of the displacement rate is noticed during the loading in the studied range.

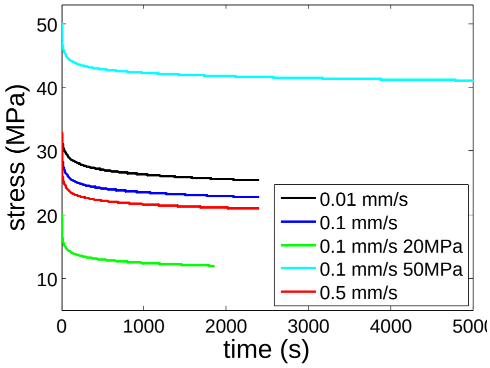

**Figure D.2:** Relaxation step, which follows the œdometric loading - Influence of the maximal applied stress and of the displacement rate.

Then the viscous part of the stress and the viscous strain rate may be related thanks to a hyperbolic sine creep law such as

$$\sigma_v = a_v \sinh^{-1}\left(\left(\frac{\dot{\varepsilon}_v}{\dot{\varepsilon}_0}\right)^{1/m}\right) \tag{D.2}$$

with $a_v$, $\dot{\varepsilon}_0$ and $m$, parameters of the model. $m$ is found to be constant while $a_v$ and $\dot{\varepsilon}_0$ depend on the void ratio.

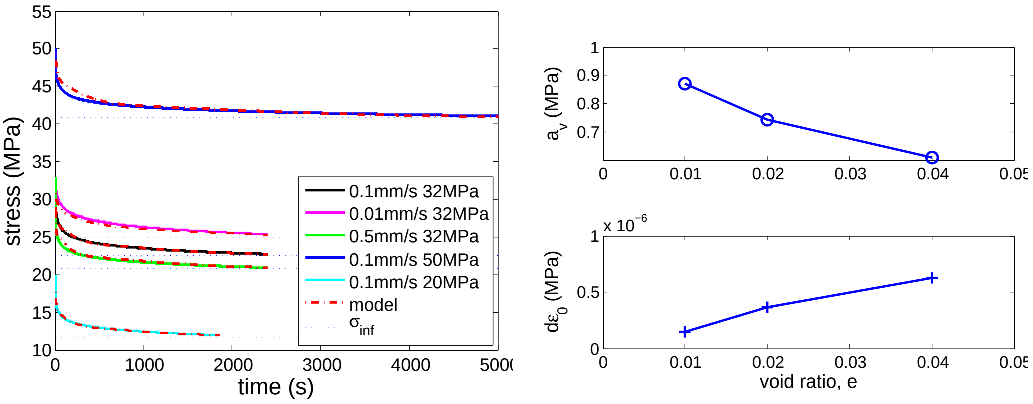

(a) Comparison between the experimental results and the identified analytical solution

(b) Identified parameters and their evolution with the void ratio - $m$ is set to 0.75

**Figure D.3:** Identification of the viscous part of the elasto-viscoplastic model from œdometric tests followed by relaxation steps.

**Implementation of the viscous part of the behavior - Issue** To model the viscous part behavior of the material, a multiplicative law, available in Drucker-Prager/cap model in Abaqus with a dependency of the parameters to the level of density, could be implemented. However the region of activity of the creep mechanism is limited : the part of the stress due to the viscosity, $p_{creep}$, cannot be higher than $p_b - p_a$ on the consolidation surface. In our case, because of the shape of the identified cap, the decrease of the stress during the relaxation step is limited to 3 MPa for the virgin PTFE, which is incompatible with the experimental observations (D.2). The implementation of the elasto viscoplastic model in a UMAT would be required to correctly describe the viscosity of the material which was not in the scope of the study. As, the material may be assumed not to be dependent to the rate of loading in the studied range during the consolidation step, the viscous part of the behavior to simulate the compaction step of the material may be neglected here.

# Appendix E

# XRD measurements

In this appendix, the different experimental data obtained to construct the Wulff's diagram or measured on other samples are presented. For each case, three curves corresponding to measurements at the three values of the $\omega_z$ rotation about the $z$ axis, $\omega_z = 0°$, $40°$ and $90°$ are shown. They represent the evolution of the relative integrated intensity as a function of $\omega_y$ the rotation angle about the $y$ axis.

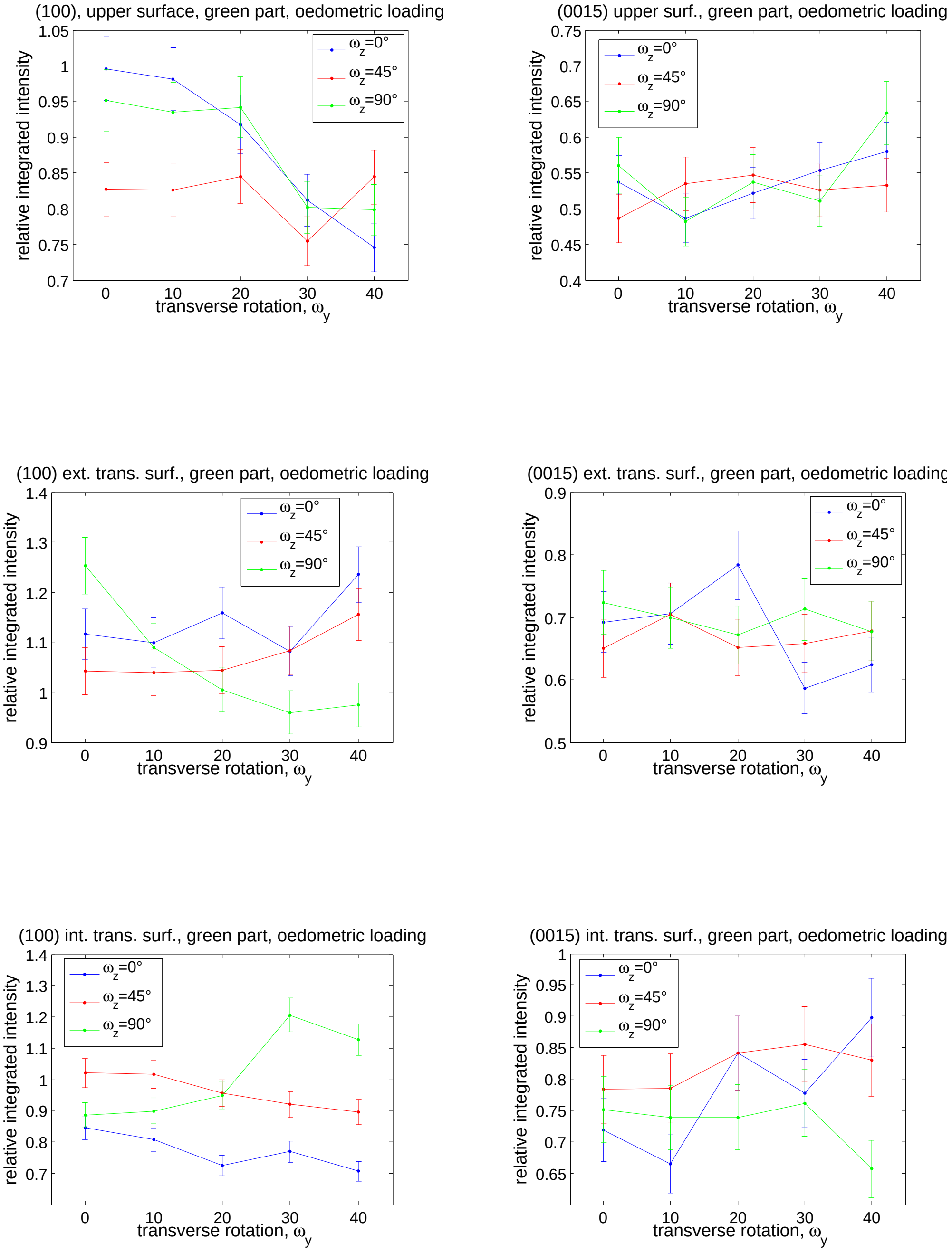

**Figure E.1:** Relative integrated intensities corresponding to planes (100) and (00.15) on the three different surfaces - oedometric sample compacted with a maximal applied stress of 32.7 MPa at a displacement rate of 0.1mm/s before sintering.

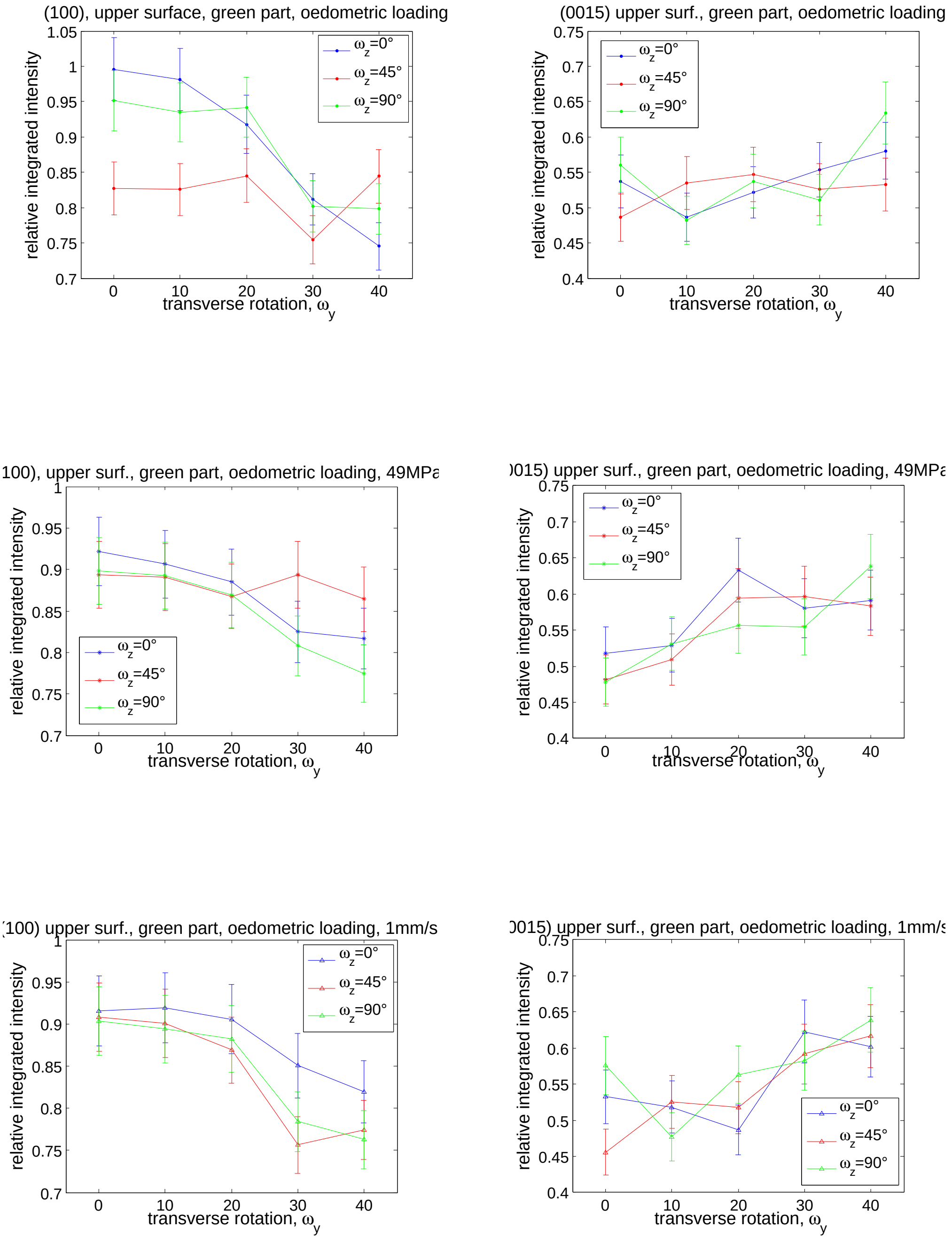

**Figure E.2:** Relative integrated intensities corresponding to planes (100) and (00.15) on the superior surface - Comparison between three oedometric samples compacted with a maximal applied stress of 32.7 MPa or 49MPa and at a displacement rate of 0.1mm/s or 1mm/s before sintering.

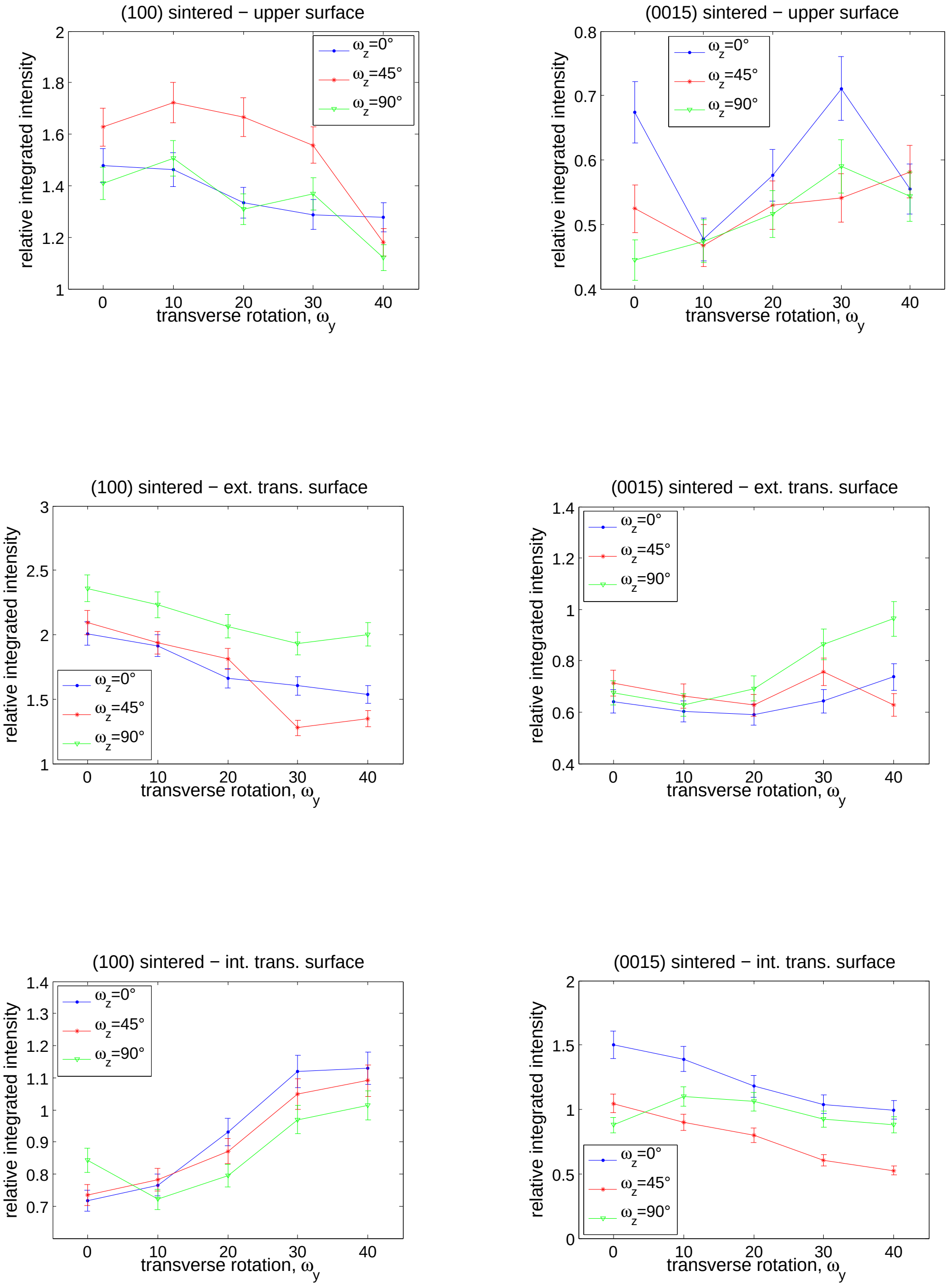

**Figure E.3:** Relative integrated intensities corresponding to planes (100) and (00.15) on the three different surfaces - sintered oedometric sample compacted with a maximal applied stress of 32.7 MPa at a displacement rate of 0.1mm/s.

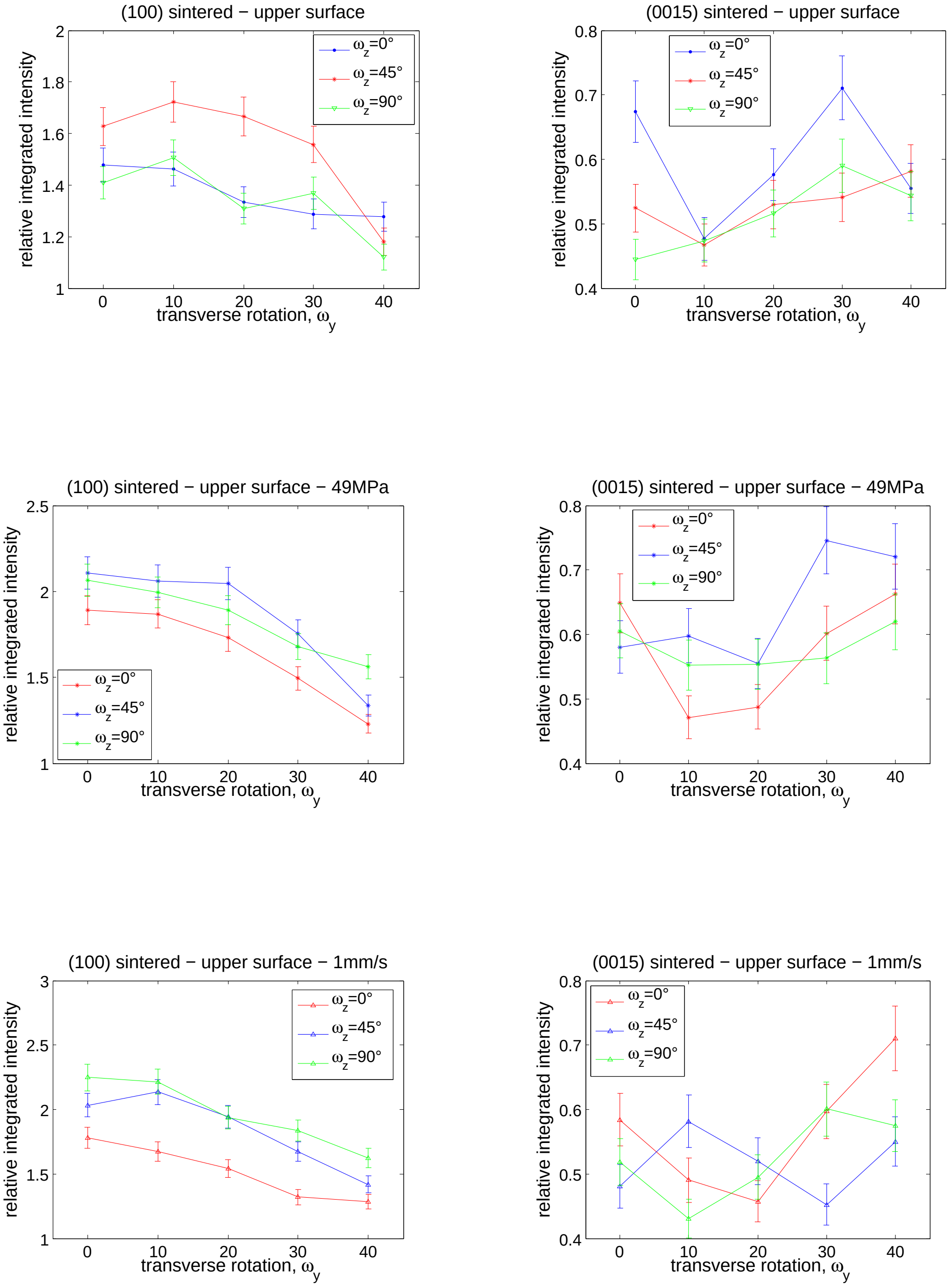

**Figure E.4:** Relative integrated intensities corresponding to planes (100) and (00.15) on the superior surface - Comparison between three oedometric samples compacted with a maximal applied stress of 32.7 MPa or 49MPa and at a displacement rate of 0.1mm/s or 1mm/s after the sintering.

# Bibliography

[Andena *et al.*, 2004] ANDENA, L., RINK, M. et POLASTRI, F. (2004). Simulation of ptfe sintering: Thermal stresses and deformation behavior. *Polymer Engineering & Science*, 44(7):1368–1378.

[Aubertin et Li, 2004] AUBERTIN, M. et LI, L. (2004). A porosity-dependent inelastic criterion for engineering materials. *International Journal of Plasticity*, 20(12):2179 – 2208.

[Aydin *et al.*, 1996] AYDIN, İ., BRISCOE, B. J. et ŞANLITÜRK, K. Y. (1996). The internal form of compacted ceramic components: a comparison of a finite element modelling with experiment. *Powder Technology*, 89(3):239 – 254.

[Bahadur et Tabor, 1984] BAHADUR, S. et TABOR, D. (1984). The wear of filled polytetrafluoroethylene. *Wear*, 98(0):1 – 13.

[Baudet *et al.*, 2011] BAUDET, C., GRANDIDIER, J.-C. et CANGÉMI, L. (2011). A damage model for the blistering of polyvinylidene fluoride subjected to carbon dioxide decompression. *Journal of the Mechanics and Physics of Solids*, 59(9):1909 – 1926.

[Beecroft et Swenson, 1959] BEECROFT, R. et SWENSON, C. (1959). Behavior of polytetrafluoroethylene (teflon) under high pressures. *Journal of Applied Physics*, 30(11): 1793–1798.

[Bergström et Hilbert, 2005] BERGSTRÖM, J. et HILBERT, L. (2005). A constitutive model for predicting the large deformation thermomechanical behavior of fluoropolymers. *Mechanics of Materials*, 37(8):899 – 913.

[Besson et Evans, 1992] BESSON, J. et EVANS, A. (1992). The effect of reinforcements on the densification of a metal powder. *Acta Metallurgica et Materialia*, 40(9):2247 – 2255.

[Bigg, 1977] BIGG, D. M. (1977). A study of the effect of pressure, time, and temperature on high-pressure powder molding. *Polymer Engineering & Science*, 17(9):691–699.

[Biswas et Vijayan, 1992] BISWAS, S. et VIJAYAN, K. (1992). Friction and wear of ptfe - a review. *Wear*, 158:193–211.

[Blumm *et al.*, 2010] BLUMM, J., LINDEMANN, A., MEYER, M. et STRASSER, C. (2010). Characterization of ptfe using advanced thermal analysis techniques. *International Journal of Thermophysics*, 31(10):1919–1927.

[Bonnenfant *et al.*, 1998] BONNENFANT, D., MAZEROLLE, F. et SUQUET, P. (1998). Compaction of powders containing hard inclusions: experiments and micromechanical modeling. *Mechanics of Materials*, 29(2):93 – 109.

[Bouterf, 2014] BOUTERF, A. (2014). *Comportement mécanique de la plaque de plâtre étudié par tomographie et essais mécaniques in-situ.* Thèse de doctorat. 2014DENS0010.

[Bouvard, 2000] BOUVARD, D. (2000). Densification behaviour of mixtures of hard and soft powders under pressure. *Powder Technology*, 111(3):231 – 239.

[Bouvard *et al.*, 1988] BOUVARD, D., LANIER, J. et STUTZ, P. (1988). Mechanical behaviour of graphite powder. *Powder Technology*, 54(3):175 – 181.

[Bowden et Tabor, 1966] BOWDEN, F. P. et TABOR, D. (1966). Friction, lubrication and wear: a survey of work during the last decade. *British Journal of Applied Physics*, 17(12):1521.

[Bowden et Young, 1974] BOWDEN, P. et YOUNG, R. (1974). Deformation mechanisms in crystalline polymers. *Journal of Materials Science*, 9(12):2034–2051.

[Briscoe et Rough, 1998] BRISCOE, B. et ROUGH, S. (1998). The effects of wall friction on the ejection of pressed ceramic parts. *Powder Technology*, 99(3):228 – 233.

[Briscoe et Tabor, 1975] BRISCOE, B. et TABOR, D. (1975). The effect of pressure on the frictional properties of polymers. *Wear*, 34(1):29 – 38.

[Brochu et Turenne, 2004] BROCHU, M. et TURENNE, S. (2004). Experimental method for determining densification function of metal powder and its validity. *Powder metallurgy*, 47(1):55–59.

[Brown *et al.*, 2007] BROWN, E., DATTELBAUM, D., BROWN, D., RAE, P. et CLAUSEN, B. (2007). A new strain path to inducing phase transitions in semi-crystalline polymers. *Polymer*, 48(9):2531 – 2536.

[Brown *et al.*, 2008] BROWN, E., RAE, P., DATTELBAUM, D., CLAUSEN, B. et BROWN, D. (2008). In-situ measurement of crystalline lattice strains in polytetrafluoroethylene. *Experimental Mechanics*, 48(1):119–131.

[Brown et Dattelbaum, 2005] BROWN, E. N. et DATTELBAUM, D. M. (2005). The role of crystalline phase on fracture and microstructure evolution of polytetrafluoroethylene (ptfe). *Polymer*, 46(9):3056 – 3068.

[Brown et Abou-Chedid, 1994] BROWN, S. et ABOU-CHEDID, G. (1994). Yield behaviour of metal powder assemblages. *Journal of the Mechanics and Physics of Solids*, 42(3):383–399.

[Brulin *et al.*, 2011] BRULIN, J., REKIK, A., JOSSERAND, L., BLOND, E., GASSER, A. et ROULET, F. (2011). Characterization and modelling of a carbon ramming mix used in high-temperature industry. *International Journal of Solids and Structures*, 48(5):854 – 864.

[Burlion *et al.*, 2001] BURLION, N., PIJAUDIER-CABOT, G. et DAHAN, N. (2001). Experimental analysis of compaction of concrete and mortar. *International Journal for Numerical and Analytical Methods in Geomechanics*, 25(15):1467–1486.

[Canto, 2007] CANTO, R. B. (2007). *Étude théorique et expérimentale du procédé de compaction et frittage du polytetrafluoréthylène (PTFE)*. Thèse de doctorat, École normale supérieure de Cachan-ENS Cachan.

[Canto *et al.*, a] CANTO, R. B., FREDY, C., RAKA, B., SCHMITT, N. et BILLARDON, R. A device for true triaxial powder compaction tests at large strains and non-proportional load paths. *to be submitted*.

[Canto *et al.*, 2011] CANTO, R. B., SCHMITT, N., DE CARVALHO, J. et BILLARDON, R. (2011). Experimental identification of the deformation mechanisms during sintering of cold compacted polytetrafluoroethylene powders. *Polymer Engineering & Science*, 51(11):2220–2235.

[Canto *et al.*, b] CANTO, R. B., SCHMITT, N., HILD, F. et BILLARDON, R. (??b). Identification of 3-d elasto-viscoplastic constitutive equations to model pure ptfe powder compaction.

[Canto *et al.*, 2009] CANTO, R. B., SCHMITT, N., HILD, F. et BILLARDON, R. (2009). Identification of 3-d elasto-viscoplastic constitutive equations to model ptfe powder compaction. *In ESMC2009 - 7th EUROMECH Solid Mechanics Conference*.

[Chen *et al.*, 2007] CHEN, Y., IMBAULT, D. et DORÉMUS, P. (2007). Simulation numérique de la compression d'empilements tri-dimensionnels de grains. *18ème Congrès Français de Mécanique (Grenoble 2007)*.

[Chtourou *et al.*, 2002] CHTOUROU, H., GUILLOT, M. et GAKWAYA, A. (2002). Modeling of the metal powder compaction process using the cap model. part i. experimental material characterization and validation. *International Journal of Solids and Structures*, 39(4):1059 – 1075.

[Chu *et al.*, 1985] CHU, T., RANSON, W. et SUTTON, M. (1985). Applications of digital-image-correlation techniques to experimental mechanics. *Experimental Mechanics*, 25(3):232–244.

[Clark, 1999] CLARK, E. (1999). The molecular conformations of polytetrafluoroethylene: forms {II} and {IV}. *Polymer*, 40(16):4659 – 4665.

[Cocks et Sinka, 2007] COCKS, A. et SINKA, I. (2007). Constitutive modelling of powder compaction - i. theoretical concepts. *Mechanics of Materials*, 39(4):392 – 403.

[Colliat-Dangus *et al.*, 1988] COLLIAT-DANGUS, J.-L., DESRUES, J. et FORAY, P. (1988). Triaxial testing of granular soil under elevated cell pressure. *Advanced triaxial testing of soil and rock, ASTM STP*, 977:290–310.

[Coube et Riedel, 2000] COUBE, O. et RIEDEL, H. (2000). Numerical simulation of metal powder die compaction with special consideration of cracking. *Powder Metallurgy*, 43(2):123–131.

[Crawford et Paul, 1980] CRAWFORD, R. et PAUL, D. (1980). Pressures transmitted through polymeric powders subjected to solid phase compaction. *Polymer*, 21(2):138–139.

[Crawford et Paul, 1981] CRAWFORD, R. et PAUL, D. (1981). Radial and axial die pressure during solid phase compaction of polymeric powders. *European Polymer Journal*, 17:1023–1028.

[Crawford *et al.*, 1979] CRAWFORD, R., PAUL, D. et ADEEBNIA, Y. (1979). Microhardness and density distributions in polymeric powder compacts. *European Polymer Journal*, 16:401–405.

[Crawford, 1982] CRAWFORD, R. J. (1982). Effect of compaction rate during the cold forming of polymeric powders. *Polymer Engineering and Science*, 22(5):300–306.

[Crawford et Paul, 1982] CRAWFORD, R. J. et PAUL, D. W. (1982). Cold compaction of polymeric powders. *Journal of Materials Science*, 17:2267–2280.

[Crawford *et al.*, 1982] CRAWFORD, R. J., PAUL, D. W. et SPREVAK, D. (1982). Solid phase compaction of polymeric powders: effects of compaction conditions on pressure and density variations. *Polymer*, 23:123–128.

[Crawford et Sprevak, 1984] CRAWFORD, R. J. et SPREVAK, D. (1984). Cold compaction of polymeric powders in tapered dies. *European Polymer Journal*, 20(5):441–446.

[Cullity et Stock, 2001] CULLITY, B. D. et STOCK, S. R. (2001). *Elements of X-ray diffraction; 3rd ed.* Pearson, Upper Saddle River, NJ.

[Cunningham *et al.*, 2004] CUNNINGHAM, J., SINKA, I. et ZAVALIANGOS, A. (2004). Analysis of tablet compaction. i. characterization of mechanical behavior of powder and powder/tooling friction. *Journal of Pharmaceutical Sciences*, 93(8):2022–2039.

[Dimaggio et Sandler, 1971] DIMAGGIO, F. L. et SANDLER, I. S. (1971). Material model for granular soils. *Journal of the Engineering mechanics Division*, 97(3):935–950.

[Dorémus *et al.*, 1995] DORÉMUS, P., GEINDREAU, C., MARTIN, A., DEBOVE, L., LECOT, R. et DAO, M. (1995). High pressure triaxial cell for metal powder. *Powder Metallurgy*, 38(4):284–287.

[Drucker D.C., 1952] DRUCKER D.C., P. W. (1952). Soil mechanics and plastic analysis on limit design. *Quat. Appl. Meth.*, 10(2):157–165.

[Ebnesajjad, 2002] EBNESAJJAD, S. (2002). *Fluoroplastics, Volume 2: Melt Processible Fluoroplastics: The Definitive User's Guide*. Access Online via Elsevier.

[Eby et Sinnott, 1961] EBY, R. et SINNOTT, K. (1961). Transitions and relaxations in polytetrafluoroethylene. *Journal of Applied Physics*, 32(9):1765–1771.

[Feldman, 1996] FELDMAN, D. (1996). *Synthetic polymers: technology, properties, applications*. Springer.

[Fleck, 1995] FLECK, N. (1995). On the cold compaction of powders. *Journal of the Mechanics and Physics of Solids*, 43(9):1409 – 1431.

[Fleck *et al.*, 1992] FLECK, N., KUHN, L. et MCMEEKING, R. (1992). Yielding of metal powder bonded by isolated contacts. *Journal of the Mechanics and Physics of Solids*, 40(5):1139 – 1162.

[Frachon, 2002] FRACHON, A. (2002). *Modélisation et Simulation Numérique de la Compression en Matrice de Poudres Métalliques*. Thèse de doctorat, Institut National Polytechnique de Grenoble.

[Frêne et Zaïdi, 2014] FRÊNE, J. et ZAÏDI, H. (2014). Introduction à la tribologie. *Techniques de l'ingénieur Frottement et usure*, base documentaire : TIB464DUO.(ref. article : tri100).

[Friedrich *et al.*, 2005] FRIEDRICH, K., ZHANG, Z. et SCHLARB, A. K. (2005). Effects of various fillers on the sliding wear of polymer composites. *Composites Science and Technology*, 65:2329 – 2343. 20th Anniversary Special Issue.

[Galen et Zavaliangos, 2005] GALEN, S. et ZAVALIANGOS, A. (2005). Strength anisotropy in cold compacted ductile and brittle powders. *Acta Materialia*, 53(18): 4801 – 4815.

[Gamboni *et al.*, ] GAMBONI, O. C., RIUL, C., SCHMITT, N., BILLARDON, R., FILHO, W. B. et CANTO, R. On the formation of defects induced by air trapping during cold pressing of ptfe powder. *to be submitted to Polymer*.

[Gao *et al.*, 1996] GAO, P., CHEUNG, M. K. et LEUNG, T. (1996). Effects of compaction pressure on cohesive strength and chain mobility of low-temperature compacted nascent {UHMWPE}. *Polymer*, 37(15):3265 – 3272.

[Gras, 2012] GRAS, R. (2012). *Identification de champs de propriétés élastiques fondée sur la mesure de champs : application sur un composite tissé 3D*. Thèse de doctorat. 2012DENS0088.

[Greenwood et Williamson, 1966] GREENWOOD, J. A. et WILLIAMSON, J. B. P. (1966). Contact of nominally flat surfaces. *Proceedings of the Royal Society of London A: Mathematical, Physical and Engineering Sciences*, 295(1442):300–319.

[Guo *et al.*, 2008] GUO, T., FALESKOG, J. et SHIH, C. (2008). Continuum modeling of a porous solid with pressure-sensitive dilatant matrix. *Journal of the Mechanics and Physics of Solids*, 56(6):2188 – 2212.

[Gurson, 1977] GURSON, A. (1977). *Continuum theory of ductile rupture by void nucleation and growth. Part I. Yield criteria and flow rules for porous ductile media.*

[Guyoncourt *et al.*, 2001] GUYONCOURT, D., TWEED, J., GOUGH, A., DAWSON, J. et PATER, L. (2001). Constitutive data and friction measurements of powders using instrumented die. *Powder Metallurgy*, 44(1):25–33.

[Hambir *et al.*, 1994] HAMBIR, S. S., JOG, J. P. et NADKARNI, V. M. (1994). Strength development in powder processing of poly(tetrafluoroethylene). *Polymer Engineering & Science*, 34(13):1065–1069.

[Hambly, 1969] HAMBLY, E. C. (1969). A new true triaxial apparatus. *Géotechnique*, 19:307–309(2).

[Han *et al.*, 2008] HAN, L., ELLIOTT, J., BENTHAM, A., MILLS, A., AMIDON, G. et HANCOCK, B. (2008). A modified drucker-prager cap model for die compaction simulation of pharmaceutical powders. *International Journal of Solids and Structures*, 45(10):3088 – 3106.

[Hashin et Shtrikman, 1963] HASHIN, Z. et SHTRIKMAN, S. (1963). A variational approach to the theory of the elastic behaviour of multiphase materials. *Journal of the Mechanics and Physics of Solids*, 11(2):127 – 140.

[Hatzikiriakos *et al.*, 2002] HATZIKIRIAKOS, S. G., ARIAWAN, A. B. et EBNESAJJAD, S. (2002). Paste extrusion of polytetrafluoroethylene (ptfe) fine powder resins. *The Canadian Journal of Chemical Engineering*, 80(6):1153–1165.

[Hermans *et al.*, 1948] HERMANS, P. H., HERMANS, J. J., VERMAAS, D. et WEIDINGER, A. (1948). Deformation mechanism of cellulose gels. iv. general relationship between orientation of the crystalline and that of the amorphous portion. *Journal of Polymer Science*, 3(1):1–9.

[Hermans et Weidinger, 1961] HERMANS, P. H. et WEIDINGER, A. (1961). On the determination of the crystalline fraction of polyethylenes from x-ray diffraction. *Die Makromolekulare Chemie*, 44(1):24–36.

[Heuvel *et al.*, 1976] HEUVEL, H. M., HUISMAN, R. et LIND, K. C. J. B. (1976). Quantitative information from x-ray diffraction of nylon-6 yarns. i. development of a model for the analytical description of equatorial x-ray profiles. *Journal of Polymer Science: Polymer Physics Edition*, 14(5):921–940.

[Hibbit *et al.*, 2011] HIBBIT, KARLSSON et SORENSEN (2011). *ABAQUS/Standard Analysis User's Manual*. Hibbit, Karlsson, Sorensen Inc., USA.

[Hild et Roux, 2012] HILD, F. et ROUX, S. (2012). *Digital image correlation*. Wiley-VCH, Weinheim.

[Hill, 1965] HILL, R. (1965). A self-consistent mechanics of composite materials. *Journal of the Mechanics and Physics of Solids*, 13(4):213 – 222.

[Huang et Yu, 2012] HUANG, H. et YU, X. (2012). Automated industrial ptfe billet sintering temperature profile optimization for residual stress reduction. *In 2012 SIMULIA Community Conference*.

[Jauffrès *et al.*, 2007] JAUFFRÈS, D., LAME, O., VIGIER, G. et DORÉ, F. (2007). Microstructural origin of physical and mechanical properties of ultra high molecular weight polyethylene processed by high velocity compaction. *Polymer*, 48(21):6374 – 6383.

[Jauffrès *et al.*, 2009] JAUFFRÈS, D., LAME, O., VIGIER, G., DORÉ, F. et DOUILLARD, T. (2009). Sintering mechanisms involved in high-velocity compaction of nascent semicrystalline polymer powders. *Acta Materialia*, 57(8):2550 – 2559.

[Jenike, 1964] JENIKE, A. W. (1964). Storage and Flow of Solids, Bulletin No. 123. *Bulletin of the University of Utah*, 53(26):198.

[Jog, 1993] JOG, J. P. (1993). Solid state processing of polymers: A review. *Advances in Polymer Technology*, 12(3):281–289.

[Jonsën et Häggblad, 2007] JONSËN, P. et HÄGGBLAD, H.-Å. (2007). Fracture energy based constitutive models for tensile fracture of metal powder compacts. *International Journal of Solids and Structures*, 44(20):6398 – 6411.

[Jordan *et al.*, 2007] JORDAN, J. L., SIVIOUR, C. R., FOLEY, J. R. et BROWN, E. N. (2007). Compressive properties of extruded polytetrafluoroethylene. *Polymer*, 48(14): 4184 – 4195.

[Joyce et Joyce, 2004] JOYCE, J. A. et JOYCE, P. J. (2004). Toughness characterization of a metal filled polytetrafluoroethylene using the j-integral. *Engineering Fracture Mechanics*, 71(16–17):2513 – 2531.

[Jr et Kasprzak, 1993] JR, B. B. B. et KASPRZAK, D. J. (1993). Thermal degradation of commercial fluoropolymers in air. *Polymer Degradation and Stability*, 42(2):181 – 188.

[Kamath et Puri, 1997] KAMATH, S. et PURI, V. (1997). Measurement of powder flow constitutive model parameters using a cubical triaxial tester. *Powder Technology*, 90(1):59 – 70.

[Kim *et al.*, 2003] KIM, K., LEE, S. et RYU, H. (2003). Densification behavior of aluminum alloy powder mixed with zirconia powder inclusion under cold compaction. *Materials Science and Engineering: A*, 340(1–2):41 – 48.

[Kirby, 1956] KIRBY, R. K. (1956). Thermal expansion of polytetrafluoroethylene (teflon) from -190° to + 300° c. *Journal of Research of the National Bureau of Standards*, 57(2):91–94.

[Krick *et al.*, 2013] KRICK, B. A., HAHN, D. W. et SAWYER, W. G. (2013). Plasmonic diagnostics for tribology: In situ observations using surface plasmon resonance in combination with surface-enhanced raman spectroscopy. *Tribology Letters*, 49(1):95–102.

[Lachambre *et al.*, 2013] LACHAMBRE, J., MAIRE, E., ADRIEN, J. et CHOQUEUSE, D. (2013). In situ observation of syntactic foams under hydrostatic pressure using x-ray tomography. *Acta Materialia*, 61(11):4035 – 4043.

[Lancaster, 1990] LANCASTER, J. (1990). A review of the influence of environmental humidity and water on friction, lubrication and wear. *Tribology International*, 23(6): 371 – 389.

[Lancaster, 1968] LANCASTER, J. K. (1968). The effect of carbon fibre reinforcement on the friction and wear of polymers. *Journal of Physics D: Applied Physics*, 1(5):549.

[Lanier, 1988] LANIER, J. (1988). Special stress paths along the limit surface of a sand specimen with the use of a true triaxial apparatus. (977):11.

[Latham et Munjiza, 2004] LATHAM, J.-P. et MUNJIZA, A. (2004). The modelling of particle systems with real shapes. *Philosophical Transactions of the Royal Society of London. Series A: Mathematical, Physical and Engineering Sciences*, 362(1822): 1953–1972.

[Lebedev *et al.*, 2010] LEBEDEV, Y., KOROLEV, Y., POLIKARPOV, V., IGNAT'EVA, L. et ANTIPOV, E. (2010). X-ray powder diffraction study of polytetrafluoroethylene. *Crystallography Reports*, 55(4):609–614.

[Li et Puri, 1996] LI, F. et PURI, V. (1996). Measurement of anisotropic behavior of dry cohesive and cohesionless powders using a cubical triaxial tester. *Powder technology*, 89(3):197–207.

[Lin *et al.*, 2012] LIN, J., XIE, S., SHAO, J.-F. et KONDO, D. (2012). A micromechanical modeling of ductile behavior of a porous chalk: Formulation, identification, and validation. *International Journal for Numerical and Analytical Methods in Geomechanics*, 36(10):1245–1263.

[Makinson et Tabor, 1964] MAKINSON, K. R. et TABOR, D. (1964). The friction and transfer of polytetrafluoroethylene. *Proceedings of the Royal Society of London. Series A. Mathematical and Physical Sciences*, 281(1384):49–61.

[Marcellan, 2003] MARCELLAN, A. (2003). *Microstructures, micromécanismes et comportement à rupture de fibres PA 66*. Engineering sciences, Ecole Nationale Superieure des Mines de Paris.

[Martin *et al.*, 2000] MARTIN, C., LAME, O. et BOUVARD, D. (2000). Cohesion and dilatation of powder compacts containing hard phase particles under highly deviatoric stress states. *Mechanics of Materials*, 32(7):405 – 421.

[Mathieu, 2013] MATHIEU, F. (2013). *Analyse de la tenue mécanique d'un liner en titane : apport des mesures de champs cinématiques*. Thèse de doctorat. 2013DENS0007.

[McCrum, 1959] MCCRUM, N. G. (1959). An internal friction study of polytetrafluoroethylene. *Journal of Polymer Science*, 34(127):355–369.

[Meimon, 2000] MEIMON, Y. (2000). Some challenges of the development of constitutive equations of semicrystalline polymers for structural calculations. *Oil & Gas Science and Technology - Rev. IFP*, 55(6):649–659.

[Millet *et al.*, 2006] MILLET, O., RAHMOUN, J. et de SAXCÉ, G. (2006). Analytic calculation of the stresses in an ensiled granular medium. *Comptes Rendus Mécanique*, 334(2):137 – 142.

[Muralikrishnan *et al.*, 2012] MURALIKRISHNAN, B., REN, W., EVERETT, D., STANFIELD, E. et DOIRON, T. (2012). Performance evaluation experiments on a laser spot triangulation probe. *Measurement*, 45(3):333 – 343.

[Myshkin *et al.*, 2005] MYSHKIN, N., PETROKOVETS, M. et KOVALEV, A. (2005). Tribology of polymers: Adhesion, friction, wear, and mass-transfer. *Tribology International*, 38:910 – 921. Tribology International A Celebration Issue.

[Pandeya et Puri, 2011] PANDEYA, A. et PURI, V. M. (2011). Rate-dependent mechanical properties of dry blended pharmaceutical powder formulations for tabletting applications. *Powder Technology*, 207(1–3):26 – 34.

[Pearce, 1971] PEARCE, J. (1971). *A New True Triaxial Apparatus*. CUED/C - soils/TR. Cambridge Univ., Engineering Department.

[Pearce, 1972] PEARCE, J. (1972). Un véritable appareil triaxial. *LE COMPORTEMENT DES SOLS AVANT LA RUPTURE*, page 31.

[Pooley et Tabor, 1972] POOLEY, C. et TABOR, D. (1972). Transfer of ptfe and related polymers in a sliding experiment. *Nature*, 237(75):88–90.

[Poquillon *et al.*, 2002] POQUILLON, D., LEMAITRE, J., BACO-CARLES, V., TAILHADES, P. et LACAZE, J. (2002). Cold compaction of iron powders—relations between powder morphology and mechanical properties: Part i: Powder preparation and compaction. *Powder Technology*, 126(1):65 – 74.

[Quinn Jr *et al.*, 1951] QUINN JR, F. A., ROBERTS, D. E. et WORK, R. (1951). Volume-temperature relationships for the room temperature transition in teflon. *Journal of Applied Physics*, 22(8):1085–1086.

[Radjai et Roux, 1995] RADJAI, F. et ROUX, S. (1995). Friction-induced self-organization of a one-dimensional array of particles. *Phys. Rev. E*, 51:6177–6187.

[Radjai *et al.*, 1999] RADJAI, F., ROUX, S. et MOREAU, J. J. (1999). Contact forces in a granular packing. *Chaos: An Interdisciplinary Journal of Nonlinear Science*, 9(3):544–550.

[Rae et Brown, 2005] RAE, P. et BROWN, E. (2005). The properties of poly(tetrafluoroethylene) (ptfe) in tension. *Polymer*, 46(19):8128 – 8140. Controlled Macromolecular Synthesis and Controlled Architectures - Supramolecular Polymer Assemblies {IUPAC} {MACRO} 2004.

[Rae et Dattelbaum, 2004] RAE, P. et DATTELBAUM, D. (2004). The properties of poly(tetrafluoroethylene) (ptfe) in compression. *Polymer*, 45(22):7615 – 7625.

[Rahmoun *et al.*, 2009] RAHMOUN, J., MILLET, O. et FORTIN, J. (2009). Friction effect on stresses in ensiled granular media. *Computers and Geotechnics*, 36(7):1113 – 1124.

[Rigby et Bunn, 1949] RIGBY, H. et BUNN, C. (1949). A room-temperature transition in polytetrafluoroethylene. *Nature*, 164:583.

[Roscoe *et al.*, 1958] ROSCOE, K., SCHOFIELD, A. et WROTH, C. (1958). On the yielding of soils. *Geotechnique*, 8(1):22–53.

[Roudsari et Puri, 2009] ROUDSARI, S. S. et PURI, V. M. (2009). Modeling of powder deposition into shallow dies for three filling methods. *KONA*, 27:228–238.

[Roux et Radjaï, 2002] ROUX, S. et RADJAÏ, F. (2002). Statistical approach to the mechanical behavior of granular media. *In* AREF, H. et PHILLIPS, J., éditeurs : *Mechanics for a New Mellennium*, pages 181–196. Springer Netherlands.

[Sawyer *et al.*, 2003] SAWYER, W., FREUDENBERG, K. D., BHIMARAJ, P. et SCHADLER, L. S. (2003). A study on the friction and wear behavior of {PTFE} filled with alumina nanoparticles. *Wear*, 254(5,ÄöÄì6):573 – 580.

[Sawyer *et al.*, 2014] SAWYER, W. G., ARGIBAY, N., BURRIS, D. L. et KRICK, B. A. (2014). Mechanistic studies in friction and wear of bulk materials. *Annual Review of Materials Research*, 44(1):395–427.

[Schofield et Wroth, 1968] SCHOFIELD, A. et WROTH, P. (1968). *Critical state soil mechanics*. McGraw-Hill (New York).

[Seguela, 2005] SEGUELA, R. (2005). On the strain-induced crystalline phase changes in semi-crystalline polymers: Mechanisms and incidence on the mechanical properties. *Journal of Macromolecular Science, Part C: Polymer Reviews*, 45(3):263–287.

[Shang *et al.*, 2011] SHANG, C., SINKA, I. et PAN, J. (2011). Constitutive model calibration for powder compaction using instrumented die testing. *Experimental mechanics*, 52(7):903–916.

[Shima et Mimura, 1986] SHIMA, S. et MIMURA, K. (1986). Densification behaviour of ceramic powder. *International journal of mechanical sciences*, 28(1):53–59.

[Sinka et Cocks, 2007] SINKA, I. et COCKS, A. (2007). Constitutive modelling of powder compaction - ii. evaluation of material data. *Mechanics of Materials*, 39(4):404 – 416.

[Sinka *et al.*, 2001] SINKA, I., COCKS, A. et TWEED, J. (2001). Constitutive data for powder compaction modeling. *Journal of engineering materials and technology*, 123(2):176–183. eng.

[Speerschneider et Li, 1963] SPEERSCHNEIDER, C. J. et LI, C. H. (1963). A Correlation of Mechanical Properties and Microstructure of Polytetrafluoroethylene at Various Temperatures. *Journal of Applied Physics*, 34:3004–3007.

[Sperati et Starkweather Jr, 1961] SPERATI, C. A. et STARKWEATHER JR, H. (1961). *Fluorine-containing polymers. II. Polytetrafluoroethylene*. Springer.

[Subhash V. Gangal, 2002] SUBHASH V. GANGAL, P. D. B. (2002). *Perfluorinated Polymers, Polytetrafluoroethylene*. John Wiley and Sons, Inc.

[Tanaka et Kawakami, 1982] TANAKA, K. et KAWAKAMI, S. (1982). Effect of various fillers on the friction and wear of polytetrafluoroethylene-based composites. *Wear*, 79(2):221 – 234.

[Tervoort *et al.*, 2002] TERVOORT, T. A., VISJAGER, J. F. et SMITH, P. (2002). Melt-processable poly(tetrafluoroethylene)—compounding, fillers and dyes. *Journal of Fluorine Chemistry*, 114(2):133 – 137. 13th European Symposium on Fluorine Chemistry (ESFC-13).

[Tomičević *et al.*, 2013] TOMIČEVIĆ, Z., HILD, F. et ROUX, S. (2013). Mechanics-aided digital image correlation. *The Journal of Strain Analysis for Engineering Design*, page 0309324713482457.

[Tripodi *et al.*, 1995] TRIPODI, M., PURI, V., MANBECK, H. et MESSING, G. (1995). Elastoplastic finite element model development and validation for low pressure uniaxial compaction of dry cohesive powders. *Powder Technology*, 85(3):241 – 251.

[Turner et Ashby, 1996] TURNER, C. et ASHBY, M. (1996). The cold isostatic pressing of composite powders—i. experimental investigations using model powders. *Acta Materialia*, 44(11):4521 – 4530.

[Tvergaard, 1981] TVERGAARD, V. (1981). Influence of voids on shear band instabilities under plane strain condition. *Int. J. Fracture Mech.*, 17:389.

[Tvergaard, 1982] TVERGAARD, V. (1982). On localization in ductile materials containing spherical voids. *Int. J. Fract.*, 18:237–251.

[Tvergaard et Needleman, 1984] TVERGAARD, V. et NEEDLEMAN, A. (1984). Analysis of the cup-cone fracture in a round tensile bar. *Acta Metallurgica*, 32(1):157 – 169.

[van Rooyen et Backofen, 1960] van ROOYEN, G. et BACKOFEN, W. (1960). A study of interface friction in plastic compression. *International Journal of Mechanical Sciences*, 1(1):1 – 27.

[Watson et Wert, 1993] WATSON, T. et WERT, J. (1993). On the development of constitutive relations for metallic powders. *Metallurgical Transactions A*, 24(9):2071–2081.

[Wecker *et al.*, 1972] WECKER, S. M., DAVIDSON, T. et BAKER, D. W. (1972). Preferred orientation of crystallites in uniaxially deformed polytetrafluoroethylene. *Journal of Applied Physics*, 43:4344–4348.

[Wu *et al.*, 2003] WU, C.-Y., DIHORU, L. et COCKS, A. C. (2003). The flow of powder into simple and stepped dies. *Powder Technology*, 134(1–2):24 – 39.

[Wu *et al.*, 2005] WU, C.-Y., RUDDY, O., BENTHAM, A., HANCOCK, B., BEST, S. et ELLIOTT, J. (2005). Modelling the mechanical behaviour of pharmaceutical powders during compaction. *Powder Technology*, 152(1 - 3):107 – 117.

[Yi et Puri, 2013] YI, H. et PURI, V. M. (2013). Stress gradient within powder en masse during hydrostatic compression. *Powder Technology*, 239(0):47 – 55.

[Young, 1975] YOUNG, R. J. (1975). Deformation mechanisms in polytetrafluoroethylene. *Polymer*, 16(6):450 – 458.

# List of Figures

# List of Tables